Geometric Models of Brain White Matter for Microstructure Imaging with Diffusion MRI

Eleftheria Panagiotaki

A dissertation submitted in partial fulfilment
of the requirements for the degree of
Doctor of Philosophy
of the
University College London.

Department of Computer Science
University College London

April 6, 2011

I, Eleftheria Panagiotaki, confirm that the work presented in this thesis is my own. Where information has been derived from other sources, I confirm that this has been indicated in the thesis.

_____

Abstract

The research presented in this thesis models the diffusion-weighted MRI signal within brain white matter tissue. We are interested in deriving descriptive microstructure indices such as white matter axon diameter and density from the observed diffusion MRI signal. The motivation is to obtain non-invasive reliable biomarkers for early diagnosis and prognosis of brain development and disease. We use both analytic and numerical models to investigate which properties of the tissue and aspects of the diffusion process affect the diffusion signal we measure.

First we develop a numerical method to approximate the tissue structure as closely as possible. We construct three-dimensional meshes, from a stack of confocal microscopy images using the marching cubes algorithm. The experiment demonstrates the technique using a biological phantom (asparagus). We devise an MRI protocol to acquire data from the sample. We use the mesh models as substrates in Monte-Carlo simulations to generate synthetic MRI measurements. To test the feasibility of the method we compare simulated measurements from the three-dimensional mesh with scanner measurements from the same sample and simulated measurements from an extruded mesh and much simpler parametric models. The results show that the three-dimensional mesh model matches the data better than the extruded mesh and the parametric models revealing the sensitivity of the diffusion signal to the microstructure.

The second study constructs a taxonomy of analytic multi-compartment models of white matter by combining intra- and extra-axonal compartments from simple models. We devise an imaging protocol that allows diffusion sensitisation parallel and perpendicular to tissue fibres. We use the protocol to acquire data from two fixed rat brains, which allows us to fit, study and evaluate the models. We conclude that models which incorporate non-zero axon radius describe the measurements most accurately. The key observation is a departure of signals in the parallel direction from the two-compartment models, suggesting restriction, most likely from glial cells or binding of water molecules to the membranes. The addition of the third compartment can capture this departure and explain the data.

The final study investigates the estimates using in vivo brain diffusion measurements. We adjust the imaging protocol to allow an in vivo MRI acquisition of a rat brain and compare and assess the taxonomy of models. We then select the models that best explain the in vivo data and compare the estimates with those from the ex vivo measurements to identify any discrepancies. The results support the addition of the third compartment model as per the ex vivo findings, however the ranking of the models favours the zero radius intra-axonal compartments.

Acknowledgements

I wish to thank all the people who helped me complete this study.

I would like to express immense gratitude to my supervisor Prof. Daniel Alexander who gave me the opportunity to study with his team, and introduced me to the wonderfully intricate world of medical imaging. He has indeed been the best advisor and teacher I ever had and has constantly encouraged, guided and helped me throughout my PhD work. It has been a great honour being one of your students. I would like to express my infinite appreciation to my co-supervisor Dr. Matt Hall for enthusiastic supervision, adventurous discussions and his generous guidance, which was always given with humour and lots of maths and physics (in a good way!). I would also like to thank my second supervisor, who was also my MSc supervisor, Dr. Simon Julier for providing a different perspective to my project with his comments and discussions, especially during the first year.

I would like to specially thank Dr. Bernard Siow, for all his help with the very long MRI acquisitions, his amazing patience when things went wrong, and good spirit. I wish to express my sincere thanks to Dr. Tim Dyrby for all his help with the in vivo acquisitions in Denmark, Prof. Yaviv Assaf for the in vivo MRI data from Tev Aviv, and Dr. Chris Thrasivoulou for his help with the confocal acquisitions. Thanks to my colleague and friend Hubert Fonteijn for helping me with the very first MRI acquisitions and showing me the ropes for analysing vast amounts of MRI data and for all the fun times. I would like to thank my friend Torben Schneider for helping me tame the numerous models, and most of all, for being able to cope with me when things did not go as planned, which was very often.

I would never have made it without the valuable help of my two dear friends Gemma Morgan and Dr. Shahrum Nedjati-Gilani. Thanks for making work a fun place to be, for all your advice and support. Special thanks to Gemma for all her time and effort, for reading my thesis multiple times and providing valuable feedback. Special thanks to Dr. Ivana Drobnjak for very patiently tutoring me for NMR physics. Also I would like to thank all the people in the Microstructure Imaging Group, especially Dr. Gary Hui Zhang for letting me borrow his expertise whenever I needed it. I wish to thank my good friends from UCL: Jenny, Kiran, Tony, Bai Yu, Sadia, James, Aitor, Christos and Teresa for all the fun times in and out of the office. Many thanks to my very initial friends in England: Maria, Rocio and Jim for their love and support from the Masters year until now.

Finally, I would like to thank my oldest friends and my family. Will for his endless patience, kind indulgence, his encouragement and understanding, who shared my happiness and kept me going during the hardships of not one, but two PhDs. Alex, who has always been the best friend anyone could ask for,

for his support and encouragement during all these years, and just for always being there for me, even though we are so far away. I would like to thank my younger sister Athina for her extraordinary love and support. She is now starting her new life in England and I am sure great things await her. Finally, I would like to express my deepest gratitude to my loving parents Tasso and Haroula, for allowing me to pursue my dreams, for their absolute confidence in me, for their encouragement and continuous support since I was born. I owe them everything.

Εξαιρετικά αφιερωμένο στους πολυαγαπημένους μου γονείς,
σας ευχαριστώ για την απέραντη αγάπη και φροντίδα σας

Contents

List of Figures

List of Tables

Chapter 1

Introduction

The brain is the most sophisticated organ in the human body, and the investigation of its intricate functionality and morphology has remained a significant area of research since the 1800s. The study of neuroanatomy and function is of paramount importance to understanding and monitoring both cognitive and bodily processes, and the development and treatment of brain disorders.

The work documented in this thesis makes a contribution towards comprehending brain morphology, with respect to accurately understanding its microstructural organisation using Magnetic Resonance Imaging (MRI) methods. The traditional methodology for investigating tissue microstructure is histology, which is a highly invasive process. This work develops and investigates non-invasive methods able to measure the same microstructure as histology, with the potential to be applied in a clinical context.

The outer layer of the brain is known as grey matter, which contains neurons, the brain's processing centres. These regions are responsible for cognitive tasks that involve thought and creativity as well as processes like breathing, heart rate and muscle control. For the operation of these tasks, grey matter regions are connected in complex networks to communicate and coordinate. White matter is the brain's electrical cabling that forms the required connections between the grey matter processing centres. At a microscopic level, white matter is mainly composed of axons which are approximately cylindrical extensions from neurons that connect different areas in the brain and other parts of the body. There are approximately 100 billion axons, occupying more than half of the brain, with diameters varying from 0.1 microns to several microns [Wax95]. The majority of axons over 0.2 microns in diameter are covered with a fatty sheath, known as myelin. It is the myelin that gives white matter its whitish appearance. The anatomical size and shape of axons alters during maturation and is also known to be altered by diseases like Alzheimer's and schizophrenia [BTP+98, HSI+98, HSK+97, MSD+72, UOV+01]. Accurate anatomical knowledge of brain microstructure is important not only for prevention and treatment of brain disorders, but also for understanding functional interactions in the brain.

Recently developed techniques such as Diffusion-Weighted Magnetic Resonance Imaging (DW-MRI) are able to capture the entangled structural organisation of brain white matter, identifying changes and alterations in microstructure. DW-MRI is a powerful imaging modality that provides unique insight into brain tissue microstructure and connectivity. The technique measures the displacement of particles, usually water molecules, non-invasively. Since the displacement of particles is affected by the presence

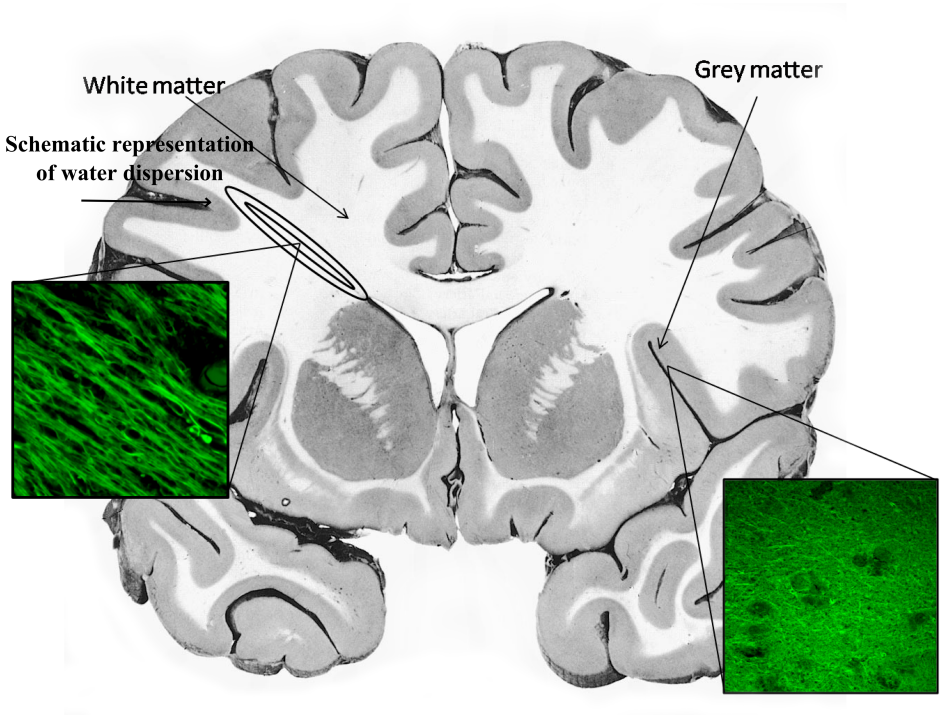

Figure 1.1: *Coronal section through the cerebrum of a human brain showing grey and white matter regions and confocal microscopy images of these regions. The figure shows a schematic representation of water diffusion in the white matter region which reveals the fibre direction. The brain section is taken from [RHM87] and the confocal miscopy images from [AK00].*

of the surrounding structure in the environment, DW-MRI can be used to make inferences about the local structure. It has become an essential probe for highlighting and monitoring tissue microstructure changes in development and disease. Diffusion MRI is particularly useful for investigating white matter because axons are arranged in parallel bundles and their myelin sheaths restrict diffusion across the bundles to a greater degree than along them, causing diffusion to be anisotropic [Bea02]. The direction of most diffusion reveals the fibre direction [BML94]. Figure 1.1 presents schematically how diffusion reveals the fibre direction in areas of white matter.

The quantitative nature of diffusion imaging is particularly well-suited for studying white matter diseases since damaged or disrupted cellular structures alter the diffusion characteristics of the tissue. For example, in Alzheimers disease, studies estimate changes in diffusion anisotropy in white matter structures caused by axonal loss or demyelination (the breakdown of the myelin sheath around the axon) [SBL$^+$95, HAS$^+$99, BFF$^+$02]. Axonal damage has also been reported in rat spinal cord injury, causing a decrease in diffusion anisotropy [FH97]. Studies of multiple sclerosis [DWC$^+$04, BMP$^+$01] show that multiple sclerosis lesions have higher diffusivity than normal appearing white matter, probably because of demyelination and axon death.

The simplest and most commonly used model for relating the DW-MRI signal to diffusion in tissue is the diffusion tensor (DT) [BML94]. This model provides useful microstructural markers of tissue integrity such as Fractional Anisotropy (FA) [BP96b], a measure of how directional diffusion is, and Mean Diffusivity (MD), the average diffusivity, which are widely used in clinical studies.

1.1 Problem Statement

The problem that motivates this work is that of obtaining specific microstructure indices, such as axon diameter and density, for brain white matter tissue. Diffusion MRI methods can provide markers, such as FA and MD, that change in different conditions due to brain development and pathology, but we cannot directly relate them to specific microstructure changes and so interpretation is problematic. Until now only histological methods can give specific information about microstructural tissue changes. However, these techniques are highly invasive and can introduce bias, altering the geometric characteristics and the chemical environment of the tissue, through dissection and fixation procedures [EmsamvI09].

Several preliminary studies in diffusion MRI [Ale08, AB05, BWJJ03, AHH+10] make progress towards direct microstructure imaging. They work by fitting more descriptive models of tissue than the DT that relate specific parameters, such as cell size and density, directly to the measured signal. However, the current literature still lacks a reliable and validated technique that can produce non-invasive microstructural parameter estimates.

Another substantial and ongoing problem is validating the accuracy and precision of diffusion MRI methods for attaining clinical use. For studies of the brain this becomes immensely difficult without invasive means. Validation against known ground truth is difficult due to the complexity of the tissue structure and the way tissue properties affect the diffusion measurements. Simulations can be used for testing and tuning of diffusion MRI techniques by providing synthetic ground truths.

1.2 Project Aims

The aims of this project are as follows:

1. Construct a model of tissue structure that approximates any biological tissue as closely as possible.

2. Identify tissue and diffusion properties that most affect the diffusion MR signal. We then use this knowledge to construct models of the diffusion MRI signal in white matter, to estimate microstructure parameters from both ex vivo and in vivo data.

3. Assess to what extent methods of modelling diffusion using tissue models with different complexities are representative of the system of interest.

4. Determine imaging protocols able to compare different complexity models of the diffusion MR signal in brain white matter.

5. Ascertain how well tissue models translate from ex vivo to in vivo. Characterise differences in the diffusion MRI signal from ex vivo and in vivo data and identify which models are appropriate to use in each situation.

1.3 Summary of contributions

The key contributions of this thesis are as follows:

- A highly detailed tissue model from microscopy images using computer-graphics methods for generation of accurate synthetic data. This model contributes to project aims 1, 2 and 3. To satisfy project aim 3 we construct mesh models with various resolutions and test the synthetic data against both scan data and data generated from simple parametric models.

- A taxonomy of analytic models. We construct a taxonomy of multi-compartment models for the diffusion MRI signal within white matter brain tissue. We highlight the relationship between all the models in the literature and reveal a range of previously untested models. We also provide a consistent naming system and implement all the models in the open-source toolkit, Camino [CBNG+06]. This taxonomy contributes towards project aims 2-5.

- Imaging protocols for comparing the different models depending on the sample. This contributes towards all project aims, allowing segregation and assessment of the models, as well as investigation of imaging parameters for sparser data.

- Determination of how faithfully a model is able to represent live and fixed tissue. The process identifies differences in which models explain the data most accurately and characterises dissimilarities in the important observed effects in live and fixed samples. This contributes to all five project aims. We perform ex vivo and in vivo MRI experiments on brain white matter, and use the taxonomy of analytic models to study, compare and assess the models. Finally, we examine the deviation of parameter estimates in vivo and ex vivo.

1.4 Thesis Structure

Chapter 2 contains background information on white matter, nuclear magnetic resonance, diffusion MRI, and in particular, the diffusion process and tissue modelling. Chapter 3 presents a method for generating three-dimensional mesh models from microscopy images using the marching cubes algorithm and an experiment on a biological phantom for assessing the quality of synthetic data from the three-dimensional tissue model against both scan data and data from simpler parametric models. Chapter 4 introduces a taxonomy of analytic models for the diffusion MRI signal in brain white matter; a selection of which we use in the experimental work documented in Chapters 5 and 6. Chapter 5 describes an MRI experiment on fixed rat brain to compare and assess a selection of multi-compartment analytic models discussed in Chapter 4. Chapter 6 details an experiment on in vivo rat brain. This experiment again employs a selection of models from Chapter 4 to compare which are feasible and appropriate to use in a live brain and explores what differences arise from the in vivo and ex vivo parameter estimates. Chapter 7 concludes and gives suggestions for future work.

Chapter 2

Background

This chapter discusses the structure of the human brain in Section 2.1, focusing on white matter to give a neuroanatomical context for the modelling work we are going to present later on. Section 2.2 then provides an overview of the principles of magnetic resonance. Section 2.3 gives background information on diffusion-weighted MRI and describes the basic sequences for acquiring diffusion MRI measurements. Then it introduces two common approximations used in diffusion-weighted MRI data synthesis and analysis: the short gradient pulse (SGP) and the Gaussian phase distribution (GPD). Section 2.4 discusses Diffusion Tensor Imaging (DTI), the most widely-used diffusion MRI method for estimating microstructural features. Section 2.5 introduces two-compartment models of the diffusion MRI signal in white matter and Section 2.6 describes more complicated models, which comprise more than two-compartments. Section 2.7 reviews numerical techniques commonly used for modelling the diffusion-weighted signal in biological tissues. Section 2.8 summarises.

2.1 Anatomy of white matter

The white matter of the central nervous system contains axons, their insulating myelin sheaths and glial cells (see Figure 2.1). Axons constitute the pathways that carry chemical and electric signals from one part of the brain to another. More precisely, they are responsible for efficiently conducting information to and from the processing centres concentrated in the grey matter. They are grouped into bundles forming tracts. Most axons are arranged in parallel bundles, such as in the optic nerve however, some distinct populations may transverse the tract in opposite directions, such as the fibres in the corpus callosum, which connect the two hemispheres of the brain (see Figure 2.2) [EmsamvI09]. The length of the axons in the central nervous system varies from a few micrometres to metres. The range of diameters of myelinated axons varies throughout white matter from 0.1 to 10 micrometres [ASFZ92a]. The speed of the signals travelling along the axons depends directly on the axon diameter. Larger diameter axons correspond to higher conduction velocities because they have low resistance, whereas smaller diameter axons have high resistance slowing down the signal transmission [Hur39].

Axons often have an insulating sheath to increase the speed at which impulses propagate along the axon. This sheath consists of a substance called myelin. The myelin sheath surrounds the axon and is composed of a layer of proteins packed between two layers of lipids (see Figure 2.1 a). The myelin

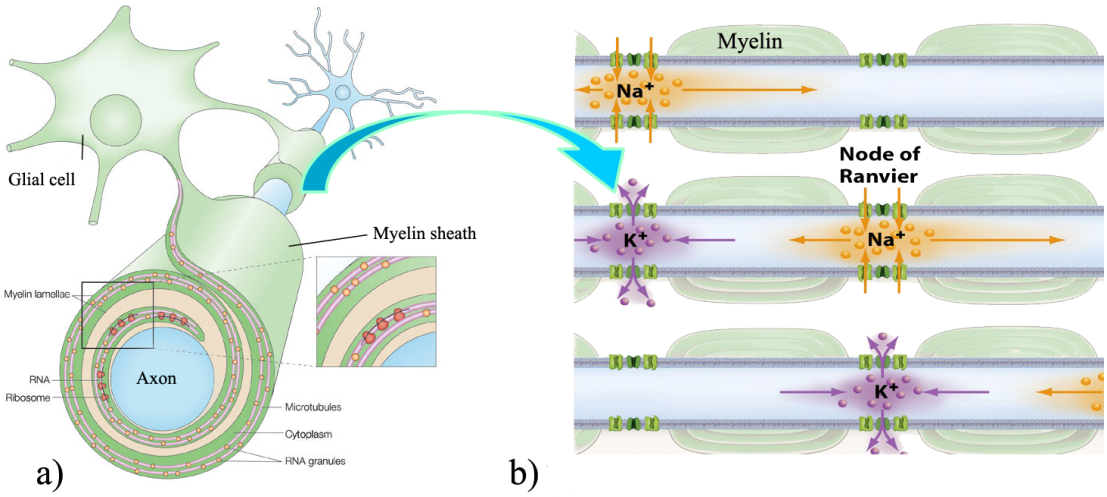

Figure 2.1: *a) Myelinated axon diagram showing the layers of myelin sheath and the oligodendrocyte glial cell. Figure taken from [SB05b]. b) Schematic representation of the axon showing the nodes of Ranvier. Figure taken from [Fre05].*

sheath does not cover the entire axon; it leaves small exposed sections uncovered which are called nodes of Ranvier (see Figure 2.1 b). The reason that the myelin sheath speeds up neural conduction is because as the charge spreads down an axon, myelination prevents ions from leaking out across the plasma membrane. The charge then spreads until it reaches a node of Ranvier (which is packed with Na^+ channels), as shown in Figure 2.1 b. In this way electrical signals continue to jump down the axon much faster than they move down an unmyelinated cell. Therefore the fastest velocities are achieved in large myelinated axons [VdKVB05].

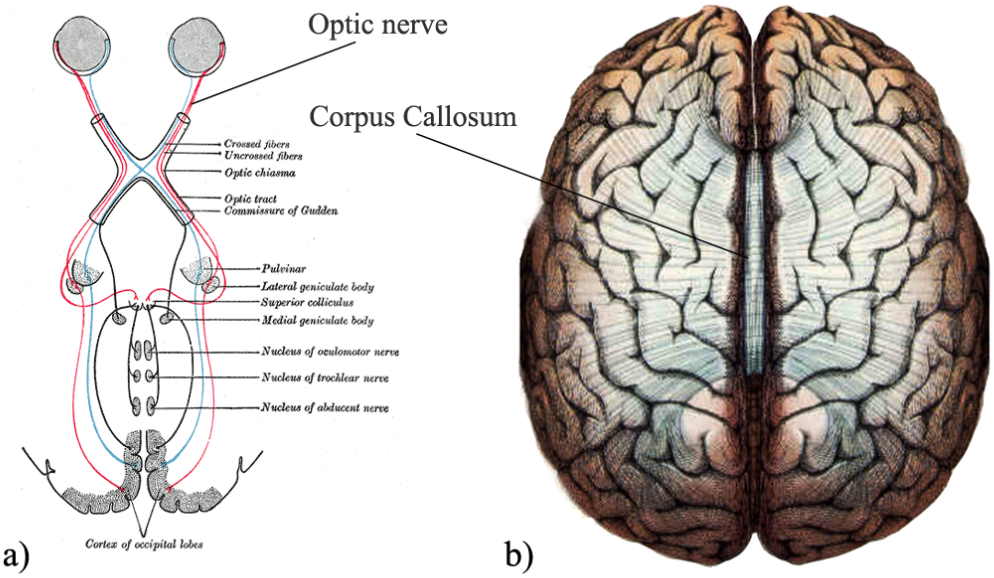

Figure 2.2: *a) Schematic representation of the optic nerve fibre tracts. b) Dorsal illustration of the brain showing the corpus callosum fibres connecting the two cerebral hemispheres. Images taken from [W+89].*

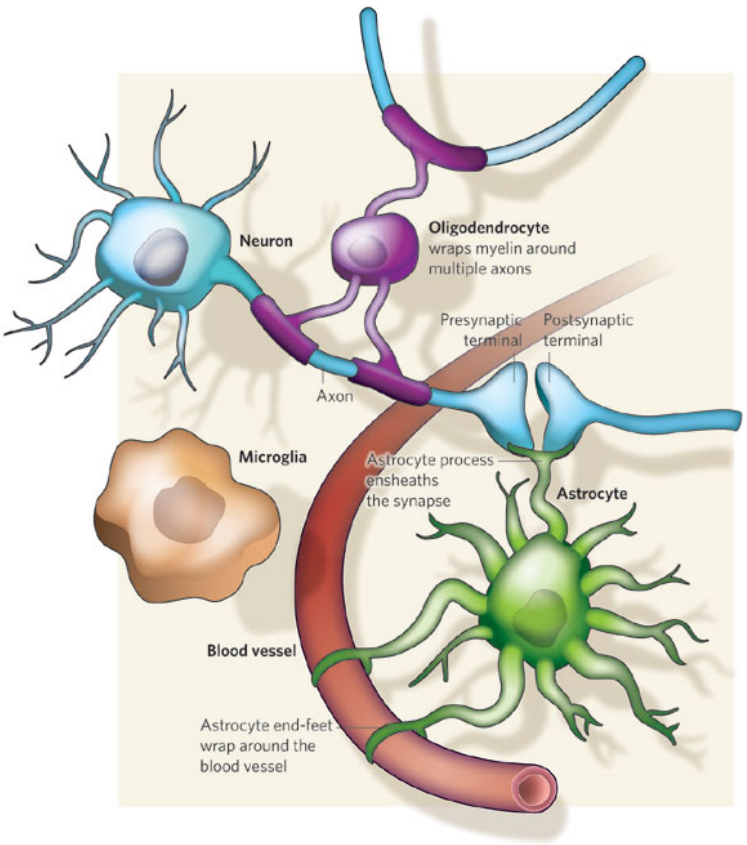

Figure 2.3: *Schematic representation of different types of glial cells. Figure taken from [AB09].*

Myelin is produced by specialized cells called glial cells (see Figure 2.1 a). There are a number of different types of glial cell in the central nervous system including: oligodendrocytes, astrocytes and microglia. The cells are named after their structure: oligodendrocytes because they have few branches, astrocytes due to their characteristic star shape and microglia because of their small size (see Figure 2.3). The primary function of oligodendrocytes is to produce the myelin sheath that insulates the axons. Both oligodendrocytes and astrocytes provide physical support to the myelin and the axons. Each oligodendrocyte can supply myelin for several axons and each axon can be supplied by several oligodendrocytes. The microglia play a part in the immunity of the nervous system, removing dead cells [LS98, ALS09].

2.1.1 Histology studies

The study of the microscopic anatomy of tissue is known as histology. The traditional tools for studying tissue are the microtome, which is a sectioning device, the tissue stain, to enhance contrast in the microscopic image of specific structures in the tissue, and the microscope. With these tools, the raw appearances of the cells can be examined in healthy and diseased tissues, enabling considerable refinement of clinical diagnosis and prognosis [MB49]. Next we review studies that report statistical details regarding the anatomy of brain white matter.

Lamantia and Rakic [LR90] use electron microscopy to determine the number, type and distribution of distinct classes of axons and glial cells in cerebral commissures of the rhesus monkey. The corpus callosum interconnects the frontal, parietal, temporal, and occipital cortices (see Figure 2.4) with more

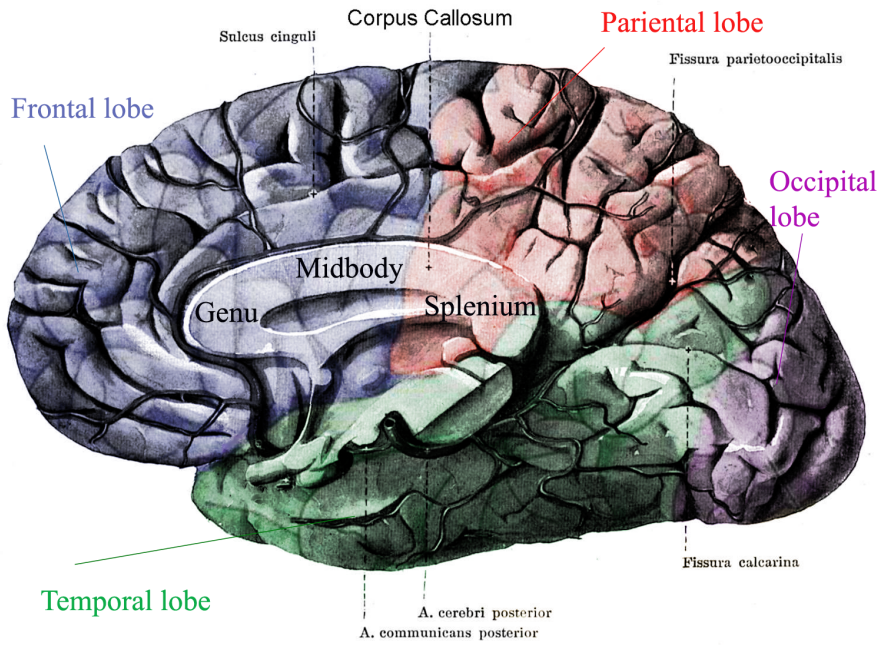

Figure 2.4: *Illustration of mid-sagittal section of a human brain indicating the corpus callosum, the areas of the genu, the midbody and the splenium, and overlaying the four lobes of the cerebral hemispheres. Figure taken from [Ana].*

than 56 million callosal fibers. They estimate the range of diameters of myelinated axons from 0.08-2.5 μm and determine that subregions of the corpus callosum consist of five classes of axons containing different proportions of myelinated to unmyelinated axons.

Partadiredja et al [PMO03] study the number, size and type of axons in rat subcortical white matter on the left and right sides of the brain. In particular, they investigate the morphological differences in diameter and proportion of myelinated and unmyelinated axons. Using transmission electron microscopy and stereological methods they compare subcortical white matter in three regions: frontal, parietal and occipital. The transmission electron microscope is the oldest form of electron microscopy and operates on the same basic principles as the light microscope but uses electrons instead of light which allows a resolution a thousand times better than with a light microscope. They estimate the range of diameters of myelinated axons between 0.04 and 2.24 μm and unmyelinated from 0.02 and 1.38 μm. Also, they found no differences between the two sides of the brain in either type of axon in any of the regions; however, there were significant differences in diameter and numerical density of axons. Compared to previous studies of the corpus callosum they determine higher proportions of unmyelinated axons in lateral white matter.

Aboitiz et al. [ASFZ92a] study the fibre composition in ten regions of the human corpus callosum. They examine 10 female and 10 male brains using light microscopy. They determine that the density of thin fibres is higher in the genu (see Figure 2.4) and decreases towards the posterior midbody, while at the splenium the density increases again. They also show that the proportion of large diameter fibres is higher in the midbody than in the genu and splenium and report individual differences in the fibre composition of the human corpus callosum [ASFZ92b].

2.1.2 Discussion

As a matter of course, histology has been an important tool for inferring tissue structures at a microscopic level and is generally regarded as the gold standard. However, there are many complications that need to be considered regarding microscopic examination. Procedures for viewing tissue using histological methods can significantly alter the original state of the tissue. Post mortem samples are subject to a lot of pre-processing that can modify microstructural features such as cell densities and size of microscopic tissue elements. These alterations may come from staining techniques, the sectioning and/or the fixation of the tissue. Another aspect that affects the integrity and proper preservation of the sample is the time interval between death and refrigeration [EmsamvI09]. To account for any discrepancies due to these issues, many histological studies (e.g. [ASFZ92a], [PMO03]) use approximate correcting factors, mainly for shrinkage of the tissue that occurs during fixation. Finally, histopathology uses biopsy to obtain tissue samples. This technique can be exceedingly difficult to perform and in many cases of advanced stages of pathology can be impossible. This motivates the need for non-invasive imaging techniques to measure the information we obtain from histology.

2.2 Nuclear Magnetic Resonance

In this section we provide a concise description of the key concepts of nuclear magnetic resonance (NMR) to understand the principles of MRI. NMR is a phenomenon which occurs when the nuclei of certain atoms are exposed to a magnetic field, and occurs due to the interaction between nuclei and electromagnetic radiation at a specific frequency.

2.2.1 Physical principles of Magnetic Resonance

This section describes the complex process of how the MR signals are generated, detected and processed into an image. We start by discussing the behaviour of one spin and then how a collection of spins is converted into a magnetisation vector $\mathbf{M}_0$, a transverse magnetisation $\mathbf{M}_{xy}$, and an electrical signal. The signal is then encoded into the image using the gradient pulse $\mathbf{G}$.

2.2.2 Magnetic Moment

When a nucleus has an odd atomic number it possesses a property called angular momentum I, also known as spin. Although the nuclear spin is a property governed by quantum mechanics, in the classical vector model it can be represented as a spinning charged sphere which creates the magnetic moment $\boldsymbol{\mu}$ [LLiMS00, Hor95]. More precisely, the magnetic moment $\boldsymbol{\mu}$ is directly proportional to I with a physical constant γ known as the gyromagnetic ratio:

$$\boldsymbol{\mu} = \gamma \boldsymbol{I}. \tag{2.1}$$

The gyromagnetic ratio defines the frequency with which a nucleus will precess around a magnetic field and is unique for each particle and environment. This means that nuclei will spin at a known frequency in a specific magnetic field. In clinical MRI hydrogen nuclei are typically used because they are the most abundant nucleus of this type in the human body, in both water and fat. Also, the value of γ

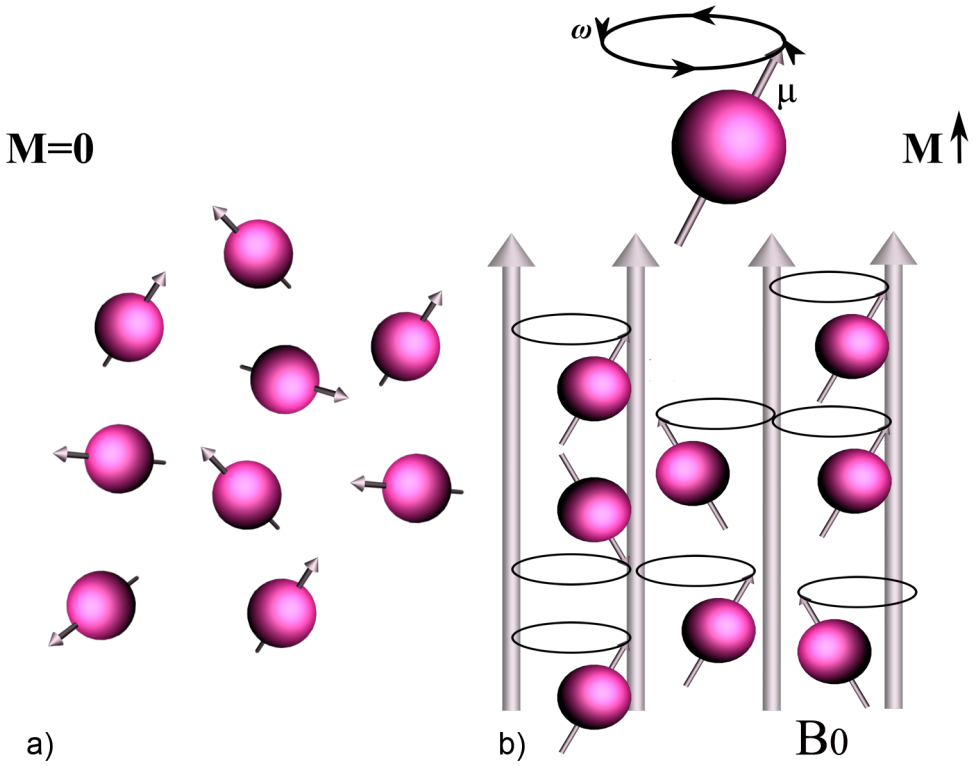

Figure 2.5: *Nuclear magnetic moment vectors a) pointing in random directions and b) aligned in the direction of an external magnetic field.*

is larger for hydrogen than for other nuclei, producing a larger magnetic moment.

2.2.2.1 Effect of the magnetic field

In the absence of an external magnetic field $\mathbf{B}_0$ the magnetic moments of the nuclei are randomly oriented, cancelling each other, giving a null net magnetisation (see Figure 2.5 a) [Sue02]. When nuclei are placed in an external magnetic field the intrinsic magnetic moment and spin cause the nuclei to precess about the axis of the static field. The nuclear spins then align either parallel or antiparallel to the external field, with the majority of spins aligning parallel to the field, since it is a lower energy state (see Figure 2.5 b) [LLiMS00]. The sum of all the magnetic moments is called the net magnetisation vector **M**, as presented in Figure 2.6.

The frequency of nuclear precession of protons in an external magnetic field $\mathbf{B}_0$ is determined by the strength of the magnetic field and the gyromagnetic ratio:

$$\omega_0 = \gamma \mathbf{B}_0 \tag{2.2}$$

where ω_0 is the angular frequency known as the Larmor frequency.

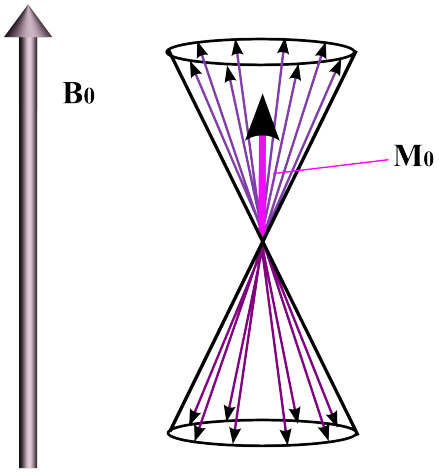

Figure 2.6: *Adding the individual spin magnetisation vectors results in a net magnetisation,* $\boldsymbol{M}_0$.

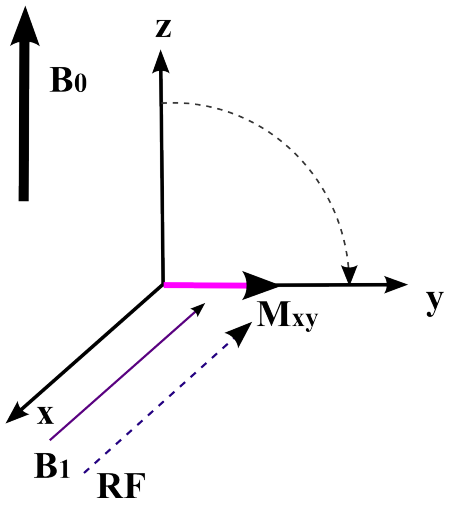

Figure 2.7: *After the RF transition the net magnetisation vector is 'flipped' away from the axis of the static magnetic field* $\boldsymbol{B}_0$ *(demonstrated here for an example flip angle of* 90° *degrees).*

2.2.2.2 Excitation

The NMR signal is generated from the net magnetisation vector $\mathbf{M}_0$ with a radiofrequency (RF) pulse. An RF pulse is an electromagnetic field $\mathbf{B}_1$ which oscillates at a certain frequency. The condition for resonance to occur is that the frequency of the RF pulse has to be the same as the Larmor frequency of the precessing protons, and transmitted perpendicular to the magnetic field $\mathbf{B}_0$. When this happens the system becomes 'excited' and is perturbed from its equilibrium state to a higher energy state.

In a rotating frame of reference, the net magnetisation vector 'flips' away from the direction of the static field during excitation. The angle that the net magnetisation vector rotates is commonly called the 'flip' angle and depends on the strength and duration of the RF pulse. For example, a common flip angle of 90° degrees, will flip the net magnetisation vector into the plane perpendicular to the direction of the static field (xy plane). This means that the longitudinal magnetisation $\mathbf{M}_z$ (along the z axis) aligned with the $\mathbf{B}_0$ decreases and a transverse magnetisation $\mathbf{M}_{xy}$ appears. So at 90° $\mathbf{M}_{xy} = \mathbf{M}_0$ and $\mathbf{M}_z = 0$ (see

Figure 2.7).

2.2.2.3 Relaxation

After the RF pulse the spins return to their original state and the magnetisation can be detected and converted into an electrical signal that we can measure. The return to equilibrium of the net magnetisation is called relaxation. During this time two separate phenomena occur: the recovery of the longitudinal magnetisation $\mathbf{M}_z$ (in the direction of the static field), and the decay of the transverse magnetisation $\mathbf{M}_{xy}$. These two processes are described by their time constants T_1 and T_2. T_1 relaxation is characterised by the longitudinal return of the net magnetisation to its low energy state in the direction of the main magnetic field. T_2 relaxation occurs when spins interact with each other (spin-spin interaction), modifying their precession rate and causing a decrease in the transverse magnetisation $\mathbf{M}_{xy}$. T_2 is characteristic of specific tissue and also determines the rate of dephasing for the protons associated with that tissue.

T_2 decay assumes that the main external field $\mathbf{B}_0$ is homogeneous. In reality, there are many factors creating imperfections in the homogeneity of a magnetic field. Every tissue has a different magnetic susceptibility which distorts the field at tissue borders, particularly at air/tissue interfaces. Dephasing due to magnetic field imperfections is called T_2^* decay or T_2^* relaxation.

2.2.2.4 MR signal and image generation

The MR signal is collected during relaxation, and it is the moving transverse magnetisation $\mathbf{M}_{xy}$, generated while the spins return to their original states. The MR signal we detect is called the Free Induction Decay or FID signal and is a signal which decays according to the T_2 relaxation. The signal is

$$S(t) = \mathbf{M}_0 \exp(\frac{-t}{T_2}) \tag{2.3}$$

where $\mathbf{M}_0$ is the steady-state magnetisation before any T_2 decay.

To generate an image we first choose a slice by exciting a selection of spins, usually in the z direction. Within the slice we encode spatial information. To achieve that we need a gradient field $\mathbf{G} = (G_x, G_y, G_z)$. A gradient magnetic field is a small spatially varying magnetic field superimposed on $\mathbf{B}_0$. The gradient G_z causes protons at different locations along the gradient direction to precess at different frequencies, and only protons precessing with frequencies belonging to the range of the RF pulse sequence will be excited

$$\omega_0 = \gamma(\mathbf{B}_0 + \mathbf{G}(t)\mathbf{R}(t)) \tag{2.4}$$

where $\mathbf{R}$ is the position of the spin at time t. The gradients G_x and G_y allows for spatial encoding within the slice. Thus, each x, y, pixel possesses a unique frequency which encode the spatial location of the pixel in the image. The signal is then received in frequency space, or k-space. The frequency information is then reconstructed into an image using a Fourier Transform [LLiMS00].

2.2.3 Pulse Sequences

A pulse sequence is a set of predefined instructions used to generate the MR signal. A pulse sequence can get very long and intricate, and small changes in the sequence can cause considerable changes in the resulting image. The pulse sequence specifies the waveform of the RF pulses and the waveform of the magnetic field gradient **G**.

2.2.3.1 Spin Echo Sequence

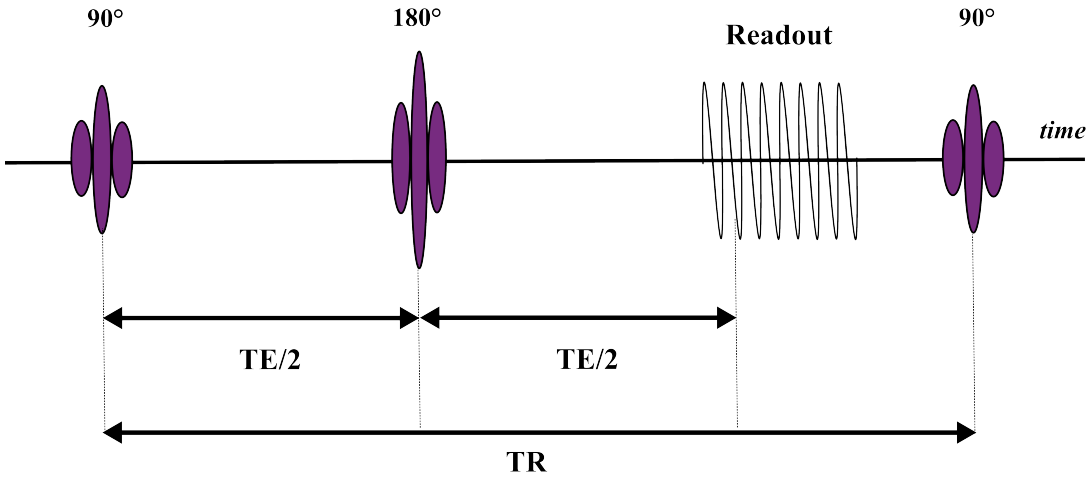

Figure 2.8: *Schematic representation of a spin-echo pulse sequence, where TR, is the time between successive excitation pulses and the echo time, TE is the time from the excitation pulse to the echo maximum.*

A spin echo sequence diagram is presented in Figure 2.8. The term "spin echo" comes from a signal property called "echo". A spin echo is formed when, during the relaxation process when the spins are dephasing, the excitation of a 180° RF pulse forces the spins to rephase, causing a regrowth in the MR signal. The complete process is as follows.

A spin echo sequence usually has a 90° excitation pulse followed by a 180° refocussing pulse. At time $t = 0$ after 90°, $\mathbf{M}_0$ is in the transverse plane. Between time $t = 0$ and $t = TE/2$ the spins dephase due to T_2^* relaxation acquiring different precessional speeds and go out of phase with each other. At $t = TE/2$ the 180° pulse is then used to 'flip' the spin vectors so that the previously slower vectors are precessing ahead of the previously faster ones. After a delay time equal with $TE/2$ all spins will be back in phase producing signal. This moment of spin coherence is called a spin echo [BS10, BKZF05]. The echo time, TE is the time it takes from the moment the spins were excited to the moment they are again in phase. Figure 2.9 illustrates the different phases of the spin vectors during the spin echo sequence.

In practice, one pulse sequence can be repeated many times. The time between successive excitation pulses is the repetition time TR. A long TR allows all of the longitudinal relaxation to occur, but also results in a long imaging time.

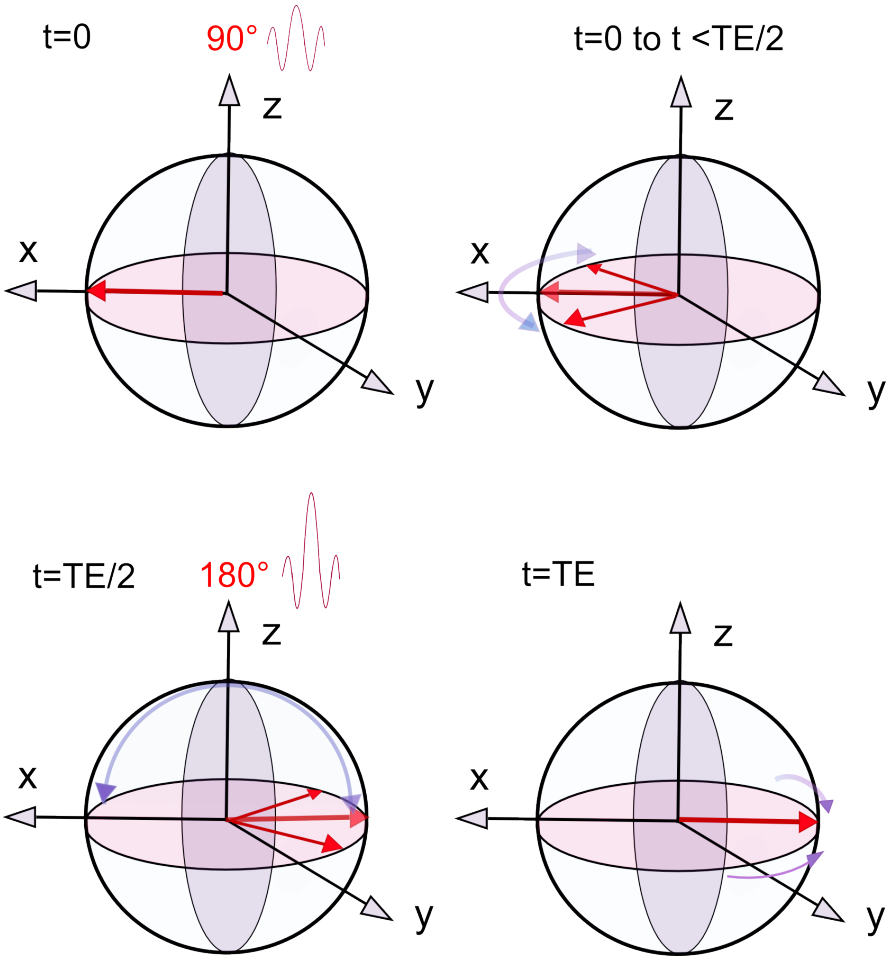

Figure 2.9: *Vector representation for the spin echo sequence.*

2.3 Diffusion-Weighted MRI

This section discusses two basic sequences used in diffusion-weighted MRI and introduces two common approximations used in diffusion-weighted MRI data synthesis and analysis: the short gradient pulse (SGP) and the Gaussian phase distribution (GPD).

2.3.1 Diffusion-weighted Sequences

An MRI pulse sequence can be modified to enhance signal loss from moving water molecules. This is called diffusion-weighting.

2.3.1.1 Pulse Gradient Spin Echo

The most common diffusion-weighted MRI pulse sequence is a spin echo sequence known as the Pulse Gradient Spin Echo (PGSE) which was developed by Tanner and Stejskal in 1965 [TS68]. We illustrate the pulse sequence in Figure 2.10.

The sequence of events is as follows. First, there is a 90° excitation pulse that aligns the spin phases. This is followed by a diffusion sensitisation pulse (or gradient pulse) **G** that adds a phase offset dependent on each individual spin's position along a chosen axis. The time δ is the gradient pulse duration. During the gradient pulse the local magnetic field is perturbed for each spin depending of their position along

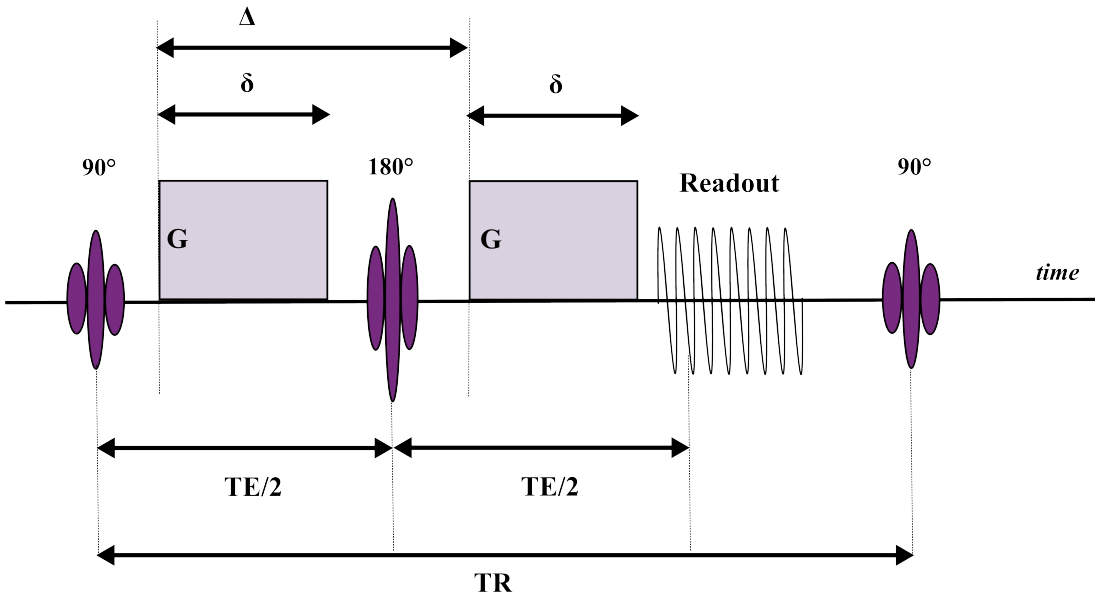

Figure 2.10: *Schematic representation of a PGSE sequence where δ is the pulse gradient duration, Δ is the time between the onsets of the two gradient pulses and **G** is the strength and direction of the diffusion sensitizing pulsed gradients.*

the gradient direction.

Because of the different precession rate of the spins during the pulse, the local displacements are encoded in the magnetisation phase

$$\Phi = \gamma \int_0^{\delta} \mathbf{G}(t)\mathbf{R}(t)\,dt. \tag{2.5}$$

Next, a 180° pulse negates the spin phases. Finally another diffusion sensitisation pulse identical to the first one adds phase shift depending on the position of the spins. Δ is the time between the onsets of the two gradient pulses which controls the diffusion time. If a spin does not move at all, the phase shift added during these symmetric pulses is the same and they will cancel out, because the effective gradient strength from the second gradient pulse is opposite to first one due to the 180° pulse. If however, a spin does move, the phase shifts added will be different and will not cancel out, causing attenuation of the signal at TE. Different phase shifts cause a distribution of phases at the echo time. With distributed phases, the net magnetisation is lower, so the signal is lower.

The durations δ and Δ are the most important parameters since they control the sensitivity of the signal to the particle displacements. The echo time is determined by the parameters Δ and δ.

2.3.1.2 Stimulated Echo

Diffusion-weighted stimulated echo sequences [CHSM89, MHF91, Bam03] are usually used to enhance SNR in MRI experiments. These sequences are produced using three RF pulses. The diffusion-weighting gradients are used after the first and the third RF pulse, as shown in Figure 2.11. The stimulated echo appears at a time delay after the third pulse equal to the interval between the first two pulses. Although classically produced with 90° pulses, any RF pulses other than a 180° can produce a stimulated echo.

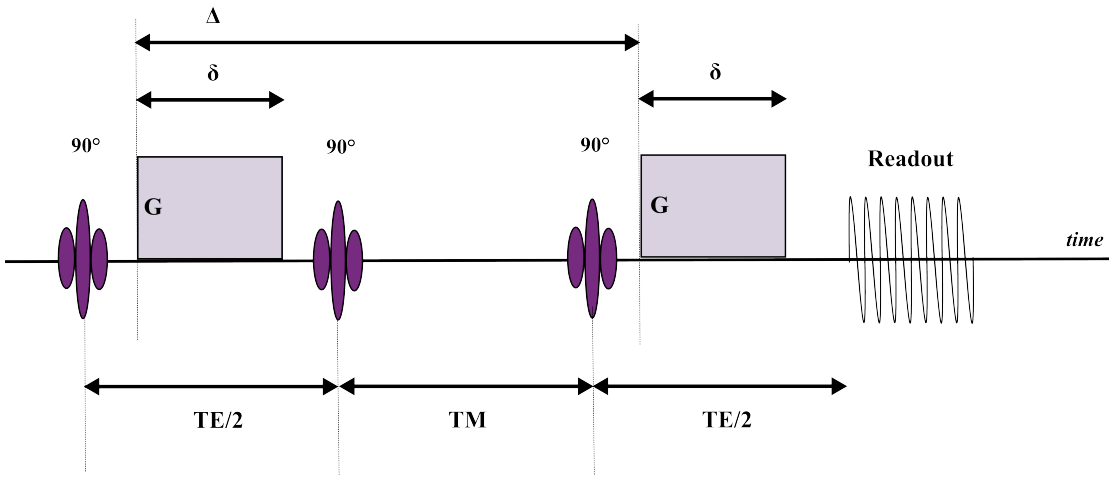

Figure 2.11: *Schematic representation of a diffusion-weighted stimulated echo sequence where a pulse with gradient strength $|\boldsymbol{G}|$ is used after the first and third RF pulses and TM is the mixing time between the second and third RF pulses.*

The second RF pulse tips half of the spins back along the z-axis. Of special interest is the fact that during the mixing time (TM) these spins are affected only by the much slower T_1 relaxation time. This period can be used to add T_1 contrast to an image, but is particularly useful in diffusion imaging because the diffusion gradients can be separated in time without incurring T_2 signal loss. Hence this sequence is frequently used for ex vivo or high field acquisitions where the T_2 is lower.

2.3.2 Short Gradient Pulse (SGP)

In this section we introduce a common approximation of the relationship between the signal and the underlying distribution of particle displacements, the Short Gradient Pulse (SGP) approximation. This approximation assumes that there is a well-defined start and end position of the displacement of the molecules [Som06]. This can be achieved by letting the gradient pulse be described by a delta function (i.e. $\delta \to 0$ and $|\mathbf{G}| \to \infty$, while the product $|\mathbf{G}|\delta$ remains finite), thus the effect of motion during the gradient pulses is ignored. Experimentally, this assumption is justified when $\delta \ll \Delta$. So the effect of the gradient, neglecting the effect of the static field, on a spin in position $\mathbf{R}$, is now :

$$\Phi(\mathbf{R}) = \gamma\delta\mathbf{G}\mathbf{R} \tag{2.6}$$

In the SGP approximation we assume that the pulse is so short that $\mathbf{R}$ does not vary, and therefore we can ignore motion during the gradient pulse, i.e. we ignore the dependence of $\mathbf{R}$ on t. If a spin moves from $\mathbf{r}_0$ to $\mathbf{r}$ between pulses its phase change is

$$\Delta\Phi(\mathbf{r}-\mathbf{r}_0) = \gamma\delta\mathbf{G}(\mathbf{r}-\mathbf{r}_0), \tag{2.7}$$

so the final magnetisation is

$$\mathbf{M}_0 = \exp\Big(i\gamma\mathbf{G}\delta(\mathbf{r}-\mathbf{r}_0)\Big). \tag{2.8}$$

The total signal is the sum of all magnetisations [Pri97]

$$S(\delta,\Delta,\mathbf{G})/S_0(TE) = \iint \rho(\mathbf{r}_0)P(\mathbf{r}_0,\mathbf{r},\Delta)\exp\Big(i\gamma\mathbf{G}\delta(\mathbf{r}-\mathbf{r}_0)\Big)\,d\mathbf{r}d\mathbf{r}_0 \tag{2.9}$$

where $S_0(TE)$ is the signal with no diffusion-weighting gradients at time TE, $\rho(\mathbf{r}_0)$ is the initial spin density (the distribution function of the spins during the first gradient pulse) and $P(\mathbf{r}_0,\mathbf{r},\Delta)$ is the probability density for a displacement of a spin from a starting position $\mathbf{r}_0$ to a position $\mathbf{r}$ during the time interval Δ. From now on we will ignore the dependence on the constant $S_0(TE)$ and assume that S is the normalised signal.

If we write the particle displacement $\mathbf{x} = \mathbf{r} - \mathbf{r}_0$, the probability density function for particle displacements $P(\mathbf{x},\Delta)$ is

$$P(\mathbf{x},\Delta) = \int \rho(\mathbf{r}_0)\rho(\mathbf{r}_0,\mathbf{r}_0+\mathbf{x},\Delta)\,d\mathbf{r}_0. \tag{2.10}$$

In the SGP approximation the diffusion signal S relates to P via the Fourier Transform. The signal S is

$$S(\mathbf{q},\Delta) = \int_{\Re^3} P(\mathbf{x},\Delta)\exp(-i\mathbf{q}\cdot(\mathbf{x}))\,d\mathbf{x}, \tag{2.11}$$

where $\mathbf{q}$ is the wavenumber that depends on the strength and the direction of the magnetic gradient $\mathbf{G}$ and the duration of the magnetic gradient δ, used in the acquisition. In general the wavenumber is written as

$$\mathbf{q} = \frac{\gamma}{2\pi}\int_0^{\delta} \mathbf{G}\,dt. \tag{2.12}$$

However for the SGP approximation [Pri97], it is

$$\mathbf{q} = \frac{\gamma\mathbf{G}\delta}{2\pi}. \tag{2.13}$$

In the case of free diffusion , $P(\mathbf{r}_0,\mathbf{r},\Delta)$ is a Gaussian function

$$P(\mathbf{r}_0,\mathbf{r},\Delta) = \frac{1}{\sqrt{(4\pi dt)^3}}\exp\left(-\frac{|\mathbf{r}-\mathbf{r}_0|^2}{4dt}\right) \tag{2.14}$$

where t is the diffusion time and d is the diffusion coefficient.

The literature contains analytic models for P within simple restricting geometries such as spheres, cylinders and parallel planes [Cal95, SJ95, Neu74]. For example, Neuman [Neu74] derives P for diffusion between planes, within a cylinder and within a sphere. The expressions for the probabilities, P, are obtained from the solution of the diffusion equation with the appropriate boundary conditions

$$\frac{\partial P}{\partial t} = d\nabla^2 P \tag{2.15}$$

where t is the diffusion time and d is the diffusion coefficient [Fou22].

For example, for the case of diffusion bounded by planes separated by distance l the solution of the Equation 2.15 is

$$P(x',x;t'-t) = (1/l) + \sum_{m>1} (2/l)\cos(m\pi x'/l)\cos(m\pi x/l)\exp[-(dm^2\pi^2/l^2)(t'-t)] \tag{2.16}$$

here $P(x',x;t'-t)$ is the probability of a spin moving from position x to x' in time $t'-t$ and $m \in \mathbb{Z}$. So, using the SGP approximation the signal from particles trapped between planes is

$$\ln S = -\frac{8\gamma^2\mathbf{G}^2 l^4}{d\pi^6} \sum_{n=0}^{\infty} \frac{1}{(2n+1)^6} \left(2\tau - \frac{3-4\exp(-d(2n+1)^2\pi^2\tau/l^2) + \exp(-d(2n+1)^2\pi^2 2\tau/l^2)}{d(2n+1)^2\pi^2/l^2}\right) \tag{2.17}$$

which comes from substituting Equation 2.16 in Equation 2.12. For Equation 2.17 the echo time is 2τ and d is the diffusion coefficient.

2.3.3 Gaussian Phase Distribution (GPD)

The Gaussian phase approximation was proposed by by Douglass and McCall [DM58] for an analysis of the MR signal in the presence of a constant gradient field for the case of unrestricted diffusion when it represents an exact solution to the problem.

This approximation accounts for finite δ in contrast to SGP that does not, providing an additional physical insight into the relationship of the spin echo to the microscopic details of diffusion [Ste04]. However, the GPD approximation assumes that the phases of the spins due to the magnetic field gradients are Gaussian distributed.

In the SGP approximation we use the probability density function of spin displacements, whereas the GPD approximation considers the distribution function of spin phases $P(\phi,\Delta)$ at the echo time TE having phase ϕ. The total signal in terms of $P(\phi,\Delta)$ is

$$S(\delta,\Delta,\mathbf{G}) = \int_{-\infty}^{+\infty} P(\phi,\Delta)\cos\phi\, d\phi. \tag{2.18}$$

For molecules undergoing free diffusion, characterised by a single diffusion coefficient d, P is Gaussian so that the signal is

$$S(\delta,\Delta,\mathbf{G}) = \exp\Big(-\gamma^2|\mathbf{G}|^2\delta^2(\Delta-\delta/3)d\Big) \tag{2.19}$$

or

$$S(\delta,\Delta,\mathbf{G}) = \exp\Big(-bd\Big), \tag{2.20}$$

where

$$b = (\Delta-\delta/3)(\gamma\delta|\mathbf{G}|)^2 \tag{2.21}$$

is the diffusion weighting factor for the PGSE sequence introduced and defined by LeBihan et al. [LBBL+86], and $\mathbf{G}$ is the gradient vector with strength $|\mathbf{G}|$ and direction $\hat{\mathbf{G}}$.

Murday and Cotts [MC84] use the GPD approximation to derive an expression for the signal for

particles diffusing in a spherical boundary of radius R specifically for the PGSE experiment with finite δ. The signal is

$$\ln S = -2\gamma^2 \mathbf{G}^2 \sum_{m=1}^{\infty} \frac{2da_n^2\delta - 2 + 2e^{-da_n^2\delta} + 2e^{-da_n^2\Delta} - e^{-da_n^2(\Delta-\delta)} - e^{-da_n^2(\Delta+\delta)}}{d^2 a_n^6 (R^2 a_n^2 - 2)} \tag{2.22}$$

where d is the free diffusion constant and a_n is the nth root of the Bessel equation $(a_n R)J'_{3/2}(a_n R) - 1/2 J_{3/2}(a_n R) = 0$, where J is the Bessel function of the first kind.

Stepisnik [Ste93] uses the same technique to derive analytic solutions for the signal in cylinders and in between planes with finite gradient pulses. The equation for the signal from particles diffusing within the cylinder of radius R is

$$\ln S = -2\gamma^2 \mathbf{G}^2 \sum_{m=1}^{\infty} \frac{2da_m^2\delta - 2 + 2e^{-da_m^2\delta} + 2e^{-da_m^2\Delta} - e^{-da_m^2(\Delta-\delta)} - e^{-da_m^2(\Delta+\delta)}}{d^2 a_m^6 (R^2 a_m^2 - 1)} \tag{2.23}$$

where a_m is the mth root of equation $J'_1(a_m R) = 0$ and J'_1 is the derivative of the Bessel function of the first kind, order one. We note that this expression is often attributed to Van Gelderen [GDZM94], however Stepisnik [Ste93] was the first to publish it.

2.4 Diffusion Tensor Imaging

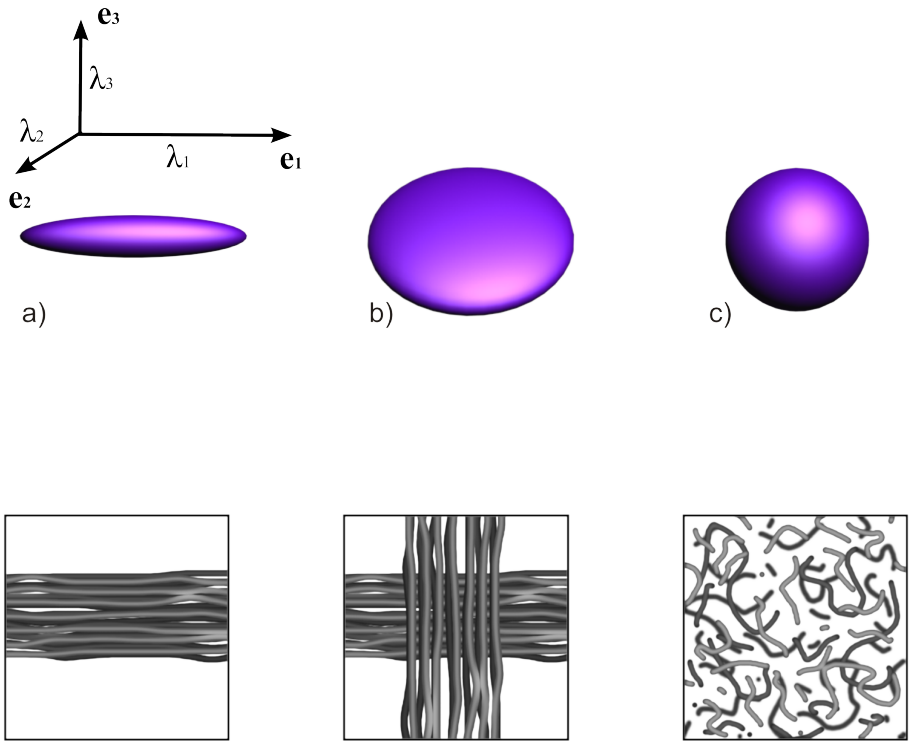

Figure 2.12: *Different shapes of the diffusion tensor according to fibre populations: a) prolate tensor for one distinct fibre orientation, b) oblate tensor for a crossing fibre configuration, c) isotropic when there is no distinct fibre orientation. Image courtesy of Kiran Seunarine.*

The most widely-used technique for estimating fibre orientations in a white matter voxel is diffusion tensor imaging (DTI) [BJ02, BML94]. DTI models the displacement of particles in 3D with a zero-mean

Gaussian distribution by fitting a 3×3 symmetric positive-definite matrix called a diffusion tensor (DT) $\mathbf{D}$, to six or more diffusion-weighted images. The probability density function P of particle displacement $\mathbf{x}$ is

$$P(\mathbf{x}) = \frac{1}{\sqrt{(4\pi t)^3 |\mathbf{D}|}} \exp\left(-\frac{\mathbf{x}^T \mathbf{D}^{-1} \mathbf{x}}{4t}\right) \tag{2.24}$$

where t is the diffusion time. The diffusion tensor $\mathbf{D}$ is

$$\mathbf{D} = \begin{pmatrix} D_{xx} & D_{xy} & D_{xz} \\ D_{xy} & D_{yy} & D_{yz} \\ D_{xz} & D_{yz} & D_{zz} \end{pmatrix} \tag{2.25}$$

The diagonal elements of the tensor D_{xx}, D_{yy} and D_{zz} are the diffusion coefficients along the x, y and z axes respectively in the reference frame of the magnetic gradients, and D_{xy}, D_{xz} and D_{yz} are the correlation coefficients between the axes.

Eigen decomposition of $\mathbf{D}$ gives the eigenvectors $\mathbf{e}_i$ and the corresponding eigenvalues λ_i, $i = 1,2,3$. The gross fibre direction is indicated by the principal eigenvector, $\mathbf{e}_1$.

P has ellipsoidal contours described by the DT, whose size and shape is determined by the eigenvalues (see Figure 2.12):

- Prolate, when $\lambda_1 \gg \lambda_2 \approx \lambda_3$ diffusion is mainly in the direction of the eigenvector of the largest eigenvalue (see Figure 2.12 a).
- Oblate, when $\lambda_1 \approx \lambda_2 \gg \lambda_3$ diffusion is mainly in the plane spanned by the two eigenvectors corresponding to the two largest eigenvalues (see Figure 2.12 b).
- Isotropic, when $\lambda_1 \approx \lambda_2 \approx \lambda_3$ there is no preferred direction of diffusion (see Figure 2.12 c).

The formula relating the diffusion tensor to the normalised signal using the diffusion weighting factor b is

$$S(\mathbf{G}, \Delta, \delta) = S_0 \exp(-b\hat{\mathbf{G}}^T \mathbf{D} \hat{\mathbf{G}}), \tag{2.26}$$

To estimate the tensor we need at least six measurements (taken along different non-collinear gradient directions), in addition to one extra measurement for S_0.

Three of the most common indices that describe the size and shape of the DT are the trace Tr($\mathbf{D}$), the fractional anisotropy (FA) and the mean diffusivity (MD) [BP96a]. Tr($\mathbf{D}$) is

$$Tr(\mathbf{D}) = \lambda_1 + \lambda_2 + \lambda_3. \tag{2.27}$$

FA measures the degree of diffusion anisotropy in each voxel. Therefore, FA is low in areas of cerebrospinal fluid (CSF) and grey matter, where there is no or little directionality in the tissue, whereas in white matter that has directionality FA is higher. FA is defined as

$$FA = \left(\frac{3}{2} \sum_{i=1}^{3} \frac{\left(\lambda_i - \frac{1}{3}\mathrm{Tr}(\mathbf{D})\right)^2}{\sum_{i=1}^{3} \lambda_i^2}\right)^{\frac{1}{2}}. \tag{2.28}$$

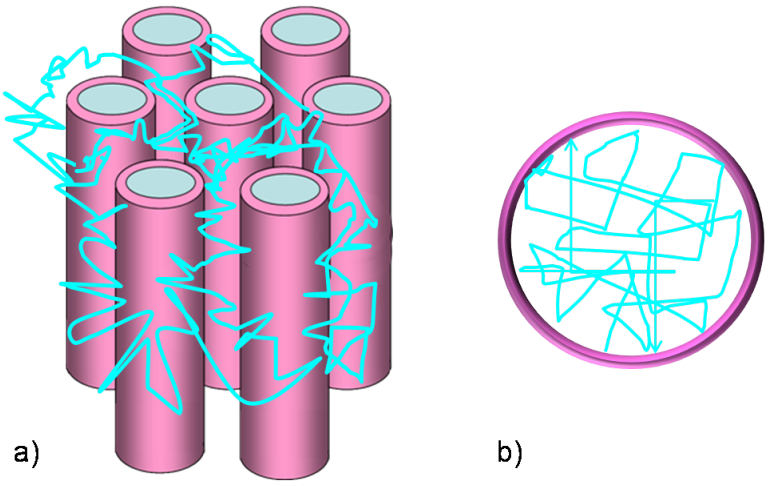

Figure 2.13: *a) Biological cells hinder the motion of extra-cellular water molecules. b) Inside each cell the motion of water molecules is restricted by the cellular walls.*

MD is an index of the magnitude of water diffusion regardless of its direction and is defined as

$$MD = \frac{1}{3}Tr(\mathbf{D}). \tag{2.29}$$

Following an opposite trend from the FA, MD is higher in areas of CSF and grey matter compared to white matter.

Both FA and MD are rotationally-invariant diffusion indices that are commonly used in clinical applications for diagnosing the pathology of neurological conditions [Tof03]. For example in schizophrenia studies [AAS01, ANH+03], they find a decrease in FA in the splenium. In Alzheimer's disease, DTI studies [BFF+02, RCC+00, TYT+02] report FA reductions in several white matter regions including the posterior corpus callosum, the posterior cingulum and the fornix.

Schmierer et al. [SWKB+07] investigate the association between histological indices of myelin content, number of axons and gliosis, and FA and MD in unfixed post mortem multiple sclerosis brain. Statistical results suggest that FA and MD are affected by myelin content and to a lesser degree axonal count in post mortem multiple sclerosis brain.

However the simplicity of the DT model limits its applicability. It is well-known that the model only works well in voxels containing one fibre-orientation, and is not capable of resolving multiple fibre-orientations in a voxel (i.e. crossing fibres, kissing fibres, fanning fibres) [Sfbtdt09]. Another limitation of the model is that it does not account for restricted diffusion within cells (see Figure 2.13), so the signal departs from the model even in single fibre populations especially as b becomes large.

2.5 Two-Compartment Models

Two-compartment models were devised to overcome some of the limitations of the DT model. Often they assume hindered diffusion in the extra-cellular space and restricted diffusion in the intra-cellular space. Figure 2.13 shows how cellular structures can hinder the otherwise free diffusion outside, and how the cell membranes restrict it inside. The signal is

$$S(\mathbf{G},\Delta,\delta) = fS_r(\mathbf{G},\Delta,\delta) + (1-f)S_h(\mathbf{G},\Delta,\delta), \tag{2.30}$$

where S_r is the signal from the intra-cellular compartment where spins exhibit restricted diffusion, S_h is the signal from the extra-cellular compartment where spins exhibit hindered diffusion and f is the volume fraction. The volume fraction is

$$f = \frac{V_I}{V_E + V_I} \in [0,1], \tag{2.31}$$

where V_I is the volume of the intra-cellular compartment and V_E is the volume of the extra-cellular compartment.

Behrens et al. [BWJJ03] propose an alternative to the simple DT model which is able to account for one or more fibre directions within each voxel. They propose a partial volume model of local diffusion, which assumes that a fraction of diffusion is along a single direction and that the rest is isotropic. Both S_r and S_h have the form of Equation 2.26. For S_r

$$\mathbf{D} = d\mathbf{n}\mathbf{n}^T \tag{2.32}$$

where d is the free diffusivity and $\mathbf{n}$ is the fibre direction, so water moves only in the fibre direction. For S_h

$$\mathbf{D} = d\mathbf{I} \tag{2.33}$$

where $\mathbf{I}$ is the identity tensor, so diffusion is isotropic. We can account for more than one principal direction with additional intra-cellular compartments with $\mathbf{D} = d\mathbf{n}\mathbf{n}^T$.

Alexander [Ale07, Ale08] investigates the feasibility of using diffusion MRI to measure axon dimensions in white matter in vivo. To relate axon radius to the diffusion MRI signal he uses a two-compartment model that incorporates a pore radius. The model of the extra-cellular space uses Equation 2.26 with a cylindrically symmetric tensor [Ale08] with principal eigenvector $\mathbf{n}$, indicating the fibre direction, so

$$\mathbf{D} = \alpha\mathbf{n}\mathbf{n}^T + \beta\mathbf{I} \tag{2.34}$$

where $\mathbf{I}$ is the identity tensor and $d_{\|} = \alpha + \beta$. The parameter $d_{\|}$ is the corresponding eigenvalue for the diffusivity parallel to the direction of the fibres, and $d_{\perp} = \beta$ is the minor eigenvalue that corresponds to the diffusivity perpendicular to the direction of the fibres. The model for the intra-cellular space accounts for non-zero pore size, unlike Behrens' stick model. The model S_r follows the GPD approximation for the signal in cylinders of radius R (see Section 2.3.3, Equation 2.23).

Assaf et al. [AFRB04, AB05], describe CHARMED (Composite Hindered And Restricted Model of Diffusion). The model also assumes cylindrical restriction in the intra-cellular space. The model is used to provide volume fraction maps of intra- and extra-axonal compartments. They use Neuman's expression [Neu74] for diffusion in cylindrical confinement, which follows the GPD approximation however, for a continuous gradient rather than PGSE. Unlike Alexander's model, which assumes a single

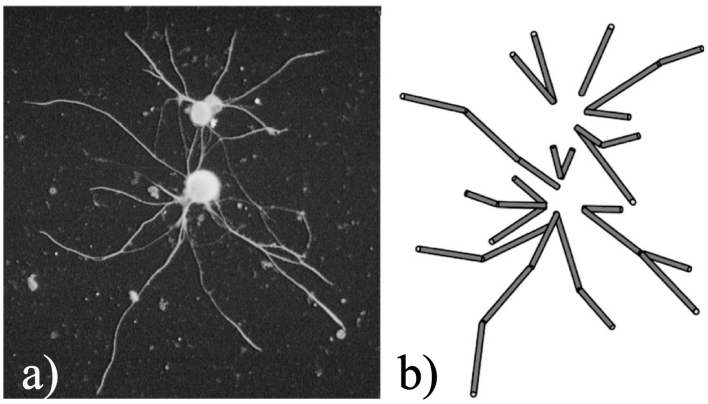

Figure 2.14: *a) Microscopy image showing neurons. b) Corresponding representation of the neurons replacing dendrites and axons with cylinders. Image taken from [JKØ+07].*

cylinder radius, the model assumes cylinders with gamma distributed radii which introduces one extra parameter. The hindered compartment uses the full DT model constrained only to have principal direction aligned with the cylinder axis. They use a high-angular-resolution diffusion imaging (HARDI) [JHS99, TRW+02] with various b values (multishell) to be able to estimate arbitrary fibre orientation.

In later work, Assaf et al. [ABKYB08] use this model in an NMR experiment to successfully extract distributions of axon diameters of bovine optic and sciatic nerve samples. They extend the CHARMED framework, by considering the diameter distribution of cylindrical axons as an unknown function to be estimated from their data. They name this model AxCaliber. To accomplish greater sensitivity for estimating the axon diameter they use a fixed gradient direction perpendicular to the axons with a combination of different diffusion times and gradient strengths. Their experiments were performed to satisfy the SGP approximation.

A standard two-compartment model in the literature is the biexponential model [NDN+96]. This model describes diffusion in white matter assuming two water diffusion pools, with a fast and a slow diffusion coefficient. The two components exhibit Gaussian diffusion with no exchange and the signal is

$$S = f_{slow}\exp(-bd_{slow}) + f_{fast}\exp(-bd_{fast}) \tag{2.35}$$

where f_{slow}, d_{slow} and f_{fast}, d_{fast} are the volume fraction and the diffusion coefficient associated with the slow and the fast pool compartments with $f_{slow} + f_{fast} = 1$.

Studies [AC98, NDN+96] have shown that the volume fraction of the fast and slow component does not fit the physiological fraction, where approximately 80% of the tissue in the brain is intra-cellular and the rest extra-cellular, therefore it cannot be related to tissue compartments. Clark and Le Bihan [CLB00] use this model in white and grey matter to demonstrate biexponential diffusion using in vivo brain data. However, this study was based on assumptions concerning the exchange rates between compartments which are largely unknown especially for the human brain.

As for the DT model, the biexponential does not account for restriction either, since it assumes Gaussian diffusion and cannot account for complex microstructure. The model given by Equation 2.35

provides only one diffusivity value for each of the compartments. We can extend the model by using a tensor in each compartment to attain estimates of the diffusivity in each of the tensors different directions (bitensor model).

Other studies [TRW+02, PA03] use a mixture of Gaussians to resolve the problem of crossing fibres as the simple DT fails. These methods are based on multiple-fibre reconstruction algorithms and generate an orientational distribution function (ODF), the maxima of which corresponds to the underlying multiple fibre orientation.

Jespersen et al. [JKØ+07, JBN+10] also introduce a biophysical model of diffusion in the brain. More precisely, they propose a model of neural cytoarchitecture with two compartments with no permeability: one to capture signal from axons and dendrites and one for all other structures. As shown in Figure 2.14 the model incorporates cylinders with a distribution of orientations. They use the SGP approximation which reduces the cylinders into cylinders with zero radius ("sticks"). To describe the orientation they use spherical harmonics and integrate over all possible angles, which provide a detailed orientational dependence. In [JKØ+07] the model aims to describe diffusion in grey matter so they use an isotropic component for the second compartment. In [JBN+10] they incorporate anisotropy to describe diffusion in both white and grey matter. They compare their model estimates with microscopy and they find stronger correlation with optical and electron microscopy reflecting the myelinated neurite density than when using DTI.

2.6 Multi-Compartment Models

Other methods describe diffusion with three or more compartments and allow exchange between them. These models include factors such as the myelin sheath, glial cells, cerebrospinal fluid (CSF) regions, and membrane permeability in their description of tissue.

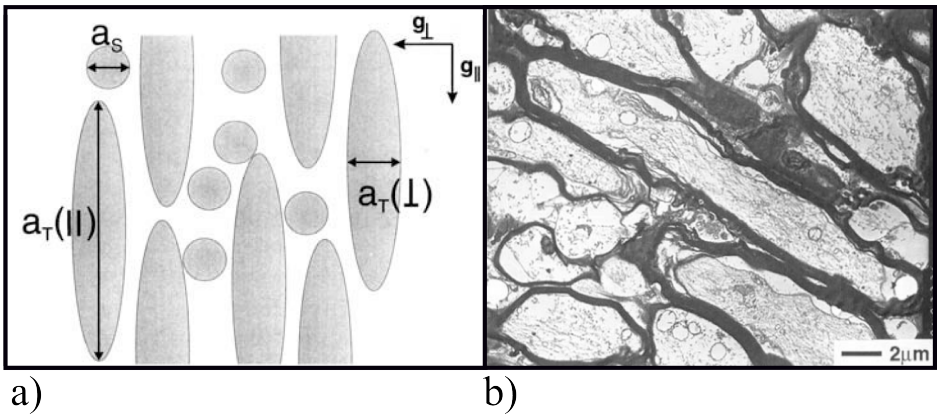

Figure 2.15: *Figure a) presents Stanisz's tissue model of prolate ellipsoids for axon and spheres for glial cells. Figure b) shows an electromicrograph of a transverse section of bovine optic nerve sample. Figures taken from [SSWH97]*

Stanisz et al. [SSWH97] develop an analytical model of restricted diffusion in bovine optic nerve using a three-pool model. They model nerve tissue as prolate ellipsoids for axons and spheres for glial cells surrounded by partially permeable membranes in a homogeneous extra-cellular medium (see Figure

2.15). They use one diffusion coefficient for the intra-cellular compartments and another for the extra-cellular. Each compartment has its own volume fraction. They fit the model to 800 NMR measurements of a fixed sample using a stimulated echo sequence. They find the minimum requirements for their model by testing it with various parameters switched on and off. They estimate successfully the fibre diameter and density, and found reasonable estimates for permeability, diffusivity and relaxivity parameters. The results also show significant departure of the diffusion MRI signal from the Gaussian model. They found that the third compartment, which describes the glial cells is essential for a good fit, while the two-compartment model that describes only the axons fails to capture the observed restriction in the parallel direction. Finally their results show that permeability improves the quality of the fit to the data. However, fitting such models requires very high quality measurements, typically using NMR spectroscopy rather than MRI. Also Stanisz's tissue model was designed specifically for the bovine optic nerve. It cannot describe compartments of different sizes which exist for example in areas of brain white matter, as in the bovine optic nerve the sizes of these compartments are relatively very small. Finally, the fibre direction was already known in the sample.

Sen and Basser [SB05a] add thickness to their tissue model to account for the myelin sheath. The tissue model consists of an array of identical cylinders, arranged in a regular lattice periodically (in square or hexagonal configurations) immersed in an extra-cellular medium (see Figure 2.16). Cylinder walls represent the myelin and are permeable to water molecules. They investigate how different parameter settings reflect observations from brain tissue in various pathological conditions.

Recently Barazany et al. [BBA09] studied the diameter distribution of axons in the rat corpus callosum in vivo using a three-compartment model. The model is an extension of the AxCaliber model [ABKYB08], with the addition of an isotropic-diffusion compartment to account for partial volume effects and contributions from areas of CSF.

Most recently, Alexander et al. [AHH+10] demonstrate orientational invariant estimation of axon diameter and density in both fixed monkey brains and in vivo human brains. Their experiment uses

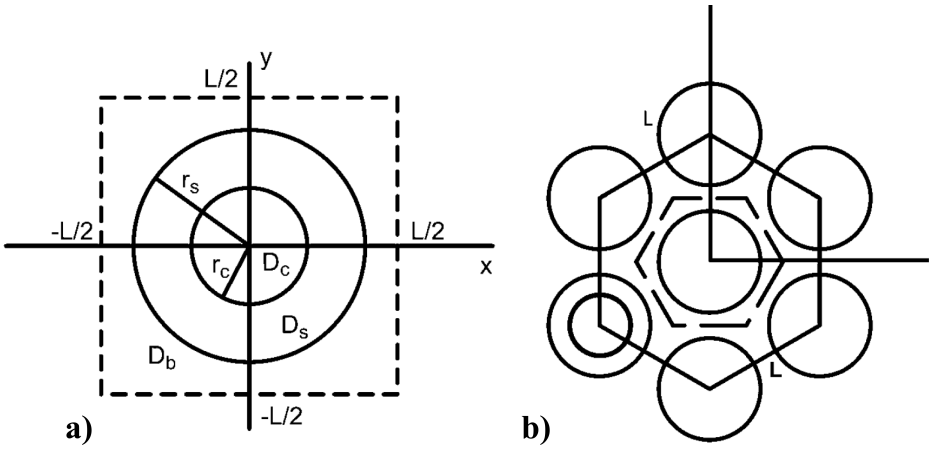

Figure 2.16: *Figure a) shows Sen and Basser's tissue model representing a white matter axon with myelin sheath. Figure b) shows the hexagonally packed axon configuration of their model. Figures taken from [SB05a]*

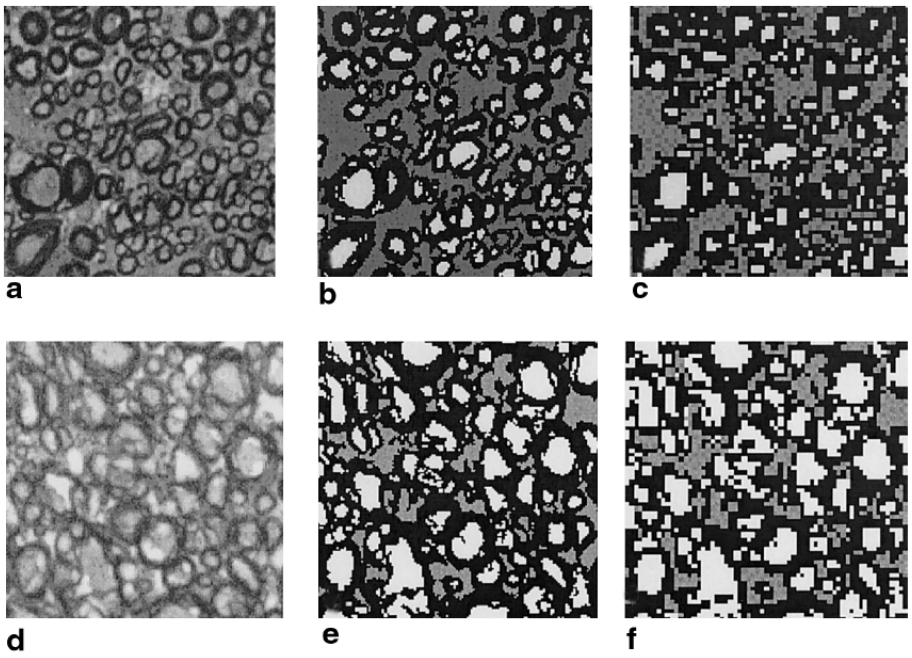

Figure 2.17: *This figure presents the original and processed light microscopy images of rat spinal cord used by Chin et al. [CWH+02] to construct their tissue model. Figure taken from [CWH+02].*

an optimised multishell high-angular-resolution PGSE acquisition. The tissue model consists of four compartments: a combination of the two-compartment model used in [Ale08] with a CSF compartment, as in Barazany [BBA09], and a fourth compartment which accounts for water coming from stationary water molecules trapped in glial cells and other subcellular structures, similar to Stanisz [SSWH97].

Zhang and Alexander [ZA10] propose a new model that captures the effect of fibre orientation dispersion. They develop a scheme to enable the axon diameter estimation by fitting their model. Synthetic data experiments demonstrate that the new model provides an axon diameter index that is robust to the presence of orientation dispersion. Results on in vivo human data show reduced axon diameter index and better agreement with histology compared to previous methods suggesting improvements in the axon diameter estimate.

2.7 Numerical Approaches

In this section we discuss numerical methods for generating synthetic diffusion MRI data.

Numerical simulations can overcome many of the shortcomings of the analytic methods. Simulations are not limited to simple geometries, as they can simulate the scattering of particles within geometric models of complex microstructure and emulate the diffusion MRI measurement process. Furthermore, simulations provide flexibility in using different interaction techniques that permit changing the behaviour of the scattering particles. The most common numerical methods are finite-difference approaches and Monte-Carlo simulations.

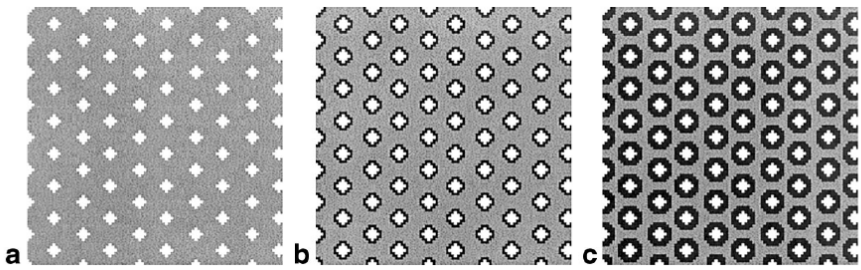

Figure 2.18: *This figure presents the tissue model used by Hwang et al. [HCWH03]. The image shows a cross-section of a hexagonal array of cylinders. The first image accounts for intra-cellular volume fraction a) $f = 0.10$, b) the second $f = 0.13$ and c) the third $f = 0.2$. Figure taken from [HCWH03]*

2.7.1 Finite-difference diffusion simulation method

Finite-difference methods rely on an approximate solution to the diffusion equation [Fle91]. The finite-difference method transforms the diffusion equation to a simulation model at a discrete number of points, i.e. on a grid. The grid is generated from a digital image by placing a node at the centre of each pixel. This technique assumes that magnetisation is discretised in space and approximates the solution to the partial differential diffusion equation numerically, using finite-differences. The model then provides information on the concentration gradients and the mobilities of the spins with respect to variables such as concentration, volume fraction and diffusion coefficient for every grid point of the finite-element mesh.

Chin et al. [CWH+02] use a finite-difference diffusion simulation to examine the causes of the non-monoexponential diffusion attenuation that is observed experimentally in the central nervous system. They base their tissue model on light microscopy images from sectioned rat spinal cord (see Figure 2.17). To construct the tissue model they segment the original images. Figure 2.17 a and d show the original images and Figure 2.17 b and e show the segmented images. They resample the images at lower resolution as shown in Figure 2.17 c and f respectively. They produce extruded tissue models by replicating these images. Their results show that the biexponential model of fast and slow diffusion is not correct.

In their later work, Hwang et al. [HCWH03] use the finite-difference diffusion simulation model to produce synthetic data to investigate the behaviour of diffusion in biological tissues and assess the status of neural injury and regeneration. In this work they use synthetic images accounting for different intra-cellular volume fractions to generate the tissue models (see Figure 2.18). The method was in agreement with the analytic solutions for cylindrical pores and hexagonal arrays, providing strong support for the effectiveness of the finite-difference simulation approach as a means to model axonal systems approximately resembling cylinders.

2.7.2 Monte-Carlo simulations

Monte-Carlo simulations of particle scattering within geometric models overcome many of the restrictions of analytic models. The simulation is flexible for material properties (e.g. diffusivity, T_2), interaction mechanisms (e.g. changing spin dynamics) and scan acquisition types.

The system simulates Brownian motion of water molecules within geometric models of tissue, or other materials and emulates the diffusion MRI data generation process. We outline the Monte-Carlo diffusion simulation as described by Hall and Alexander [HA09].

The technique maintains a population of spins undergoing Brownian motion within a tissue model of arbitrary complexity. Spins are initially uniformly distributed across the environment and they update their position as follows

1. Generate a step vector $\Delta\mathbf{x}$. Steps are of constant length l and random orientation.

2. Check if the step crosses a barrier.

   (a) If no barrier is crossed then the spin executes the step and has a new position $\mathbf{x} \rightarrow \mathbf{x} + \Delta\mathbf{x}$.

   (b) If the step crosses a barrier, the step is executed with probability p, otherwise the spin elastically reflects on the barrier. The spin's position is then $\mathbf{x} \rightarrow \mathbf{x} + \Delta\mathbf{x}'$ where $\Delta\mathbf{x}'$ is the vector of the reflected step.

Spins accumulate a net phase shift Φ_j according to their trajectories during an applied pulse sequence with signal generated from

$$S = \sum_{j \in \text{voxel}} e^{i\Phi_j}. \tag{2.36}$$

The unweighted signal is equal to the number of spins as $\Phi_j = 0, \forall j$

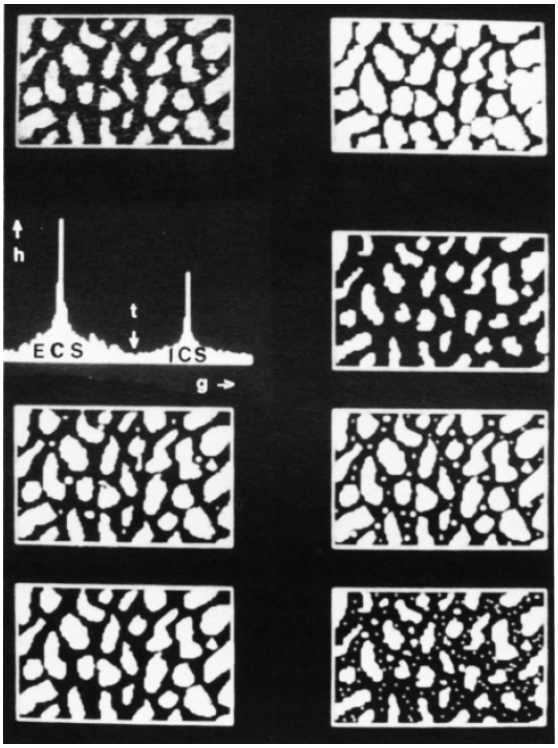

Figure 2.19: *Lipinski's [Lip90] tissue model from digitised images of histological preparation (guinea pig hippocampus) using morphological operations of erosion and dilation to simulate cell shrinkage and swelling.*

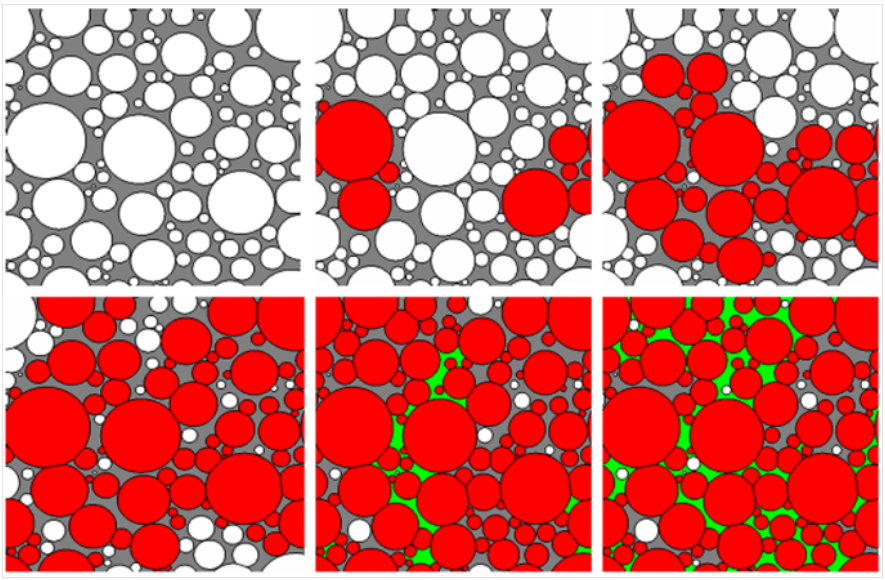

Figure 2.20: *This figure presents the swelling tissue model by Hall and Alexander [HA09]. The figure shows a cross-section of cylinders while the degree of swelling increases across the rows. The abutting cylinders are shown in red and in green is the extra-cellular space when it becomes highly restricted.*

2.7.3 Monte-Carlo studies

Numerical simulations are very commonly used for for developing, optimizing, evaluating and comparing diffusion MRI techniques. For example Szafer [SZG95], Stanisz [SSWH97] and Duh [DMS01] use Monte-Carlo simulation to validate their analytic models of diffusion in brain tissue. Regan and Kuchel [RK03] use Monte-Carlo simulations to model diffusion within red-blood cells and consider the potential for measuring red-blood cell wall permeability. Liu et al. [LBAM04] generate synthetic data to test multiple fiber reconstruction algorithms (DTI, higher-order tensor (HOT) coefficients, diffusion-weighted imaging at high angular resolution) within various configurations of impermeable cylinders.

Lipinski [Lip90] in 1990 was the first to use histological images in combination with Monte-Carlo simulations, despite the computational constraints of that time, to study the diffusion signal in a more realistic environment than basic geometric shapes. He uses two-dimensional Monte-Carlo simulations to investigate the effects of cell swelling on measured diffusivity. The tissue model is constructed by segmenting digitised histological preparation images from guinea pig brain white matter (see Figure 2.19). However, the model is oversimplified as the images are downsampled and thresholded repeatedly, losing most of the tissue shape details. He uses the resulting tissue models to simulate cell shrinking and swelling using image morphology on the processed images.

Ford et al. [FH97] use Monte-Carlo simulations to predict diffusivity changes after injury in rat spinal cord. They model rat spinal cord with close-packed cylinders. Their model also accounts for the distribution of the axon diameters and permeability.

Hall and Alexander [HA09] use Monte-Carlo simulations to synthesize diffusion-weighted measurements in a model of tissue undergoing swelling. They use their tissue model to simulate oedema. They model white matter as parallel cylinders with gamma distributed radii (see Figure 2.20). The cylinders expand and deform to simulate oedema. Finally, they compare their resulting data to the predictions

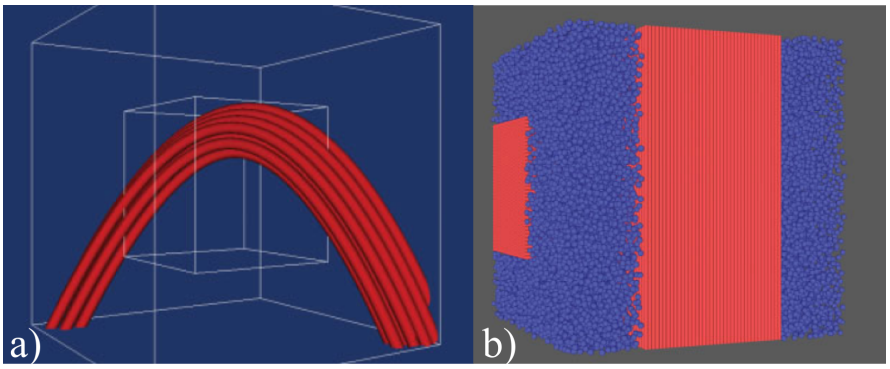

Figure 2.21: *Figure a) shows a curved fibre bundle. Figure b) presents a tissue model by Balls and Frank [BF09] of crossing packed fibres surrounded by randomly oriented ellipsoidal cells. Figures taken from [BF09].*

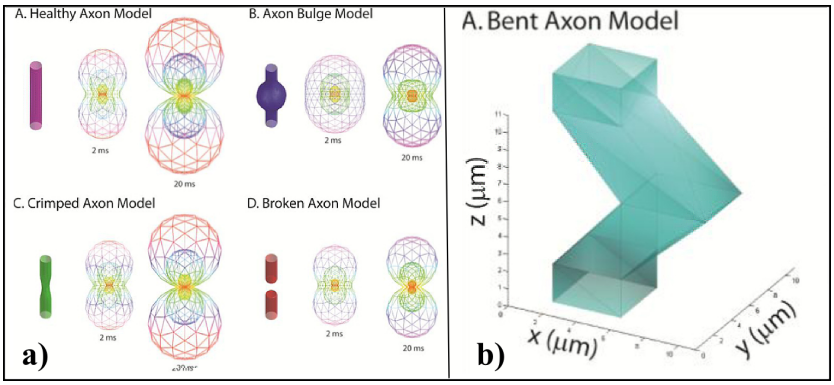

Figure 2.22: *This figure presents tissue models used as substrates in simulations by Landman et al [LFS+09]. Figure a) presents four geometric models of axon damage and Figure b) presents a mesh model of a bent axon. Figure taken from [LFS+09].*

of an analytical model of diffusion in parallel cylinders similar to the CHARMED model (see Section 2.5). They find that the diffusion-weighted signal increases more rapidly when the effects of abutting cylinders are taken into account.

Balls and Frank [BF09] present flexible Monte-Carlo simulations in arbitrarily complex polygonal geometries. They test their simulations with many tissue configurations such as aligned fibres with varying packing density and permeability, bent, and crossing straight fibres (see Figure 2.21).

Landman et al. [LFS+09] also present simulations of diffusion in complex geometries and use models to emulate healthy and damaged white matter. Their models include compartments with different diffusivities, permeabilities, and T_2 time constants using both parametric (e.g. spheres and cylinders) and mesh-based geometries. In Figure 2.22 we present the tissue models they used to simulate healthy and damaged axons. Figure 2.22 a presents the parametric models and Figure 2.22 b shows an example of their mesh model.

2.8 Summary

In this chapter we described the anatomy of white matter to give an insight into the complexity and sensitive integrity of the structure of the tissue and to identify the need for a non-invasive technique that

can provide specific microstructural information. We gave general background information on magnetic resonance and diffusion-weighted MRI, and we introduced the PGSE and stimulated echo sequences for acquiring diffusion-weighted MRI data. We discussed two common approximations, the SGP and the GPD, which approximate the signal based on different assumptions that are appropriate in different situations.

We discussed the DT, a simple model relating the diffusion MRI signal to diffusion in tissue. This model provides markers such as FA and MD which are widely used in clinical applications. However, the simplicity of the model leads to critical limitations. One of them is that FA and MD are difficult to interpret unambiguously, since more than one microstructural tissue element can affect them so they cannot be related directly to specific tissue alterations. Another serious limitation of the DT model is that it does not account for restricted diffusion within cells and hence cannot capture information about true tissue microstructure. To address these limitations some studies have turned towards more descriptive models.

We reviewed methods that use two-compartment and higher complexity analytical models to investigate the diffusion signal. Two-compartment models are more descriptive of tissue microstructure whilst remaining simple enough for model fitting using clinically feasible data. However, approaches using complex analytical models require a large number of measurements with high magnetic field gradient strengths that cannot be obtained in vivo. There are however, many combinations of these models, creating intermediate models involving less complexity, that have not been explored and could potentially be used to provide microstructural estimates for sparser measurements (see Chapter 4).

We have seen that analytic methods produce data with low computational overhead, however the approximation of the diffusion measurement process is crude. Simulations increase the computational cost but they allow increased complexity in models of the diffusion environment and measurement process. Furthermore, numerical approaches allow the distinct investigation of subtle effects that are unattainable using analytical methods, for example, effects of permeability, the binding of water molecules to tissue, non-parallel fibres and effects of the presence of other structures such as glial cells. We reviewed numerical methods that use more complex models than basic geometric ones, some of them based on histological data. However, these methods roughly approximate the actual tissue structure and frequently ignore the third dimension. This motivates our development of an accurate three-dimensional model of tissue in an elaborate simulation (see Chapter 3).

To conclude, modelling - whether analytical or via simulations - can provide insight into the mechanisms underpinning the diffusion signal characteristics in tissue, can be used to interpret complicated experimental diffusion data [Sta03] and most importantly can provide us with information about the microstructure of the tissue itself. In this work we build analytic models of the diffusion MR signal in brain white matter using simple models of intra-axonal and extra-axonal compartments. We test their feasibility of estimating accurate microstructure parameters and their utilisation for in vivo studies. We also create a numerical model using computer graphics techniques, which go beyond the simple assumptions of the analytic models, and treats the three-dimensional structure in a more natural way than in previous

studies [CWH+02, Lip90]. Thus we depict the detailed architecture of the tissue as closely as possible and study how the complexity of the tissue affects the diffusion MR signal.

Chapter 3

High-Fidelity Tissue Models

This chapter presents a method to construct detailed three-dimensional geometric models of tissue microstructure, represented by meshes. Our aim is to estimate the three-dimensional tissue structure as closely as possible, and create accurate synthetic diffusion MRI data. We use confocal laser scanning microscopy (CLSM) to collect an image stack from the tissue sample and then use the marching cubes algorithm on the stack to construct the three-dimensional surface of the sample. The intention is to use the meshes to simulate the diffusion-weighted MRI signal from the tissue by running random walk simulations (see Section 2.7.2) within the resulting mesh. This chapter expands the work described in [PHZ+10].

Various studies use simple geometric models of white matter e.g. cuboids [SZG95], ellipsoids [SSWH97] or cylinders [Ale08, ABKYB08], which grossly simplify the complexity of tissue microstructure. The precise simulated data from our method can provide a mechanism for evaluating the quality of simple parametric models and the parameter estimates they provide.

First we discuss the mesh generation and then we describe the application. Section 3.1 provides an overview of the tissue reconstruction method. Section 3.2 discusses our choices of confocal microscopy and the marching cubes algorithm for constructing three-dimensional mesh models of tissue. Section 3.3 describes an MRI experiment for testing and evaluating the three-dimensional mesh models and generating accurate synthetic diffusion MRI data using a biological phantom. In Section 3.3.1 we explain our choice for the phantom and we provide details of the sample preparation, and the MRI and confocal acquisitions. This section also describes the procedure of constructing the mesh models and gives details of the simulations. In Section 3.3.2 we describe the experiments performed to optimise the simulation parameters, the sample's diffusivity, and the mesh resolution. Using these optimised parameters, we generate synthetic data within the three-dimensional mesh. For the evaluation of the synthesised data we compare it with scanner data and with data generated from simpler models. We conclude the chapter in Section 3.4.

3.1 High-Fidelity Tissue Model Pipeline

In this section we describe the complete procedure for creating high-fidelity tissue models. The motivation for constructing a tissue model using CLSM images and the marching cubes algorithm is to achieve

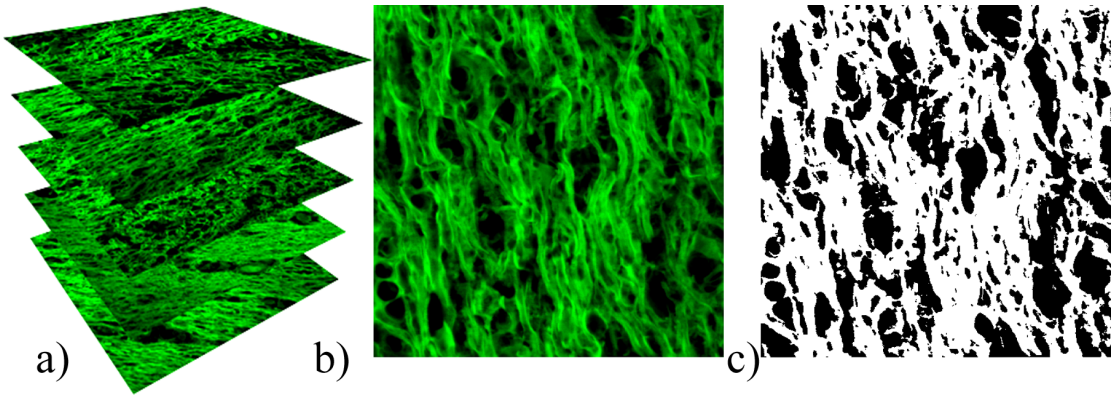

Figure 3.1: *Figure a) shows a stack of confocal laser scanning microscopy image from brain white matter. Figure b) presents one of the confocal laser scanning microscopy images and c) shows the thresholded image that is subsequently used for the mesh reconstruction.*

a highly-detailed tissue model. We aim to demonstrate that the mesh model can produce synthetic data closer to the observed MRI signal than synthesised data from primitive geometrical models.

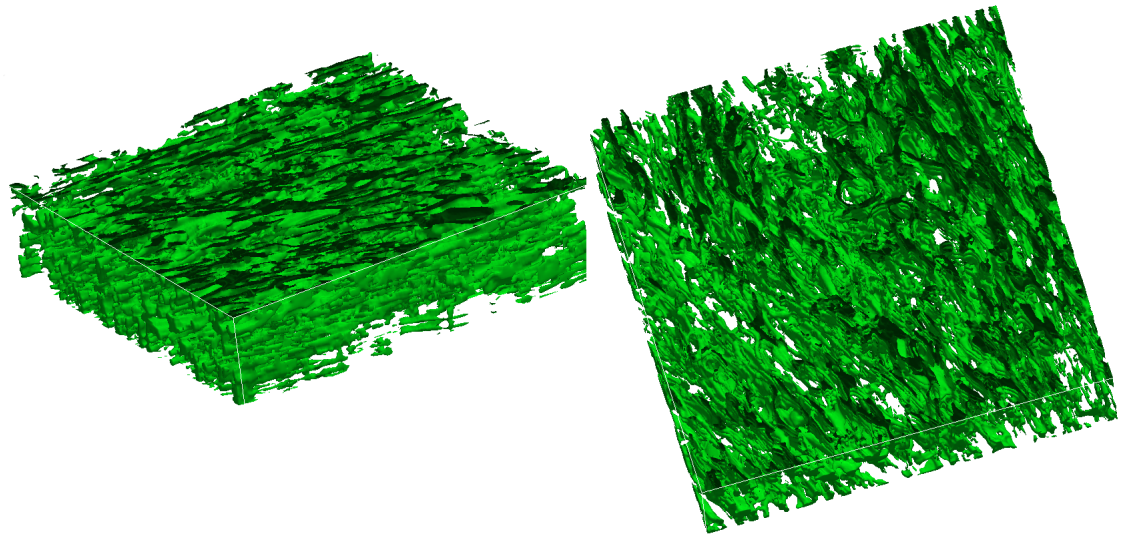

Figure 3.2: *Constructed three-dimensional surface from CLSM images of human brain tissue, shown from two different angles.*

The tissue mesh model is generated as follows:

1. We acquire a stack of confocal laser scanning microscopy images from the tissue sample. To demonstrate the method here we use CLSM images (transverse sections) from a small volume of human corpus callosum tissue. The CLSM images are courtesy of Dr. Hubertus Axer [AK00]. For the main experiment I will use a biological phantom and perform the imaging. Figure 3.1 a) presents the stack of the CLSM images and Figure 3.1 b) shows a single CLSM image.

2. We then process the stack into binary images, using for example Otsu's method [Ots75], to separate pixels belonging inside and outside the surface. Otsu's algorithm assumes that the image to be thresholded contains two classes of pixels (e.g foreground and background or intra-cellular and

extra-cellular space) and then calculates the optimum threshold. The method chooses the threshold to minimize the intra-class variance of the black and white pixels. Figure 3.1 c) presents the thresholded CLSM image.

3. As a final step we run the marching cubes algorithm with the stack of binary images to create the mesh. Figure 3.2 presents the reconstructed three-dimensional surface from the stack of CLSM images.

3.2 Confocal Microscopy and Meshing

This section provides background on the methods we use to construct the mesh models, confocal microscopy and the meshing algorithms.

3.2.1 Confocal Microscopy

Microscopy has been a tool in science, primarily in medicine, chemistry and biology, for over 350 years [Hog54]. A microscopic investigation of brain white matter features requires detail at the nanometre scale (see Section 2.1) that conventional widefield microscopy is not adequate to reveal. Limitations in resolution may be overcome by utilizing confocal microscopy [PM08, SW05].

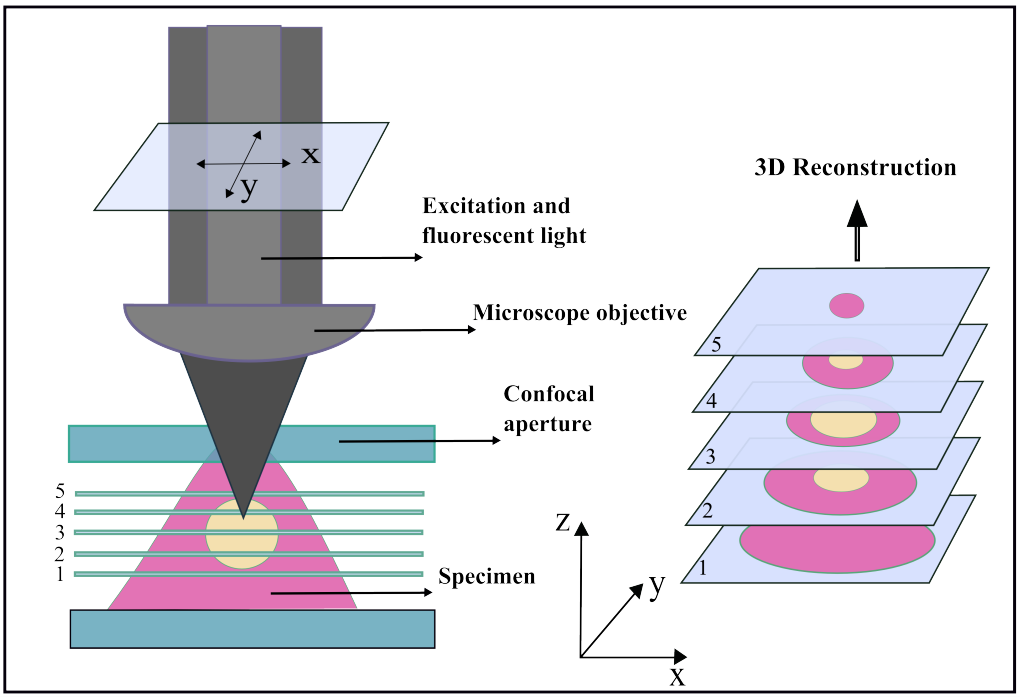

Figure 3.3: *Schematic representation of the optical imaging. The figure is adapted from [Arn].*

Confocal microscopy is an optical imaging technique used to increase micrograph contrast and/or to reconstruct three-dimensional images. A confocal laser scanning microscope is a type of confocal microscope optimised for resolution with depth selectivity from thick specimens [PM08]. In comparison to other scanning techniques, like that of the scanning electron microscope (SEM), CLSM has the advantage of not requiring a probe to be suspended nanometres from the surface, where the image is obtained

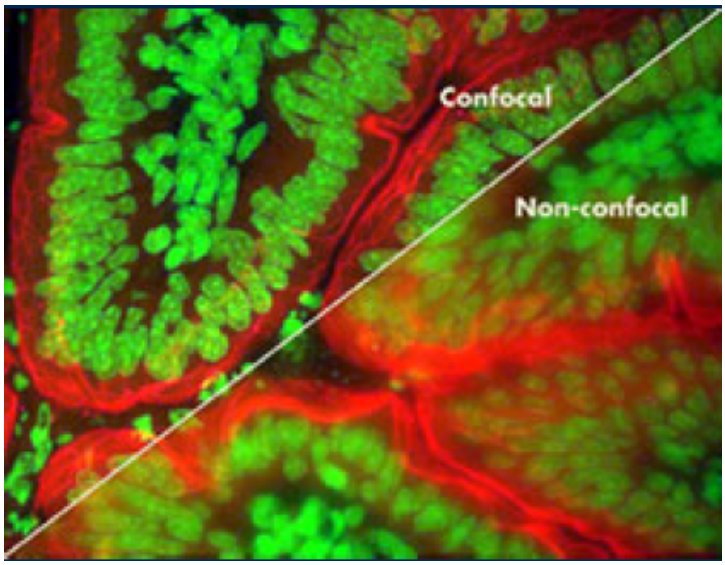

Figure 3.4: *This figure illustrates a section of mouse intestine imaged with both confocal and non-confocal microscopy. Figure taken from [Arn]*

by scanning with a fine tip. The process of acquiring in-focus images from selected depths is known as optical sectioning. Optical sectioning acquires images of thin slices of the specimen by removing the contribution of out-of-focus light in each of the images. The removal of unwanted light provides greater contrast and enables three-dimensional reconstructions by computationally combining the image data from a stack of images [CL05]. Figure 3.3 shows a schematic representation of the optical sectioning which allows the three-dimensional reconstruction. The maximum depth that can be achieved exceeds 150 μm depending on the constituency of the sample.

The technique provides a series of non-invasive high-resolution, blur-free, detailed images of very small scale structures unobtainable by other conventional widefield optical microscopy methods or scanning techniques [PM08]. In Figure 3.4 we demonstrate the image quality of a section of mouse intestine imaged with both confocal and non-confocal microscopy.

Figure 3.5 presents a schematic diagram of the principal components in a confocal laser scanning microscope. A beam of laser light is focused by an objective lens (see Figure 3.5) onto a small point in the focal plane of the specimen where it excites, for example, fluorescence. The fluorescent radiation is collected by the objective and directed onto the detector via a dichromatic mirror. The dichromatic (scanning) mirror can move or scan the laser beam in the XY direction in the focal plane, hence the name "scanning" microscopy. The wavelength range of the fluorescence spectrum is selected by an emission filter, which also acts as a barrier, blocking the excitation laser line. The pinhole (or confocal aperture) is arranged in front of the detector, on a plane conjugate to the focal plane of the objective. Light coming from the planes above or below the focal plane is out of focus when it hits the pinhole, so most of it cannot pass through the pinhole and therefore does not contribute to forming the image. This is the most important feature of the confocal microscope, the capability of isolating and collecting a plane of focus from within a sample, thus eliminating the out of focus "haze" which is normally seen with a fluorescent sample. Fine detail is often obscured by the haze and cannot be detected in a non-confocal, fluorescence

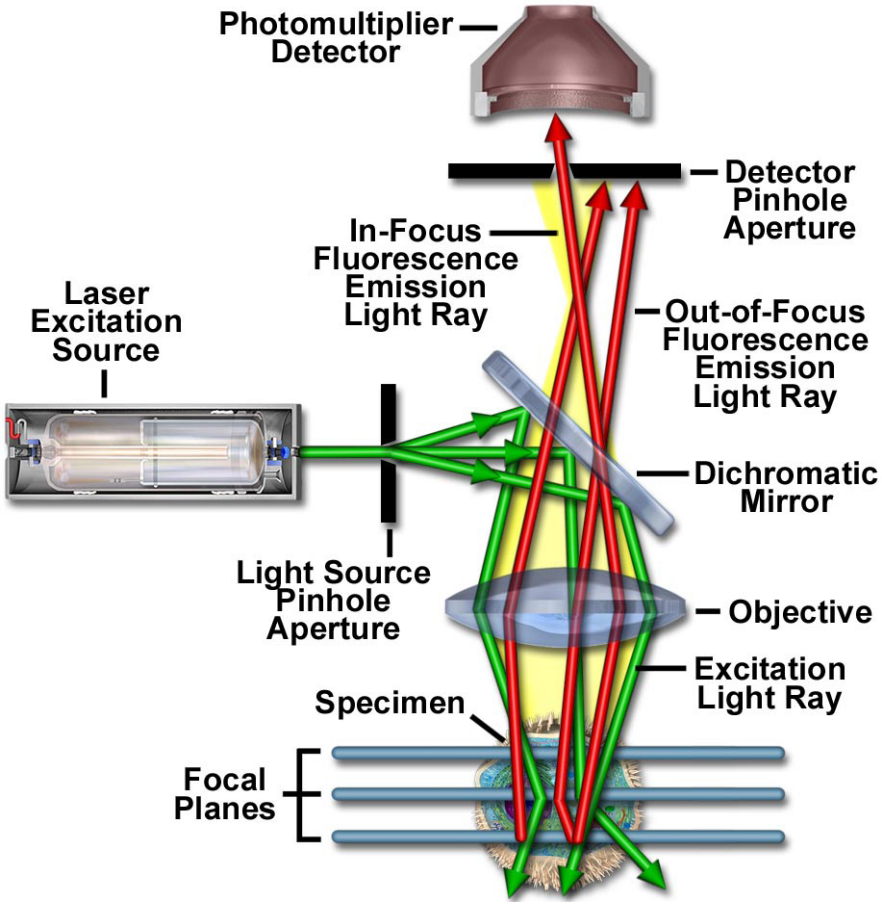

Figure 3.5: *Schematic diagram of the optical pathway and principal components in a confocal laser scanning microscope. The excitation light is directed by the dichromatic mirror and focused on the specimen. The mirror also separates the fluorescent emission from the excitation. The light is then emitted from the location of the scanning spot (which is at the centre of the in-focus plane) goes through the pinhole in front of the photomultiplier detector. Figure taken from [CFD06]*

microscope (see Figure 3.4).

There are various studies on brain anatomy that utilise confocal laser scanning microscopy. Axer et al [AK00] use confocal scanning laser microscopy combined with polarised light [LGG+07] to perform detailed anatomical mapping of fibre orientations in the internal capsule using post-mortem human brains. They give a detailed description of how fibre tracts are anatomically defined in various areas of white matter. In later work [ASvK99], they test the possibility of real-time impedance monitoring in post-mortem brains and analyse the value of the measurements in intact cerebral structures. They use confocal scanning laser microscopy to verify the regions from where the measurements were taken.

Jinnoet et al. [JAFK98] estimate the numerical densities of glutamic acid decarboxylase (GAD) 67 immunoreactive (IR) neurons in the mouse hippocampus according to the optical dissector method (stereological estimation of neurons) using a confocal laser scanning microscope, and measure the cell sizes of dissector-counted neurons. Gage et al. [GCP+95] study the survival and differentiation of adult neuronal progenitor cells transplanted to adult rat brain. The labelled cells and sections of interest are visualized using confocal scanning laser microscopy.

3.2.2 Mesh Generation

This section discusses techniques used to generate meshes and details a commonly used reconstruction method, the marching cubes algorithm.

A mesh is a collection of polygons that approximates a surface. It can produce complex geometry from a few basic geometric primitives [Ede01]. Meshes are commonly used in simulations of physical phenomena such as realistic animation of fluids [KFCO06], deformable solids [THMG05] and biomedical imaging. Three dimensional surfaces of the anatomy are very useful in medical studies for processing medical data. Typically, these data are acquired by computed tomography (CT), MR or single photon emission computed tomography (SPECT). There are several meshing techniques for visualizing extracted surfaces [LBPH08].

3.2.2.1 Meshing algorithms

The 'advancing front' algorithm constructs the mesh by progressively adding mesh elements (faces) starting at the boundaries [LP88]. All the faces that describe the surface are treated as fronts and are expanded into the volume in order to achieve a final 3D representation. The selection of points (or nodes) to create the new faces encourages the use of existing points. One of the main drawbacks to this approach is that the resulting surface needs local or regional refinement with either use of another technique or use of external libraries.

'Mesh matching' is an algorithm that begins with a generic volume mesh and tries to match it to the specific surface [CPL00]. The base volume is obtained from an interpolation of several sample models. To obtain a new mesh, one needs to find a transformation function that will be applied to the entire base mesh and in that manner produce the final volume mesh. A limitation of this technique is that the new mesh needs to be sufficiently close to the base mesh to achieve convergence [CPL00].

The 'octree' technique starts from a bounding box of the surface of the mesh [SG91]. This bounding box or 'octant' is split into eight new octants. Each octant is then iteratively split into eight new ones, unless it resides outside the input surface mesh, in which case it is removed from the list. The algorithm stops when a predefined maximum level of iterations is reached or when a condition of surface approximation is satisfied. The octree does not consider a surface approximation algorithm once the split process is done. Therefore this method has to be combined with other techniques in order to produce a final mesh that represents the surface well. Finally, surface extraction using octree-based approaches is computationally expensive.

The 'marching cubes' algorithm is probably the most popular surface extraction algorithm and a subject of ongoing visualization research [NY06, WSHH02]. It is a direct image-based approach, since it combines the geometric detection and mesh creation stages in one step. A significant benefit of the method is that it can robustly generate meshes for topologies of arbitrary complexity and also allow multiple surface reconstruction, hence is ideal for mesh generation from image stacks. In the following section we provide details of the marching cubes algorithm.

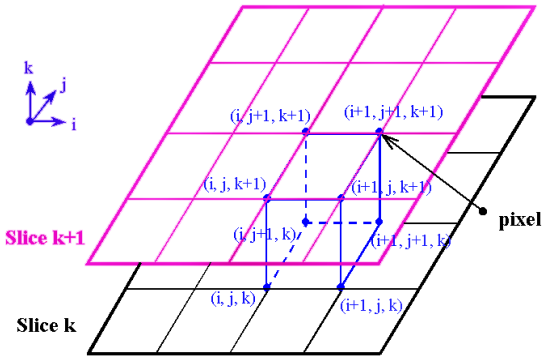

Figure 3.6: *This figure demonstrates the positioning of a logical cube between two images.*

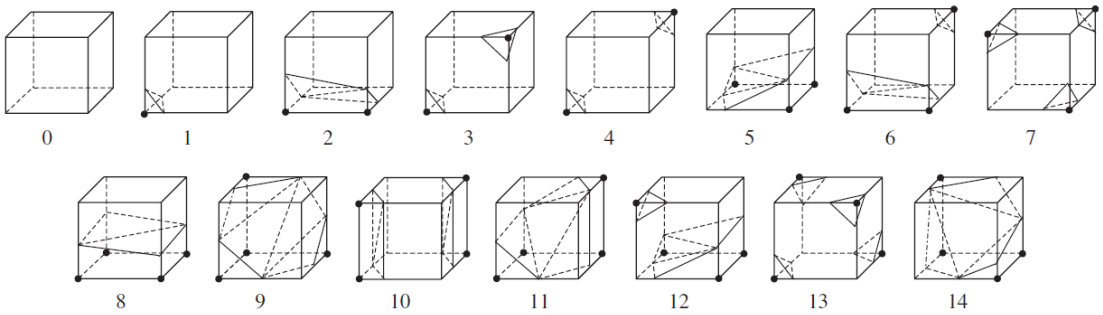

Figure 3.7: *Representation of the 15 topological states of the cube accounting for rotations and symmetries. Figure taken from [NY06]*

3.2.2.2 Marching Cubes

In 1987, Lorensen and Harvey [LC87] designed the marching cubes algorithm for mesh models that represent isosurfaces. In medical images, an isosurface can correspond to skin or an organ surface. The algorithm takes a stack of 2D images as its input and produces a 3D triangular mesh. The algorithm defines a cube by the intensity values at pixel corners between adjacent 2D images (see Figure 3.6). The cube moves between all corners and slices in the image stack. If one or more pixels of a cube have values less than a pre-specified value that corresponds to the surface, and one or more have values greater than this value, then the cube must contribute some component to the surface. By determining which edges of the cube are intersected by the surface, triangles can be created that divide the cube into regions inside and outside the surface. The algorithm can produce between one and four triangles within a voxel that contains the surface. Figure 3.7 presents the topological stages of the cube that can be created from the triangles, accounting for rotations and symmetries. We then connect all the triangles together to form the reconstructed surface.

Problems and Alternatives: One of the practical problems with the marching cubes algorithm is the amount of memory needed to store the resulting surface. As each boundary cube can generate up to four sub-pixel facets, the resulting mesh can contain a large number of triangles. We can reduce this by sharing vertices and edges, or even merging coplanar patches into larger facets. Another solution might be to try and fit parametric surfaces to groups of boundary points, though this may be difficult for complex surface geometries [WW92]. Additionally, to smooth out the surface and reduce the number of

triangles in the models we can use one of the triangle reduction methods [SZL+92].

3.3 Biological Phantom

This section demonstrates the high-fidelity mesh models using a biological phantom (green asparagus). Experiments optimise simulation parameters and complexity of the meshes to achieve accuracy and reproducibility while minimizing computation time. Finally we assess the quality of the synthesised data from the mesh models by comparison with scanner data as well as synthetic data from simple geometric models and simplified meshes that vary only in two dimensions.

3.3.1 Methods

The full experimental procedure has several stages. First, we acquire DW-MRI data with a wide range of diffusion times and diffusion weightings with gradient directions both parallel and perpendicular to the asparagus stem. These directions are the most sensitive to the microstructural parameters we want to estimate. We identify a region of interest (ROI) in the DW-MRI data containing one of the vascular bundles (Figure 3.8 a) where diffusion anisotropy is observed due to thick membranes, which we cut from the stem and image with CLSM to obtain a stack of images (Figure 3.8 b). We construct the three-dimensional mesh model with the marching cubes algorithm [LC87] and use it as a substrate in Monte-Carlo simulations [HA09] to synthesise DW-MRI data.

3.3.1.1 Choice of Phantom

We decided to use green asparagus (*Asparagus officinalis*) as our phantom to measure the diffusion-weighted MRI signal. The green asparagus is a well-used biological phantom [CRSS07, LNR+07, SS06, BLEO01] with similar diffusion anisotropy to white matter tissue. The vascular bundles in the asparagus consist of highly-organised cylindrical fibres with thick walls and have a distribution of capillary sizes similar to brain white matter tissue [LNR+07]. Most axons in brain white matter have a diameter between 0.2 and 20 μm [WKS95], while asparagus capillaries range from 0.1 up to 50 μm. Furthermore, asparagus is cheap and easy to work with, providing an excellent sample for developing and tuning new computational methods.

Structural description of asparagus officinalis tissue: Figure 3.9 shows a confocal microscopy image of a cross-section of the asparagus stem. The peripheral epidermis (a) typically contains one row of cells which form the outer layer covering the entire body of the plant. These rectangularly shaped cells surround a thick bundle of fibres (b) which form the pro-epidermis fibre tips. These are highly organised fibres parallel to the axis of the asparagus stem. The cells have particularly thin walls and long columns that unite vertically to form sieve tubes. The pro-epidermis fibres (b) surrounds a large region called pith (c). The pith is a heterogenous area of almost spherical cells. Most of these cells have thin walls and are responsible for the photosynthesis, support, storage of materials and lateral transport. The pith also contains thick-walled cells which are involved primarily in the transportation of water (sap fluid) (d) [BLEO01, Bla32]. A prestudy was done to find a suitable ROI in the biological phantom to study water diffusion. We tested all the different regions we described above as well as the whole cross-section of the asparagus stem. Results show that the area of the pith containing the vascular bundles (d) exhibit

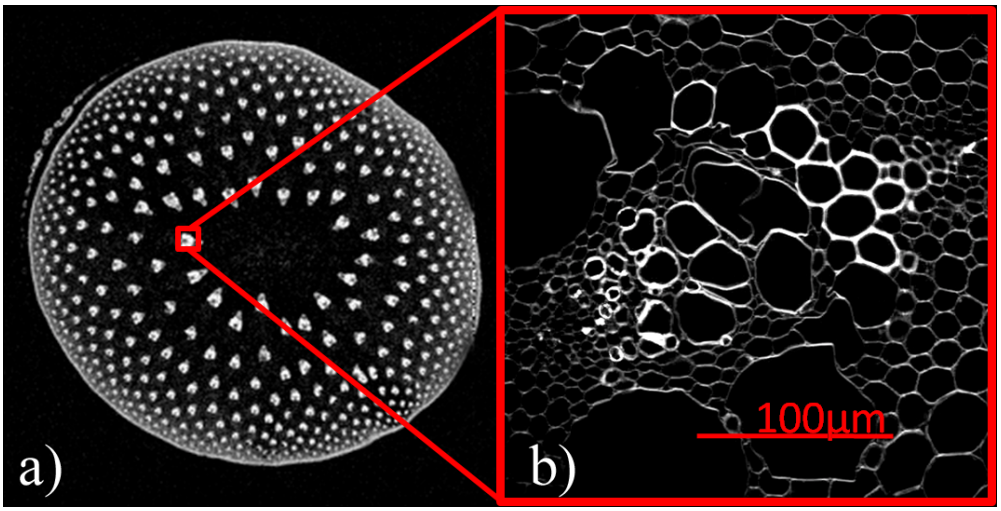

Figure 3.8: *Figure a) presents a DW-MRI image of a transverse section of the asparagus stem. The red square indicates the ROI, containing one of the vascular bundles, appearing white in the MRI image. Figure b) presents a CLSM image of the same ROI.*

the highest diffusion anisotropy. Also in agreement with previous studies [LNR+07] it was shown that mainly these vascular bundles contributed to the signal and not the cellular structure between the bundles.

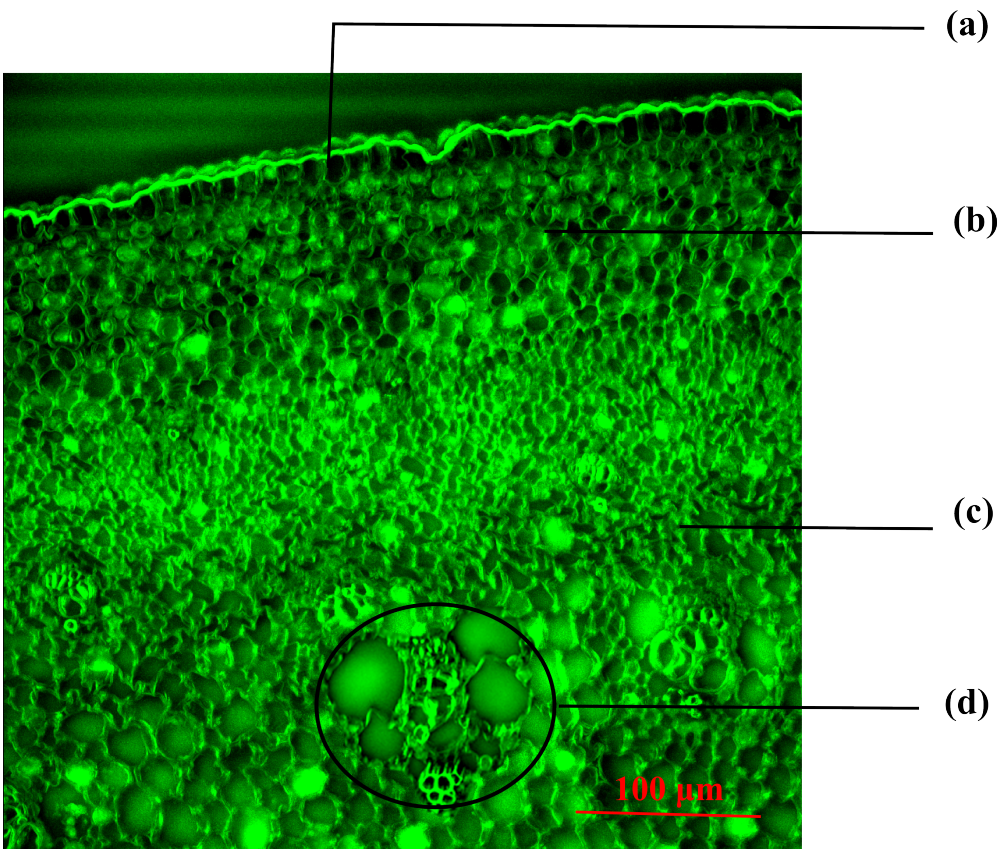

Figure 3.9: *Image from the confocal acquisition performed for this experiment on the same sample. Cross-section of the asparagus stem showing microstructural details. In (a) the figure shows the peripheral epidermis, (b) indicates the pro-epidermis fibres, (c) indicates the pith and (d) shows the vascular bundles in the pith.*

3.3.1.2 Sample preparation

We place a stem of green asparagus in a syringe padded with cotton soaked in pure water (see Figure 3.10). This keeps the sample hydrated, preventing tissue shrinkage and changes in the diffusion properties during the course of the scan.

Figure 3.10: *Preparation of the sample for the MRI scanning.*

3.3.1.3 MRI acquisition

We acquire diffusion-weighted MR images with a small bore 9.4T Varian scanner with maximum gradient strength 400 mT/m and use a controlled air-flow mechanism to keep the sample at a constant temperature of $\pm 1\,^{\circ}$C. The temperature was 19 °C. The two-direction encoding scheme has one direction parallel to the asparagus stem and one perpendicular. We acquire 64 pulse-gradient spin-echo (PGSE) measurements with six diffusion times, $\Delta = 10, 30, 50, 70, 80, 100$ ms, three gradient durations $\delta = 3, 10, 20$ ms and gradient strength $|\mathbf{G}|$ varying from 40 to 400 mT/m in ten steps of 40 mT/m. Measurements with a b value greater than 6.5×10^9 sm^{-2} were not acquired due to poor SNR (< 3) i.e all combinations with $|\mathbf{G}| = 400$ mT/m, Δ =70, 80, 100 ms with $\delta = 20$ ms. In total we acquired 64 measurements. We use the minimum echo time (TE) possible for each measurement and set the repetition time (TR) to 3 s to minimise gradient heating effects. The total acquisition time is approximately 40 hours. We correct for T_2 dependence by acquiring separate $b = 0$ images for each parameter combination. The in-plane field of view is 16 mm. The matrix size is 256×256 and the slice thickness is 0.5 mm. In Figure 3.11 we plot the parallel and the perpendicular direction of the log normalized signal from voxels in the region of interest and show diffusion MRI images for various b values.

The combinations of the imaging parameters Δ, δ and $|\mathbf{G}|$ were chosen to cover the signal range as evenly as possible. The imaging protocol is originally based on previous studies of the diffusion MR signal in white matter [SSWH97, ABKYB08] however, the specific parameters were established into our final protocol experimentally. We adjusted the parameters so that we could observe restriction in our sample from all the capillary sizes in our ROI. Furthermore, the novelty of this protocol is the long gradient durations δ which we can use due to the GPD approximation. The full imaging protocol is provided in Tables D.1, D.2, D.3 in Appendix D.

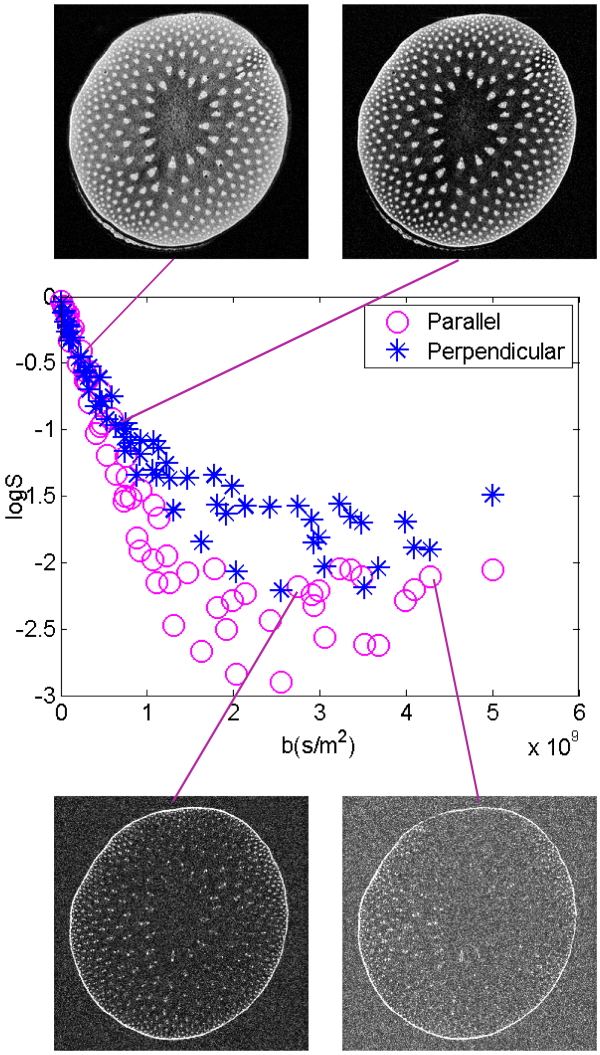

Figure 3.11: *Plot of the parallel and the perpendicular direction of the log signal from voxels in the ROI and demonstration of diffusion MRI images (parallel direction) for various b values.*

3.3.1.4 Confocal acquisition

We use a vibratome to acquire samples from the stem. A vibratome is an instrument similar to a microtome but uses a vibrating razor blade to cut through tissue. We glue a 0.5 cm thick sample of the stem to a metal block and section it while submerged in a buffer bath. We acquire four 600 μm thick sections which we collect with a fine brush and transfer to multiwell plates for staining. We then stain the samples with Eosin for 10 minutes and subsequently wash thoroughly with phosphate buffered saline. The purpose of staining the tissue is to add visual contrast to otherwise transparent or unclear structures, so they will be easier to view and study under the microscope.

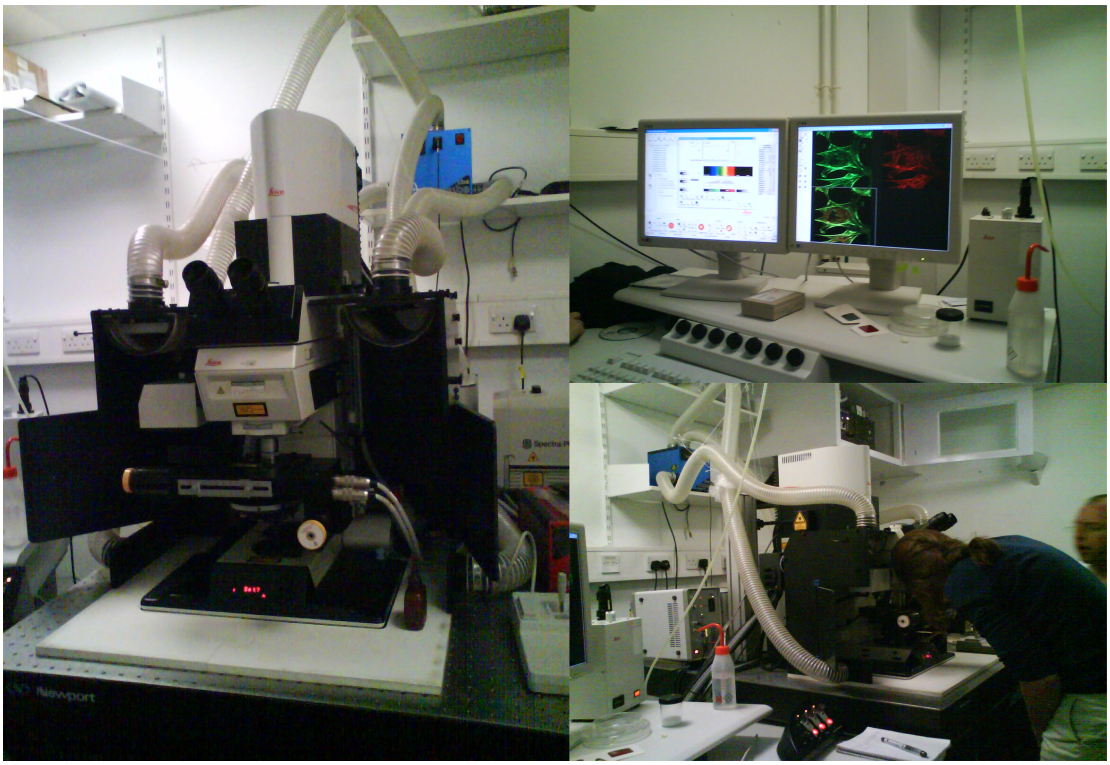

Figure 3.12: *Experimental setup of the confocal laser scanning microscope.*

We use a Leica SP2 AOBS confocal multi-photon laser scanning microscope coupled to a Leica DMRE upright microscope (Leica, Milton Keynes, UK), equipped with a pulsed, mode locked femtosecond (fs) Ti:Sapphire Tsunami laser synchronously pumped by a Millenia VII (Spectra-Physics, Mountain View CA), diode pumped solid state (DPSS) frequency doubled laser, capable of delivering up to 8.5 W pumping power at 532 nm. In Figure 3.12 we present the experimental setup of the confocal microscope we used for this acquisition.

We perform all image acquisitions at 800 nm with a pulse width 80 fs and a pulse repetition rate of 80 Mhz. We set the emission spectral detection between 470 - 700 nm. We record the laser power output at the microscope objective with a coherent power meter and calibrate it for all samples to deliver 60 mW peak power. We couple an IST laser spectrum analyzer to a Tektronix TDS 210 oscilloscope and use it to tune the laser to the desired wavelength. We receive the laser output with an electro-optical modulator (EOM) (Linos LIV20) before delivering to the confocal microscope through a series of optical mirrors. The EOM allows the laser intensity at the objective to be controlled and optimized. We set the EOM at 90% for imaging to ensure that the polarization of the incidental laser beam remained consistent across all specimens.

We image the specimens with a 40×1.25NA oil Plan Apo objective to give image dimensions of $375\,\mu$m $\times$ $375\,\mu$m. We acquire optical z-sections of $1\,\mu$m thickness reaching a maximum depth of $100\,\mu$m with an image averaging set to 3 per z-slice. Image averaging is a digital image processing technique that is employed to enhance images that have been corrupted by random noise. The algorithm operates by computing an average of the intensity values for each pixel position in a set of captured

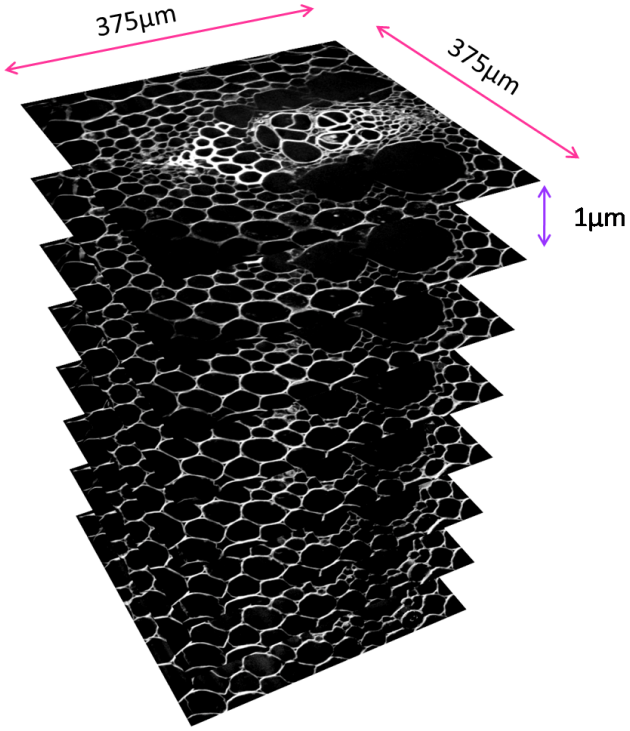

Figure 3.13: *Stack of confocal microscopy images from the asparagus sample.*

images [WNJ00]. Figure 3.13 presents a stack with some of the confocal microscopy images. The image size is 1024×1024 pixels. In total we acquire 100 images.

3.3.1.5 Mesh construction

To construct the mesh models we follow the mesh construction pipeline as described in Section 3.1. We segment the stack of the confocal images, as shown in Figure 3.13, by thresholding using Otsu's method [Ots75]. This way we create binary images that separate the intra- and extra-capillary space (see Figure 3.14). The intra-cellular volume fraction is determined by counting the pixels below the threshold. We use the marching cubes algorithm [LC87] on the binary stack to produce the three-dimensional mesh model, as shown in Figure 3.15.

Memory limitations require that we downsample the 100 CLSM images to 144×144 pixels (Figure 3.14 c) while keeping the three-dimensional aspect ratio of the voxels the same as the original image stack, which also makes computation times manageable. The algorithm typically produces a mesh containing approximately 500,000 triangles.

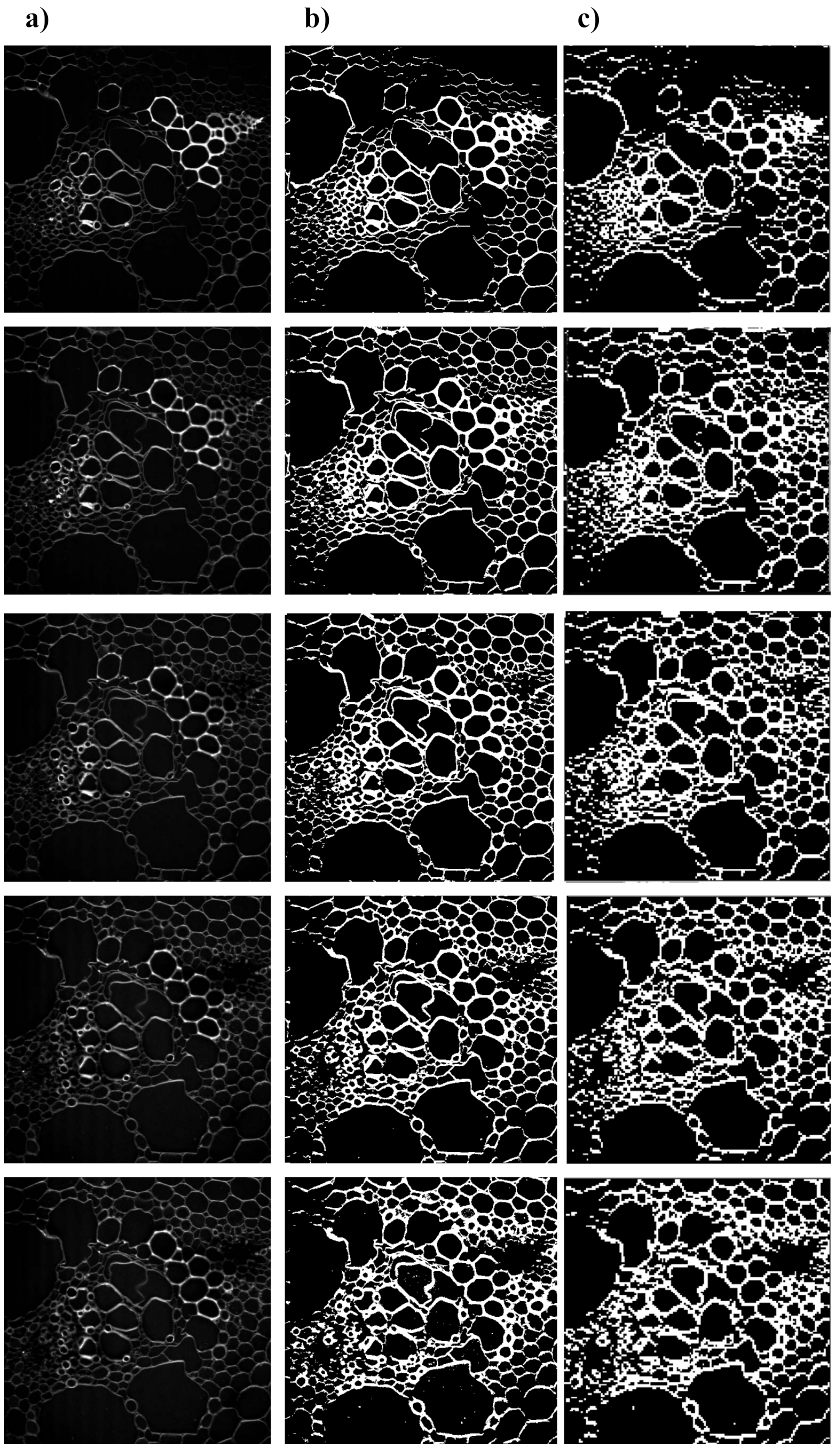

Figure 3.14: *Presentation of a) an original confocal microscopy image, b) the thresholded image and c) the downsampled thresholed image from 5 images of the stack, each 10 µm apart.*

3.3.1.6 Simulation

We use the simulation system in [HA09], described in Section 2.7.2, which generates synthetic measurements for each combination of scan parameters from diffusing spins constrained by the structure of the mesh. Each triangle in the mesh acts as an impermeable reflecting boundary. For computational efficiency the system checks only for intersections with triangles within the range of each step. Spins are initialized uniformly across the mesh, in both intra- and extra-cellular spaces. We assume the same properties (i.e. diffusivity, relaxation times) for both.

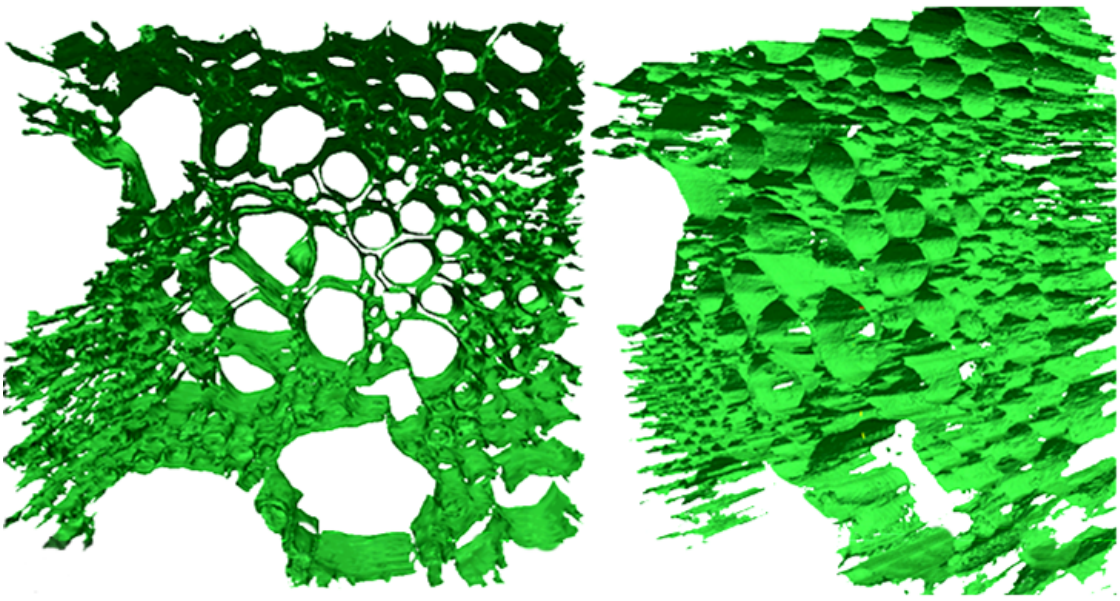

Figure 3.15: *The constructed three-dimensional mesh model of the ROI, shown from two different angles.*

3.3.2 Experiments

This section outlines three sets of experiments. The first identifies a suitable combination of number of spins and updates within a fixed simulation runtime. The second explores the effect of the mesh resolution. The final experiment compares synthetic data from the three-dimensional mesh with scanner data and synthetic data from simpler geometric models.

3.3.2.1 Simulation parameter optimization

The aim is to maximize precision and accuracy of the synthetic measurements while minimizing computational cost. The complexity of the simulation is of order

$$U = NT \tag{3.1}$$

where N is the number of spins and T is the number of updates. Without a ground truth, the accuracy of the simulation is hard to establish. However, [HA09] shows on simpler substrates that with fixed U accuracy tends to increase up to a certain N and suddenly departs although standard deviation keeps decreasing. Here we search for the same trend to identify the best trade off.

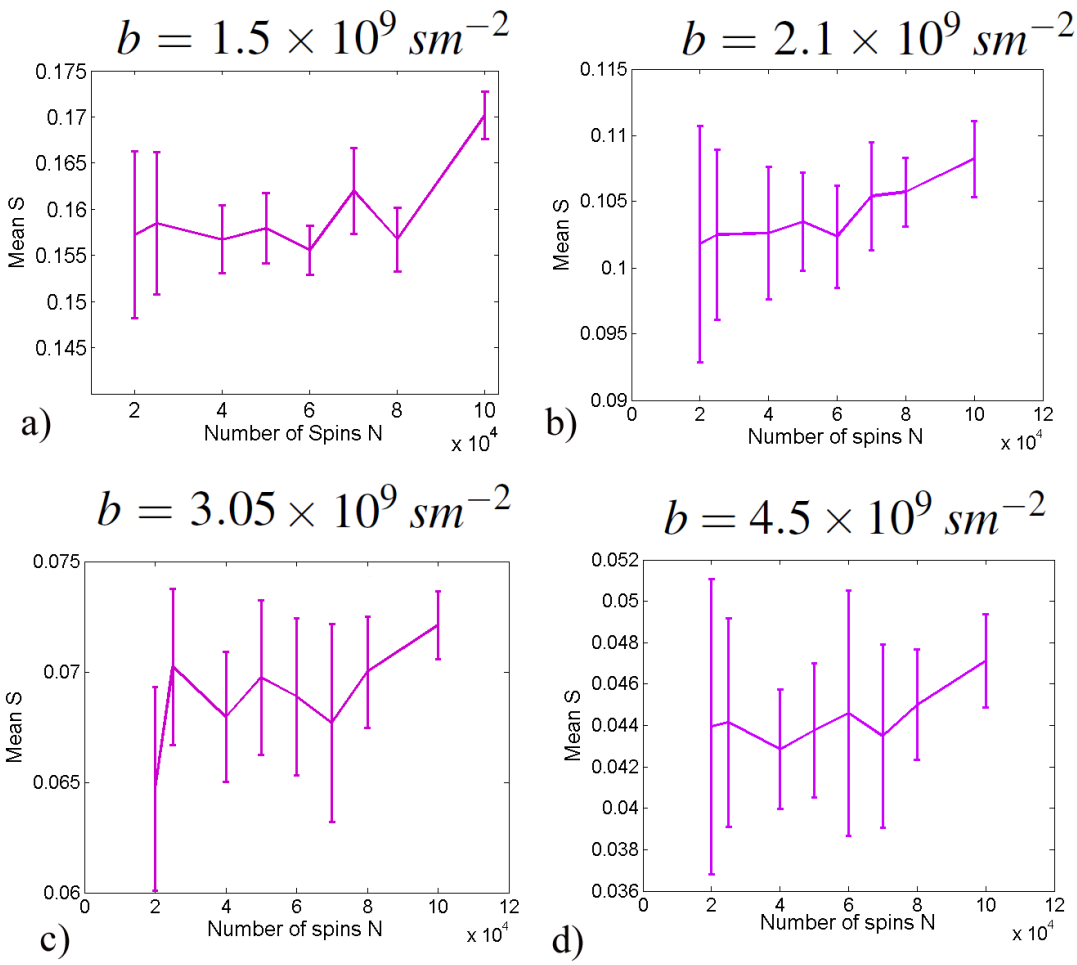

Figure 3.16: *Plot of the mean normalised signal S for the perpendicular direction for simulations with different pairs of N, T for constant* $U = 10^8$ *using the* 144×144 *mesh. Error bars indicate the standard deviation over 10 different initial spin positions for each simulation. Here we present results for four measurements with different b values: a)* $b = 1.5 \times 10^9\ sm^{-2}$*, b)* $b = 2.1 \times 10^9\ sm^{-2}$*, c)* $b = 3.05 \times 10^9\ sm^{-2}$ *and d)* $b = 4.5 \times 10^9\ sm^{-2}$.

We use the 144×144 mesh as substrate with the same acquisition protocol as the scanner data and diffusivity $d = 2.1 \times 10^{-9}\ \mathrm{m}^2/\mathrm{s}$. We estimate the diffusivity from scanner measurements with low b value using the monoexponential model. Simulations with various combinations of N and T for $U = 10^8$, as in [HA09], are repeated 10 times with different initial spin positions. Each simulation runs in approximately 48 hours.

Results: Figure 3.16 shows the mean signal S and the standard deviation for the perpendicular direction for simulations with different pairs of N, T. The signal is similar among b values as N increases from low $N \simeq 1 \times 10^4$ until $N \simeq 1 \times 10^5$. We present the results for $b = 1.5 \times 10^9\ \mathrm{sm}^{-2}$, $b = 2.1 \times 10^9\ \mathrm{sm}^{-2}$, $b = 3.05 \times 10^9\ \mathrm{sm}^{-2}$ and for $b = 4.5 \times 10^9\ \mathrm{sm}^{-2}$. All measurements of different b values have similar trends with small variations that do not affect the final choice.

Conclusions: As in [HA09], we observe a gradual increase in reproducibility as N increases i.e. error bars reduce. The mean signal remains approximately consistent from low N until $N \simeq 8 \times 10^4$, above which it increases noticeably. The increase is most likely a bias introduced by the timesteps being too

long. The step length is calculated using a free diffusion approximation which does not take restriction into account. Therefore, when the step length exceeds the typical length scale of the structure it ceases to be valid due to restriction. We choose $N = 8 \times 10^4$ and $T = 1250$ to keep reproducibility high while remaining safely within the region of sufficiently short timesteps. We use this combination of N and T in all remaining experiments.

3.3.2.2 Optimal diffusivity

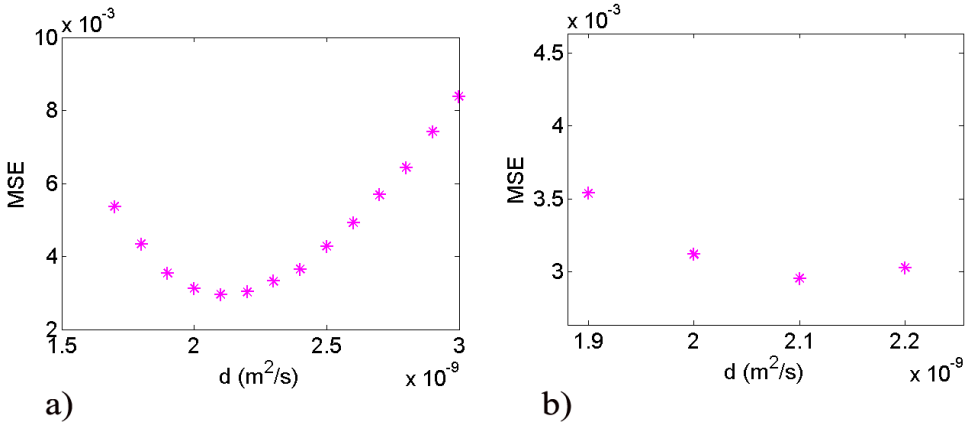

Figure 3.17: *a) Plot of the MSE of the signal in the parallel direction against the synthesized data from different values of diffusivities. b) is a magnified view of a) and indicates that* $d = 2.1 \times 10^{-9}\, m^2/s$ *minimizes the MSE.*

This experiment searches for the optimal value for the diffusivity parameter d. We synthesize data using the high resolution mesh and the different diffusivities with values varying from $d = 1.7 \times 10^{-9}\,\mathrm{m}^2/\mathrm{s}$ up to $d = 3.0 \times 10^{-9}\,\mathrm{m}^2/\mathrm{s}$. We calculate the Mean Squared Error (MSE) of the synthesized data for the parallel direction with the different diffusivities and the scanner data to reveal which diffusivity value captures the observed signal.

Results: Figure 3.17 a) plots the *MSE* against all the different values for diffusivity used for synthesizing data. We exclude all measurements with $S < 0.1$ from the plots and the MSE calculations to avoid significant noise-floor effects. Figure 3.17 b) reveals that $d = 2.1 \times 10^{-9}\,\mathrm{m}^2/\mathrm{s}$ minimizes the *MSE*.

Conclusions: The diffusivity value that best explains the data is $d = 2.1 \times 10^{-9}\,\mathrm{m}^2/\mathrm{s}$, which is in agreement with studies studying diffusion anisotropy using asparagus [LNR+07]. Also this value confirms the theoretically derived diffusivity using the simple exponential model and agrees with the diffusivity of the water at room temperature (19 °C) [HHS00]. We use this value for the diffusivity d in all remaining experiments.

3.3.2.3 Signal dependency on mesh fidelity

This experiment compares meshes constructed from different resolution CLSM images to investigate the effect of varying mesh resolution on synthetic DW-MRI data. The highest image resolution we use is 144×144 pixels and the lowest 9×9 pixels with four intermediate stages 108×108, 72×72, 36×36 and 18×18. Figure 3.19 presents the different resolution mesh models. We synthesize data from the different resolution meshes using the parameters from experiment 3.3.2.1. We calculate the

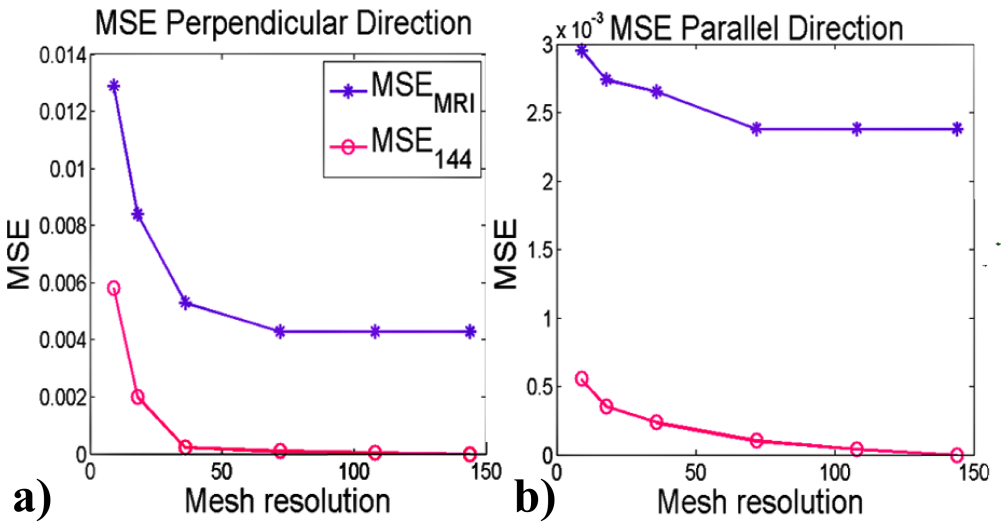

Figure 3.18: *Plot of the MSE of the signal in a) the parallel and b) the perpendicular direction in comparison with the high-resolution mesh and the scanner data, against mesh resolution.*

Mean Squared Error (MSE_{144}) compared to the 144×144 mesh to show differences in synthesizing data with different resolution meshes, and the MSE_{MRI} compared to the scanner data to reveal which of these differences are significant.

Results: Figure 3.18 plots the MSE_{144} and MSE_{MRI} of the normalised signal for both directions against mesh resolution. We exclude all measurements with $S < 0.1$ from the plots and the MSE calculations to

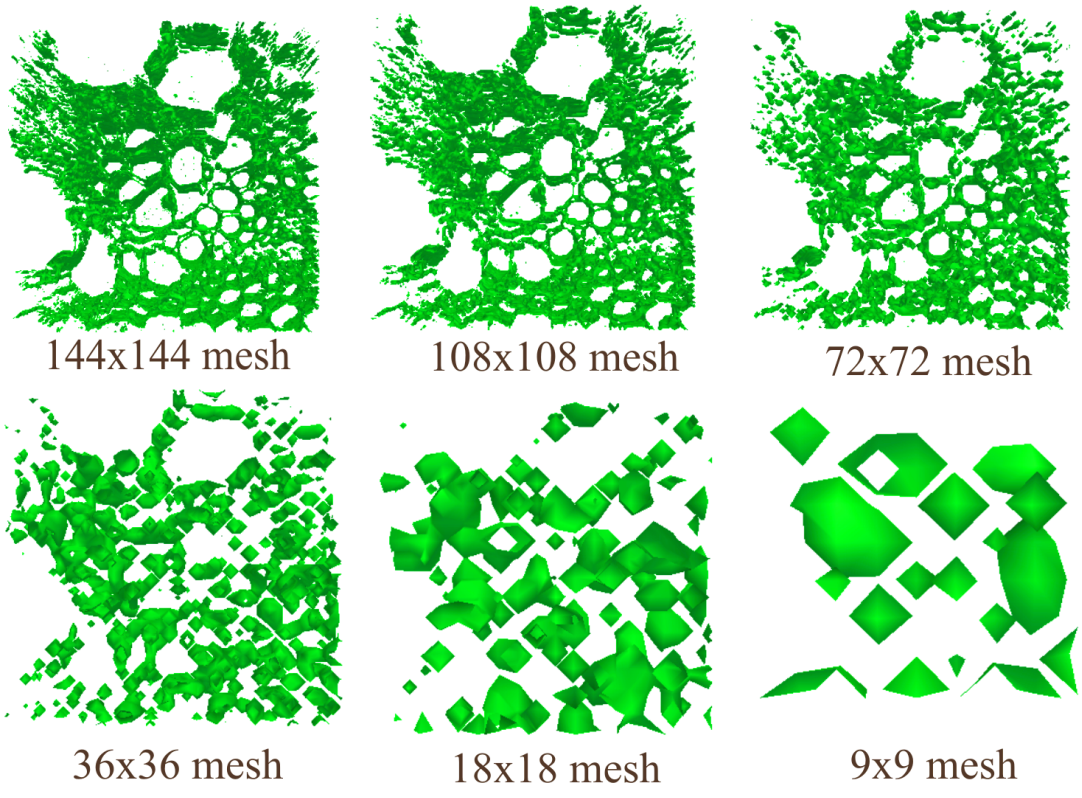

Figure 3.19: *Illustration of the different complexity meshes used in the simulations.*

avoid significant noise-floor effects. In the perpendicular direction the MSE_{144} shows very little variation between the 144×144 and 36×36 resolution meshes. In the parallel direction, the MSE_{144} starts to increase at 72×72 resolution. The MSE_{MRI} however, shows little difference in both directions for the meshes with resolution 144×144 to 72×72.

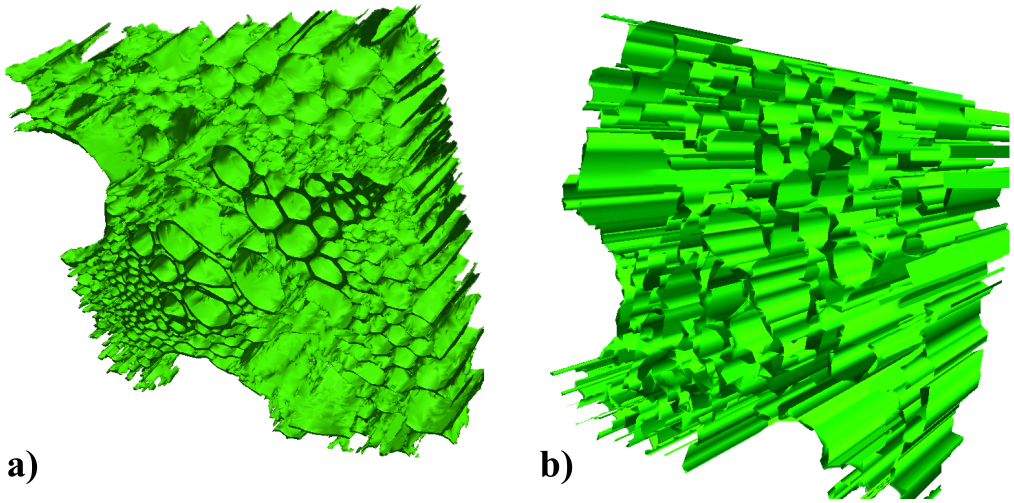

Figure 3.20: *This figure presents a) the three-dimensional mesh and b) the extruded mesh model.*

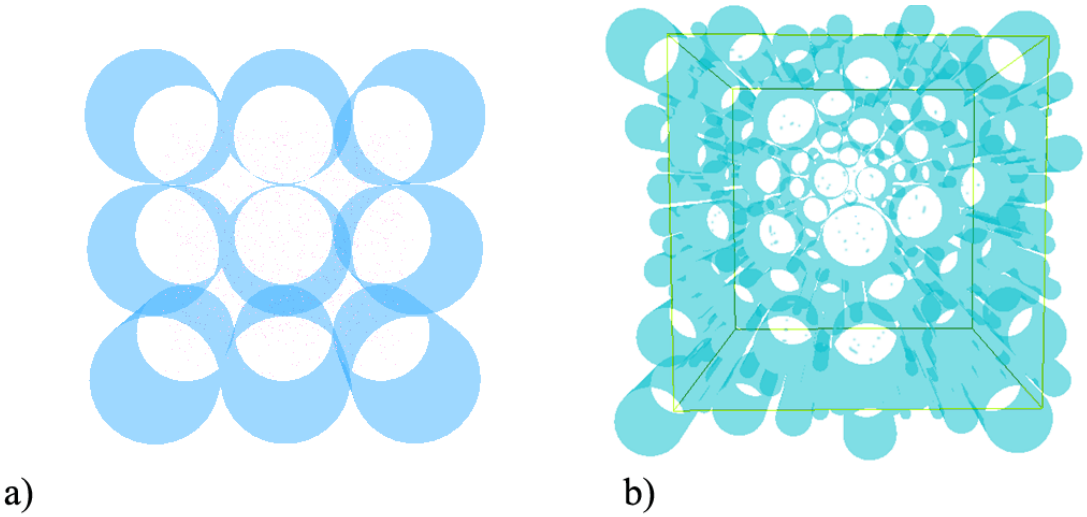

Figure 3.21: *This figure presents a) the square-packed cylinder substrate and b) the gamma distributed radii cylinder substrate.*

Conclusions: In both directions the MSE_{MRI} remains similar for the meshes with resolution 144×144 to 72×72 meshes. At 36×36 we see slight elevation that becomes more obvious in lower resolution meshes. The results suggest that 72×72 resolution approximates the geometry closely enough to capture variations in water diffusion that MR signals are sensitive to.

3.3.2.4 Model comparison with scanner data

The last experiment assesses the quality of MRI data synthesised using the mesh models. For comparison, we generate four sets of synthetic data: the 72×72 three-dimensional mesh from experiment

3.3.2.3, an extruded two-dimensional mesh model (see Figure 3.20) and two packed-cylinder substrates with parametric axon radius distributions (see Figure 3.21). One has constant radius and the other gamma distributed radii.

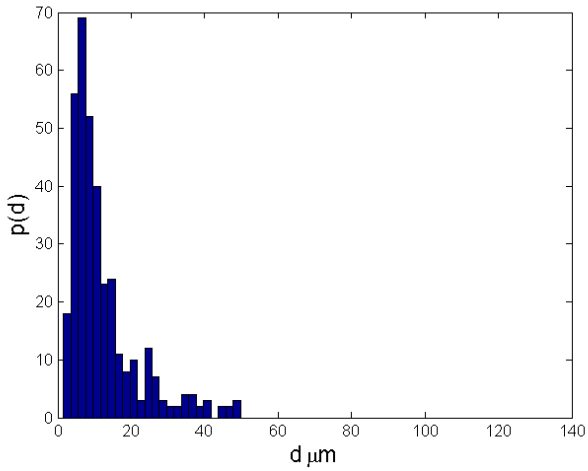

Figure 3.22: *Histogram of the capillary radii in the ROI for which the gamma distribution was calculated for the gamma distributed cylinders model.*

To construct the extruded mesh we choose an image from the stack used for the three-dimensional mesh model with $f = 0.78$, which is consistent with the three-dimensional model, and replicate it to have the same number of slices used to generate the 72×72 mesh and run the same meshing algorithm. The packed-cylinder substrate has square-packed cylinders with radius $25\,\mu$m. The choice of single radius comes from the mean capillary radius in the mesh weighted by capillary volume. The capillary radii were measured by hand from the CLSM images. The second parametric model has gamma distributed radii derived from the histogram of capillary radii in the ROI assessed from the CLSM images (see Figure 3.22). In both parametric models we pick the packing density so that the intra-capillary volume fraction is $f = 0.78$, which is consistent with the three-dimensional mesh model.

Results: Figure 3.23 compares data synthesised from the three models to the scanner data by plotting the normalised signal S for selected values of Δ and δ as a function of the gradient strength $|\mathbf{G}|$ for the parallel and perpendicular direction. Table 3.1 presents the Mean-squared error (MSE) of the parallel and perpendicular direction for each model. Again we exclude all measurements with $S < 0.1$ from the plots and the MSE calculations to avoid significant noise-floor effects.

Predictions from simulations with the cylinders of constant radii and the extruded mesh model are unable to capture the data as well as the three-dimensional mesh model. For example the cylinders underestimate the perpendicular signals with Δ = 10, 30 ms and δ= 3, 10 ms while the extruded model overestimates them.

The gamma distributed radii model and the three-dimensional mesh agree closely and both capture the broad trend of the MRI data. The MSE is lower for the three-dimensional mesh in both directions, suggesting that although the gamma distributed cylinders provide a good model, the three-dimensional mesh captures some added subtleties. In particular the fit to the data improves in the parallel direction,

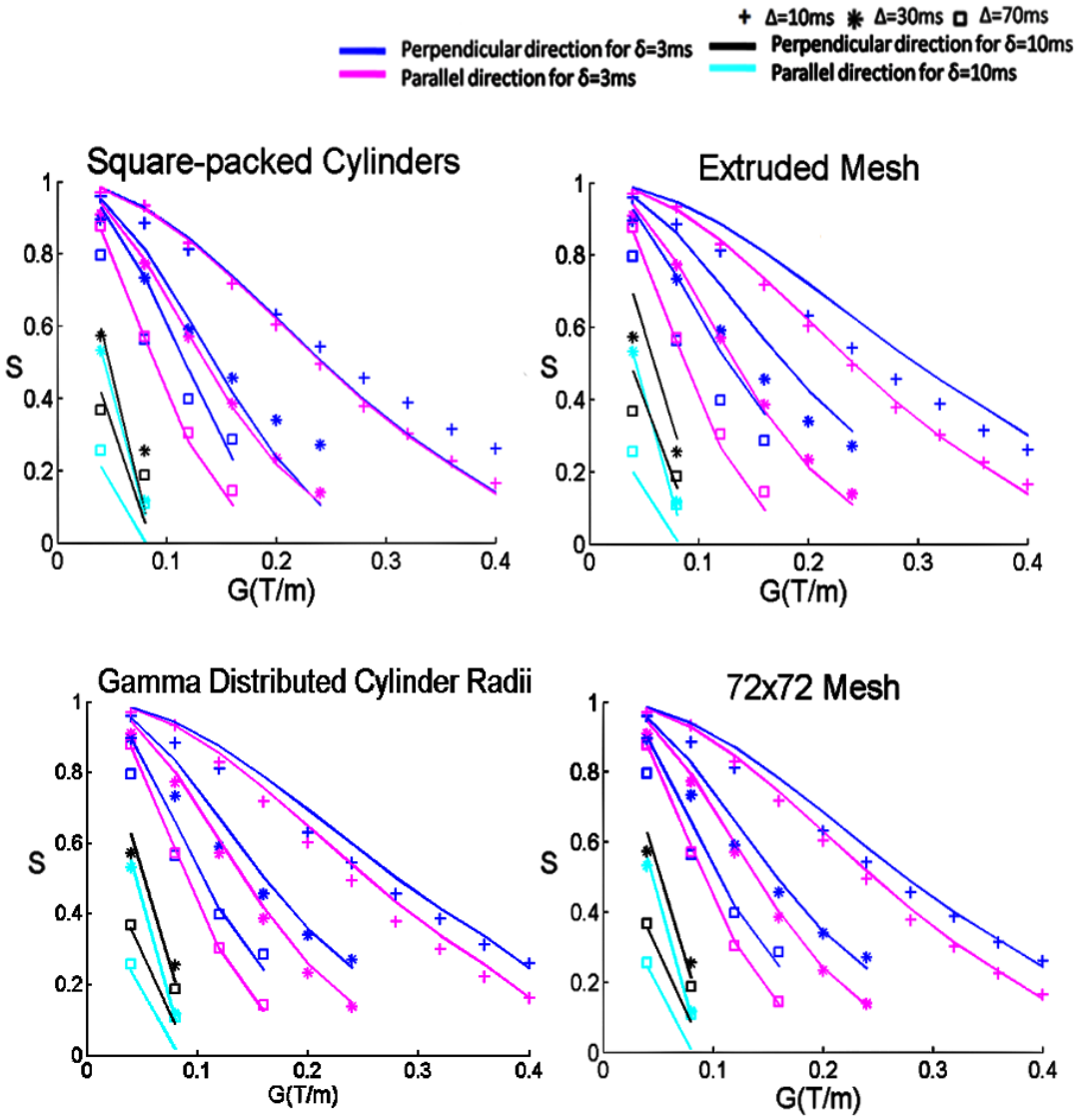

Figure 3.23: *Comparison of data synthesised from the cylinder model, the extruded mesh and the three-dimensional mesh with the scanner data from the PGSE experiment. For clarity, the normalised signal S is plotted only for selected values of Δ and δ as a function of the gradient strength $|\boldsymbol{G}|$ for the parallel and the perpendicular direction. The scanner data are plotted with marks and synthetic data from the models are plotted with lines.*

most likely because the three-dimensional mesh can capture heterogeneity in capillary orientation.

Conclusions: The complex three-dimensional mesh model minimizes the MSE and accurately captures the diffusion-weighted MRI data in both parallel and perpendicular directions for Δ = 10, 30, 70 ms and δ= 3, 10 ms.

3.4 Discussion and Conclusions

This chapter introduced a method for constructing detailed three-dimensional tissue mesh models using CLSM to generate realistic diffusion-weighted MRI data. The chapter aimed to present and validate a new mesh-based approach to diffusion MRI simulation. First, we provided background information on

Models	*MSE* parallel	*MSE* perpendicular
Square Packed Cylinders	0.0035	0.0114
Gamma Distributed Cylinder Radii	0.0035	0.0044
Extruded Mesh Model	0.0035	0.0068
Mesh Model	0.0024	0.0043

Table 3.1: *Mean-squared error of the parallel and perpendicular direction for each model.*

our choices of confocal microscopy and the computer-graphics technique, the marching cubes algorithm, for the meshing. We then detailed an experiment demonstrating our method on a biological phantom.

We created a new MRI protocol suitable for the biological phantom. The purpose of the MRI protocol in this study was to provide the most stringent validation of the mesh simulation possible. Mesh construction and data acquisition are separate steps of the method. Once constructed, the mesh can produce synthetic data for any imaging protocol, in-vivo or specialized.

We investigated optimal simulation and mesh properties for precision and accuracy of the synthesised data. We tested the simulated data from the three-dimensional mesh model against scanner data, a simpler extruded mesh model and simple parametric models. Results from the three-dimensional mesh model were very promising. They agreed with scanner data well and matched the data better than the extruded and parametric models in both directions.

The method proposed in this chapter can be refined in a number of ways. So far, we optimize the simulation parameters without a ground truth. In a similar experiment in [HA09], they compare results to an analytic model of restriction, however the mesh model here is much more complex and analytic solutions cannot provide a ground truth. The quality of the generated mesh also depends on the segmentation process and the downsampling of the confocal images. So far we use a simple thresholding algorithm. We could improve the accuracy and smoothness of the mesh by using more sophisticated segmentation algorithms. To avoid downsampling while preserving the topology with the minimum number of triangles we could use a meshing algorithm combined with decimation [SZL+92]. However, preliminary experiments with decimation reveal problems that cause the simulation to fail. In particular, decimation created a slight mismatch between the edges of triangles causing trapped spins. This was caused by floating point inaccuracies in the decimation which are invisible in rendering but critical in the simulation. Exploitation of more sophisticated meshing remains a focus for further work.

The Monte-Carlo simulation approach with a tissue model of high fidelity provides a mechanism for high quality data synthesis for testing and developing diffusion MR algorithms. It also allows for separately testing the influence of subtle effects such as permeability and surface-particle interactions (e.g. particles temporarily trapped on the surface) that analytic models cannot capture.

Future work will extend the experiments to other samples, in particular, to brain tissue. Accurate synthetic data from brain white matter regions can allow testing, comparison and evaluation of analytic models in a similar way to [PFS+09]. The mesh models could also represent diseased tissue. Constructing three-dimensional models of diseased brain areas can be used for testing new biomarkers. Also one can create mesh models from different stages of a disease to monitor and explore disease progression.

Along these lines we can model the development of the brain to study aging in different regions.

Chapter 4

Taxonomy of Analytic Models

This chapter studies analytic compartment models of the diffusion MRI signal in brain white matter. Specifically, we consider multi-compartment models with no exchange, which model the signal as the sum of signals from water both inside and outside cellular structures with impermeable cell walls. The models incorporate specific biological parameters, such as axon radius and axon density, to predict the diffusion MRI signal. We construct a taxonomy of multi-compartment models of white matter from combinations of simple models for the intra- and extra-axonal spaces. The study includes well-known models from the literature, such as the ball and stick model [BWJJ03], CHARMED [AB05, ABKYB08], the simplified version of CHARMED [Ale08], and the minimal model of white matter diffusion (MMWMD) [AHH$^+$10], each of which uses different intra- and extra-axonal models. The taxonomy accentuates the relationship between these models in the literature and reveals new models from previously untested combinations. Finally, the study provides a consistent naming system for all the models in the taxonomy. The models in the taxonomy are implemented in the open-source diffusion MRI toolkit Camino [CBNG$^+$06].

Section 4.1 specifies the tissue models, provides details for the individual compartment models and explains the naming system. Section 4.2 discusses potential variations of diffusion parameters and compartment models that can be used to extend existing models.

4.1 Tissue Models

We model brain white matter with combinations of three types of compartments. Each of the compartments provides a separate normalised MR signal S_1, S_2, S_3. The signals come from a) water inside the axons, b) water from outside the axons and c) water from other cellular structures, such as glial cells, trapped water on membranes or non-parallel fibres. We refer to these three types of compartments as a) intra-axonal, which are restricted models of diffusion, b) extra-axonal, which include isotropic and anisotropic non-restricted models and c) compartments of isotropic restriction.

Intra-Axonal Compartments		
Model	**Form**	**Degrees of Freedom**
 STICK	$\mathbf{D} = d\mathbf{n}\mathbf{n}^T$	d, θ, ϕ
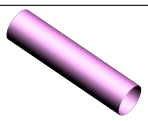 CYLINDER	GPD approx. [GDZM94]	d, θ, ϕ, R
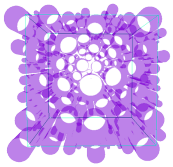 GDRCYLINDERS	$P(x;k,\vartheta) = \frac{x^{k-1}e^{\frac{-x}{\vartheta}}}{\Gamma(k)\vartheta^k}$	$d, \theta, \phi, k, \vartheta$

Table 4.1: *Intra-axonal compartment models. The fibre orientation* $\mathbf{n}$ *is defined by the angles* θ, φ.

The total diffusion MR signal for a multi-compartment model is

$$S = \sum_{i=0}^{3} f_i S_i, \tag{4.1}$$

where f_i is the proportion of water molecules in population $i, 0 \leq f_i \leq 1$ and

$$\sum_{i=0}^{3} f_i = 1. \tag{4.2}$$

4.1.1 Intra-Axonal Compartments

There are many options in the literature for models of the restricted signal S_r. Here we investigate three models for the intra-axonal compartment, as shown in Table 4.1:

1. The first is Behrens' "stick" model [BWJJ03] which has fibre direction $\mathbf{n}$ and diffusivity d as parameters. The "stick" model describes diffusion in an idealised cylinder with zero radius.

2. The second is the "cylinder" model , as used in [Ale08], which accounts for non-zero cylinder radius. This model has an extra parameter, R, representing the axon radius. We assume a single R as in [Ale08, AHH+10]. The signal for this model is given by Equation 2.23, Section 2.3.3.

3. The third model is an extension of the "cylinder" but instead of a single radius it has gamma distributed radii as used in [AB05]. The radii are drawn from a gamma distribution

$$P(x;k,\vartheta) = \frac{x^{k-1}e^{\frac{-x}{\vartheta}}}{\Gamma(k)\vartheta^k} \tag{4.3}$$

We refer to this model as "GDRcylinders". Instead of the parameter R, this model has two parameters to define the cylinder's radii, the shape parameter k and the scale parameter ϑ, where $k\vartheta$ is the mean, $k\vartheta^2$ is the variance and $\Gamma(k) = (k-1)!$.

Extra-Axonal Compartments		
Model	**Form**	**Degrees of Freedom**
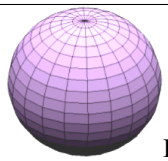 BALL	$\mathbf{D} = d\mathbf{I}$	d
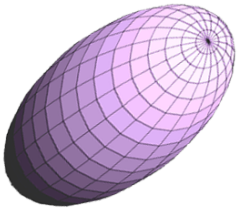 ZEPPELIN	$\mathbf{D} = \alpha\mathbf{n}\mathbf{n}^T + \beta\mathbf{I}, d_{\parallel} = \alpha + \beta, d_{\perp} = \beta$	$d_{\parallel}, d_{\perp}, \theta, \phi$
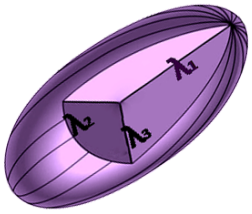 TENSOR	$\mathbf{D} = d_{\parallel}\mathbf{n}\mathbf{n}^T + d_{\perp_1}\mathbf{n}_{\perp_1}\mathbf{n}_{\perp_1}^T + d_{\perp_2}\mathbf{n}_{\perp_2}\mathbf{n}_{\perp_2}^T$	$d_{\parallel}, d_{\perp_1}, d_{\perp_2}, \theta, \phi$

Table 4.2: *Extra-axonal compartment models.*

4.1.2 Extra-Axonal Compartments

The candidate models for the extra-axonal compartment assume hindered diffusion and provide signal S_h. We investigate three models for the extra-axonal compartment. We illustrate the models in Table 4.2. Each one is a diffusion tensor (DT) model with different constraints:

1. The first, referred to as a "ball", is isotropic , as in [BWJJ03]. The signal is Equation 2.26 with $\mathbf{D}$ as in Equation 2.33. "Ball" has only one parameter, the diffusivity d.

2. The second is an anisotropic, but cylindrically symmetric DT, as in [Ale08] and we refer to this as a "zeppelin". The signal is Equation 2.26 with $\mathbf{D}$ as in Equation 2.34. The model has the following parameters: the fibre direction $\mathbf{n}$, $d_{\parallel}$ which is the diffusivity parallel to the fibre direction and $d_{\perp}$ perpendicular to the fibre direction.

3. Finally we consider a full tensor, which we refer to as a "tensor". This model has three diffusivity parameters: parallel diffusivity $d_{\parallel}$ and $d_{\perp_1}, d_{\perp_2}$ perpendicular with $d_{\perp_1} \neq d_{\perp_2}$. It has an additional three degrees of freedom for the orthogonal eigenvectors $\mathbf{n}$, $\mathbf{n}_{\perp_1}$ and $\mathbf{n}_{\perp_2}$. The signal is Equation 2.26 and the form of the DT is

$$\mathbf{D} = d_{\parallel}\mathbf{n}\mathbf{n}^T + d_{\perp_1}\mathbf{n}_{\perp_1}\mathbf{n}_{\perp_1}^T + d_{\perp_2}\mathbf{n}_{\perp_2}\mathbf{n}_{\perp_2}^T. \tag{4.4}$$

Isotropic Restriction Compartments		
Model	**Form**	**Degrees of Freedom**
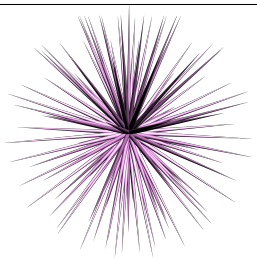 ASTROSTICKS	$S_G = \int S_r p(\mathbf{n}) d\mathbf{n}, R = 0$	d
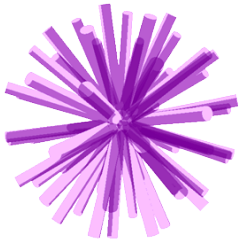 ASTROCYLINDERS	$S_G = \int S_r p(\mathbf{n}) d\mathbf{n}, R \neq 0$	d, R
 SPHERE	GPD approx. [MC84], $R \neq 0$	d, R
 DOT	$d = 0, R = 0, S = 1$	-

Table 4.3: *Third compartment models.*

4.1.3 Isotropic Restriction Compartments

We consider four extra models intended to capture other cellular structures that can be combined with two-compartment models from combinations of the intra- and extra-axonal models. These models assume isotropic restriction in the brain tissue. Two of the models, the "astrosticks" and the "astrocylinders" (see list below and Table 4.3), assume restriction from isotropically orientated cylinders. The other two, the "sphere" and "dot" (see list below and Table 4.3), assume restriction from spherical boundaries. The models of isotropic restriction are as follows:

1. Uniformly distributed cylinders with zero diameter. We refer to this model as "astrosticks". The model represents signal coming from a type of glial cells called astrocytes, or populations of axons with arbitrary orientation.

2. This model is an extension of the previous model assuming particles diffusing in uniformly distributed cylinders with non-zero radius R. We refer to this model as "astrocylinders". The model represents signal coming from astrocytes and non-parallel axons as well.

3. This model is for modelling the signal from particles diffusing inside spherical boundaries with non-zero radius R. We refer to this compartment as a "sphere". The "sphere" models signal

coming from water molecules inside spherical glial cells.

4. This model is a special case of the "sphere" with zero radius in which particles do not move, as used in [AHH+10]. We refer to this model as "dot". Alexander et al.[AHH+10] suggests that the "dot" models signal coming from molecules stuck into cellular membranes in fixed tissue.

4.1.3.1 Signal Models

Next we discuss the mathematical derivation of the signal model for each of the models of isotropic restriction. First we discuss the derivation of the signal model of isotropically oriented cylinders and then of spherical boundaries.

To model the restricted signal S_r from particles diffusing within a cylinder we assume that it can be regarded as the product of the signals parallel and perpendicular to the cylinder axis, $\mathbf{n}$ [AFRB04]

$$S_r = S_{r\parallel} S_{r\perp}. \tag{4.5}$$

In the parallel direction to the fibres we assume free diffusion, then

$$S_{r\parallel} = \exp(-(\Delta - \delta/3)(\gamma\delta\mathbf{G}\cdot\mathbf{n})^2 d) = \exp(L_\parallel(\mathbf{G}\cdot\mathbf{n})^2), \tag{4.6}$$

where

$$L_\parallel = -(\Delta - \delta/3)(\gamma\delta)^2 d_\parallel, \tag{4.7}$$

$\mathbf{G}\cdot\mathbf{n}$ represents the component of the gradient parallel to the fibres and $d_\parallel$ is the free diffusivity within the cylinder.

To model $S_{r\perp}$ we can consider the following generalised form:

$$S_{r\perp} = \exp(L_\perp(\mathbf{G}\cdot\mathbf{G} - (\mathbf{G}\cdot\mathbf{n})^2)), \tag{4.8}$$

where $\mathbf{G}\cdot\mathbf{G} - (\mathbf{G}\cdot\mathbf{n})^2$ is the square of the magnitude of the component of the gradient perpendicular to $\mathbf{n}$. Stepisnik's expression [Ste93, GDZM94] provides a model for $S_{r\perp}$ (Equation 2.23, Section 2.3.3) , using the Gaussian phase distribution approximation:

$$L_\perp = -2\gamma^2 \sum_{m=1}^{\infty} \frac{2d_\parallel\beta_m^2\delta - 2 + 2Y(\delta) + 2Y(\Delta) - Y(\Delta-\delta) - Y(\Delta+\delta)}{d_\parallel^2\beta_m^6((\alpha/2)^2\beta_m^2 - 1)} \tag{4.9}$$

where $Y(x) = \exp(d_\parallel\beta_m^2 x)$, β_m is the mth root of equation $J_1'(\beta\alpha/2) = 0$ and J_1' is the derivative of the Bessel function of the first kind, order one.

To obtain the signal S_G from water inside cylinders with a distribution of orientations p, we integrate the signal S_r for a cylinder with axis $\mathbf{n}$ over all $\mathbf{n}$:

$$S_G = \int S_r p(\mathbf{n}) d\mathbf{n} \tag{4.10}$$

Here we assume uniform p so $p(\mathbf{n}) = (4\pi)^{-1}$ and

$$S_G = \pi^{1/2}(2|\mathbf{G}|(L_\perp - L_\parallel)^{1/2})^{-1}\exp(|\mathbf{G}|^2 L_\perp)\phi(|\mathbf{G}|(L_\perp - L_\parallel)^{1/2}), \tag{4.11}$$

where ϕ is the error function

$$\phi(z) = 2\pi^{-1/2}\int_0^z \exp(-t^2)dt \tag{4.12}$$

To model the signal from particles trapped inside spherical boundaries, we use Murday and Cotts expression [MC84], using the GPD approximation. The form for $L_\perp$ is similar to Equation 4.9, and is given by Equation 2.22, Section 2.3.3. A special case is spheres with zero diameter, in which particles do not move, so the signal remains unattenuated.

Next we present a summary for the signal of each isotropic restriction model:

1. The signal from "astrosticks" S_G comes from substituting Equation 4.7 and $L_\perp$ in Equation 4.11. The model has only one parameter the diffusivity $d_\parallel$.

2. The signal from "astrocylinders" S_G comes from substituting Equation 4.7 and 4.9 in Equation 4.11. The model has two parameters, the diffusivity $d_\parallel$ and the radius R.

3. The signal for the "sphere" is given by Equation 2.22, Section 2.3.3. The model has two parameters, the diffusivity $d_\parallel$ and the radius R.

4. The signal from the "dot" remains unattenuated so $S_G = 1$.

4.1.4 Naming System

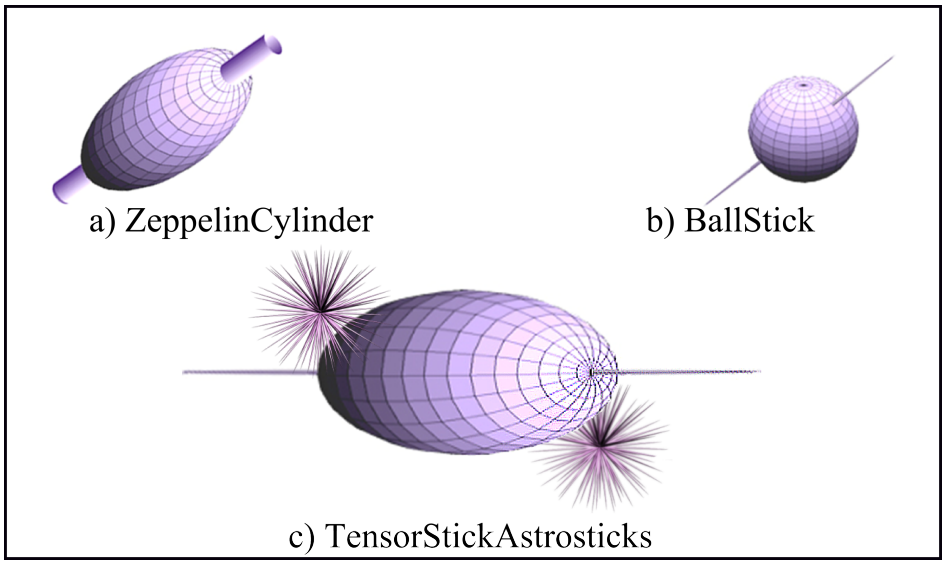

Figure 4.1: *Multi-compartment models.*

We use combined terms to refer to specific two- and three- compartment models. For example "ZeppelinStick" assumes zero radius cylinders for the intra-axonal space and cylindrical symmetry for the extra-axonal space and no isotropically restricted compartment. The taxonomy includes models from

previous studies such as CHARMED [AB05, ABKYB08], which is the "TensorGDRCylinders" model, the simplified version of CHARMED as used in [Ale08], which is the "ZeppelinCylinder" model, and the minimal model of white matter diffusion (MMWMD) in [AHH+10] without the fourth compartment, which is the "ZeppelinCylinderDot" model. Figure 4.1 presents some of the multi-compartment models.

4.2 Variations and Special Cases

This section considers some variations for analytic models to incorporate other important effects in biological tissue. These variations are only included in this chapter for a complete description of the multi-compartment models and the naming system and they are not considered in the following experimental chapters. The variations are as follows:

1. We can construct a simple isotropic compartment with volume fraction f_{csf} and higher diffusivity, compared to the diffusivities of the other compartments, d_{csf}, for modelling partial volume effects from CSF contamination, as in [BBA09, AHH+10].

   The signal of the model is

   $$S_{csf} = \exp(-bd_{csf}) \tag{4.13}$$

   and we refer to this model as "CSF". For example, the name for the full MMWMD model, including this compartment is "ZeppelinCylinderDotCSF".

2. We can use different diffusivity d_i for each compartment $i = 1,2,3$. To refer to the model we will append the model's original name with the abbreviation "Dif". For example the "TensorCylinder" model will be renamed "TensorCylinderDif" indicating that the intra-axonal compartment has a different parallel diffusivity from the extra-axonal compartment.

3. Another variation uses a simple tortuosity model as proposed by Szafer [SZG95], as used in [AHH+10], so that

   $$d_\perp = d_\parallel(1-f) \tag{4.14}$$

   where f is the intra-axonal volume fraction. The name tortuosity for the diffusivity model comes from the tortuous movement of water molecules in the extra-axonal space. To refer to the model we will append the model's original name with the abbreviation "Tor".

4. This variation uses a different T_1 and T_2 relaxation times for every compartment. For example for the different T_2 we use Equation 2.3, as in [PCR+99]. To refer to the model we will append the model's original name with the abbreviation "Rel1" and "Rel2" respectively.

5. We could model membrane permeability as in [KPH88, SSWH97]. To refer to the model we will append the model's original name with the abbreviation "Perm".

4.3 Discussion and Conclusions

This chapter presented multi-compartment models for the diffusion-weighted MRI signal in brain white matter. We examined a variety of individual models for the intra- and extra- axonal spaces, and we

further introduced models to capture other effects, such as water molecules trapped on membranes and signal coming from water populations in other cellular structures such as glial cells.

We combined these models to construct a taxonomy which includes simple models, such as the DT (renamed here as an extra-axonal compartment, the "tensor"), and multi-compartment models, with two, three or more compartments. The models can also account for restriction and incorporate a distribution of axon diameters. The study included well-known models from the literature, as well as other models from previously untested compartment combinations.

Additionally we introduced some variations for these models, considering an additional partial volume model and taking into account different effects. It is important to note that we can have several combinations of these variations to enrich and expand the taxonomy of the multi-compartment analytic models. Finally, we devised a consistent naming system for all the models in the taxonomy and implemented all the combinations of the two- and three compartment models presented here (excluding the variations) in Camino [CBNG+06].

Chapters 5 and 6 will study, compare and assess a selection of these models using diffusion-weighted MRI data from ex vivo and in vivo brain white matter tissue. The selection of analytic models will include all the multi-compartment models from combinations of the intra- and extra-axonal models and the models of isotropic restriction. The model comparison will also include the DT and a bitensor model.

Chapter 5

Fixed Brain Tissue

This chapter describes an MRI experiment on fixed rat brain to compare a selection of the multi-compartment analytic models described in Chapter 4. It expands work described in [PFS+09], where we study two-compartment analytic models of brain white matter by combining simple intra-axonal ("stick", "cylinder") and extra-axonal ("ball","zeppelin", "tensor") models (see Section 4.1, Chapter 4). This study aims to identify the minimum requirements for an accurate model of the diffusion MRI signal in brain white matter. We investigate three important classes of models: one-, two- and three-compartment models with no exchange. These model the overall signal as the sum of contributions from water inside and outside structures with impermeable cell walls (see Section 4.1, Chapter 4). We define a new diffusion MRI protocol to allow evaluation and comparison of the analytic models for parallel and perpendicular signals to the axons in brain white matter over a wide range of scan parameters. Such a study is challenging in brain tissue because fibre orientation varies, so most previous studies use simpler tissue samples such as spinal cord [CWH+02, CWM00, FHA+94, GWDL01, SH03]. The new protocol enables extension of these studies to the brain.

Section 5.1 details the tissue models, the tissue samples, the MRI acquisition, the model fitting and parameter estimation procedures. Section 5.2 describes the experiment, and Section 5.3 presents results on microstructure parameter estimation and the evaluation of the models. Finally, Section 5.4 concludes and discusses limitations and future directions.

5.1 Methods

This section provides details for the tissue models, tissue samples and MRI acquisition from two fixed rat brains, as well as the procedures for fitting the multi-compartment models to the diffusion-weighted MRI images.

5.1.1 Tissue models

We model brain white matter with combinations of three types of compartment models: a) intra-axonal b) extra-axonal and c) models of isotropic restriction, as described in Section 4.1, Chapter 4. Table 5.1 presents all the individual candidate models that we combine in order to construct the analytic multi-compartment models.

In this experiment we will study all the combinations of these three compartments, as well as the

Intra-Axonal	Extra-Axonal	Isotropic Restriction
 STICK	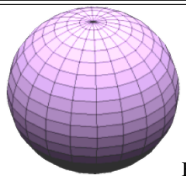 BALL	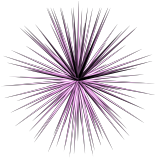 ASTROSTICKS
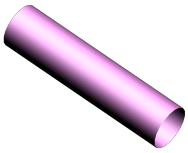 CYLINDER	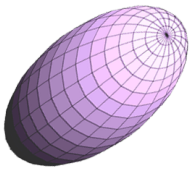 ZEPPELIN	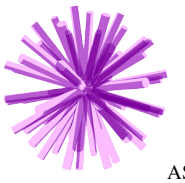 ASTROCYLINDERS
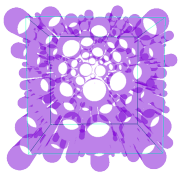 GDRCYLINDERS	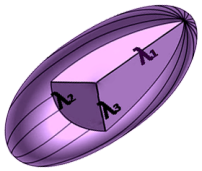 TENSOR	 SPHERE
		 DOT

Table 5.1: *Candidate models for the intra- and extra-axonal space and for isotropic restriction.*

diffusion tensor (DT) model [BJ02, BML94] and a bitensor model [TRW+02, PA03, AHL+01]. The single DT is the same as the extra-axonal "tensor" compartment, and the bitensor model is a mixture of two "zeppelin" compartments with the same principal direction [ABA01]. In total we consider 47 analytic models. Where appropriate we constrain the extra-axonal models so that the DT's principal direction is equal to the intra-axonal compartments' ("cylinder" or "stick" or "GDRCylinders") axis and the parallel extra-axonal and isotropic restriction diffusivity is $d_{\|}$.

5.1.2 Tissue Samples

The brains of two male Sprague-Dawley rats were perfusion fixed through the left ventricle using isotonic saline, followed by 4% paraformaldehyde (PFA) in phosphate-buffered saline (PBS). The rat brains were extracted and immersion-fixed in fresh 4% PFA for at least two weeks. The T_2 reduction due to fixation in PFA was reversed by immersion in 4% PBS with 1% Penicillin Streptomycin solution for at least 2 weeks [STSB09]. Finally, each brain was embedded in 1% agarose gel in PBS in order to reduce motion during the diffusion MRI acquisition.

5.1.3 MRI acquisition

We are interested in diffusion in the brain in directions parallel and perpendicular to the fibre orientation, since these directions reveal most about the underlying brain microstructure. However, it is challenging to acquire such measurements from brain tissue, because fibre orientation varies throughout the white matter (see Section 2.1). Our approach is to select one central parallel direction and several perpendicular directions and identify voxels in which the fibres align with those directions after imaging. We focus analysis only on these voxels and discard all others.

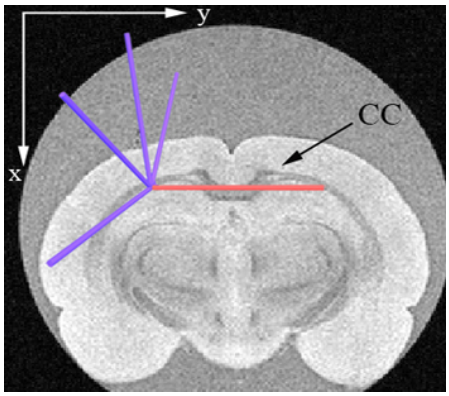

Figure 5.1: *Diffusion-weighted MRI image of a fixed rat brain. The red arrow indicates the central gradient direction used for the encoding scheme and the blue arrows indicate the four directions perpendicular to the central one.*

We acquire diffusion-weighted MR images of two perfusion-fixed rat brains, using a small bore 9.4T Varian scanner with maximum gradient strength $|\mathbf{G}|_{max} = 400\,\text{mT/m}$. We use a five direction-encoding scheme and place the sample in the scanner oriented to ensure that some fibres in the corpus callosum (CC) are parallel to our central direction. We also choose four evenly spaced directions perpendicular to the central direction in our chosen voxels (see Figure 5.1). We use the PGSE sequence for 70 diffusion weightings: five diffusion times Δ = 10, 20, 30, 40, 50 ms, gradient durations δ = 3 ms for all Δ and δ = 30 ms for Δ = 40, 50 ms, gradient strength $|\mathbf{G}|$ varied from 40 to 400 mT/m in ten steps of 40 mT/m. Measurements with b value greater than $7.7 \times 10^{10}\,\text{sm}^{-2}$ were not performed due to poor SNR (< 2.6), i.e all combinations with $|\mathbf{G}|$ = 200 to 400 mT/m and δ = 30 ms for both rat brains. In total we acquired images with 59 diffusion weightings in each direction. We refer to the first rat brain dataset as dataset A and the second as dataset B. In Figure 5.2 we plot the parallel and the mean of the four perpendicular directions of the log normalized signal from voxels in the region of interest (see Section 5.2) in the CC and show MRI images for various b values from both datasets.

We use minimum echo times (TE) to maximise SNR and choose repetition times (TR) to minimise gradient heating effects. For each combination of diffusion-weighting parameters we acquire $b = 0$ images to correct for T_1 and T_2 dependence. We also perform a separate DTI acquisition using a 42-direction scheme with b value $4.5 \times 10^9\,\text{sm}^{-2}$, as suggested by Dyrby et al. [DBA+] for fixed brain tissue, and six $b = 0$ measurements. The in-plane field of view is 2 cm. The matrix size is 256×256 and the slice thickness is 0.5 mm. We acquire 402 images in approximately 65 hours for each sample. The full imaging protocol is provided in Tables D.4, D.5, D.6 in Appendix D.

As in the biological phantom experiment, the sequence parameters were chosen to cover the signal range as evenly as possible and was based on previous studies of the diffusion MR signal in white matter [SSWH97, ABKYB08]. Again the specific parameters were established experimentally according to the sample. We note that this acquisition protocol contains a much more comprehensive set of measurements than we can acquire on live subjects. However, it is rich enough to ensure good fit of the models, identification of important effects and thus a reliable selection of appropriate models for sparser in vivo data.

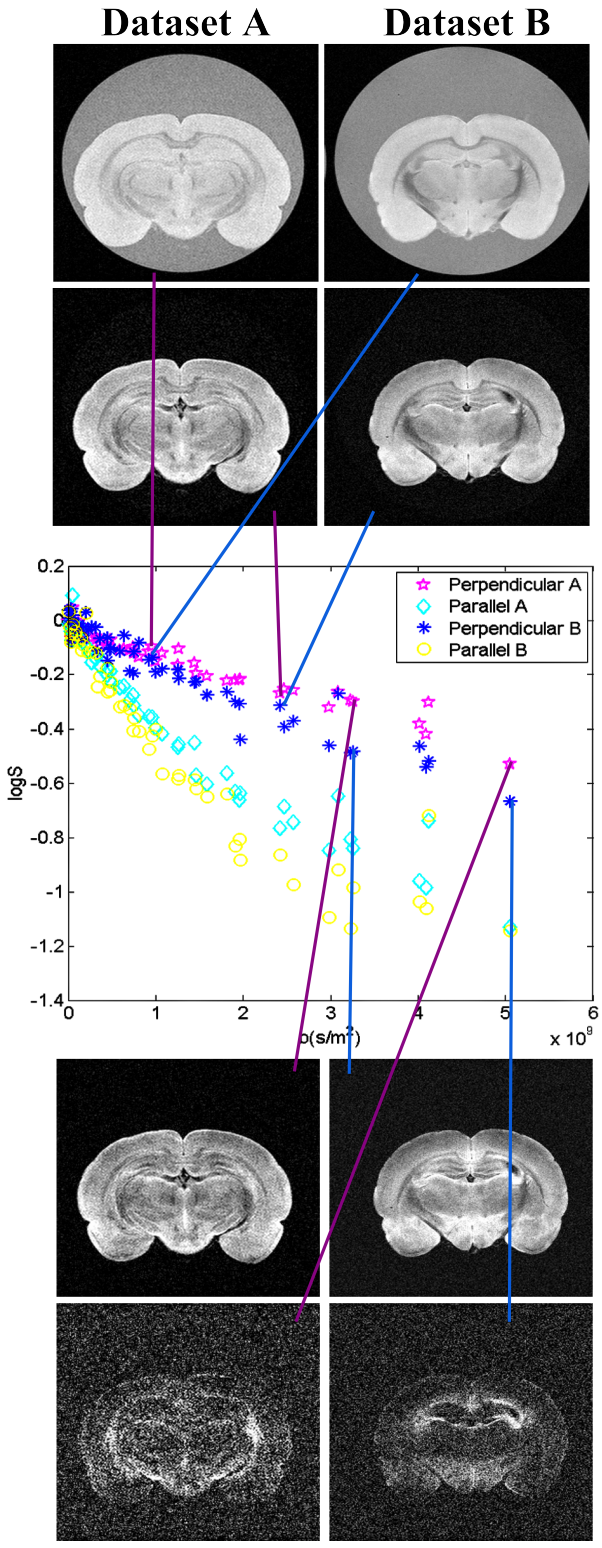

Figure 5.2: *Plot of the parallel and the mean of the four perpendicular directions of the log signal from voxels in a region of interest in the CC and demonstration of MRI images (perpendicular direction) for various b values from both datasets.*

5.1.3.1 Temperature

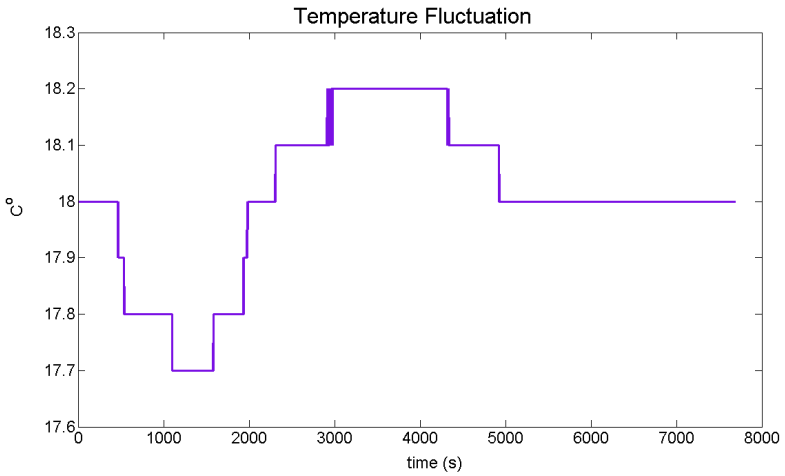

Figure 5.3: *Temperature fluctuation using* $1.5\times$ *the maximum b value of the imaging protocol.*

Since water diffusion in tissue is highly temperature sensitive, it is critical to avoid temperature changes. We use an airflow mechanism to maintain the sample's temperature during the acquisitions. To ensure that the sample was scanned at a consistent temperature while using a wide range of b values, we tested the temperature fluctuation using the $1.5\times$ the maximum b value of our imaging protocol. Results show that the temperature at which it reached a plateau was less than 1 degree above the 'baseline' start temperature (see Figure 5.3). The temperature measurements in the protocol with the maximum gradient duty cycle provide further evidence that the temperature did not fluctuate more than $\pm 1\,^{\circ}$C. Furthermore, although the temperature data was not continuous for all the acquisitions (due to power supply issues), the temperature remained within the limits specified for all temperature measurements acquired.

5.1.4 Model Fitting

We fit each model to the data using an iterative optimization procedure and synthesise diffusion-weighted data from the fitted models. The model parameters do not relate linearly to the measurements, therefore we have to fit the models to the data by non-linear optimization. Here we use a Levenberg-Marquardt algorithm [PFT88]. The objective function we use for this optimization is the sum of squared errors:

$$SSE = \sum_{n=1}^{M} (S_n(\delta,\Delta,\mathbf{G}) - \tilde{S}_n(\delta,\Delta,\mathbf{G}))^2, \tag{5.1}$$

where M is the number of measurements, $S_n(\delta,\Delta,\mathbf{G})$ is the model predicted signal and $\tilde{S}_n(\delta,\Delta,\mathbf{G})$ is the signal for the n_{th} measurement.

Fits of the simplest models are relatively independent of starting position. More complex models are more sensitive to the starting position therefore we use parameter estimates of simpler models to provide initial estimates. For example, to get the starting point for the three-compartment "TensorGDR-CylindersSphere" we use the estimate from the two-compartment "TensorCylinder". For this starting point we use estimates from two models: the "BallCylinder" and the "TensorStick". The "TensorStick" starting point depends on the "BallStick" and the linear DT inversion. The "BallCylinder" depends on

the "BallStick". Finally the "BallStick" depends on the estimate of the linear DT inversion. Despite the simplicity of the "BallStick" model, we must still initialise it using the DT model, since the fibre orientation is particularly difficult to fit with the non-linear optimisation. Figure 5.4 illustrates how the starting point estimations of the "TensorGDRCylindersSphere" model is computed from the output of simpler models.

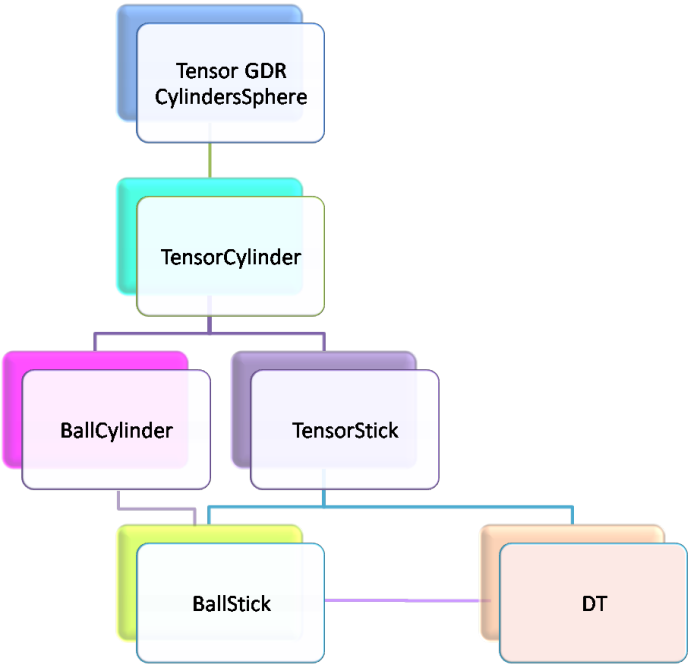

Figure 5.4: *Flow diagram indicating how the starting point estimations of the "TensorGDRCylinders-Sphere" model is computed from the output of simpler models.*

We choose the best fit parameters from the models after 1000 perturbations of the starting parameters to ensure a good minimum. The starting parameters are selected after 100 perturbations. We also calculate the histogram of the objective function when we perturb the starting parameters to monitor the frequency of the best parameter estimation and the stability of the fitting procedure.

5.1.4.1 Parameter Constraints

For the "cylinder" model we constrain the single axon radius R to be within biologically plausible limits so that $0.1\,\mu\text{m} < R < 20\,\mu\text{m}$. For the "GDRCylinders" model we constrain the scale parameter ϑ so that $0.1\,\mu\text{m} < \vartheta < 20\,\mu\text{m}$ and allow a broad range for the shape parameter k so that $0 < k < 20$. For the isotropic restriction models "astrocylinders" and "sphere" we constrain their diameter to be the same as the diameter of the intra-axonal "cylinder" model, in agreement with measured sizes of glial cells from histology [RSGR98]. For all the compartments we ensure that the parallel diffusivity $d_{\parallel}$, and perpendicular diffusivities $d\perp_1$, $d\perp_2$ are always positive. For the extra-axonal "zeppelin" we constrain the perpendicular diffusivity $d\perp$ to be lower than the parallel diffusivity $d_{\parallel}$, and for the "tensor" the perpendicular diffusivity $d\perp_2$ to be lower than $d\perp_1$, which is constrained to be lower than the parallel diffusivity $d_{\parallel}$. Finally, we constrain the volume fraction f to be in $[0,1]$.

5.2 Experiments

To study parallel and perpendicular signal attenuation we choose a region of interest (ROI) with fibre direction in alignment with the central direction. To achieve this, we manually segment the CC on a FA map from the DTI acquisition and threshold for voxels with FA > 0.5 in which the principal direction of the DT is parallel to the central gradient direction within a tolerance of 2°. We average the data contained within all the resulting 21 and 36 voxels of the ROI from datasets A and B respectively.

5.3 Results

This section presents the evaluation and assessment of the models to construct an analytic model ranking, and the parameter estimation from fitting the models to the data.

5.3.1 Model Ranking

The Bayesian information criterion (BIC) [Sch78] evaluates the models. BIC chooses the most economical analytic model by rewarding those that minimise the objective function, while simultaneously penalising the increasing number of model parameters:

$$\mathrm{BIC} = n\ln(MSE) + k\ln(n) \tag{5.2}$$

where n is the sample size, k is the number of free model parameters to be estimated, and MSE is the mean-squared error. The MSE shows that the most flexible model, which has the most parameters, provides the best fit. However, here we seek a compromise between a model that fits well and does not have too many parameters. Thus, we choose to use the BIC because it places a high value on parsimony. The model which provides the lower value of the BIC is the one to be preferred.

Tables 5.2 and 5.3 present the ranking of the models, according to BIC for datasets A and B. We also provide the MSE. As expected, MSE decreases with model complexity, however the BIC reveals which reductions are significant.

The ranking of the models according to BIC is similar for datasets A and B: both the 9 highest-performing and the 12 lowest-performing models are identical between the two datasets. The "dot" models with intra-axonal compartments that account for non-zero radius ("cylinder" and "GDRCylinders"), consistently perform the best. We also observe that the extra-axonal compartments of the "tensor" and the "zeppelin" are favoured over the isotropic "ball" compartment. Following the "dot" models, are the "astrosticks", again combined with "cylinder" and "GDRCylinders". The models that are ranked the lowest, are the DT and two-compartment models with the intra-axonal "stick" model. Another important observation is that the "Bitensor" model is ranked very low as well, highlighting the importance of restriction in describing these data.

The ranking of the remaining models exhibits only small variations between datasets. The "TensorGDRCylinders" minimizes the BIC for the two-compartment models and the "TensorGDRCylindersDot" minimizes the BIC overall.

Models	MSE		BIC		No. Parameters
	dataset A	dataset B	dataset A $\times 10^3$	dataset B $\times 10^3$	
TensorGDRCylindersDot	0.00079	0.00063	-2.461	-2.543	11
TensorCylinderDot	0.00081	0.00065	-2.459	-2.539	10
ZeppelinGDRCylindersDot	0.00093	0.00075	-2.426	-2.493	9
ZeppelinCylinderDot	0.00092	0.00079	-2.425	-2.481	8
BallGDRCylindersDot	0.00109	0.00086	-2.377	-2.451	8
BallCylinderDot	0.00109	0.00117	-2.372	-2.348	7
ZeppelinStickDot	0.00131	0.00118	-2.307	-2.344	7
TensorGDRCylindersAstrosticks	0.00140	0.00124	-2.275	-2.322	11
TensorCylinderAstrosticks	0.00136	0.00121	-2.270	-2.318	10
TensorStickAstrocylinders	0.00139	0.00206	-2.269	-2.129	10
TensorGDRCylindersSphere	0.00166	0.00142	-2.267	-2.254	11
TensorCylinderSphere	0.00141	0.00125	-2.264	-2.307	10
TensorCylinderAstrocylinders	0.00121	0.00126	-2.263	-2.304	10
TensorStickSphere	0.00143	0.00127	-2.258	-2.300	10
TensorStickAstrosticks	0.00142	0.00133	-2.257	-2.289	9
TensorGDRCylindersAstrocylinders	0.00146	0.00133	-2.245	-2.289	11
BallCylinderAstrocylinders	0.00161	0.00152	-2.234	-2.255	7
BallCylinderAstrosticks	0.00163	0.00156	-2.231	-2.247	7
BallStickAstrocylinders	0.00164	0.00154	-2.228	-2.250	7
BallGDRCylindersAstrosticks	0.00166	0.00136	-2.227	-2.287	8
ZeppelinCylinderAstrosticks	0.00163	0.00145	-2.225	-2.265	8
BallStickAstrosticks	0.00169	0.00147	-2.224	-2.272	6
ZeppelinStickAstrocylinders	0.00164	0.00145	-2.222	-2.264	8
BallCylinderSphere	0.00167	0.00145	-2.220	-2.270	7
ZeppelinCylinderAstrocylinders	0.00161	0.00141	-2.219	-2.276	8
BallGDRCylindersAstrocylinders	0.00165	0.00143	-2.219	-2.271	8
ZeppelinStickAstrosticks	0.00169	0.00156	-2.217	-2.245	7
BallStickDot	0.00172	0.00201	-2.216	-2.161	6
ZeppelinCylinderSphere	0.00167	0.00145	-2.215	-2.266	8
ZeppelinGDRCylindersSphere	0.00168	0.00145	-2.214	-2.265	9
BallStickSphere	0.00171	0.00149	-2.214	-2.262	7
BallGDRCylindersSphere	0.00168	0.00146	-2.213	-2.262	8
ZeppelinGDRCylindersAstrocylinders	0.00166	0.00144	-2.212	-2.262	9
ZeppelinGDRCylindersAstrosticks	0.00167	0.00141	-2.211	-2.270	9
ZeppelinStickSphere	0.00170	0.00148	-2.208	-2.258	8
TensorStickDot	0.00181	0.00239	-2.182	-2.083	9
TensorGDRCylinders	0.00282	0.00239	-2.019	-2.077	10
TensorCylinder	0.00301	0.00255	-2.002	-2.060	9
BallGDRCylinders	0.00312	0.00265	-2.001	-2.058	7
ZeppelinGDRCylinders	0.00306	0.00262	-2.001	-2.056	8
BallCylinder	0.0032	0.00274	-1.998	-2.053	6
ZeppelinCylinder	0.00321	0.00296	-1.991	-2.019	7
TensorStick	0.00326	0.00284	-1.979	-2.028	8
Bitensor	0.00343	0.00290	-1.967	-2.026	7
BallStick	0.00350	0.00306	-1.965	-2.018	5
ZeppelinStick	0.00351	0.00331	-1.965	-1.986	6
DT	0.0421	0.0306	-1.081	-1.193	7

Table 5.2: *Table of the ranked models showing the mean-squared fitting error (MSE), the Bayesian information criterion (BIC) and the number of parameters (counting the S_0) for each model. The order of the models is according to the BIC score of dataset A.*

Models	MSE		BIC		No. Parameters
	dataset A	dataset B	dataset A $\times 10^3$	dataset B $\times 10^3$	
TensorGDRCylindersDot	0.00079	0.00063	-2.461	-2.543	11
TensorCylinderDot	0.00081	0.00065	-2.459	-2.539	10
ZeppelinGDRCylindersDot	0.00093	0.00075	-2.426	-2.493	9
ZeppelinCylinderDot	0.00092	0.00079	-2.425	-2.481	8
BallGDRCylindersDot	0.00109	0.00086	-2.377	-2.451	8
BallCylinderDot	0.00109	0.00117	-2.372	-2.348	7
ZeppelinStickDot	0.00131	0.00118	-2.307	-2.344	7
TensorGDRCylindersAstrosticks	0.00140	0.00124	-2.275	-2.322	11
TensorCylinderAstrosticks	0.00136	0.00121	-2.270	-2.318	10
TensorCylinderSphere	0.00141	0.00125	-2.264	-2.307	10
TensorCylinderAstrocylinders	0.00121	0.00126	-2.263	-2.304	10
TensorStickSphere	0.00143	0.00127	-2.258	-2.300	10
TensorStickAstrosticks	0.00142	0.00133	-2.257	-2.289	9
TensorGDRCylindersAstrocylinders	0.00146	0.00133	-2.245	-2.289	11
BallGDRCylindersAstrosticks	0.00166	0.00136	-2.218	-2.287	8
ZeppelinCylinderAstrocylinders	0.00161	0.00141	-2.219	-2.276	8
BallStickAstrosticks	0.00169	0.00147	-2.223	-2.272	6
BallGDRCylindersAstrocylinders	0.00165	0.00143	-2.219	-2.271	8
BallCylinderSphere	0.00167	0.00145	-2.220	-2.270	7
ZeppelinGDRCylindersAstrosticks	0.00167	0.00141	-2.211	-2.270	9
ZeppelinCylinderSphere	0.00167	0.00145	-2.215	-2.266	8
ZeppelinGDRCylindersSphere	0.00168	0.00145	-2.214	-2.265	9
ZeppelinCylinderAstrosticks	0.00163	0.00145	-2.225	-2.265	8
ZeppelinStickAstrocylinders	0.00164	0.00145	-2.222	-2.264	8
BallStickSphere	0.00171	0.00149	-2.214	-2.262	7
BallGDRCylindersSphere	0.00168	0.00146	-2.213	-2.262	8
ZeppelinGDRCylindersAstrocylinders	0.00166	0.00144	-2.212	-2.262	9
ZeppelinStickSphere	0.00170	0.00148	-2.208	-2.258	8
BallCylinderAstrocylinders	0.00161	0.00152	-2.234	-2.255	7
TensorGDRCylindersSphere	0.00166	0.00142	-2.267	-2.254	11
BallStickAstrocylinders	0.00164	0.00154	-2.228	-2.250	7
BallCylinderAstrosticks	0.00163	0.00156	-2.231	-2.247	7
ZeppelinStickAstrosticks	0.00169	0.00156	-2.217	-2.245	7
BallStickDot	0.00172	0.00201	-2.216	-2.161	6
TensorStickAstrocylinders	0.00139	0.00206	-2.269	-2.129	10
TensorStickDot	0.00181	0.00239	-2.182	-2.083	9
TensorGDRCylinders	0.00282	0.00239	-2.019	-2.077	10
TensorCylinder	0.00301	0.00255	-2.002	-2.060	9
BallGDRCylinders	0.00312	0.00265	-2.001	-2.058	7
ZeppelinGDRCylinders	0.00306	0.00262	-2.001	-2.056	8
BallCylinder	0.0032	0.00274	-1.998	-2.053	6
ZeppelinCylinder	0.00321	0.00296	-1.991	-2.019	7
TensorStick	0.00326	0.00284	-1.979	-2.028	8
Bitensor	0.00343	0.00290	-1.967	-2.026	7
BallStick	0.00350	0.00306	-1.965	-2.018	5
ZeppelinStick	0.00351	0.00331	-1.965	-1.986	6
DT	0.0421	0.0306	-1.081	-1.193	7

Table 5.3: *Table of the ranked models showing the mean-squared fitting error (MSE), the Bayesian information criterion (BIC) and the number of parameters (counting the S_0) for each model. The order of the models is according to the BIC score of dataset B.*

5.3.2 Parameter estimation

The best fit microstructure parameters, starting points and objective functions for all the models are shown in Appendix B, in Tables B.1, B.2 , B.3 , B.4 and B.5. We summarise some of the key models in Table 5.4.

Table B.1 presents the resulting parameters for all the two-compartment models and the DT. We see that "cylinder" models give higher values for the intra-axonal volume fraction f_1 and diffusivity parameter $d_{\parallel}$ than the "stick" models, and consistently estimate R around 2 μm. The DT and the "BallStick" models provide low estimates for the diffusivity $d_{\parallel}$. The "GDRCylinders" models give higher values for the f_1 than the "cylinder" models, while they estimate the diffusivity $d_{\parallel}$ at similar levels. To compare the radius estimate between the "GDRCylinders" and the "cylinder" model we calculate the mean $k\vartheta$ and compare it to the R. The "GDRCylinders" models predict R a little higher than the "cylinder" models, around 2.5 μm.

Table B.2 presents the resulting parameters for the three-compartment "dot" models. We observe that "cylinder" models give higher values for the intra-axonal volume fraction f_1 than "stick" models except when combined with the extra-axonal "tensor" model. All three-compartment "dot" models give higher values in comparison with the two-compartment models, for the intra-axonal volume fraction f_1, the diffusivity parameter $d_{\parallel}$ and the radius R, which they estimate at around 3.5 μm. Compared to the "cylinder" models, the "GDRCylinders" models give higher values for f_1 and lower values for the volume fraction of the extra-axonal compartment f_2 and the diffusivity $d_{\parallel}$. The "GDRCylinders" models give higher estimate than the "cylinder" models for R, and estimate it at approximately 8 μm .

The three-compartment "astrosticks" models presented in Table B.3, give lower values for the intra-axonal f_1 and extra-axonal f_2 volume fractions in comparison with the "dot" models. The "cylinder" models estimate the axon radius R around 2 μm, in agreement with the two-compartment models. Compared to the "cylinder" models, the "GDRCylinders" models give higher values for the intra-axonal volume fraction f_1, while their radius estimate R is approximately the same. Table B.4 presents the estimates from the "astrocylinders" models which are in agreement with the "astrosticks" models.

The three-compartment "sphere" models presented in Table B.3 provide higher values for f_1 and $d_{\parallel}$ compared to the "astrocylinders" models. The "GDRCylinders" models estimate the radius at approximately the same level as the "cylinders" models.

Finally we observe that all the two-and three-compartment models give good estimates of the left-right fibre direction in the CC, as well as S_0. The trend of the results we describe here is consistent in both datasets.

Models	Startpoint		Best Estimates		FOBJ	
	dataset A	dataset B	dataset A	dataset B	dataset A	dataset B
DT	-	-	$d_{\parallel}$=2.494×10^{-11} $d\perp_1$= 1.781×10^{-11} $d\perp_2$=1.660×10^{-11} θ=1.573 ϕ=4.712	$d_{\parallel}$=1.852×10^{-11} $d\perp_1$= 1.734×10^{-11} $d\perp_2$=1.394×10^{-11} θ=1.570 ϕ=-1.570	14.901	10.832
Bitensor	S_0=1 f_1=0.52608 f_2=0.47392 $d_{\parallel}$=3.3943×10^{-10} θ=1.509954 ϕ=-4.75342 $d\perp_{1a}$=3.3943×10^{-10} $d\perp_{1b}$=5.111×10^{-12}	S_0=1 f_1=0.4236 f_2=0.5764 $d_{\parallel}$=2.847×10^{-10} θ=4.594 ϕ=-1.624 $d\perp_{1a}$=2.846×10^{-10} $d\perp_{1b}$=5.122×10^{-12}	S_0=0.985221 f_1=0.522898 f_2=0.477101 $d_{\parallel}$=3.41568×10^{-10} θ=1.49926 ϕ=-4.763612 $d\perp_{1a}$=3.41568×10^{-10} $d\perp_{1b}$=4.775×10^{-12}	S_0=0.987 f_1=0.433 f_2=0.566 $d_{\parallel}$=2.891×10^{-10} θ=4.592 ϕ=-1.607 $d\perp_{1a}$=2.880×10^{-10} $d\perp_{1b}$=5.211×10^{-12}	1.137	1.137
ZeppelinCylinder	S_0=1 f_1=0.503 f_2=0.496 $d_{\parallel}$=3.392×10^{-10} θ=1.516 ϕ=1.519 R=2.045×10^{-6} $d\perp_1$=3.392×10^{-10}	S_0=1 f_1=0.565 f_2=0.434 $d_{\parallel}$=2.908×10^{-10} θ=1.454 ϕ=-1.605 R=1.880×10^{-6} $d\perp_1$=2.551×10^{-10}	S_0=0.98699 f_1=0.5035 f_2=0.4964 $d_{\parallel}$=3.392308×10^{-10} θ=1.516 ϕ=1.519 R=2.04530×10^{-6} $d\perp_1$=3.392307×10^{-10}	S_0=0.988 f_1=0.565 f_2=0.434 $d_{\parallel}$=2.908×10^{-10} θ=1.687 ϕ=-1.535 R=1.880×10^{-6} $d\perp_1$=2.551×10^{-10}	1.09077	0.94170
TensorGDRCylinders	S_0=1 f_1=0.524 f_2=0.475 k = 1.114 ϑ = 2.198×10^{-6} $d_{\parallel}$=3.328×10^{-10} θ=1.558 ϕ=1.570 $d\perp_1$=3.320×10^{-10} $d\perp_2$=2.290×10^{-10} α=14.929	S_0=1 f_1=0.677 f_2=0.322 k = 1.868 ϑ = 1.456×10^{-6} $d_{\parallel}$=2.912×10^{-10} θ=1.610 ϕ=-1.563 $d\perp_1$=2.910×10^{-10} $d\perp_2$=1.930×10^{-10} α=0.575	S_0=1.078 f_1=0.574 f_2=0.426 k = 1.388 ϑ = 1.855×10^{-6} $d_{\parallel}$=3.547×10^{-10} θ=1.568 ϕ=1.575 $d\perp_1$=3.233×10^{-10} $d\perp_2$=2.488×10^{-10} α=0.744	S_0=1 f_1=0.566 f_2=0.434 k = 1.587 ϑ = 1.755×10^{-6} $d_{\parallel}$=2.977×10^{-10} θ=1.522 ϕ=-1.588 $d\perp_1$=2.894×10^{-10} $d\perp_2$=1.748×10^{-10} α=2.543	1	0.847
ZeppelinCylinderDot	S_0=1 f_1=0.345 f_2=0.330 f_3=0.324 $d_{\parallel}$=8.304×10^{-10} θ=1.292 ϕ=1.3092 R=4.313×10^{-6} $d\perp_1$=3.597×10^{-10}	S_0=1 f_1=0.392 f_2=0.281 f_3=0.326 $d_{\parallel}$=6.621×10^{-10} θ=1.290 ϕ=-1.729 R=3.513×10^{-6} $d\perp_1$=2.997×10^{-10}	S_0=0.99633 f_1=0.345 f_2=0.330 f_3=0.324 $d_{\parallel}$=8.304×10^{-10} θ=1.292 ϕ=1.3092 R=4.313×10^{-6} $d\perp_1$=3.597×10^{-10}	S_0=0.997 f_1=0.392 f_2=0.281 f_3=0.326 $d_{\parallel}$=6.619×10^{-10} θ=1.290 ϕ=-1.728 R=3.512×10^{-6} $d\perp_1$=2.994×10^{-10}	0.32441	0.2667
TensorGDRCylindersDot	S_0=1 f_1=0.529 f_2=0.201 f_3=0.268 k=1.621 ϑ=5.413×10^{-6} $d_{\parallel}$=6.774×10^{-10} θ=1.674 ϕ=1.579 $d\perp_1$=5.5615×10^{-10} $d\perp_2$=1.185×10^{-10} α=19.658	S_0=1 f_1=0.555 f_2=0.184 f_3=0.263 k=1.557 ϑ=4.182×10^{-6} $d_{\parallel}$=5.612×10^{-10} θ=1.406 ϕ=-1.582 $d\perp_1$=4.533×10^{-10} $d\perp_2$=8.276×10^{-11} α=0.660	S_0=1.10 f_1=0.525 f_2=0.212 f_3=0.261 k=1.523 ϑ=5.971×10^{-6} $d_{\parallel}$=6.775×10^{-10} θ=1.688 ϕ=1.601 $d\perp_1$=5.544×10^{-10} $d\perp_2$=1.414×10^{-10} α=19.662	S_0=1.19 f_1=0.541 f_2=0.215 f_3=0.243 k=1.45 ϑ=3.526×10^{-6} $d_{\parallel}$=5.612×10^{-10} θ=1.407 ϕ=-1.599 $d\perp_1$=4.545×10^{-10} $d\perp_2$=1.49×10^{-10} α=0.651	0.270	0.214

Table 5.4: *Fitted parameters for the DT, the bitensor, the simplified version of CHARMED (ZeppelinCylinder), the MMWMD model (ZeppelinCylinderDot) and the best two- (CHARMED - TensorGDRCylinders) and three-compartment (TensorGDRCylindersDot) models .*

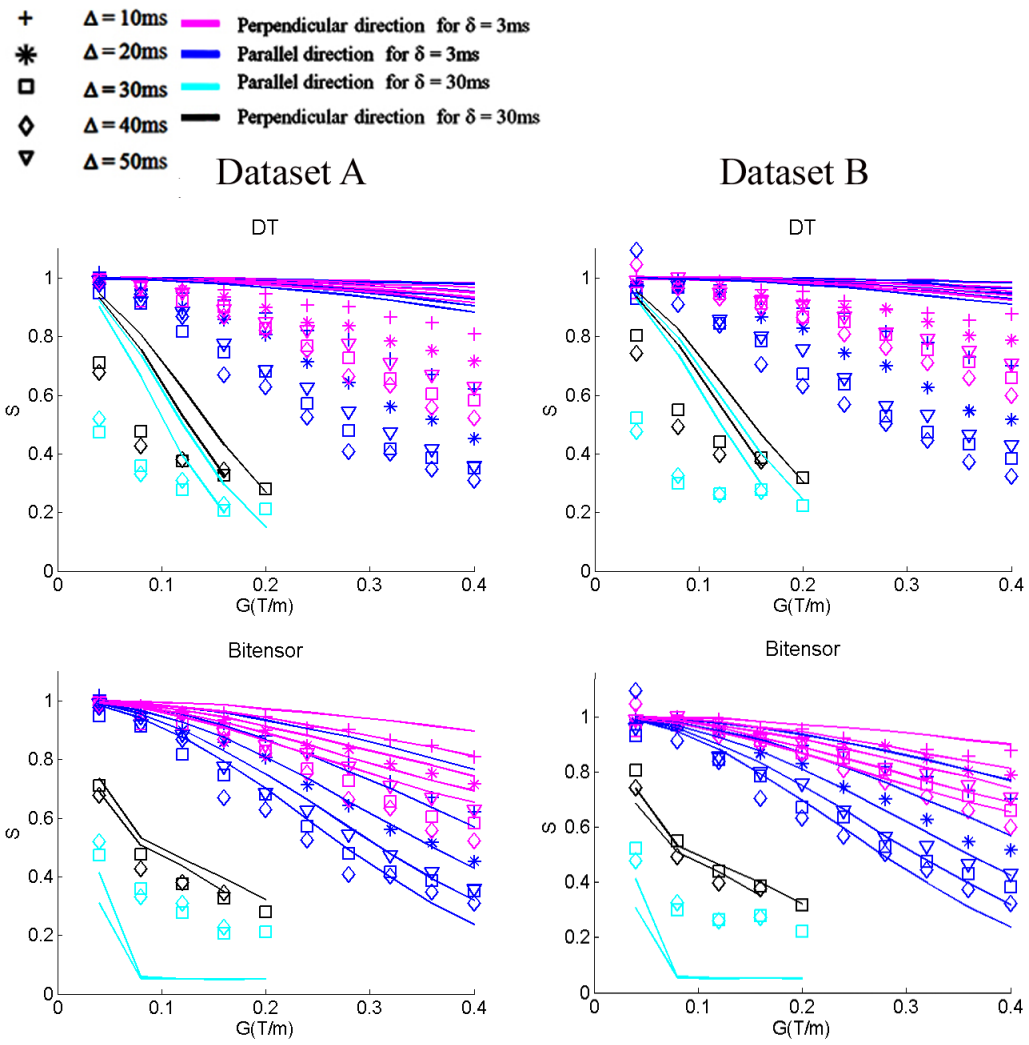

Figure 5.5: *Results of data synthesised from the DT and bitensor model and the scan data from the PGSE experiment for both data sets. The normalised signal S is plotted for all the values of* Δ, δ *as a function of the gradient strength* $|\boldsymbol{G}|$ *for the parallel and the mean of the four perpendicular directions.*

5.3.3 Synthesis and fitting

Figure 5.5 visualises the fit of the data synthesised from the DT [BJ02, BML94] and the bitensor model to the scanner data. Figure 5.6 presents data synthesised from the the simplified version of CHARMED (ZeppelinCylinder), the MMWMD model (ZeppelinCylinderDot) and the best two-compartment (CHARMED - TensorGDRCylinders) and three-compartment (TensorGDRCylindersDot) models. In both figures the symbols represent the scan data and the lines show the corresponding measurements predicted by each model with the fitted parameters. To account for possible offsets that can arise from Rician noise, the plots actually show the mean signals over 500 trials adding independent Rician noise at approximately the level in the scan data. However, this procedure only significantly affects measurements with very low signal. We compare data synthesised from the analytical models by plotting the signal S for all values of Δ and δ as a function of the gradient strength $|\mathbf{G}|$ for the parallel and the mean of the four perpendicular directions.

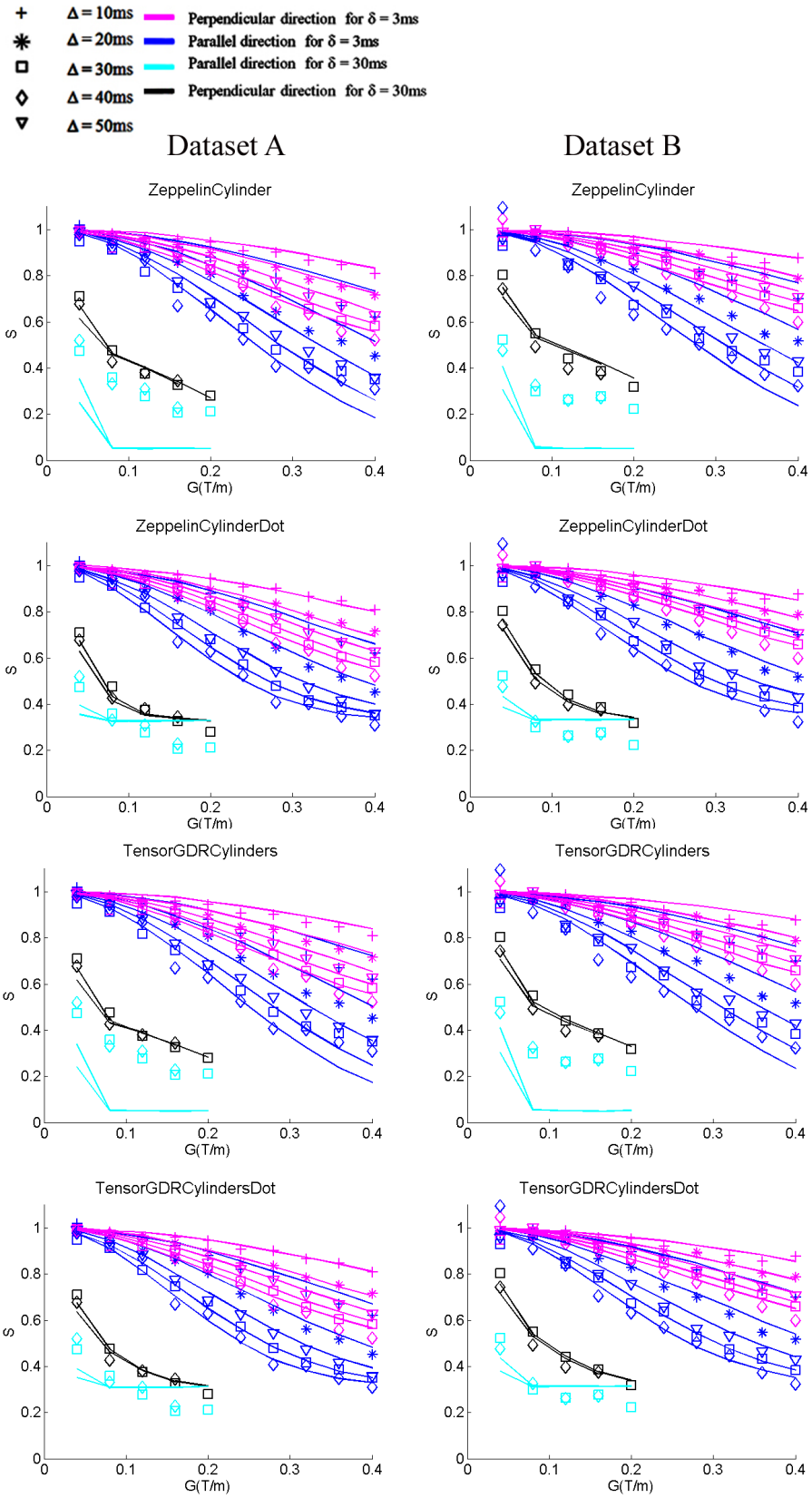

Figure 5.6: *Results of data synthesised from the key analytical models and the scan data from the PGSE experiment for both datasets. The normalised signal S is plotted for all the values of* Δ, δ *as a function of the gradient strength* $|\boldsymbol{G}|$ *for the parallel and the mean of the four perpendicular directions.*

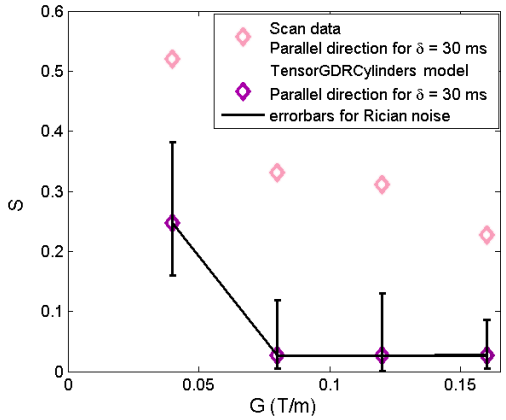

Figure 5.7: *Plot of the normalised signal for the parallel direction at $\delta = 30$ ms and $\Delta = 50$ ms from the scan data and the "TensorGDRCylinders" model against the gradient strength. The error bars indicate the minimum and maximum signal over 500 Rician noise trials.*

Figure 5.5 shows that the DT model significantly departs from the scan data in both directions. In contrast, all two-compartment models capture the broad trends of the data and the anisotropy that separates the parallel and perpendicular signals. Also in the same figure we see the simple bitensor model improves the fit in both directions. The subtle variations that improve the fit for the "ZeppelinCylinder" and "TensorGDRCylinder" model (see Figure 5.6) over the bitensor model are difficult to observe qualitatively.

In all two-compartment models we observe the biggest departures for large δ in the parallel direction. We hypothesise that these departures are not solely due to noise. Figure 5.7 compares the signal S for the scan data from representative dataset A and the "TensorGDRCylinders" model with $\delta = 30$ ms and $\Delta = 50$ ms for the parallel direction indicating the range of Rician noise over 500 realisations, confirming the hypothesis.

All three-compartment models capture the observed departure in the parallel direction. Figure 5.8 shows the normalised signal S for the "TensorGDRCylinders" model and all the combinations of this model with each isotropic restriction model. We observe that the best performing "dot" models can capture more of the restriction compare to the other third compartments. These models perform better than the two-compartment models in the parallel direction, however there is still a notable underestimation of the signal especially for $|\mathbf{G}| = 120$, 160 and 200 mT/m. Finally, the addition of the gamma distributed cylinder radii instead of the single radius improves both two- and three-compartment "tensor" models.

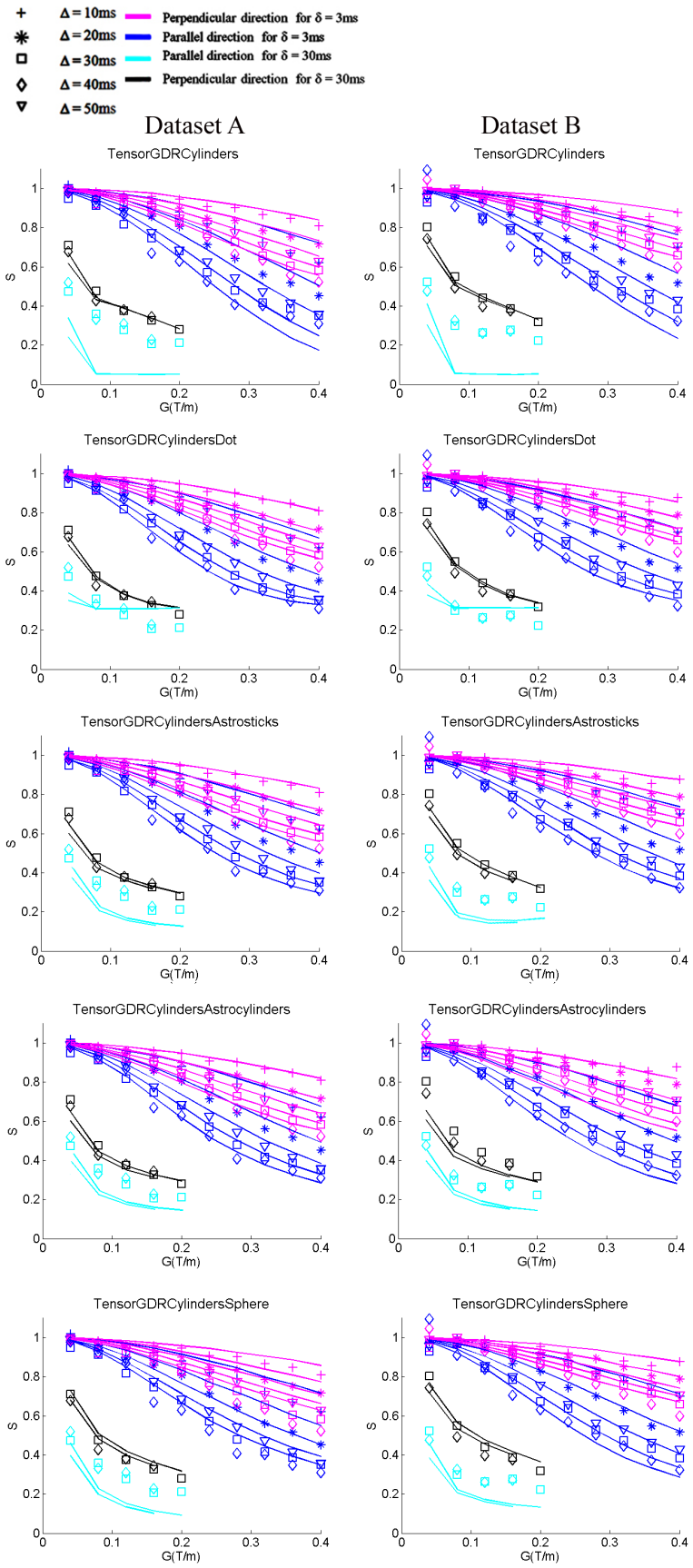

Figure 5.8: *Results of data synthesised from the "TensorGDRCylinders" model and all the resulting three-compartment models when this model is combined with each of the isotropic restriction compartments. The normalised signal S is plotted for all the values of* Δ, δ *as a function of the gradient strength* $|\boldsymbol{G}|$ *for the parallel and the mean of the four perpendicular directions.*

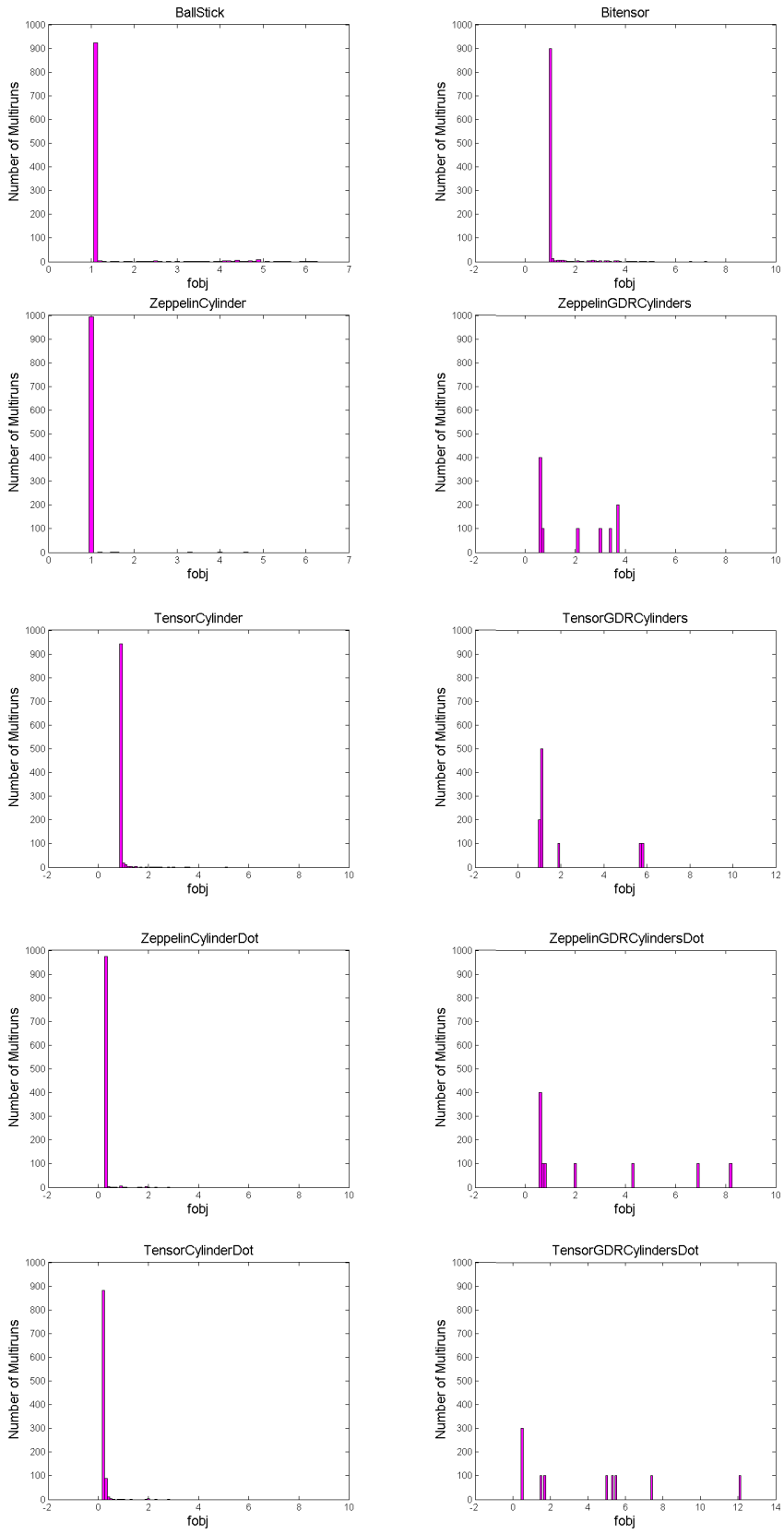

Figure 5.9: *Histograms of the objective function of 1000 multiruns for a selection of the models using dataset B.*

Models	N^o of Multiruns for $P > 0.99$
BallStick	2
Bitensor	2
ZeppelinCylinder	1
ZeppelinGDRCylinders	9
TensorCylinder	2
TensorGDRCylinders	21
ZeppelinCylinderDot	2
ZeppelinGDRCylindersDot	9
TensorCylinderDot	3
TensorGDRCylindersDot	13

Table 5.5: *Table indicating the number of runs required to obtain the best solution in each model with probability $P > 0.99$ for dataset B.*

5.3.4 Stability

To evaluate the stability of the models to the data we compute the histogram of the objective function for the 1000 perturbations of the starting parameters. Figure 5.9 shows that the "cylinder" model is much more stable, providing a lower objective function more times than the models which incorporate gamma distributed cylinder radii. The "GDRCylinders" give the overall lowest objective function, fitting the data better than the "cylinder" model. The solution however, is hard to find, which makes the fitting computationally very expensive unlike the "cylinder" model.

Table 5.5 indicates the number of multiruns required for each of these models to ensure obtaining the lowest objective function with probability $P > 0.99$. The table suggests that the most stable model is the "ZeppelinCylinder" model, followed by the "TensorCylinder", which requires the same number of multiruns as the very simple "BallStick" model and the "Bitensor". Finally, we see that the most demanding models comprise of the "GDRCylinders".

5.4 Discussion and Conclusions

We have constructed, studied, evaluated and compared a taxonomy of two- and three-compartment models for the diffusion-weighted MRI signal in brain white matter. In our study we also included widely used models such as the DT [BJ02, BML94] and the bitensor model [ABA01, TRW$^+$02, PA03, AHL$^+$01]. This is the first comprehensive study of analytic models. Previous diffusion studies [Ale08, AB05, SSWH97, ABKYB08] have been limited to using one analytic model. In this work we presented a model selection procedure to choose the model which best describes the data, while minimising the number of parameters. In this way we can use the model that most efficiently describes the diffusion MR signal on a voxel by voxel basis.

We devised a new imaging protocol which provided parallel and perpendicular signals from brain tissue and allowed fitting the taxonomy of models to the diffusion MRI measurements to obtain specific microstructure estimates. The models we presented here are applicable and feasible for whole brain imaging but the acquisition protocol is purposefully not. The aim of this work was to compare models using a sample with known orientation, which allowed many more measurements to support the model comparison. Once we have established appropriate models, we can subsequently find more economical

protocols for whole brain imaging. For example, we can use the ideas in [Ale08] for optimising the experiment design for diffusion MRI with fixed maximum gradient strengths.

The results reveal that the DT model shows a significant departure from the scan data and confirms expectations that the model is poor for high b value data, because it does not account for restriction. The two-compartment "stick" models also perform poorly and are at the bottom of the ranking, however, they still perform much better than the DT model. One key conclusion from studying the two-compartment models is that the effects of restriction are important for modelling diffusion in white matter, even if done crudely as in the "dot" and "sphere" models.

The departure of the signals from the two-compartment models in the parallel direction most likely comes from a small amount of restriction parallel to the fibres from glial cells and/or non-parallel fibres, which supports Stanisz's findings [SSWH97]. The models that capture this restriction and describe the diffusion signal the best are the three-compartment "dot" models. The model comparison in Tables 5.2 and 5.3 clearly demonstrates that the data support the non-zero axon radius parameters, for both the "cylinder" and the "GDRCylinders" models. This adds credence to techniques that estimate the parameter [Ale08, AB05, SSWH97, BBA09, AHH$^+$10], as well as anisotropy of the extra-axonal compartment.

Results show that the "GDRCylinders" model fits the data better than the "cylinder" model, although it is less stable. According to the histogram presented in Figure 5.9, the "cylinder" model results in the minimum objective function much more frequently than the "GDRCylinders" model and is less sensitive to the starting parameters, revealing greater efficiency. Another aspect that should be taken into account when choosing a model is the computational time of the fitting, especially for whole brain analysis. The "cylinder" model is approximately 5 times faster than the "GDRCylinders" model, particularly as it requires less random starts, which makes it a much more useable model.

To compare the radius parameter estimates with rat corpus callosum studies we calculate the single radius R which comes from the mean axon radius weighted by axon volume and compare this value with the results from the Barazany et al. study [BBA09], which are in agreement with the histology they performed. We extract R from the distributions of diameters which are given for five segments of the corpus callosum. We multiply each diameter in the histology data by 1.5 to correct for shrinkage during histological preparation, as [ASFZ92a] suggest. In the first two regions, which belong to the genu, R was 1.07 μm and 1 μm; in the next two regions, which belong to the midbody, R was 1.6 μm and 1.2 μm; in the last region, which belongs to the splenium, R was 0.99 μm. The R estimate for the whole corpus callosum was 1.25 μm. They also calculate the volume fraction for areas of CSF, intra- and extra- axonal spaces. They find that the CSF volume fraction ranged from 0.02 to 0.18, the intra-axonal volume fraction from 0.15 to 0.3 and the extra-axonal volume fraction from 0.5 to 0.62.

Considering the two-compartment models, the ones that are closest to these values for the axonal radii and the volume fractions are the "ZeppelinCylinder", the "TensorCylinder" and "ZeppelinGDRCylinder". These models are also ranked on the top among the other two-compartment models. The three-compartment models that are closest to these criteria are the "BallCylinderAstrosticks", the "BallGDRCylindersAstrosticks" and the "TensorGDRCylindersSphere", which are all in the top 20 models

overall.

Regarding the axon radius estimate we have to note that it is only a crude approximation and we cannot base the model comparison and ranking on these results. This also stands for the volume fraction estimation, since in the Barazany study [BBA09] the model includes a CSF compartment which our models do not. Future work will incorporate the CSF compartment as described in Section 4.2.

Also, we find that the axon radius estimation from the "GDRCylinders" model is in agreement with the "cylinder" model. The diffusivity is low compared to reported estimates in in vivo studies [BBA09], however this is to be expected due to the lower temperature, changes in the chemical environment during fixation and loss of active function after death.

As a final observation, the best ranked models appear to be the ones with the most parameters (degrees of freedom). This implies that there may still be effects that are not captured by the multi-compartment models presented here. There are a number of hypotheses as to why this may be the case. A possible explanation is the constraints we impose on our models to have the same parallel diffusivity for all compartments. Hence we could improve the models by using different diffusivities for each of the compartments. A second explanation could be that the models do not account for the difference in T_2 for each compartment. We could also include fibre dispersion in our modelling, as in [ZA10]. Finally another cause may arise from permeability effects, which allow exchange between compartments, such as in [SSWH97].

An important limitation of this work is that the axon radius is either represented by a single index R or by two parameters for the case of the gamma distributed radii cylinders. Both cases are a coarse approximation compared to neuroanatomical studies which use actual distributions of axon diameter derived by counting using electron microscopy [ASFZ92a]. In addition, there is no histology for validation and comparison of the microstructural estimates.

The fitting uses as an objective function the sum of squares which is the log-likelihood of the data on the assumption of Gaussian noise. However, the noise on MRI measurements in not Gaussian, but Rician [Hen85]. The sum of squares objective function does not account for this bias, which the Rician noise introduces, which means that parameter estimates from its minimization are systematically biased. One simple way to correct for the bias [JB04] is to include this constant offset as an extra parameter in the model and fit by minimising least squares [Ale09].

Despite these limitations, the model hierarchy provides useful biological indices and could be used in a variety of applications. This ex vivo technique offers a major advantage over the classical histological techniques for assessing axon diameter and density, because it is non-invasive and can be easily extended to the whole brain. The microstructural parameter estimates could potentially be used as biomarkers for studying normal development as well as brain diseases. Accurate estimation of the variation of indices such as the axon diameter and density as well as diffusivity could help diagnosis and prognosis. Another useful application of these microstructural estimates could be the creation of images in a similar way to FA images, using for example the volume fraction of the intra-axonal compartment. Finally these analytic models can be used in combination with tractography algorithms, as in [SRA10] for whole brain

microstructure estimates. This could help resolve ambiguities that occur from problematic regions such as crossing, kissing and fanning fibres. All these models are implemented in the open-source diffusion toolkit Camino [CBNG+06].

Chapter 6

In Vivo Brain

This chapter documents a diffusion MRI experiment on a live rat to compare the taxonomy of analytic models previously used for the ex vivo MRI experiment described in Chapter 5. The aim of this experiment is to find a model that best describes the in vivo diffusion measurements and investigate the variation of microstructure parameter estimates and appropriate model choice between in vivo and ex vivo brain measurements.

As in the ex vivo experiment in Chapter 5, we employ a similar imaging protocol, however using lower maximum gradient strengths than the ex vivo protocol, to allow in vivo acquisition from the rat brain for parallel and perpendicular signals in white matter. We also create a second dataset by correcting for Rician noise. We then fit the analytic models to both datasets to obtain estimates of microstructure parameters. We then evaluate the models and compare the estimated parameters from both in vivo and ex vivo measurements to identify the variations.

6.1 Methods

This section specifies the tissue models and provides details of the sample, the diffusion MRI acquisition for the in vivo brain imaging and the model-fitting procedure.

6.1.1 Tissue Models

We model brain white matter with the same analytic models used in the ex vivo experiment in Chapter 5, Section 5.1.1 (see Table 5.1).

6.1.2 Animal

One male Wistar rat was anaesthetised with 2% isoflurane in oxygen for the whole course of the MRI experiment. Body temperature was monitored and maintained at 38°C using a warm circulation system. The rat was placed in a prone position and the respiration was monitored by measuring the pressure in a pneumatic sensor placed under the animal. All procedures were in accordance with the animal protection laws and approved by the responsible governmental authority.

6.1.3 MRI Acquisition

In general, in vivo diffusion-weighted MR studies are much more challenging than ex vivo acquisitions as they are impeded by technical and practical factors. A very common and important difficulty is motion

sensitivity, which can cause severe ghosting artifacts or complete signal loss. As diffusion-weighted MRI is sensitive to molecular displacement on the order of micrometers, any motion, even unavoidable involuntary head motion or physiological, blood pressure-related pulsations of the brain tissue, would interfere with these measurements [LB06]. We established our final imaging protocol and acquisition technique after long consultations and experimentation with many of our collaborators. However, the in vivo imaging protocol follows closely the ex vivo protocol, which allowed us a wide coverage of the signal range and was rich enough for the model comparison. The main differences in the sequence parameters are the shorter gradient durations and lower gradient strengths due to SNR limitations. We also had less total acquisition time available due to the in vivo sample. The following paragraphs briefly discuss some of the technical and practical issues that occurred during the initial problematic in vivo MRI acquisitions. We then provide details of the successful one.

Originally, we scanned in London at the Centre for Advanced Biomedical Imaging (CABI), UCL, where the biological phantom and ex vivo MRI experiments took place. We used the PGSE sequence, as in the previous MRI experiments. However, the in vivo images had insufficient SNR, especially when using high b values ($> 2 \times 10^9$ sm^{-2}) for which the attenuation was already within the noise levels. Furthermore, due to the diffusion time requirements of our imaging protocol, which we discuss in detail later in this section, there was a significant T_2 decay that also contributed to poor signal attenuation. The imaging parameters we tested are included in the imaging protocol we used in Copenhagen and which is provided in Tables D.10, D.11, D.9 in Appendix D.

Another acquisition took place in the Danish Research Centre for Magnetic Resonance at the Copenhagen University Hospital, Hvidovre, Denmark. We used 4 animals (male rats) for diffusion MRI scanning with our experienced collaborators. Again we used the PGSE sequence which produced images with SNR similar to the ones from the London acquisition. For each animal we performed a DW-MRI acquisition which was approximately 2 hours long and a separate DTI acquisition using a 42-direction scheme with b value 1×10^9 sm^{-2} and six $b = 0$ measurements, which lasted approximately for 20 minutes. Further analysis of the diffusion MRI data revealed strange artifacts, that were not visible in the individual MRI images. This was caused by a technical fault of the scanner, which made the data inappropriate for the purposes of our experiment. More precisely we found that the sequence was switching to using a bipolar gradient when the 180 degree pulse was applied. The imaging protocol is provided in Tables D.10, D.11, D.9 in Appendix D.

The final in vivo MRI acquisition was performed at Tel Aviv Sourasky Medical Center, Tel Aviv University, Israel, on a 7 T/30 Bruker MRI scanner equipped with a gradient system with a maximal gradient strength of 400 mT/m. For excitation we used a body-coil (outer/inner diameter of 112/72 mm) and a surface coil (10 mm diameter) as a receiver. We used a four direction-encoding scheme and placed the animal in the scanner oriented to ensure that some fibres in the CC are parallel to our central direction. We also chose three evenly spaced directions perpendicular to the central direction in our chosen voxels. We used stimulated-echo echo-planar imaging (EPI) sequence [CHSM89, MHF91], instead of the PGSE, for the following diffusion weightings: five diffusion times Δ = 10, 20, 30, 40,

50 ms, gradient durations δ = 3 ms for all Δ, as for the ex vivo protocol, and δ = 12 ms for Δ = 30, 40, 50 ms, instead of δ = 30 ms used for the ex vivo experiment, because the resulting b values would be too high which would result in fewer measurements with good SNR. The gradient strength $|\mathbf{G}|$ varied from 30 to 300 mT/m in ten steps of 30 mT/m. For the ex vivo acquisition the highest b value was 7.7×10^{10} sm^{-2}, however the in vivo measurements with b value greater than 8.6×10^{9} sm^{-2} were not performed due to poor SNR (< 2.0), i.e. all combinations with δ = 12 ms and $|\mathbf{G}|$ = 150 to 300 mT/m for Δ = 50 ms, $|\mathbf{G}|$ = 180 to 300 mT/m for Δ = 40 ms, and $|\mathbf{G}|$ = 210 to 300 mT/m, for Δ = 30 ms.

In total we acquired images with 65 diffusion weightings in each direction. We used minimum TE to maximise SNR and chose TR to minimise gradient heating effects. For each combination of Δ, δ we acquired $b = 0$ images to correct for T_1 and T_2 dependence. Figure 6.1 plots the parallel and the mean of the three perpendicular directions of the log normalized signal from voxels in the region of interest (see Section 6.2) in the CC and shows MRI images for various b values.

We also performed a separate DTI acquisition using a 42-direction scheme with b value 1×10^{9} sm^{-2} and six $b = 0$ measurements. The field of view was 16 mm^2. The matrix size was 128×128 and the slice thickness was 1.25 mm. All diffusion scans were done with respiratory gating to reduce the effects of respiratory motion. The animal was scanned for 3 hours in total. There was no time available for repeat scans because the animal, which was under anesthesia for 6 hours (this time includes animal preparation and scanning), becomes unstable and close to death, resulting in a very weak signal. The imaging protocol is provided in Tables D.7, D.8, D.9 in Appendix D.

6.1.4 Model Fitting

We follow the same fitting procedure as described in Chapter 5, Section 5.1.4 with a few minor modifications. To choose the best fit parameters from the models we perform 100 perturbations of the starting parameters instead of 1000, since the experiment on the fixed brain showed that the models produced the lowest objective function more than 10% so we can reduce the number of perturbations. The starting parameters are selected after 10 perturbations.

6.2 Experiments

As for the ex vivo MRI experiment in Section 5.2, we use the same procedure to study parallel and perpendicular signal attenuation in the brain. However, when we choose the region of interest (ROI) we allow a tolerance of 4° instead of 2° in which the principal direction of the DT is parallel to the defined central gradient direction. We average the data contained within all the resulting 10 voxels of the ROI.

6.2.1 Noise Correction

The SNR for the in vivo diffusion-weighted data was approximately 15, almost half the SNR of the ex vivo measurements (32). A simple way to improve the levels of SNR is to filter out the noise in the images. MRI images in the presence of noise are governed by a Rician distribution [GP95]. The sum of squares objective function estimation assumes Gaussian noise with zero mean. At low SNR (high b values) the signal is dominated by the Rician noise floor. This can cause estimation errors demonstrated by [JB04, LFH$^+$08]. Here we create a second dataset by correcting for Rician noise to examine the effect

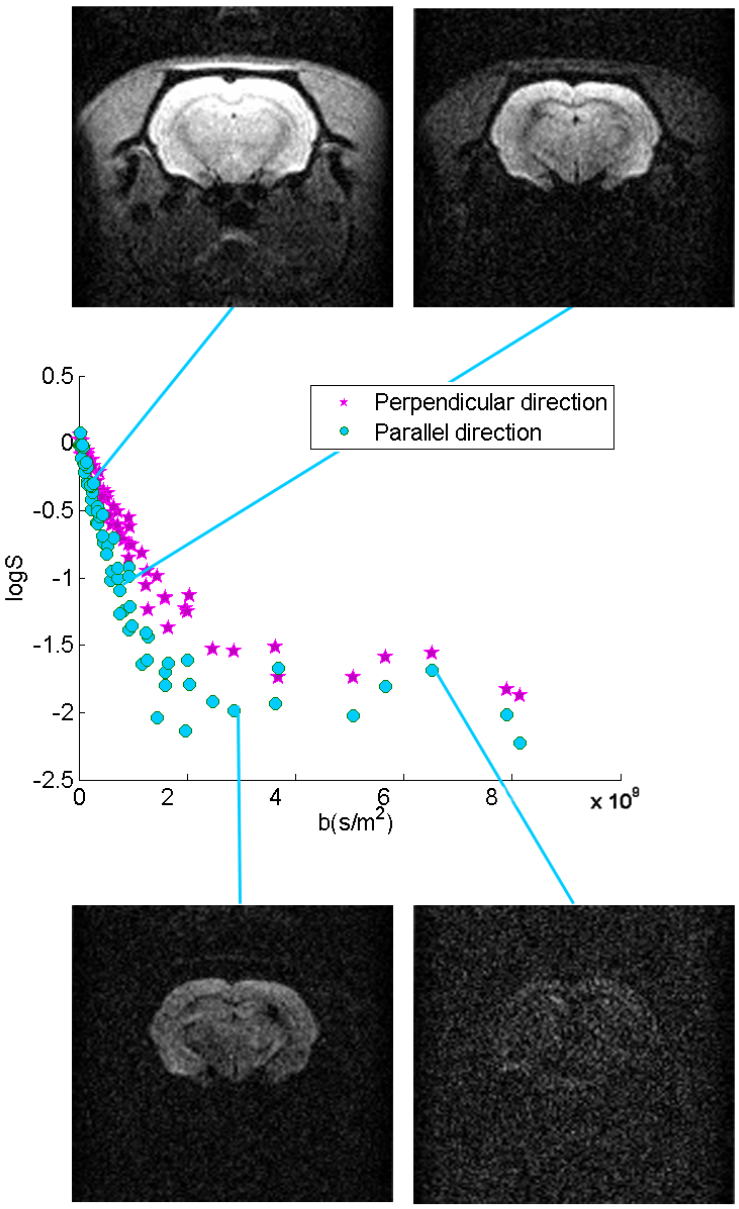

Figure 6.1: *Plot of the parallel and the mean of the three perpendicular directions of the log signal from voxels in a region of interest in the CC and demonstration of MRI images (parallel direction) for various b values.*

of filtering noise in the model comparison. We use NA-MIC, an open source software supported by the community of National Alliance for Medical Image Computing [PLSK06]. We refer to the original data as dataset A and the noise corrected data as dataset B.

To correct for Rician noise in the diffusion-weighted data, the NA-MIC system uses a linear minimum mean square error (LMMSE) estimator [Kay93]. The method provides a Rician noise filter that automatically estimates the local noise statistic from homogenous regions within the image. The technique uses the LMMSE implementation in [AFNK+08], which provides a computationally efficient

closed-form analytic solution of the LMMSE estimator, making it appropriate when dealing with large volumes of diffusion-weighted data.

6.3 Results

This section presents the evaluation and assessment of the analytic models and the parameter estimation from fitting the models to the diffusion-weighted data.

6.3.1 Model Ranking

As in the ex vivo experiment (see Section 5.3), we use the BIC [Sch78] to evaluate the models. Tables 6.1 and 6.2 present the ranking of the models according to the BIC of dataset A and B respectively. The tables also provide the MSE for each model.

6.3.1.1 Comparison between dataset A and B

According to the BIC the best two-compartment model for dataset A is the "BallStick", whereas for dataset B the best two-compartment model is the "Bitensor". Overall, the "ZeppelinStickDot" model minimizes the BIC for dataset A, whereas the "ZeppelinStickAstrosticks" minimises the BIC for dataset B. However, the "ZeppelinCylinderDot", which is the second best model for dataset A and the "TensorCylinderSphere", which is among the top five models for dataset B, also perform well. The second best model for dataset B is the "ZeppelinStickSphere". The worst performing model for both datasets is the DT.

Table 6.1 shows that the "zeppelin" in combination with the "dot" and either the zero or single radius intra-axonal compartment is ranked the highest. The same table also indicates that the models which perform poorly are the two-compartment models with the intra-axonal "GDRCylinders" compartment. Table 6.2 places the "zeppelin" in combination with the zero radius intra-axonal compartment and all the isotropic restriction compartments, except the "dot", at the highest rank. At the lowest rank in the same table are three-compartment models, in contradiction with dataset A where the two-compartment models perform the worst. The "ball" in combination with the "GDRCylinders" and all the isotropic restriction compartments are ranked the lowest.

6.3.1.2 Comparison with ex vivo findings

Compared to the ex vivo ranking, we observe a great change in the in vivo model ordering. The best ex vivo two- and three-compartment model comprised the non-zero radius intra-axonal "GDRCylinders" model and the full tensor. In particular, the non-zero radius intra-axonal compartment was the dominant characteristic of the best performing models, while the in vivo results show clear preference to the zero radius intra-axonal model. However, there is agreement for adding the third compartment to the model, which improves the BIC in both experiments. Both ex vivo and in vivo experiments using dataset A rank the "dot" model highest, and the combination of the "dot" with the "cylinder" model is also ranked highly. Finally, we observe that the DT model is unable to adequately describe either the ex vivo or the in vivo data. For more details see Section 5.3.1.

6.3.1.3 Conclusions

In dataset A we observe that all two-compartment models perform worse than the three-compartment models, which are ranked at the top for both datasets. This trend is also observed in the ex vivo experiment (see Section 5.3), revealing the importance of the third compartment. However, the BIC heavily penalises the number of parameters and shows preference to the simplest models. Finally, in dataset B we see a substantially different ranking of the models compared to dataset A. The noise correction appeared to penalise the complexity of the models even more, allowing worse performing two-compartment models to score a better BIC than some three-compartment models. We have to note that the only possible explanation is that this is caused by the noise reduction algorithm. The algorithm cannot distinguish Rician noise from the signal coming from the isotropic restriction models, especially from the "dot".

6.3.2 Parameter estimation

The best fit microstructure parameters from the models are shown in Tables: C.1, C.2, C.3, C.4 and C.5 in Appendix C. We summarise some of the key models (best and worst two- and three compartment models as well as the well-used models from the literature) in Table 6.3.

6.3.2.1 Comparison between dataset A and B

Table C.1 presents the resulting parameters for all the two-compartment models and the DT. In both datasets we see that "cylinder" models give higher estimates for the volume fraction f_1 than the "stick" models, and "GDRCylinders" provide higher f_1 than the "cylinder". Compared to the "cylinder" models the "GDRCylinders" give lower estimates for the radius R for dataset A and higher for dataset B (except when combined with the extra-axonal "tensor").

Compared to all the two compartment models the "Bitensor" estimates the highest f_1 for dataset A and second highest for dataset B after the "BallGDRCylinders" model. The DT provides the lowest estimate for the parallel diffusivity $d_{\parallel}$ compared to all models for both datasets. The rest of the two-compartment models consistently estimate $d_{\parallel}$ around 1.4×10^{-9} m^2/s for both datasets.

Table C.2 presents the resulting parameters for the three-compartment "dot" models. The "cylinder" models provide a higher f_1 than the "stick" models for dataset A (except when combined with the "tensor" model). For dataset B the estimates are approximately the same level. The "GDRCylinders" provide a higher estimate for f_1 than the "cylinder" models for both datasets (except when combined with the "tensor" model). However, for many of these models we observe a very low value for f_1. For example, the "zeppelin" estimates $f_1 < 0.1$, except when combined with the "GDRCylinders" for dataset A, and all the "tensor" models estimate f_1 at approximately 0.1 except when combined with the "stick".

All the "dot" models provide higher values for the $d_{\parallel}$ compared to the corresponding two-compartment models. They also give higher estimates for the radius R, for both datasets (except when combined with the "tensor" for dataset A). The "GDRCylinders" estimate the radius R higher than the "cylinder" models (except when combined with the "zeppelin") for dataset A. There is no obvious agreement between the radius estimates from the "GDRCylinders" and the "cylinder" models for dataset B.

The three-compartment "astrosticks" models are presented in Table C.3. All the "astrosticks" models estimate a lower volume fraction f_1 than the "dot" models (except for the "ZeppelinStickAstrosticks"

Models	MSE		BIC		No. Parameters
	dataset A	dataset B	dataset A $\times 10^3$	dataset B $\times 10^3$	
ZeppelinStickDot	0.00334	0.00291	-1.489	-1.526	7
ZeppelinCylinderDot	0.00334	0.00292	-1.483	-1.519	8
ZeppelinStickAstrosticks	0.00341	0.00285	-1.482	-1.531	7
ZeppelinStickAstrocylinders	0.00339	0.00281	-1.478	-1.530	8
TensorStickDot	0.00334	0.00288	-1.478	-1.516	9
ZeppelinCylinderAstrocylinders	0.00340	0.00283	-1.478	-1.527	8
ZeppelinStickSphere	0.00340	0.00279	-1.478	-1.531	8
ZeppelinCylinderSphere	0.00341	0.00284	-1.477	-1.527	8
ZeppelinCylinderAstrosticks	0.00343	0.002864	-1.476	-1.524	8
TensorCylinderDot	0.00331	0.00279	-1.475	-1.520	10
TensorStickAstrosticks	0.00337	0.00276	-1.474	-1.528	9
ZeppelinGDRCylindersAstrocylinders	0.00341	0.00284	-1.471	-1.521	9
ZeppelinGDRCylindersSphere	0.00342	0.00289	-1.471	-1.516	9
TensorGDRCylindersDot	0.00330	0.00278	-1.470	-1.515	11
TensorStickAstrocylinders	0.00336	0.00272	-1.470	-1.527	10
TensorStickSphere	0.00336	0.00272	-1.470	-1.527	10
TensorCylinderSphere	0.00337	0.00271	-1.470	-1.527	10
TensorCylinderAstrocylinders	0.00337	0.00274	-1.469	-1.524	10
TensorCylinderAstrosticks	0.00339	0.002764	-1.467	-1.522	10
TensorGDRCylindersSphere	0.00336	0.00273	-1.464	-1.520	11
TensorGDRCylindersAstrocylinders	0.00337	0.00273	-1.464	-1.519	11
TensorGDRCylindersAstrosticks	0.003384	0.00276	-1.463	-1.517	11
ZeppelinGDRCylindersAstrosticks	0.00359	0.002835	-1.458	-1.521	9
BallStickDot	0.00389	0.00337	-1.453	-1.4924	6
BallStickAstrosticks	0.00390	0.00333	-1.453	-1.4952	6
BallStickAstrocylinders	0.00389	0.00324	-1.448	-1.4968	7
ZeppelinGDRCylindersDot	0.00334	0.002917	-1.447	-1.514	9
BallStickSphere	0.00389	0.00324	-1.4477	-1.496	7
BallCylinderAstrosticks	0.00392	0.003336	-1.447	-1.4892	7
BallCylinderSphere	0.00390	0.00333	-1.447	-1.490	7
BallCylinderDot	0.00391	0.003365	-1.446	-1.486	7
BallCylinderAstrocylinders	0.00391	0.00333	-1.4461	-1.4895	7
BallGDRCylindersSphere	0.00390	0.00330	-1.442	-1.486	8
BallGDRCylindersDot	0.003906	0.0033507	-1.4415	-1.482	8
BallGDRCylindersAstrosticks	0.00390	0.003320	-1.441	-1.485	8
BallGDRCylindersAstrocylinders	0.00401	0.00335	-1.434	-1.482	8
BallStick	0.00482	0.003385	-1.4015	-1.4964	5
ZeppelinStick	0.00472	0.0030485	-1.401	-1.519	6
Bitensor	0.00471	0.002973	-1.397	-1.520	7
TensorStick	0.004611	0.00291	-1.396	-1.520	8
BallCylinder	0.00482	0.003386	-1.396	-1.491	6
ZeppelinCylinder	0.00472	0.003037	-1.396	-1.519	7
TensorCylinder	0.00461	0.00291	-1.3911	-1.515	9
ZeppelinGDRCylinders	0.00473	0.00304	-1.390	-1.509	8
BallGDRCylinders	0.00483	0.00337	-1.390	-1.487	7
TensorGDRCylinders	0.00461	0.00291	-1.386	-1.509	10
DT	0.1874	0.1544	-0.409	-0.461	7

Table 6.1: *Table of the ranked models showing the mean-squared fitting error (MSE), the Bayesian information criterion (BIC) and the number of parameters (counting the S_0) for each model. The order of the models is according to the BIC score of dataset A.*

Models	MSE		BIC		No. Parameters
	dataset A	dataset B	dataset A $\times 10^3$	dataset B $\times 10^3$	
ZeppelinStickAstrosticks	0.00341	0.00285	-1.4833	-1.5313	7
ZeppelinStickSphere	0.00340	0.00279	-1.478	-1.531	8
ZeppelinStickAstrocylinders	0.00339	0.00281	-1.4786	-1.530	8
TensorStickAstrosticks	0.00337	0.00276	-1.4748	-1.5283	9
TensorCylinderSphere	0.00337	0.00271	-1.470	-1.5275	10
ZeppelinCylinderAstrocylinders	0.00340	0.00283	-1.478	-1.5272	8
TensorStickAstrocylinders	0.00336	0.00272	-1.470	-1.527	10
TensorStickSphere	0.00336	0.00272	-1.470	-1.527	10
ZeppelinCylinderSphere	0.00341	0.00284	-1.477	-1.527	8
ZeppelinStickDot	0.00334	0.00291	-1.489	-1.5262	7
TensorCylinderAstrocylinders	0.003376	0.00274	-1.469	-1.5246	10
ZeppelinCylinderAstrosticks	0.00343	0.002864	-1.476	-1.5245	8
TensorCylinderAstrosticks	0.003395	0.002764	-1.4677	-1.5228	10
ZeppelinGDRCylindersAstrosticks	0.00359	0.002835	-1.4584	-1.5216	9
ZeppelinGDRCylindersAstrocylinders	0.00341	0.00284	-1.4718	-1.521	9
Bitensor	0.00471	0.002973	-1.397	-1.520	7
TensorStick	0.004611	0.00291	-1.3968	-1.520	8
TensorCylinderDot	0.00331	0.00279	-1.475	-1.520	10
TensorGDRCylindersSphere	0.00336	0.00273	-1.4645	-1.520	11
TensorGDRCylindersAstrocylinders	0.00337	0.00273	-1.464	-1.5197	11
ZeppelinCylinder	0.00472	0.003037	-1.396	-1.5193	7
ZeppelinCylinderDot	0.00334	0.00292	-1.483	-1.5192	8
ZeppelinStick	0.00472	0.0030485	-1.401	-1.519	6
TensorGDRCylindersAstrosticks	0.003384	0.00276	-1.463	-1.5175	11
TensorStickDot	0.00334	0.00288	-1.478	-1.5167	9
ZeppelinGDRCylindersSphere	0.00342	0.00289	-1.471	-1.516	9
TensorCylinder	0.00461	0.00291	-1.3911	-1.515	9
TensorGDRCylindersDot	0.003302	0.00278	-1.470	-1.515	11
ZeppelinGDRCylindersDot	0.00334	0.002917	-1.4477	-1.514	9
ZeppelinGDRCylinders	0.00473	0.00304	-1.3902	-1.509	8
TensorGDRCylinders	0.00461	0.00291	-1.386	-1.509	10
BallStickAstrocylinders	0.00389	0.00324	-1.448	-1.4968	7
BallStickSphere	0.00389	0.00324	-1.4477	-1.4965	7
BallStick	0.00482	0.003385	-1.4015	-1.4964	5
BallStickAstrosticks	0.00390	0.00333	-1.453	-1.4952	6
BallStickDot	0.00389	0.00337	-1.453	-1.4924	6
BallCylinder	0.00482	0.003386	-1.396	-1.491	6
BallCylinderSphere	0.00390	0.00333	-1.447	-1.490	7
BallCylinderAstrocylinders	0.00391	0.00333	-1.4461	-1.4895	7
BallCylinderAstrosticks	0.00392	0.003336	-1.447	-1.4892	7
BallGDRCylinders	0.00483	0.00337	-1.390	-1.487	7
BallCylinderDot	0.00391	0.003365	-1.4466	-1.4868	7
BallGDRCylindersSphere	0.00390	0.00330	-1.442	-1.4867	8
BallGDRCylindersAstrosticks	0.00390	0.003320	-1.4413	-1.485	8
BallGDRCylindersDot	0.003906	0.00335	-1.4415	-1.4824	8
BallGDRCylindersAstrocylinders	0.00401	0.00335	-1.434	-1.4824	8
DT	0.1544	0.8874	-0.4614	-0.6101	7

Table 6.2: *Table of the ranked models showing the mean-squared fitting error (MSE), the Bayesian information criterion (BIC) and the number of parameters (counting the S_0) for each model. The order of the models is according to the BIC score of dataset B.*

Models	Startpoint		Best Estimates		FOBJ	
	dataset A	dataset B	dataset A	dataset B	dataset A	dataset B
DT	-	-	$d_{\parallel}$=2.565×10^{-10} $d\perp_1$= 2.285×10^{-10} $d\perp_2$=1.381×10^{-8} θ=1.573 ϕ=-0.783	$d_{\parallel}$=4.536×10^{-10} $d\perp_1$= 4.421×10^{-10} $d\perp_2$=1.161×10^{-8} θ=1.571 ϕ=-3.923	50.2	41.37
Bitensor	S_0=1 f_1=0.297 f_2=0.702 $d_{\parallel}$=1.404×10^{-9} θ=1.686 ϕ=3.141 $d\perp_{1a}$=1.244×10^{-9} $d\perp_{1b}$=5.718×10^{-11}	S_0=1 f_1=0.170 f_2=0.829 $d_{\parallel}$=1.313×10^{-9} θ=1.546 ϕ=-3.141 $d\perp_{1a}$=5.096×10^{-10} $d\perp_{1b}$=8.612×10^{-10}	S_0=1.011 f_1=0.709 f_2=0.290 $d_{\parallel}$=1.414×10^{-9} θ=1.439 ϕ=18.849 $d\perp_{1a}$=1.238×10^{-9} $d\perp_{1b}$=4.289×10^{-11}	S_0=1.018 f_1=0.383 f_2=0.616 $d_{\parallel}$=1.396×10^{-9} θ=1.656 ϕ=-3.141 $d\perp_{1a}$=2.996×10^{-10} $d\perp_{1b}$=1.351×10^{-9}	1.261	0.791
BallStick	S_0=1 f_1=0.311 f_2=0.689 $d_{\parallel}$=1.412×10^{-9} θ=1.331 ϕ=0.189	S_0=1 f_1=0.259 f_2=0.741 $d_{\parallel}$=1.267×10^{-9} θ=1.186 ϕ=-2.734	S_0=1.101 f_1=0.321 f_2=0.678 $d_{\parallel}$=1.443×10^{-9} θ=1.349 ϕ=0.19	S_0=1.024 f_1=0.260 f_2=0.729 $d_{\parallel}$=1.319×10^{-9} θ=1.199 ϕ=-2.741	1.293	0.907
ZeppelinCylinder	S_0=1 f_1=0.32 f_2=0.68 $d_{\parallel}$=1.627×10^{-9} θ=1.422 ϕ=0.085 R=1.411×10^{-7} $d\perp_1$=1.034×10^{-9}	S_0=1 f_1=0.125 f_2=0.875 $d_{\parallel}$=1.401×10^{-9} θ=1.587 ϕ=-3.15 R=4.122×10^{-6} $d\perp_1$=9.766×10^{-10}	S_0=1.01 f_1=0.24 f_2=0.76 $d_{\parallel}$=1.427×10^{-9} θ=1.426 ϕ=0.07 R=1.370×10^{-7} $d\perp_1$=1.134×10^{-9}	S_0=1.014 f_1=0.112 f_2=0.888 $d_{\parallel}$=1.382×10^{-9} θ=1.681 ϕ=-3.141 R=4.075×10^{-6} $d\perp_1$=9.644×10^{-10}	1.267	0.814
TensorGDRCylinders	S_0=1 f_1=0.420 f_2=0.580 k = 2.103 $beta$ = 1.321×10^{-7} $d_{\parallel}$=1.468×10^{-9} θ=1.427 ϕ=-3.142 $d\perp_1$=1.463×10^{-9} $d\perp_2$=9.122×10^{-10} α=5.622	S_0=1 f_1=0.160 f_2=0.840 k = 1.143 $beta$ = 1.036×10^{-7} $d_{\parallel}$=1.376×10^{-9} θ=1.756 ϕ=-3.147 $d\perp_1$=1.354×10^{-9} $d\perp_2$=5.877×10^{-10} α=-18.076	S_0=1.181 f_1=0.406 f_2=0.594 k = 2.444 $beta$ = 1×10^{-7} $d_{\parallel}$=1.447×10^{-9} θ=1.366 ϕ=-3.142 $d\perp_1$=1.444×10^{-9} $d\perp_2$=9.472×10^{-10} α=5.658	S_0=1.049 f_1=0.153 f_2=0.847 k = 1.029 $beta$ = 1.217×10^{-7} $d_{\parallel}$=1.398×10^{-9} θ=1.807 ϕ=-3.142 $d\perp_1$=1.388×10^{-9} $d\perp_2$=6.036×10^{-10} α=-18.116	1.235	0.780
ZeppelinCylinderDot	S_0=1 f_1=0.065 f_2=0.654 f_3=0.281 $d_{\parallel}$=2.021×10^{-9} θ=1.622 ϕ=0.187 R=2.001×10^{-6} $d\perp_1$=1.455×10^{-9}	S_0=1 f_1=0.070 f_2=0.867 f_3=0.063 $d_{\parallel}$=1.489×10^{-9} θ=1.526 ϕ=-3.174 R=2.995×10^{-6} $d\perp_1$=1.003×10^{-9}	S_0=1.020 f_1=0.079 f_2=0.787 f_3=0.132 $d_{\parallel}$=1.865×10^{-9} θ=1.632 ϕ=0.195 R=2.609×10^{-6} $d\perp_1$=1.082×10^{-9}	S_0=1.018 f_1=0.050 f_2=0.906 f_3=0.044 $d_{\parallel}$=1.465×10^{-9} θ=1.599 ϕ=-3.14 R=4.286×10^{-6} $d\perp_1$=9.680×10^{-10}	0.896	0.783
ZeppelinStickDot	S_0=1 f_1=0.065 f_2=0.720 f_3=0.215 $d_{\parallel}$=2.011×10^{-9} θ=1.542 ϕ=0.223 $d\perp_1$=1.203×10^{-9}	S_0=1 f_1=0.050 f_2=0.908 f_3=0.044 $d_{\parallel}$=1.520×10^{-9} θ=1.611 ϕ=-3.141 $d\perp_1$=9.603×10^{-10}	S_0=1.01 f_1=0.077 f_2=0.790 f_3=0.132 $d_{\parallel}$=1.896×10^{-9} θ=1.581 ϕ=0.199 $d\perp_1$=1.074×10^{-9}	S_0=1.015 f_1=0.049 f_2=0.907 f_3=0.044 $d_{\parallel}$=1.516×10^{-9} θ=1.623 ϕ=-3.141 $d\perp_1$=9.595×10^{-10}	0.895	0.779
ZeppelinStickAstrosticks	S_0=1 f_1=0.111 f_2=0.494 f_3=0.395 $d_{\parallel}$=2.466×10^{-9} θ=1.623 ϕ=-3.141 $d\perp_1$=1.177×10^{-9}	S_0=1 f_1=0.064 f_2=0.785 f_3=0.151 $d_{\parallel}$=2.655×10^{-9} θ=1.573 ϕ=-3.143 $d\perp_1$=1.006×10^{-9}	S_0=1.029 f_1=0.109 f_2=0.471 f_3=0.420 $d_{\parallel}$=2.521×10^{-9} θ=1.642 ϕ=-3.141 $d\perp_1$=1.237×10^{-9}	S_0=1.020 f_1=0.039 f_2=0.800 f_3=0.161 $d_{\parallel}$=2.671×10^{-9} θ=1.520 ϕ=-3.144 $d\perp_1$=9.947×10^{-10}	0.914	0.764

Table 6.3: *Fitted parameters for the DT, the bitensor, the simplified version of CHARMED (ZeppelinCylinder), the MMWMD model (ZeppelinCylinderDot), CHARMED (TensorGDRCylinders) and the best two- and three-compartment models for each data set.*

for dataset A), and a higher parallel diffusivity $d_{\parallel}$ for both datasets.

The "stick" models give a slightly higher f_1 than the "cylinder" models for dataset A, while for dataset B we observe this trend in reverse. The "GDRCylinders" provide the lowest estimate for f_1 (except when combined with the extra-axonal "ball") for dataset A and the highest for dataset B (except when combined with the "zeppelin"). We have to note here that a selection of the "astrosticks" models provide unrealistically low estimates for the volume fraction ($f_1 < 0.1$). In particular these models consist of the extra-axonal "zeppelin" and "tensor" models in combinations with all the intra-axonal compartments. Estimates of R from the "GDRCylinders" are similar to the "cylinder" models for both datasets, except when combined with the "zeppelin" in dataset B, where the "cylinder" model provides a higher estimate.

Table C.4 presents the estimates from the "astrocylinders" models. All "astrocylinders" provide approximately the same estimate of f_1 compared to the equivalent "astrosticks" models for both datasets (except "BallGDRCylindersAstrocyinders", where it is higher). Also the "astrocylinders" models give higher estimates for $d_{\parallel}$ for both datasets with a few exceptions ("ZeppelinCylinderAstrocylinders" and "TensorCylinderAstrocylinders" for dataset A and "ZeppelinGDRCylindersAstrocylinders" for dataset B).

The "GDRCylinders" estimate R lower than the "cylinder" models for dataset A, except when combined with the extra-axonal "tensor" model. In dataset B, the radius estimate is approximately the same, except when combined with the "ball" model, where the "GDRCylinders" estimate R higher than the "cylinder" models.

The three-compartment "sphere" models are presented in Table C.5. The "GDRCylinders" give higher f_1 compared to the equivalent "astrocylinders" models for both datasets, while the other intra-axonal compartments give approximately the same estimates. All "sphere" models give approximately the same estimate for the parallel diffusivity $d_{\parallel}$ as the equivalent "astrocylinders" models for both datasets, except the "TensorGDRCylindersSphere" which gives a lower estimate. The "GDRCylinders" provide a higher estimate for the volume fraction f_1 and the radius R than the "cylinder" models for both datasets.

6.3.2.2 Comparison with ex vivo findings

Regarding the two-compartment models, we observe in both the ex vivo and in vivo experiments that the "cylinder" model provides a higher f_1 than the "stick", and the "GDRCylinders" provides a higher f_1 than the "cylinder" model. Another common trend observed in the data is that the third compartment "sphere" in combination with most of the intra- and extra-axonal models provides a higher value for f_1 than all the other third compartments. The in vivo values for f_1 from many of the three-compartment models were very low, often lower than 0.1, which is a trend we did not observe in the ex vivo data. The third compartment "dot" model consistently provides higher values for the diffusivity than the two-compartment models in both experiments.

The radius estimation in the ex vivo experiment appears to be very consistent amongst the different models and estimates R between 2 μm and 3.5 μm. However, the in vivo data showed a great variation

Models	In vivo A	In vivo B	Ex vivo A	Ex vivo B
TensorCylinder	1.36×10^{-6}	3.4×10^{-7}	1.98×10^{-6}	1.85×10^{-6}
ZeppelinCylinderDot	2.6×10^{-6}	4.2×10^{-6}	4.3×10^{-6}	3.5×10^{-6}
TensorCylinderAstrosticks	3.2×10^{-6}	1×10^{-7}	1.82×10^{-6}	1.83×10^{-6}
ZeppelinCylinderAstrocylinders	2.18×10^{-6}	4.4×10^{-6}	1.95×10^{-6}	1.7×10^{-6}
TensorCylinderAstrocylinders	2.06×10^{-6}	3.9×10^{-6}	1.85×10^{-6}	1.57×10^{-6}
ZeppelinCylinderSphere	1.09×10^{-6}	3.66×10^{-6}	2.1×10^{-6}	1.8×10^{-6}
TensorCylinderSphere	1.9×10^{-6}	4.07×10^{-6}	1.95×10^{-6}	1.74×10^{-6}

Table 6.4: *Table comparing in vivo and ex vivo results for the radius estimates from a selection of two- and three-compartment models for both datasets.*

in the radius estimate between the models. The values for R varied from 0.1 μm to 5.3 μm. Also, the radius estimate from the "GDRCylinders" in the ex vivo data is in good agreement with the "cylinders" model, whereas there is no clear agreement in the in vivo data. For more details see Section 5.3.2.

6.3.2.3 Conclusions

One of the main effects we observe in the in vivo data is the low estimation of the intra-axonal volume fraction f_1 from many of the models. This results in the instability of the axon radius estimation because the signal from which the radius is estimated directly depends on the intra-axonal volume fraction. The effect becomes more obvious and frequent with the addition of the third compartment. Even though the three-compartment models are ranked the highest, as in the ex vivo data, their estimates of f_1 are very low and R is not as often reasonable as in the ex vivo data. Considering the two-compartment models, the "TensorCylinder" model provides sensible estimates for f_1, R and $d_{\|}$, however, due to its complexity it is ranked poorly. Regarding the three-compartment models, the "astrocylinders" and the "sphere" models give slightly higher estimates for f_1 and more frequently sensible estimates for R, when combined with the extra-axonal "tensor" and "zeppelin" and intra-axonal "cylinder" model. The models which provide sensible estimates for the in vivo data are presented in Table 6.4. It is also apparent that the noise reduction algorithm biased the fitting procedure and estimated R higher, almost double from the estimated value in dataset A (except from the "TensorCylinder" and "TensorCylinderAstrosticks").

Finally, all the two-and three-compartment models recover the principal fibre direction, as well as S_0. Compared to the ex vivo data we see some dependency of the diffusivity $d_{\|}$ on the third compartment. The two-compartment models estimate $d_{\|}$ the lowest compared to when we add the isotropic restriction models. This happens because the two-compartment models estimate the diffusivity accounting only for the contribution from the axons, whereas in biological systems, the other cellular structures surrounding the axons contribute as well. Thus the three-compartment models provide higher values for $d_{\|}$ that are potentially more representative of a biological system.

6.3.3 Synthesis and fitting

Figure 6.2 visualises the fit of the data synthesised from the DT and the bitensor model to the scan data. Figure 6.3 presents data synthesised from the simplified version of CHARMED (ZeppelinCylinder), CHARMED (TensorGDRCylinders) and the MMWMD model (ZeppelinCylinderDot). Figure 6.4 shows the best two- and three-compartment models and the worst performing model for each of the

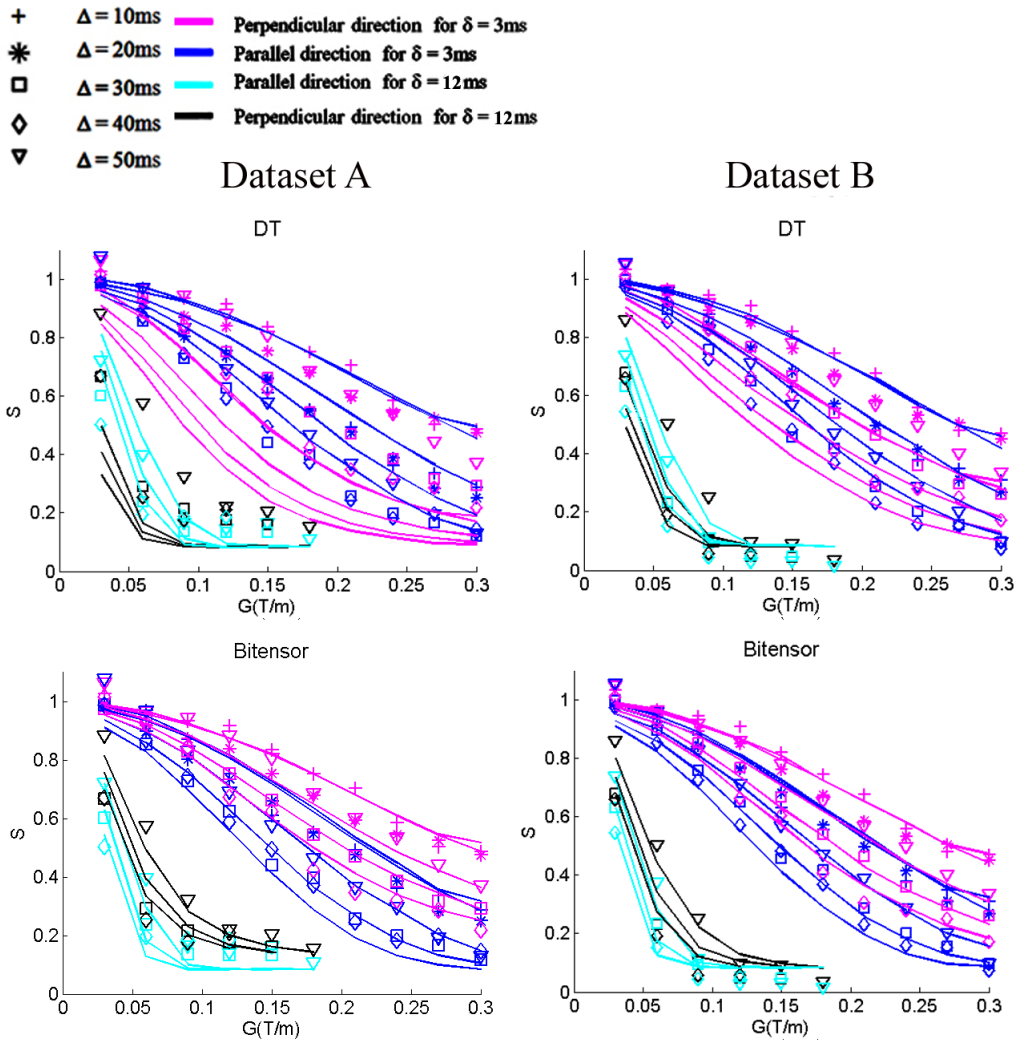

Figure 6.2: *Results of data synthesised from the DT, the bitensor model and the scan data from the in vivo experiment for both datasets. The normalised signal S is plotted for all the values of* Δ, δ *as a function of the gradient strength* $|\boldsymbol{G}|$ *for the parallel and the mean of the three perpendicular directions.*

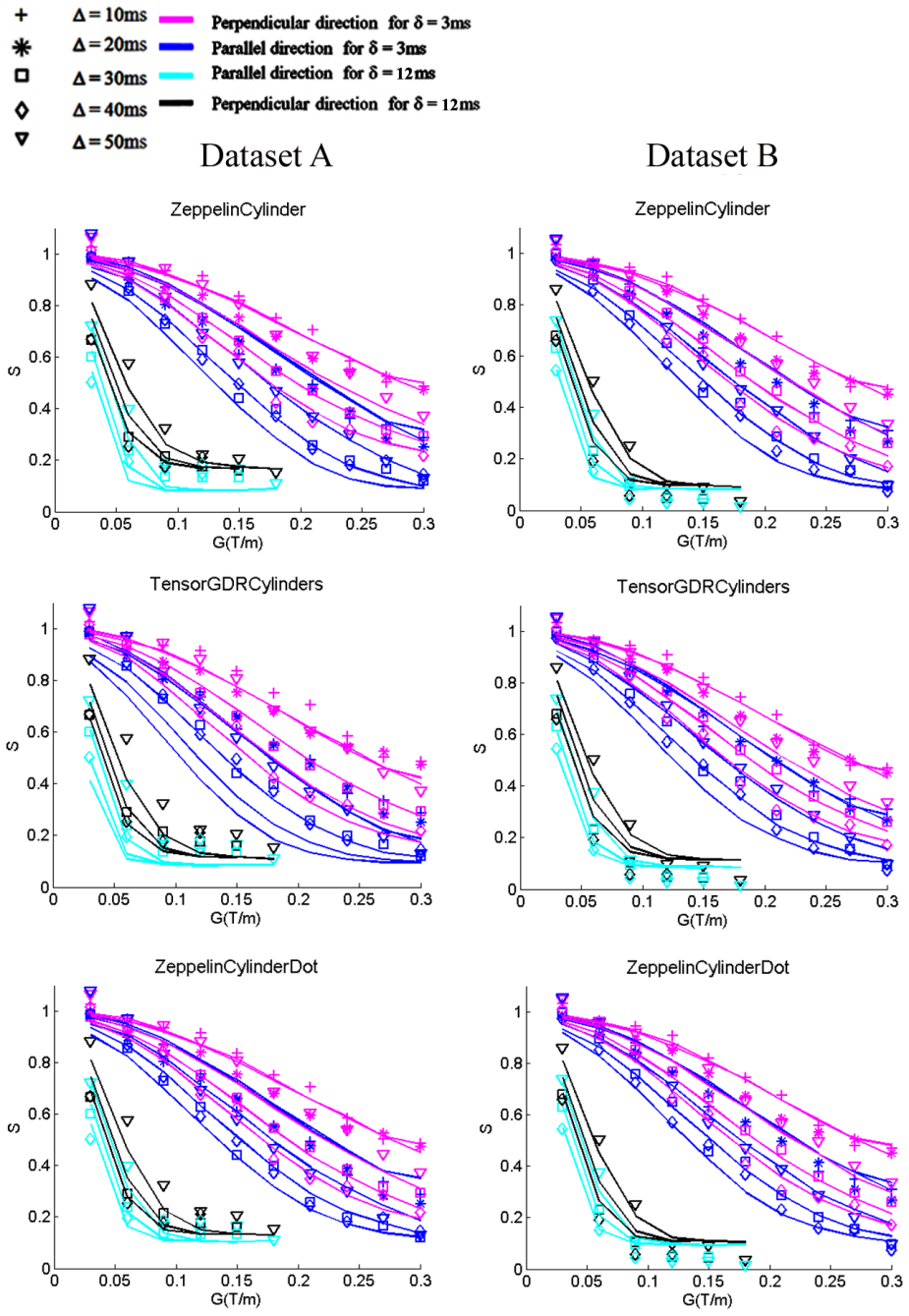

Figure 6.3: *Results of data synthesised from the simplified version of CHARMED (ZeppelinCylinder), CHARMED (TensorGDRCylinders), the MMWMD model (ZeppelinCylinderDot) and the scan data from the MRI experiment for both data sets. The normalised signal S is plotted for all the values of* Δ, δ *as a function of the gradient strength* $|\boldsymbol{G}|$ *for the parallel and the mean of the three perpendicular directions.*

Models	N^o of Multiruns for $P > 0.99$, A	N^o of Multiruns for $P > 0.99$, B
BallStick	2	3
Bitensor	8	8
ZeppelinCylinder	4	8
ZeppelinGDRCylinders	4	21
TensorCylinder	13	8
TensorGDRCylinders	21	6
ZeppelinStickDot	6	2
ZeppelinStickAstrosticks	6	2
ZeppelinCylinderDot	12	4

Table 6.5: *Table indicating the number of runs required to obtain the best solution in each model with probability $P > 0.99$ for dataset A and B.*

datasets. In all figures, the symbols represent the scan data, and the lines show the corresponding measurements predicted by each model with the fitted parameters. To account for possible offsets that can arise from Rician noise, the plots actually show the mean signals over 500 trials adding independent Rician noise at approximately the level in the scan data. However, this procedure only significantly affects measurements with very low signal. For clarity we compare data synthesised from the analytical models by plotting the signal S only for selected values of Δ and δ as a function of the gradient strength $|\mathbf{G}|$ for the parallel and perpendicular directions.

6.3.3.1 Comparison between dataset A and B

In Figure 6.2 the DT model shows a significant departure from the scan data in both directions, predicting the parallel and perpendicular signals reversed. In contrast, the "Bitensor" model captures the broad trends of the data. In Figure 6.3 the "ZeppelinCylinder", "TensorGDRCylinder" and the three-compartment "ZeppelinCylinderDot" models capture the trends of the data as well. However, there is no apparent improvement due to the addition of the third compartment over the two-compartment models.

In Figure 6.4, we show that the best two- and three-compartment models capture the broad trends of the data and it is difficult to distinguish the variations that improve the three-compartment models over the two-compartment models.

6.3.3.2 Comparison with ex vivo findings

In both in vivo and ex vivo experiments, the DT model fails to describe the data correctly. In the ex vivo experiment we observe large departures from the data, whereas for the in vivo experiment, the model predicts the signals reversed. Also, in the ex vivo data the signal showed restriction in the parallel direction, which the two-compartment models fail to describe. The death of tissue and the fixation process changes the diffusion of water in tissue, increasing the contribution of an isotropic restricting compartment. The addition of the third compartment improved the ex vivo fitting, and the "dot" model captured this restriction the best. In the in vivo data, the signal does not show an obvious departure and therefore there is no clear improvement in the synthesis between two- and three-compartment models.

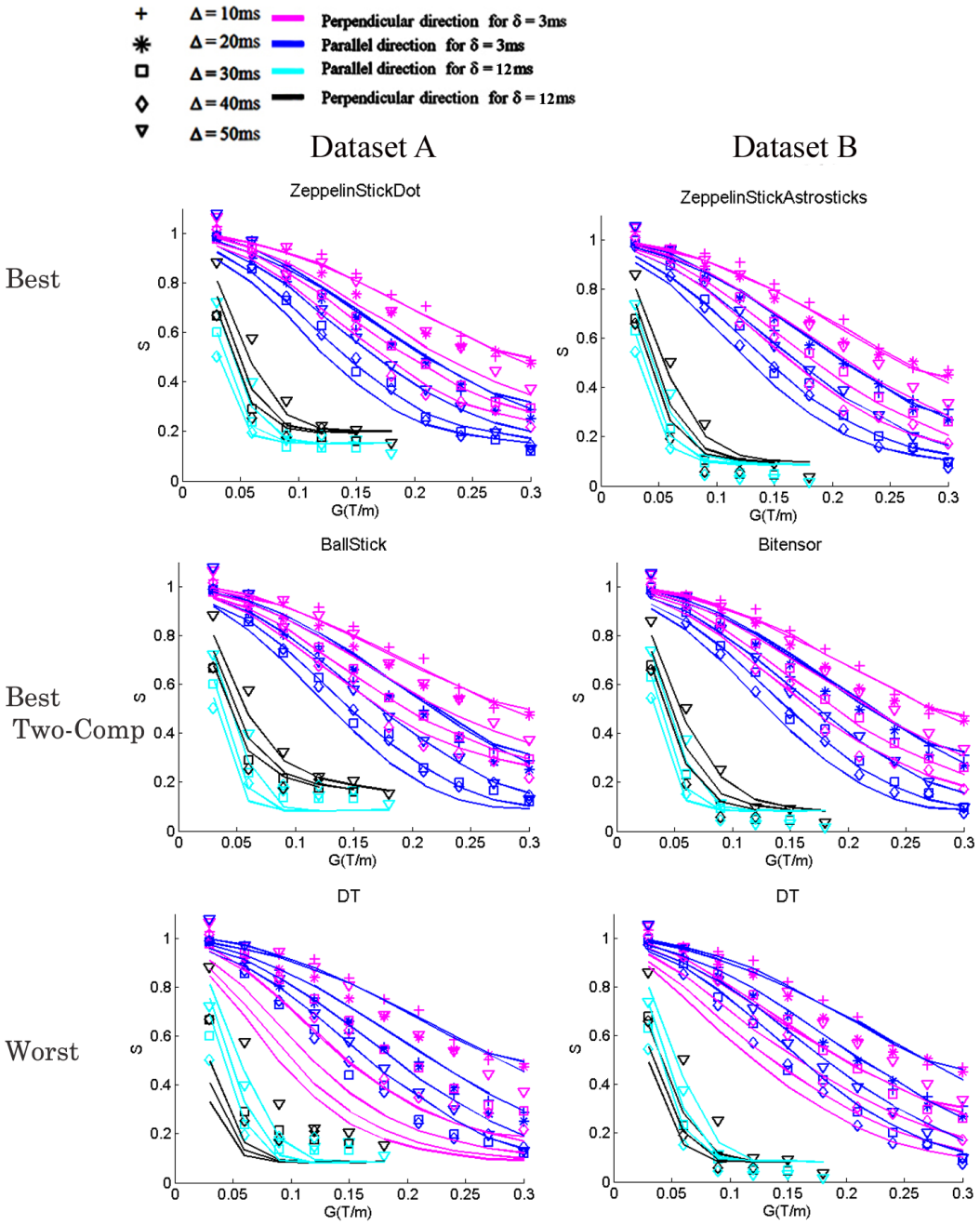

Figure 6.4: *Results of data synthesised from the best and worst performing models, and the scan data from the MRI experiment for both data sets. The normalised signal S is plotted for values of Δ, δ as a function of the gradient strength $|\boldsymbol{G}|$ for the parallel and the mean of the three perpendicular directions.*

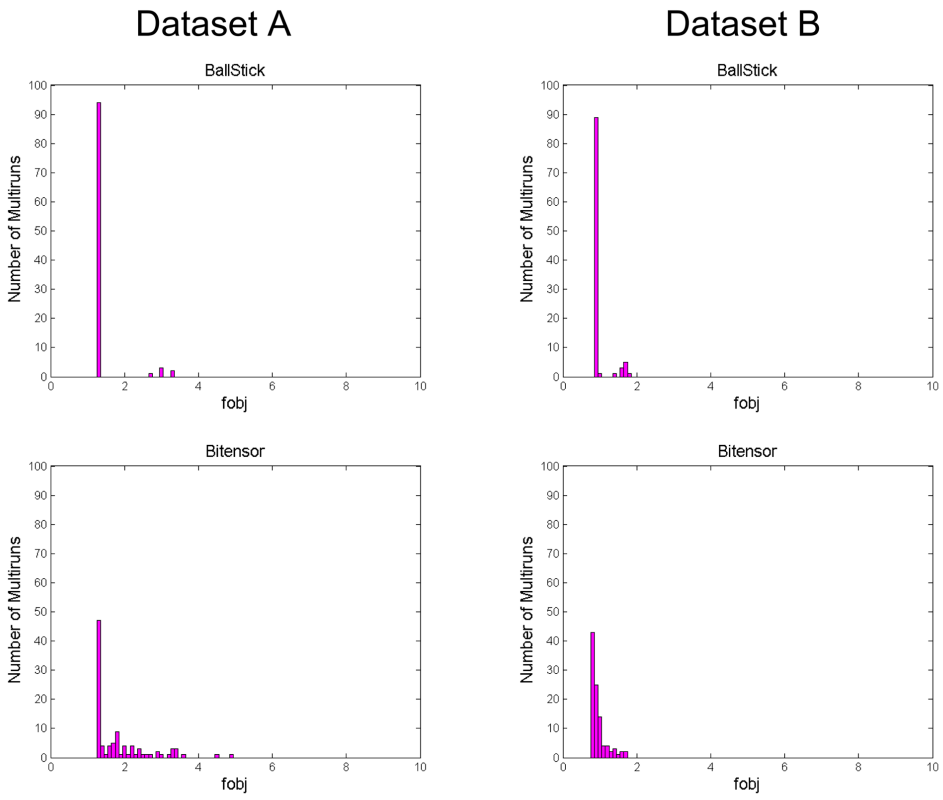

Figure 6.5: *Histograms of the objective function of 100 multiruns for the best two-compartment models comparing results from datasets A and B.*

6.4 Stability

To evaluate the stability of the models we compute a histogram of the objective function for 100 perturbations of the starting parameters. Figure 6.6 shows histograms for a selection of the key two-compartment models and Figure 6.7 shows histograms for a selection of three-compartment models. In both figures we compare results from the MRI scan data (dataset A) and the noise corrected data (dataset B). In Table 6.5 we indicate the number of multiruns required for each of these models to ensure obtaining the lowest objective function with probability $P > 0.99$.

6.4.1 Comparison between dataset A and B

Figure 6.6 shows that the data without the noise correction obtain the minimum objective function more frequently than the noise-corrected data. The only exception is the "TensorGDRCylinders" model. Figure 6.7 shows that for the three-compartment models the noise correction improves the frequency of obtaining the minimum objective function in all the models. However this is not reliable, since as we mentioned earlier the noise correction disrupts the fitting of the three-compartment models. Table 6.5 shows that the "BallStick" model requires a very small number of multiruns in contrast with the "Bitensor" model. The "ZeppelinCylinder" is one of the most stable models for dataset A. The most demanding model for the same dataset is the "TensorGDRCylinders" model, whereas for dataset B it is the "ZeppelinGDRCylinders" model.

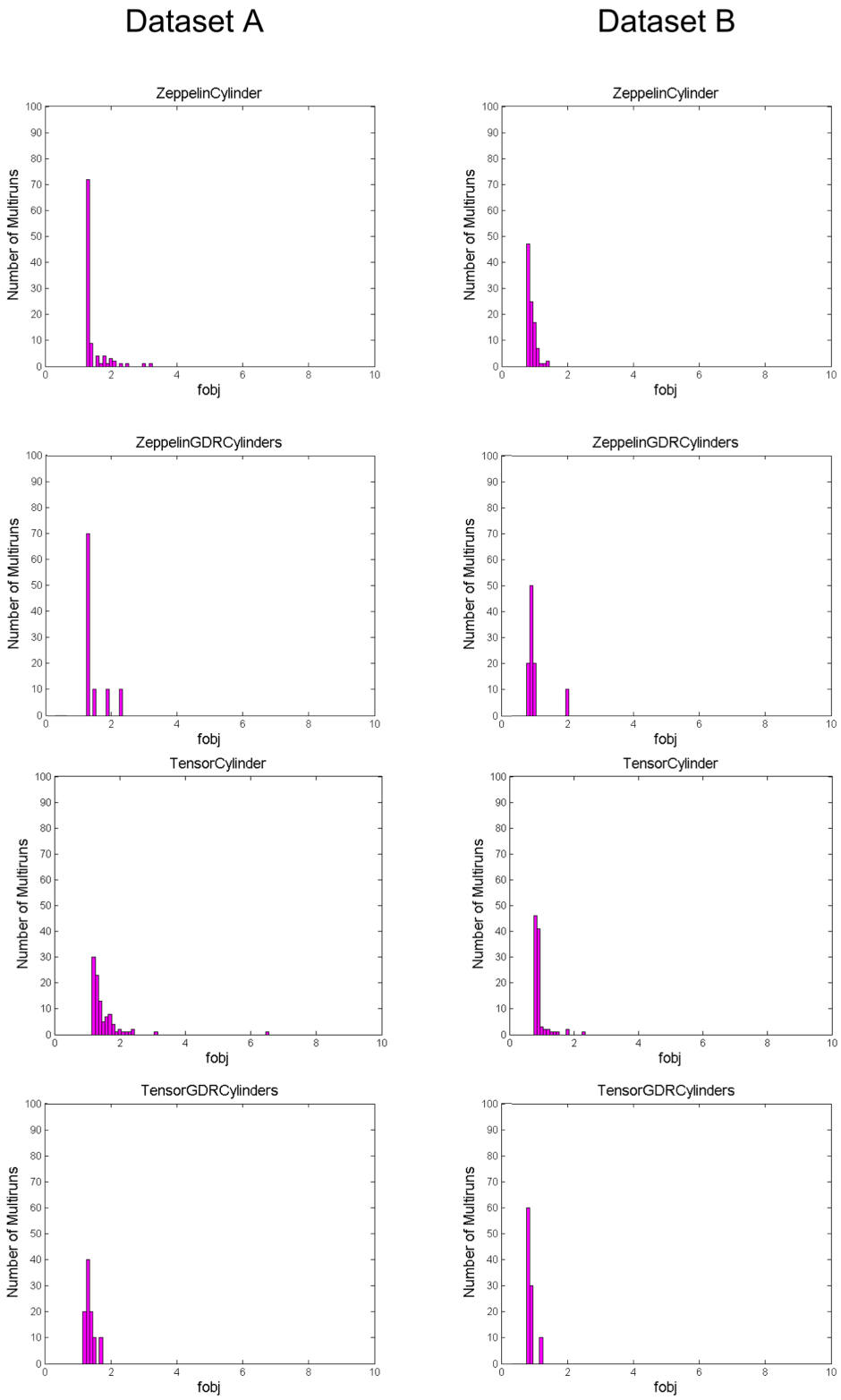

Figure 6.6: *Histograms of the objective function of 100 multiruns for a selection of the key two-compartment models comparing results from datasets A and B.*

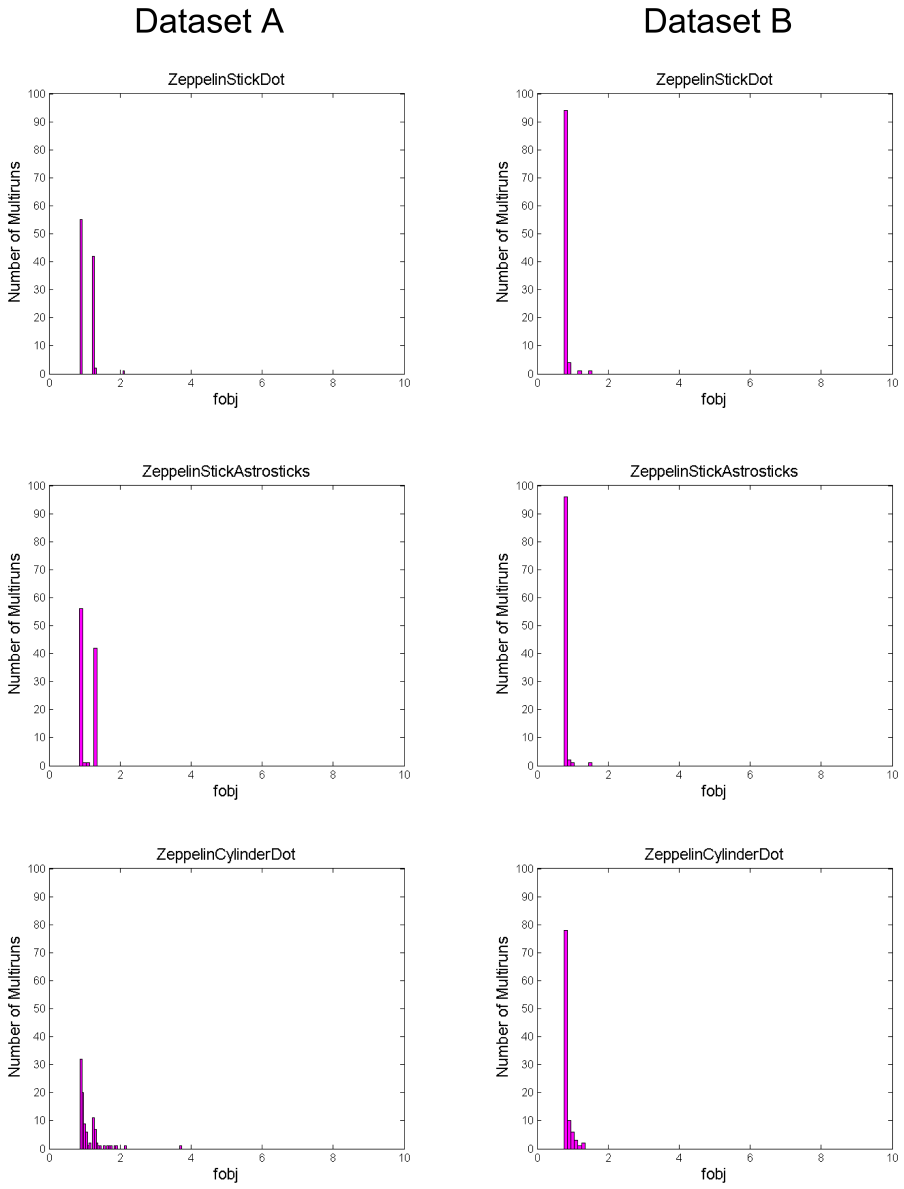

Figure 6.7: *Histograms of the objective function of 100 multiruns for a selection of the key three-compartment models comparing results from datasets A and B.*

6.4.2 Comparison with ex vivo findings

The main observation from the ex vivo experiment regarding the quality of the fit was the stability of the extra-axonal "cylinder" model over the "GDRCylinders" model. In the in vivo data however, we do not see the effect so vividly. The "cylinder" model still produces the minimum objective function more frequently than the "GDRCylinders" model, but the differences are smaller than in the ex vivo data. Table 6.5 shows that the "BallStick" and "ZeppelinCylinder" model for dataset A are the most stable models for both ex vivo and in vivo experiments.

6.5 Discussion and Conclusions

This work compared and evaluated two- and three-compartment models for the diffusion-weighted MRI signal in in vivo brain white matter, demonstrated on a rat's corpus callosum. Previous studies use only one model to extract microstructural estimates. Here we test 47 analytic models in vivo, including well-used analytic models from the literature. Previous studies which use complex analytic models with many parameters fix some of the model parameters when fitting models to diffusion data for stability. Here we do not fix any of the parameters and reveal how these complex models behave in vivo. We also test the analytic models with two datasets, one with the scan data (dataset A) and one that compensates for Rician noise (dataset B).

The results from fitting the models to the in vivo data using the BIC showed that the best two-compartment model for dataset A is the "BallStick" model, and for dataset B the "Bitensor" model. The best performing multi-compartment model was the "ZeppelinStickDot" model, which minimised the BIC for dataset A, while the "ZeppelinStickAstrosticks" was the best model for dataset B. Very closely ranked was the "ZeppelinCylinderDot" for dataset A and the "TensorCylinderSphere" for dataset B, which additionally provide a sensible estimate for the radius R. The worst performing model for both datasets is the DT.

This study revealed differences in microstructural parameter estimates from the analytical models between the in vivo and ex vivo measurements. In the ex vivo experiment all of the radius estimates were approximately 2μm. In the in vivo experiment we observed a larger variation of radius estimates among the different models. However, the "cylinder" models combined with full or cylindrically symmetric tensors and all the third compartment models agreed in the radius estimates with our ex vivo findings, as demonstrated in Table 6.4. The simple DT model could not adequately explain the data in both the ex vivo and in vivo experiments, and was ranked at the bottom of the taxonomy, showing the importance of restriction.

As expected, in the in vivo experiment all the models estimated the parallel diffusivity higher than the ex vivo experiment by about an order of magnitude. The best performing intra-axonal model for the ex vivo experiment was the "GDRCylinders". However, the comparison and evaluation of the taxonomy in vivo ranked the model low, heavily penalising the extra number of parameters. Overall the third compartment was favoured both in vivo and ex vivo, ranking the isotropic restriction "dot" model at the top. In the ex vivo experiment, the best "dot" model was combined with the intra-axonal "GDRCylinders". However, in the in vivo experiment, the intra-axonal "stick" performed the best, followed closely by the "cylinder" model which provided a sensible estimate for the axon radius.

Additionally, in the ex vivo studies we observed clear departures from Gaussian displacements along the fibre direction, as in previous studies [SSWH97, PFS+09]. However, the effect in the in vivo data is much less prominent than the ex vivo data, in agreement with Alexander et al. [AHH+10]. One possible explanation is the different gradient durations δ in the ex vivo and in vivo imaging protocols. The departure in the parallel direction in the ex vivo protocol occurs when $\delta = 30$ ms, whereas in the in vivo data the longest δ is 12 ms. The most likely explanation for not observing this phenomenon in vivo,

which also contributes towards the difference in the microstructural estimates, arises from the fixation process and the death of the tissue [WWV+09].

A crucial difference between the in vivo and ex vivo studies that potentially contributes to the discrepancy in the ranking of the models and their microstructural estimates is the use of different pulse sequences. In the ex vivo PGSE experiment the effects of the imaging gradients are small and can be neglected, whereas in the in vivo experiment with the stimulated echo sequence the imaging gradients can contribute significantly to the diffusion-weighting affecting the signal.

However, there are several limitations in this work. All the limitations we discuss in Section 5.4 for the ex vivo experiment apply here as well. These limitations regard refining the tissue modelling and a more appropriate fitting procedure to account for the Rician noise bias. Also there is no histology for comparison and evaluation of the microstructural estimates for both the ex vivo and in vivo experiments. For this in vivo experiment it would be interesting to add a CSF compartment to account for CSF contamination due to the small volume of the CC structure as in [BBA09, AHH+10]. Also, effects like T_1 relaxation do not influence the signal in the PGSE sequence, however, T_1 decay is significant when using stimulated echo sequences. A T_1 parameter could be an important addition to the tissue model to account for different amounts of T_1 decay, when using stimulated echo sequences.

Future work will use more animals for this study. We would like to use at least two more animals to verify the findings we report here. We would also like to repeat the experiment estimating the microstructural parameters after 1000 multiruns instead of 100, to see if this would affect the resulting model ranking, and also constrain the intra-axonal volume fraction, for more stability, so that it stays within biologically feasible limits.

With future refinements and further evaluation, these models are likely to have great potential for in vivo application, as discussed in Section 5.4. In particular, we could use the models in the taxonomy to develop biomarkers, which can measure microstructure accurately. These markers would assist towards a better diagnosis and prognosis of diseases, as well as monitoring normal development. These models could also lead towards practical clinical applications by creating images using microstructural estimates, similar to FA maps. Finally, these models can be extended to represent different tissue types, such as grey matter.

Chapter 7

Conclusions

Over the last 15 years diffusion-weighted MRI (DW-MRI) has become popular because it provides a unique insight into brain tissue microstructure and connectivity. The technique has become an essential probe for highlighting and monitoring tissue microstructure changes in development and disease. The simplest and most commonly used model for relating the DW-MRI signal to diffusion in tissue is the diffusion tensor (DT) [BML94]. The model provides useful microstructural markers of tissue integrity such as fractional anisotropy (FA) and mean diffusivity (MD). However these indicators are vague and non-specific, because they are affected by many features of the microstructure.

To address this limitation, the recent trend in the diffusion MRI field [Ale08, AB05, BWJJ03, AHH$^+$10] is towards more direct microstructure imaging by fitting more descriptive models of tissue that relate specific parameters, such as cell size and density, directly to the signal. However, to trust the parameter estimates we obtain from fitting these models, we must ensure that they include all the important physiological parameters of the tissue that affect the signal. Also, questions remain about how well these microstructural indices from diffusion MRI reflect the actual tissue microstructure since it is difficult to obtain ground truth information.

Synthetic data is therefore an essential tool for developing, optimising, evaluating and comparing diffusion MRI techniques. Unlike scanner data, it comes with a ground truth, thereby allowing performance evaluation of methods within a controlled environment. Additionally, synthetic data may be adjusted to enable optimisation of analysis techniques for sensitivity under varying conditions to calibrate derived measures to known underlying microstructures.

The work in this thesis has developed and studied both analytic and numerical models of the diffusion MRI signal in brain white matter. The overarching goal of this work was to investigate which properties of the tissue and aspects of the diffusion process affect the diffusion signal we measure and incorporate them in a model. Chapter 3 explored the accurate representation of the structure of biological tissue by constructing a three-dimensional mesh model. Chapter 4 constructed a taxonomy of analytical models for the diffusion MRI signal in brain white matter. Chapter 5 used a selection of analytic models from the taxonomy to study the diffusion signal in fixed brain and derive microstructural indices. Chapter 6 used the same analytic models to investigate the diffusion signal in the live brain and derive microstructural indices.

This closing chapter summarises the work presented in this thesis. Firstly, the key findings and conclusions of each experiment are recounted, followed by the contributions related back to the research aims established in Chapter 1. Finally, we discuss potential directions for future work beyond the scope of this project.

7.1 Biological Phantom Experiment

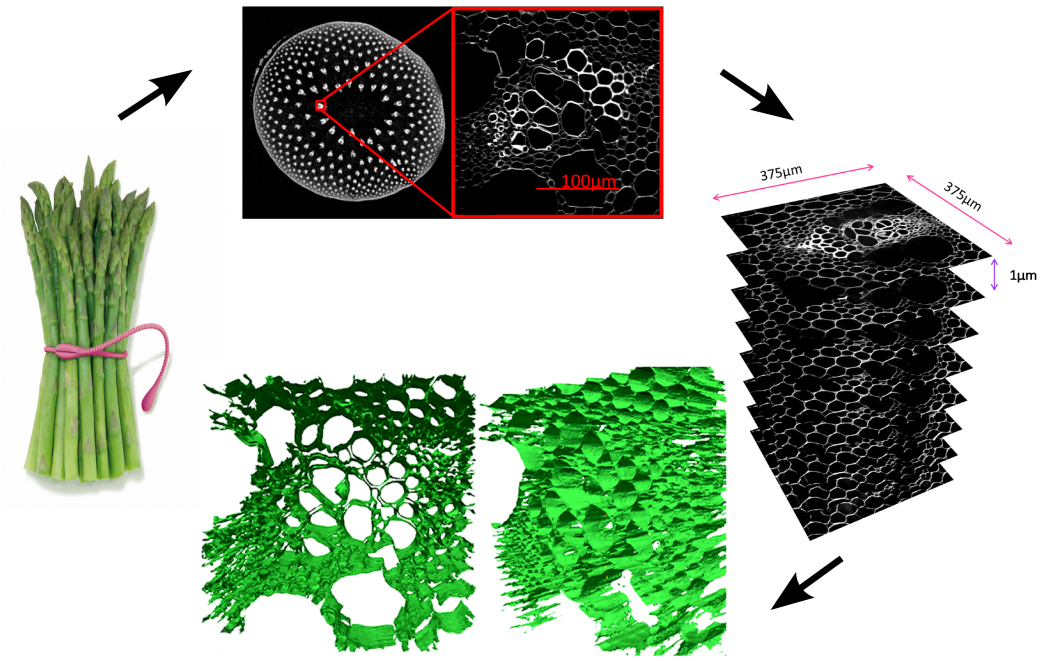

Figure 7.1: *The biological phantom experiment in Chapter 3.*

The first experiment, investigating the effect of an accurate representation of tissue in synthetic diffusion MRI data, was reported in Chapter 3. We created numerical models by introducing a method for constructing detailed tissue mesh models using confocal laser scanning microscopy (CLSM) images. We used these models to generate realistic diffusion MRI data by running Monte-Carlo diffusion simulations within the resulting meshes. To demonstrate the method we used a biological phantom (green asparagus), utilising a specifically designed acquisition protocol. Figure 7.1 summarises the experimental procedure of this chapter. We tested the simulated data from the three-dimensional mesh model against scan data, a simpler (extruded) mesh model and simulated measurements from simple parametric models.

Findings indicated that the mesh model correlates more closely with the data than the extruded mesh models and the parametric models. The agreement was more pronounced in the parallel direction where the three-dimensional mesh model captures part of the observed parallel restriction in a natural way.

7.2 Taxonomy of Analytic Models

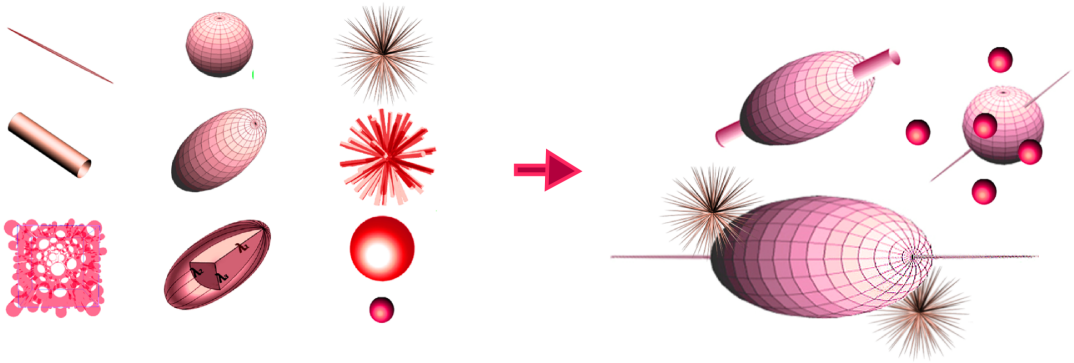

Figure 7.2: *The taxonomy of analytic models in Chapter 4.*

Chapter 4 studied analytic models of the diffusion MRI signal in brain white matter. Specifically, we considered multi-compartment models with no exchange, which model the signal as the sum of signals from water inside and outside cellular structures with impermeable cell walls. The models incorporate specific biological parameters, such as axon radius and axon density, to predict the diffusion MRI signal. We constructed a taxonomy of multi-compartment models of white matter from combinations of simple models for the intra- and extra-axonal spaces (see Figure 7.2). The study included well-known models from the literature, such as the ball and stick model [BWJJ03], CHARMED [AB05, ABKYB08], the simplified version of CHARMED in [Ale08] and the minimal model of white matter diffusion (MMWMD) in [AHH$^+$10], each of which uses different intra- and extra-axonal models.

The taxonomy accentuated the relationship between these widely-used models and revealed new models from previously untested combinations. Finally, the study provided a consistent naming system for all the models in the taxonomy. The models in the taxonomy are implemented in the open-source diffusion MRI toolkit Camino [CBNG$^+$06].

7.3 Ex vivo Brain Experiment

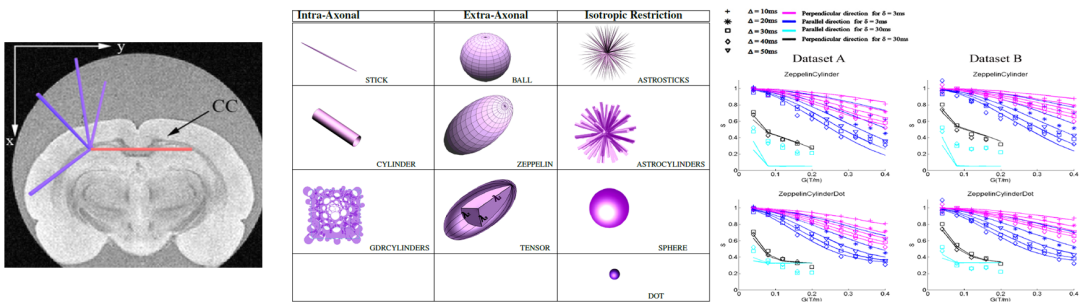

Figure 7.3: *The ex vivo brain tissue experiment in Chapter 5.*

The experiment reported in Chapter 5 sought to investigate the diffusion MRI signal in the fixed

brain (see Figure 7.3). We use a selection of multi-compartment models from the taxonomy, for testing and evaluation. We devised an imaging protocol for parallel and perpendicular measurements from the brain which allowed fitting and comparison of the models.

Results from studying the two-compartment models showed that it is important to include the axon radius in the analytic model and also, that anisotropy in the extra-axonal compartment gives slightly advantageous results. The key conclusion was that the effects of restriction are important for modelling the diffusion signal in ex vivo tissue. We observed a significant departure of the synthesised signals from the scan data in the parallel direction from all models. This is due to restriction in the parallel direction, possibly caused by non-parallel fibres, glial cells or the binding of water to cell walls. Finally, the model comparison showed that the addition of the third compartment to capture isotropic restriction significantly improved the fitting. The best performing model incorporated non-zero axon radius with a full tensor and a static third compartment for isotropic restriction which captured the observed departure in the data. The worst performing model was the DT, which was unable to capture the trends of the data. The models that provided the best approximation to the data with respect to histological studies, were the two-compartment models: 'ZeppelinCylinder", "TensorCylinder", "ZeppelinGDRCylinder", and the three-compartment models: "BallCylinderAstrosticks", the "BallGDRCylindersAstrosticks", "TensorGDRCylindersSphere".

7.4 In vivo Brain Experiment

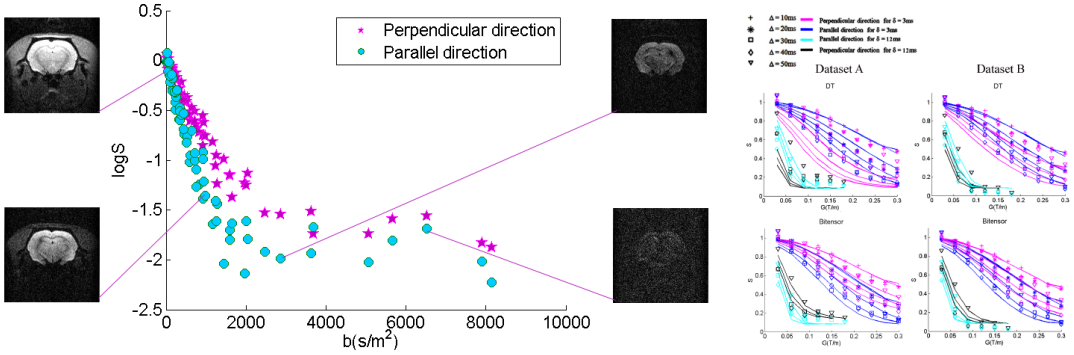

Figure 7.4: *The in vivo brain tissue experiment in Chapter 6.*

Chapter 6 presented the final experimental study which described a diffusion MRI experiment on a live rat utilising the analytic models previously used for the ex vivo MRI experiment (see Figure 7.4). The aim of this experiment was to find a model that describes the in vivo diffusion measurements and investigate the variation of microstructure parameter estimates and appropriate model choice between in vivo and ex vivo brain measurements.

The results support the addition of the third compartment to the model as in the ex vivo experiment. However, the improvement to the fitting is not as obvious in vivo, since the observed restriction in the parallel direction is not as prominent as in the ex vivo data. Concerning the ranking of the models, we observe a different trend in the taxonomy in vivo, where the zero radius intra-axonal compartments are

favoured over the more complex non-zero ones.

However, the model ranking presented in this chapter cannot be conclusive, since the data from the in vivo MRI acquisition was poor and affected by low SNR. Future work will repeat the model comparison with a larger sample of animals, using acquisition protocols optimized using the techniques developed by [Ale08].

7.5 Contributions

This thesis made the following key contributions:

- A technique for constructing high-fidelity mesh models that can accurately represent the structure of the biological tissue for synthesising realistic diffusion MRI data. In Chapter 3 we used confocal laser scanning microscopy images and computer graphics techniques to create a model of tissue with accurate morphology that allows the simulation of highly accurate synthetic data. The study explored different resolutions for the model as well as diffusion characteristics to identify which affect the diffusion signa the most. The mesh model was thoroughly tested against real MRI data and synthesised data from simpler but well-used models.

- A taxonomy of analytic models. In Chapter 4 we built a taxonomy of multi-compartment models for the diffusion MRI signal within brain white matter tissue. For the first time we classified all the models in the literature, highlighting their relationships and unveiled a wide range of previously untested models. We also established a naming system and implemented the models in the open-source toolkit, Camino [CBNG+06].

- Imaging protocols for comparing and assessing both analytic and numerical models of the diffusion MR signal of varying complexity, depending on the biological sample. In the experimental Chapters 4, 5 and 6 we used extensive imaging protocols for a biological phantom (asparagus) and fixed and live brain tissue, each especially devised for the different relaxation times and microstructure features of the samples.

- Determination of the characteristics of the most representative models for live and fixed tissue. In Chapters 5 and 6 we fitted a range of multi-compartment models to ex vivo and in vivo data to obtain tissue microstructure estimates and identified which models follow the trends of the data most accurately. By comparison of the in vivo and ex vivo results we identified differences and similarities in the important observed effects in live and fixed samples.

7.6 Directions for Future Work

The findings of this research prompt many areas of further work. The numerical models we propose in Chapter 3 can be refined in a number of ways. The quality of the generated mesh depends heavily on the segmentation process and downsampling of the confocal images. So far we use a simple thresholding algorithm. We could improve the fidelity and smoothness of the mesh by using more sophisticated segmentation algorithms. To avoid downsampling while preserving the topology with the minimum number

of triangles we could use a meshing algorithm combined with decimation [SZL+92]. An important improvement for this work would be to validate the method using white matter tissue. We could create mesh models from different parts of the brain creating a library. The tissue models can include different fibre configurations, such as kissing, fanning and bending.

Regarding the analytic taxonomy of models, we could further increase the number of compartments and the complexity of the models to capture more effects, such as the variations described in Section 4.2. In the ex vivo data we observed a good agreement between the best ranked model and the data, however, in the in vivo data the agreement was reduced, suggesting that other effects have to be taken into account in our models. In addition we could expand the analytic model taxonomy to represent other types of tissue besides white matter, such as grey matter or even diseased tissue.

To further enhance the analytic models' microstructural parameter estimation, we could substitute the standard PGSE sequence with other diffusion-sensitive sequences, such as oscillating gradients [CS95, DPG03, DSA10], or twice-refocused spin echo sequences [RHWW03, CNH+09], which have shown promising results. Also we could optimise the imaging protocols to allow testing and assessment of the models using the ideas in [Ale08].

Future work could improve the current model fitting procedures. At the moment the fitting is based on the assumption of Gaussian noise. However, the noise on MRI measurements is Rician [Hen85]. Accounting for Rician noise would provide more unbiased and perhaps more stable microstructure estimates, especially in vivo. With respect to the model comparison procedure, we can investigate more elaborate methods for assessing the analytic models than the Bayesian information criterion, such as Bayesian model comparison [Mac03].

From an applications perspective, the numerical models described in detail in Chapter 3 can be used to test the feasibility of microstructural analysis techniques. They offer a simple and inexpensive validation since they can provide a known ground truth for methods that try to estimate microstructure parameters. Also they can be used instead of expensive MRI measurements to assess new acquisition protocols and sequences. Another possible application for these numerical models could be simulation of pathological symptoms and investigation of specific diseases. Finally, Monte-Carlo simulations can be used with the three-dimensional mesh models to investigate subtle effects such as permeability and surface-particle interactions that simple parametric models of the signal generally ignore. The microstructural parameters estimated from the models can be used to create images in a similar way to FA images, using for example the volume fraction or the radius of the intra-axonal compartment.

Finally, this work concentrates on modelling brain white matter tissue, however, the general modelling and model comparison framework can be extended to other types of tissue, such as grey matter, and pathological changes that occur in different brain diseases.

Appendices

Appendix A

Publications

The following publications, all appearing in peer-reviewed international conferences, are presented in chronological order according to date of publication. Where appropriate, the section in this thesis corresponding to the work presented in the publication is referenced.

Panagiotaki, E., Fonteijn, H., Siow, B., Hall, M.G., Price, A., Lythgoe, M.F., Alexander, D.C. (2009). Two-compartment models of the diffusion MR signal in brain white matter.
Medical Image Computing and Computer Assisted Intervention (MICCAI) London: Springer, 1, 329-336 (2009)(ORAL, 32% acceptance, 5% oral)
Features extracts of work presented in Chapter 4, 5.

Panagiotaki, E., Fonteijn, H.M., Nedjati-Gilani, S., Hall, M.G., Alexander, D.C. (2009). Exploring analytic models of the diffusion MR signal in fixed rat brain tissue.
Proceedings of the 17th meeting of the International society for magnetic resonance in medicine, Hawaii, USA (2009)
Features extracts of work presented in Chapter 4, 5.

Panagiotaki, E., Hall, M.G., Zhang, H., Siow, B., Lythgoe, M.F., Alexander, D.C. (2010). High-fidelity meshes from tissue samples for diffusion MRI simulations.
Medical Image Computing and Computer Assisted Intervention (MICCAI) China: Springer (2010)(accepted, 32% acceptance)
Features extracts of work presented in Chapter 4, 5.

Panagiotaki, E., Hall, M.G., Siow, B.,Lythgoe, M.F., Alexander, D.C. (2010). Three-dimensional models of tissue microstructure for simulating high-precision diffusion MRI data.
Proceedings of the 18th meeting of the International society for magnetic resonance in medicine, Stockholm, Sweden (2010)
Features extracts of work presented in Chapter 3.

Panagiotaki, E., Hall, M.G., Siow, B.,Lythgoe, M.F., Alexander, D.C. (2010). Three-dimensional model construction from confocal microscopy images.
British Machine Vision Association symposium on 'Microscopy Image Analysis for Biomedical Appli-

cations', London, UK (2010)(ORAL)

Features extracts of work presented in Chapter 3.

Panagiotaki, E., Schneider, T., Hall, M.G., Siow, B.,Lythgoe, M.F., Alexander, D.C. (2011). A hierarchy of analytic models for the diffusion MRI signal in brain white matter.

Proceedings of the 19th meeting of the International society for magnetic resonance in medicine, Montreal, Canada (2011) (submitted)

Features extracts of work presented in Chapter 5.

Appendix B

Tables with ex vivo microstructural estimates

Models	Startpoint		Best Estimates		FOBJ	
	dataset A	dataset B	dataset A	dataset B	dataset A	dataset B
DT	-	-	$d_{\parallel}$=2.494×10^{-11} $d\perp_1$= 1.781×10^{-11} $d\perp_2$=1.660×10^{-11} θ=1.573 ϕ=4.712	$d_{\parallel}$=1.852×10^{-11} $d\perp_1$= 1.734×10^{-11} $d\perp_2$=1.394×10^{-11} θ=1.570 ϕ=-1.570	14.901	10.832
Bitensor	S_0=1 f_1=0.526 f_2=0.473 $d_{\parallel}$=3.394×10^{-10} θ=1.509 ϕ=-4.753 $d\perp_{1a}$=3.394×10^{-10} $d\perp_{1b}$=5.111×10^{-12}	S_0=1 f_1=0.423 f_2=0.576 $d_{\parallel}$=2.847×10^{-10} θ=4.594 ϕ=-1.624 $d\perp_{1a}$=2.846×10^{-10} $d\perp_{1b}$=5.122×10^{-12}	S_0=0.985 f_1=0.522 f_2=0.477 $d_{\parallel}$=3.415×10^{-10} θ=1.499 ϕ=-4.763 $d\perp_{1a}$=3.415×10^{-10} $d\perp_{1b}$=4.775×10^{-12}	S_0=0.987 f_1=0.433 f_2=0.566 $d_{\parallel}$=2.891×10^{-10} θ=4.592 ϕ=-1.607 $d\perp_{1a}$=2.880×10^{-10} $d\perp_{1b}$=5.211×10^{-12}	1.137	1.137
BallStick	S_0=1 f_1=0.439 f_2=0.560 $d_{\parallel}$=3.238×10^{-11} θ=1.676 ϕ=4.617	S_0=1 f_1=0.522 f_2=0.477 $d_{\parallel}$=2.747×10^{-11} θ=1.394 ϕ=-1.624	S_0=0.985 f_1=0.442 f_2=0.557 $d_{\parallel}$=3.276×10^{-11} θ=1.675 ϕ=-1.673	S_0=0.988 f_1=0.522 f_2=0.478 $d_{\parallel}$=2.747×10^{-11} θ=1.395 ϕ=-1.625	1.188	1.056
ZeppelinStick	S_0=1 f_1=0.422 f_2=0.577 $d_{\parallel}$=3.375×10^{-10} θ=1.477 ϕ=1.478 $d\perp_1$=3.010×10^{-10}	S_0=1 f_1=0.477 f_2=0.522 $d_{\parallel}$=2.891×10^{-10} θ=1.718 ϕ=-1.528 $d\perp_1$=2.219×10^{-10}	S_0=0.983 f_1=0.422 f_2=0.577 $d_{\parallel}$=3.375×10^{-10} θ=1.664 ϕ=-1.663 $d\perp_1$=3.010×10^{-10}	S_0=0.985 f_1=0.477 f_2=0.522 $d_{\parallel}$=2.891×10^{-10} θ=1.718 ϕ=-1.526 $d\perp_1$=2.219×10^{-10}	1.179	1.179
TensorStick	S_0=1 f_1=0.402 f_2=0.598 $d_{\parallel}$=3.428×10^{-10} θ=1.484 ϕ=1.506 $d\perp_1$=3.428×10^{-10} $d\perp_2$=2.239×10^{-11} α=22.774	S_0=1 f_1=0.466 f_2=0.533 $d_{\parallel}$=2.877×10^{-10} θ=1.712 ϕ=-1.557 $d\perp_1$=2.862×10^{-10} $d\perp_2$=1.541×10^{-11} α=3.778	S_0=0.982 f_1=0.399 f_2=0.600 $d_{\parallel}$=3.439×10^{-10} θ=1.488 ϕ=1.505 $d\perp_1$=3.439×10^{-10} $d\perp_2$=2.215×10^{-10} α=-143.72	S_0=0.985 f_1=0.466 f_2=0.533 $d_{\parallel}$=2.877×10^{-10} θ=1.712 ϕ=-1.557 $d\perp_1$=2.862×10^{-10} $d\perp_2$=1.541×10^{-11} α=3.778	1.079	0.922
BallCylinder	S_0=1 f_1=0.503 f_2=0.497 $d_{\parallel}$=3.386×10^{-10} θ=1.6205 ϕ=4.666 R=2.060×10^{-6}	S_0=1 f_1=0.594 f_2=0.405 $d_{\parallel}$=2.860×10^{-10} θ=1.447 ϕ=-1.608 R=1.938×10^{-6}	S_0=1.001 f_1=0.503 f_2=0.497 $d_{\parallel}$=3.392×10^{-10} θ=1.625 ϕ=1.621 R=2.044×10^{-6}	S_0=0.990 f_1=0.594 f_2=0.405 $d_{\parallel}$=2.860×10^{-10} θ=1.447 ϕ=-1.608 R=1.938×10^{-6}	1.090	0.947
ZeppelinCylinder	S_0=1 f_1=0.503 f_2=0.496 $d_{\parallel}$=3.392×10^{-10} θ=1.516 ϕ=1.519 R=2.045×10^{-6} $d\perp_1$=3.392×10^{-10}	S_0=1 f_1=0.565 f_2=0.434 $d_{\parallel}$=2.908×10^{-10} θ=1.454 ϕ=-1.605 R=1.880×10^{-6} $d\perp_1$=2.551×10^{-10}	S_0=0.986 f_1=0.503 f_2=0.496 $d_{\parallel}$=3.392×10^{-10} θ=1.516 ϕ=1.519 R=2.045×10^{-6} $d\perp_1$=3.392×10^{-10}	S_0=0.988 f_1=0.565 f_2=0.434 $d_{\parallel}$=2.908×10^{-10} θ=1.687 ϕ=-1.535 R=1.880×10^{-6} $d\perp_1$=2.551×10^{-10}	1.090	0.941
TensorCylinder	S_0=1 f_1=0.465 f_2=0.534 $d_{\parallel}$=3.564×10^{-10} θ=1.577 ϕ=1.589 R=2.056×10^{-6} $d\perp_1$=3.564×10^{-10} $d\perp_2$=2.338×10^{-10} α=22.777	S_0=1 f_1=0.540 f_2=0.459 $d_{\parallel}$=2.957×10^{-10} θ=1.477 ϕ=-1.583 R=1.894×10^{-6} $d\perp_1$=2.945×10^{-10} $d\perp_2$=1.649×10^{-10} α=3.756	S_0=0.985 f_1=0.457 f_2=0.542 $d_{\parallel}$=3.520×10^{-10} θ=1.569 ϕ=1.572 R=1.986×10^{-6} $d\perp_1$=3.520×10^{-10} $d\perp_2$=2.353×10^{-10} α=51.013	S_0=0.987 f_1=0.532 f_2=0.467 $d_{\parallel}$=2.948×10^{-10} θ=1.478 ϕ=-1.583 R=1.854×10^{-6} $d\perp_1$=2.946×10^{-10} $d\perp_2$=1.660×10^{-10} α=-52.814	1.004	0.850
BallGDRCylinders	S_0=1 f_1=0.584 f_2=0.415 k = 1.968 ϑ = 1.202×10^{-6} $d_{\parallel}$=3.440×10^{-10} θ=1.523 ϕ=1.525	S_0=1 f_1=0.696 f_2=0.303 k = 1.019 ϑ = 3.130×10^{-6} $d_{\parallel}$=2.928×10^{-10} θ=1.459 ϕ=-1.604	S_0=1.192 f_1=0.752 f_2=0.247 k = 3.146 ϑ = 7.01×10^{-7} $d_{\parallel}$=3.430×10^{-10} θ=1.523 ϕ=1.526	S_0=1.091 f_1=0.689 f_2=0.310 k = 0.999 ϑ = 2.982×10^{-6} $d_{\parallel}$=2.933×10^{-10} θ=1.459 ϕ=-1.603	1.091	0.939
ZeppelinGDRCylinders	S_0=1 f_1=0.579 f_2=0.420 k = 0.935 ϑ = 2.949×10^{-6} $d_{\parallel}$=3.412×10^{-10} θ=1.508 ϕ=1.511 $d\perp_1$=3.304×10^{-10}	S_0=1 f_1=0.663 f_2=0.336 k = 1.621 ϑ = 1.491×10^{-6} $d_{\parallel}$=2.912×10^{-10} θ=1.460 ϕ=-1.604 $d\perp_1$=2.901×10^{-10}	S_0=1.139 f_1=0.608 f_2=0.391 k = 1.877 ϑ = 1.423×10^{-6} $d_{\parallel}$=3.443×10^{-10} θ=1.532 ϕ=1.532 $d\perp_1$=3.400×10^{-10}	S_0=1.0723 f_1=0.602 f_2=0.398 k = 1.334 ϑ = 1.622×10^{-6} $d_{\parallel}$=2.945×10^{-10} θ=1.534 ϕ=-1.588 $d\perp_1$=2.433×10^{-10}	1.085	0.930
TensorGDRCylinders	S_0=1 f_1=0.524 f_2=0.475 k = 1.114 ϑ = 2.198×10^{-6} $d_{\parallel}$=3.328×10^{-10} θ=1.558 ϕ=1.570 $d\perp_1$=3.320×10^{-10} $d\perp_2$=2.290×10^{-10} α=14.929	S_0=1 f_1=0.677 f_2=0.322 k = 1.868 ϑ = 1.456×10^{-6} $d_{\parallel}$=2.912×10^{-10} θ=1.610 ϕ=-1.563 $d\perp_1$=2.910×10^{-10} $d\perp_2$=1.930×10^{-10} α=0.575	S_0=1.078 f_1=0.574 f_2=0.426 k = 1.388 ϑ = 1.855×10^{-6} $d_{\parallel}$=3.547×10^{-10} θ=1.568 ϕ=1.575 $d\perp_1$=3.233×10^{-10} $d\perp_2$=2.488×10^{-10} α=0.744	S_0=1 f_1=0.566 f_2=0.434 k = 1.587 ϑ = 1.755×10^{-6} $d_{\parallel}$=2.977×10^{-10} θ=1.522 ϕ=-1.588 $d\perp_1$=2.894×10^{-10} $d\perp_2$=1.748×10^{-10} α=2.543	1	0.847

Table B.1: *Fitted parameters for the two-compartment models.*

Models	Startpoint		Best Estimates		FOBJ	
	dataset A	dataset B	dataset A	dataset B	dataset A	dataset B
BallStickDot	S_0=1 f_1=0.356 f_2=0.365 f_3=0.278 $d_\parallel$=6.542×10^{-10} θ=1.194 ϕ=4.877	S_0=1 f_1=0.438 f_2=0.254 f_3=0.306 $d_\parallel$=6.199×10^{-10} θ=1.156 ϕ=-1.757	S_0=1 f_1=0.369 f_2=0.342 f_3=0.287 $d_\parallel$=6.819×10^{-10} θ=1.984 ϕ=1.772	S_0=1 f_1=0.438 f_2=0.254 f_3=0.306 $d_\parallel$=6.199×10^{-10} θ=1.156 ϕ=-1.758	0.609	0.519
ZeppelinStickDot	S_0=1 f_1=0.142 f_2=0.533 f_3=0.323 $d_\parallel$=8.169×10^{-10} θ=1.242 ϕ=1.370 $d\perp_1$=2.9×10^{-10}	S_0=1 f_1=0.214 f_2=0.458 f_3=0.327 $d_\parallel$=6.620×10^{-10} θ=1.246 ϕ=-1.720 $d\perp_1$=2.258×10^{-10}	S_0=0.990 f_1=0.142 f_2=0.533 f_3=0.323 $d_\parallel$=8.166×10^{-10} θ=1.242 ϕ=1.370 $d\perp_1$=2.901×10^{-10}	S_0=0.992 f_1=0.214 f_2=0.458 f_3=0.327 $d_\parallel$=6.620×10^{-10} θ=1.246 ϕ=-1.720 $d\perp_1$=2.258×10^{-10}	0.438	0.362
TensorStickDot	S_0=1 f_1=0.298 f_2=0.422 f_3=0.278 $d_\parallel$=5.308×10^{-10} θ=1.190 ϕ=1.383 $d\perp_1$=5.305×10^{-10} $d\perp_2$=5.231×10^{-10} α=22.774	S_0=1 f_1=0.381 f_2=0.276 f_3=0.342 $d_\parallel$=6.929×10^{-10} θ=1.789 ϕ=-1.063 $d\perp_1$=6.551×10^{-10} $d\perp_2$=4.398×10^{-12} α=103.82	S_0=0.999 f_1=0.351 f_2=0.331 f_3=0.317 $d_\parallel$=7.501×10^{-10} θ=1.353 ϕ=1.0553 $d\perp_1$=7.43×10^{-10} $d\perp_2$=4.55×10^{-10} α=22.657	S_0=0.992 f_1=0.432 f_2=0.237 f_3=0.330 $d_\parallel$=7.703×10^{-10} θ=1.789 ϕ=-1.410 $d\perp_1$=7.647×10^{-10} $d\perp_2$=9.098×10^{-12} α=103.82	0.5800	0.4881
BallCylinderDot	S_0=1 f_1=0.510 f_2=0.177 f_3=0.311 $d_\parallel$=3.375×10^{-10} θ=1.477 ϕ=1.478 R=2.060×10^{-6}	S_0=1 f_1=0.535 f_2=0.142 f_3=0.321 $d_\parallel$=6.340×10^{-10} θ=1.272 ϕ=-1.746 R=3.786×10^{-6}	S_0=1.001 f_1=0.510 f_2=0.177 f_3=0.311 $d_\parallel$=7.480×10^{-10} θ=1.283 ϕ=1.308 R=4.502×10^{-6}	S_0=1 f_1=0.535 f_2=0.142 f_3=0.321 $d_\parallel$=6.340×10^{-10} θ=1.272 ϕ=-1.746 R=3.786×10^{-6}	0.385	0.308
ZeppelinCylinderDot	S_0=1 f_1=0.345 f_2=0.330 f_3=0.324 $d_\parallel$=8.304×10^{-10} θ=1.292 ϕ=1.309 R=4.313×10^{-6} $d\perp_1$=3.597×10^{-10}	S_0=1 f_1=0.392 f_2=0.281 f_3=0.326 $d_\parallel$=6.621×10^{-10} θ=1.290 ϕ=-1.729 R=3.513×10^{-6} $d\perp_1$=2.997×10^{-10}	S_0=0.996 f_1=0.345 f_2=0.330 f_3=0.324 $d_\parallel$=8.304×10^{-10} θ=1.292 ϕ=1.309 R=4.313×10^{-6} $d\perp_1$=3.597×10^{-10}	S_0=0.997 f_1=0.392 f_2=0.281 f_3=0.326 $d_\parallel$=6.619×10^{-10} θ=1.290 ϕ=-1.728 R=3.512×10^{-6} $d\perp_1$=2.994×10^{-10}	0.324	0.266
TensorCylinderDot	S_0=1 f_1=0.284 f_2=0.416 f_3=0.3 $d_\parallel$=7.07×10^{-10} θ=1.447 ϕ=1.537 R=3.95×10^{-6} $d\perp_1$=5.352×10^{-10} $d\perp_2$=2.651×10^{-10} α=22.777	S_0=1 f_1=0.336 f_2=0.363 f_3=0.299 $d_\parallel$=5.765×10^{-10} θ=1.403 ϕ=-1.608 R=3.267×10^{-6} $d\perp_1$=4.020×10^{-10} $d\perp_2$=1.901×10^{-10} α=0.65	S_0=0.996 f_1=0.283 f_2=0.415 f_3=0.3 $d_\parallel$=7.07×10^{-10} θ=1.700 ϕ=1.603 R=3.96×10^{-6} $d\perp_1$=5.35×10^{-10} $d\perp_2$=2.65×10^{-10} α=22.763	S_0=0.996 f_1=0.336 f_2=0.363 f_3=0.299 $d_\parallel$=5.765×10^{-10} θ=1.403 ϕ=-1.608 R=3.267×10^{-6} $d\perp_1$=4.020×10^{-10} $d\perp_2$=1.901×10^{-10} α=0.65	0.271	0.216
BallGDRCylindersDot	S_0=1 f_1=0.326 f_2=2.987×10^{-8} f_3=0.673 k=1.731 ϑ=1.274×10^{-6} $d_\parallel$=9.209×10^{-10} θ=1.576 ϕ=1.568	S_0=1 f_1=0.442 f_2=1.076×10^{-4} f_3=0.556 k=0.659 ϑ=2.348×10^{-6} $d_\parallel$=7.057×10^{-10} θ=1.501 ϕ=-1.594	S_0=1.114 f_1=0.732 f_2=1.94×10^{-8} f_3=0.267 k=1.718 ϑ=5.053×10^{-6} $d_\parallel$=7.415×10^{-10} θ=1.294 ϕ=1.348	S_0=1.122 f_1=0.729 f_2=0.017 f_3=0.252 k=1.238 ϑ=5.602×10^{-6} $d_\parallel$=6.097×10^{-10} θ=1.850 ϕ=-1.434	0.370	0.292
ZeppelinGDRCylindersDot	S_0=1 f_1=0.512 f_2=0.202 f_3=0.285 k=1.195 ϑ=1.054×10^{-6} $d_\parallel$=8.368×10^{-10} θ=1.289 ϕ=1.287 $d\perp_1$=9.153×10^{-11}	S_0=1 f_1=0.511 f_2=0.200 f_3=0.287 k=1.237 ϑ=8.266×10^{-6} $d_\parallel$=6.700×10^{-10} θ=1.283 ϕ=-1.645 $d\perp_1$=2.954×10^{-11}	S_0=1.113 f_1=0.483 f_2=0.229 f_3=0.286 k=1.870 ϑ=2.011×10^{-6} $d_\parallel$=8.164×10^{-10} θ=1.293 ϕ=1.318 $d\perp_1$=1.188×10^{-10}	S_0=1.114 f_1=0.529 f_2=0.187 f_3=0.283 k=1.124 ϑ=1.012×10^{-5} $d_\parallel$=6.555×10^{-10} θ=1.291 ϕ=-1.721 $d\perp_1$=3.476×10^{-11}	0.317	0.253
TensorGDRCylindersDot	S_0=1 f_1=0.529 f_2=0.201 f_3=0.268 k=1.621 ϑ=5.413×10^{-6} $d_\parallel$=6.774×10^{-10} θ=1.674 ϕ=1.579 $d\perp_1$=5.561×10^{-10} $d\perp_2$=1.185×10^{-10} α=19.658	S_0=1 f_1=0.555 f_2=0.184 f_3=0.263 k=1.557 ϑ=4.182×10^{-6} $d_\parallel$=5.612×10^{-10} θ=1.406 ϕ=-1.582 $d\perp_1$=4.533×10^{-10} $d\perp_2$=8.276×10^{-11} α=0.660	S_0=1.10 f_1=0.525 f_2=0.212 f_3=0.261 k=1.523 ϑ=5.971×10^{-6} $d_\parallel$=6.775×10^{-10} θ=1.688 ϕ=1.601 $d\perp_1$=5.544×10^{-10} $d\perp_2$=1.414×10^{-10} α=19.662	S_0=1.19 f_1=0.541 f_2=0.215 f_3=0.243 k=1.45 ϑ=3.526×10^{-6} $d_\parallel$=5.612×10^{-10} θ=1.407 ϕ=-1.599 $d\perp_1$=4.545×10^{-10} $d\perp_2$=1.49×10^{-10} α=0.651	0.270	0.214

Table B.2: *Fitted parameters for the three-compartment dot models.*

Models	Startpoint		Best Estimates		FOBJ	
	dataset A	dataset B	dataset A	dataset B	dataset A	dataset B
BallStickAstrosticks	S_0=1 f_1=0.265 f_2=3.3×10^{-9} f_3=0.735 $d_\parallel$=9.183×10^{-10} θ=1.611 ϕ=4.667	S_0=1 f_1=0.332 f_2=6.4×10^{-12} f_3=0.667 $d_\parallel$=6.632×10^{-10} θ=1.666 ϕ=-1.544	S_0=0.995 f_1=0.264 f_2=3.4×10^{-9} f_3=0.735 $d_\parallel$=9.182×10^{-10} θ=1.612 ϕ=1.617	S_0=0.995 f_1=0.331 f_2=5.647×10^{-12} f_3=0.668 $d_\parallel$=6.676×10^{-10} θ=1.664 ϕ=-1.544	0.595	0.514
ZeppelinStickAstrosticks	S_0=1 f_1=0.001 f_2=0.266 f_3=0.732 $d_\parallel$=9.187×10^{-10} θ=1.608 ϕ=1.608 $d\perp_1$=6.210×10^{-13}	S_0=1 f_1=7.358×10^{-5} f_2=0.337 f_3=0.662 $d_\parallel$=6.669×10^{-10} θ=1.484 ϕ=-1.598 $d\perp_1$=6.663×10^{-13}	S_0=0.9960 f_1=0.001 f_2=0.267 f_3=0.733 $d_\parallel$=9.187×10^{-10} θ=1.534 ϕ=1.534 $d\perp_1$=6.207×10^{-13}	S_0=0.995 f_1=1.273×10^{-6} f_2=0.337 f_3=0.662 $d_\parallel$=6.669×10^{-10} θ=1.657 ϕ=-1.546 $d\perp_1$=6.663×10^{-13}	0.595	0.5128
TensorStickAstrosticks	S_0=1 f_1=0.251 f_2=0.0905 f_3=0.657 $d_\parallel$=8.097×10^{-10} θ=1.657 ϕ=1.537 $d\perp_1$=3.428×10^{-10} $d\perp_2$=2.239×10^{-11} α=22.657	S_0=1 f_1=0.313 f_2=0.093 f_3=0.592 $d_\parallel$=5.942×10^{-10} θ=1.658 ϕ=-1.576 $d\perp_1$=5.942×10^{-10} $d\perp_2$=2.498×10^{-15} α=3.737	S_0=0.995 f_1=0.248 f_2=0.094 f_3=0.656 $d_\parallel$=8.073×10^{-10} θ=1.603 ϕ=1.548 $d\perp_1$=8.073×10^{-10} $d\perp_2$=2.039×10^{-11} α=22.78	S_0=0.995 f_1=0.313 f_2=0.095 f_3=0.591 $d_\parallel$=5.930×10^{-10} θ=1.658 ϕ=-1.575 $d\perp_1$=5.930×10^{-10} $d\perp_2$=1.632×10^{-13} α=3.730	0.498	0.439
BallCylinderAstrosticks	S_0=1 f_1=0.283 f_2=1.6×10^{-9} f_3=0.716 $d_\parallel$=8.575×10^{-10} θ=1.599 ϕ=1.592 R=2.036×10^{-6}	S_0=1 f_1=0.360 f_2=9.325×10^{-9} f_3=0.639 $d_\parallel$=6.439×10^{-10} θ=1.647 ϕ=-1.549 R=1.985×10^{-6}	S_0=0.995 f_1=0.288 f_2=5×10^{-9} f_3=0.711 $d_\parallel$=8.93×10^{-10} θ=1.577 ϕ=1.577 R=2.235×10^{-6}	S_0=0.995 f_1=0.360 f_2=4.054×10^{-9} f_3=0.639 $d_\parallel$=6.434×10^{-10} θ=1.496 ϕ=-1.591 R=2.005×10^{-6}	0.574	0.493
ZeppelinCylinderAstrosticks	S_0=1 f_1=0.288 f_2=3×10^{-9} f_3=0.711 $d_\parallel$=8.892×10^{-10} θ=1.566 ϕ=1.569 R=2.245×10^{-6} $d\perp_1$=8.711×10^{-10}	S_0=1 f_1=0.357 f_2=1.46×10^{-4} f_3=0.642 $d_\parallel$=6.473×10^{-10} θ=1.494 ϕ=-1.592 R=1.974×10^{-6} $d\perp_1$=6.471×10^{-10}	S_0=0.996 f_1=0.2884 f_2=9×10^{-9} f_3=0.711 $d_\parallel$=8.973×10^{-10} θ=1.561 ϕ=1.561 R=2.232×10^{-6} $d\perp_1$=8.728×10^{-12}	S_0=0.996 f_1=0.360 f_2=2.388×10^{-7} f_3=0.639 $d_\parallel$=6.516×10^{-10} θ=1.643 ϕ=-1.549 R=1.997×10^{-6} $d\perp_1$=6.499×10^{-10}	0.574	0.493
TensorCylinderAstrosticks	S_0=1 f_1=0.280 f_2=0.088 f_3=0.630 $d_\parallel$=7.864×10^{-10} θ=1.567 ϕ=1.574 R=2.196×10^{-6} $d\perp_1$=7.861×10^{-10} $d\perp_2$=2.438×10^{-10} α=22.776	S_0=1 f_1=0.339 f_2=0.089 f_3=0.571 $d_\parallel$=5.748×10^{-10} θ=1.525 ϕ=-1.570 R=1.993×10^{-6} $d\perp_1$=5.742×10^{-10} $d\perp_2$=4.634×10^{-14} α=3.731	S_0=0.995 f_1=0.255 f_2=0.092 f_3=0.651 $d_\parallel$=7.934×10^{-10} θ=1.560 ϕ=1.577 R=1.82×10^{-6} $d\perp_1$=7.934×10^{-10} $d\perp_2$=1.744×10^{-11} α=19.641	S_0=0.995 f_1=0.333 f_2=0.092 f_3=0.574 $d_\parallel$=5.835×10^{-10} θ=1.631 ϕ=-1.573 R=1.839×10^{-6} $d\perp_1$=5.812×10^{-10} $d\perp_2$=3.442×10^{-14} α=0.584	0.485	0.423
BallGDRCylindersAstrosticks	S_0=1 f_1=0.326 f_2=2.8×10^{-8} f_3=0.674 k = 1.731 ϑ = 1.247×10^{-6} $d_\parallel$=9.209×10^{-10} θ=1.587 ϕ=1.556	S_0=1 f_1=0.443 f_2=1.7×10^{-4} f_3=0.556 k = 0.658 ϑ = 2.348×10^{-6} $d_\parallel$=7.057×10^{-10} θ=1.501 ϕ=-1.594	S_0=1.055 f_1=0.319 f_2=2.756×10^{-11} f_3=0.680 k = 1.702 ϑ = 1.256×10^{-6} $d_\parallel$=8.810×10^{-10} θ=1.589 ϕ=1.588	S_0=1.08 f_1=0.397 f_2=9.9×10^{-10} f_3=0.602 k = 0.907 ϑ = 2.104×10^{-6} $d_\parallel$=7.057×10^{-10} θ=1.500 ϕ=-1.590	0.564	0.464
ZeppelinGDRCylindersAstrosticks	S_0=1 f_1=0.277 f_2=0.0947 f_3=0.627 k = 2.571 ϑ = 9.667×10^{-7} $d_\parallel$=8.902×10^{-10} θ=1.544 ϕ=1.546 $d\perp_1$=1.436×10^{-12}	S_0=1 f_1=0.393 f_2=0.066 f_3=0.534 k = 2.413 ϑ = 8.684×10^{-7} $d_\parallel$=6.552×10^{-10} θ=1.496 ϕ=-1.591 $d\perp_1$=1.385×10^{-12}	S_0=1.065 f_1=0.299 f_2=2.045×10^{-4} f_3=0.699 k = 2.861 ϑ = 8.243×10^{-7} $d_\parallel$=9.162×10^{-10} θ=1.585 ϕ=1.556 $d\perp_1$=1.368×10^{-10}	S_0=1.09 f_1=0.386 f_2=0.001 f_3=0.613 k = 1.958 ϑ = 9.011×10^{-7} $d_\parallel$=6.788×10^{-10} θ=1.509 ϕ=-1.582 $d\perp_1$=1.087×10^{-15}	0.563	0.478
TensorGDRCylindersAstrosticks	S_0=1 f_1=0.333 f_2=0.053 f_3=0.613 k = 0.989 ϑ = 2.489×10^{-6} $d_\parallel$=8.413×10^{-10} θ=1.541 ϕ=1.552 $d\perp_1$=8.327×10^{-10} $d\perp_2$=5.4142×10^{-11} α=7.0764	S_0=1 f_1=0.356 f_2=0.079 f_3=0.564 k = 1.766 ϑ = 1.099×10^{-6} $d_\parallel$=5.950×10^{-10} θ=1.684 ϕ=-1.654 $d\perp_1$=4.464×10^{-10} $d\perp_2$=6.680×10^{-11} α=0.402	S_0=1.002 f_1=0.426 f_2=0.069 f_3=0.503 k = 1.525 ϑ = 1.628×10^{-6} $d_\parallel$=5.815×10^{-10} θ=1.643 ϕ=1.576 $d\perp_1$=5.543×10^{-10} $d\perp_2$=8.321×10^{-12} α=15.097	S_0=1.062 f_1=0.355 f_2=0.054 f_3=0.591 k = 1.74 ϑ = 1.05×10^{-6} $d_\parallel$=6.323×10^{-10} θ=1.623 ϕ=-1.550 $d\perp_1$=3.031×10^{-10} $d\perp_2$=9.256×10^{-13} α=43.1	0.456	0.418

Table B.3: *Fitted parameters for the three-compartment astrosticks models.*

Models	Startpoint		Best Estimates		FOBJ	
	dataset A	dataset B	dataset A	dataset B	dataset A	dataset B
BallStickAstrocylinders	S_0=1 f_1=0.270 f_2=2.57×10^{-9} f_3=0.729 $d_\parallel$=8.623×10^{-10} θ=1.604 ϕ=4.668 R=2.060×10^{-6}	S_0=1 f_1=0.335 f_2=4.56×10^{-9} f_3=0.664 $d_\parallel$=6.37×10^{-10} θ=1.664 ϕ=-1.545 R=1.701×10^{-6}	S_0=0.996 f_1=0.268 f_2=5.9×10^{-9} f_3=0.7313 $d_\parallel$=8.584×10^{-10} θ=1.606 ϕ=4.607 R=2.02×10^{-6}	S_0=0.995 f_1=0.336 f_2=1.05×10^{-9} f_3=0.664 $d_\parallel$=6.37×10^{-10} θ=1.665 ϕ=-1.545 R=1.727×10^{-6}	0.580	0.5062
ZeppelinStickAstrocylinders	S_0=1 f_1=0.0467 f_2=0.223 f_3=0.729 $d_\parallel$=8.613×10^{-10} θ=1.608 ϕ=1.608 R=2.050×10^{-6} $d\perp_1$=1.88×10^{-12}	S_0=1 f_1=0.114 f_2=0.225 f_3=0.659 $d_\parallel$=6.473×10^{-10} θ=1.657 ϕ=-1.546 R=1.685×10^{-6} $d\perp_1$=1.302×10^{-12}	S_0=0.996 f_1=0.016 f_2=0.254 f_3=0.729 $d_\parallel$=8.614×10^{-10} θ=1.533 ϕ=1.533 R=2.048×10^{-6} $d\perp_1$=1.66×10^{-13}	S_0=0.996 f_1=0.021 f_2=0.319 f_3=0.659 $d_\parallel$=6.399×10^{-10} θ=1.484 ϕ=-1.594 R=1.685×10^{-6} $d\perp_1$=9.126×10^{-13}	0.579	0.5049
TensorStickAstrocylinders	S_0=1 f_1=0.251 f_2=0.097 f_3=0.650 $d_\parallel$=7.631×10^{-10} θ=1.587 ϕ=1.553 R=2.05×10^{-6} $d\perp_1$=7.621×10^{-10} $d\perp_2$=2.31×10^{-11} α=19.641	S_0=1 f_1=0.318 f_2=0.092 f_3=0.589 $d_\parallel$=5.761×10^{-10} θ=1.482 ϕ=-1.562 R=1.553×10^{-6} $d\perp_1$=5.760×10^{-10} $d\perp_2$=1×10^{-15} α=32.0	S_0=0.996 f_1=0.248 f_2=0.093 f_3=0.658 $d_\parallel$=7.719×10^{-10} θ=1.589 ϕ=1.549 R=1.873×10^{-6} $d\perp_1$=7.719×10^{-10} $d\perp_2$=1.942×10^{-11} α=22.78	S_0=0.995 f_1=0.315 f_2=0.094 f_3=0.589 $d_\parallel$=5.774×10^{-10} θ=1.655 ϕ=-1.578 R=1.530×10^{-6} $d\perp_1$=5.765×10^{-10} $d\perp_2$=3.5×10^{-14} α=32.0	0.487	0.43362
BallCylinderAstrocylinders	S_0=1 f_1=0.288 f_2=5×10^{-9} f_3=0.711 $d_\parallel$=8.93×10^{-10} θ=1.577 ϕ=1.577 R=2.235×10^{-6}	S_0=1 f_1=0.354 f_2=1.4×10^{-9} f_3=0.646 $d_\parallel$=6.209×10^{-10} θ=1.486 ϕ=-1.594 R=1.717×10^{-6}	S_0=0.995 f_1=0.255 f_2=0.092 f_3=0.651 $d_\parallel$=7.934×10^{-10} θ=1.560 ϕ=1.577 R=2.235×10^{-6}	S_0=0.996 f_1=0.351 f_2=1.5×10^{-9} f_3=0.648 $d_\parallel$=6.275×10^{-10} θ=1.653 ϕ=-1.548 R=1.694×10^{-6}	0.569	0.494
ZeppelinCylinderAstrocylinders	S_0=1 f_1=0.283 f_2=2×10^{-9} f_3=0.716 $d_\parallel$=8.559×10^{-10} θ=1.544 ϕ=1.545 R=2.032×10^{-6} $d\perp_1$=8.528×10^{-10}	S_0=1 f_1=0.352 f_2=6.72×10^{-5} f_3=0.647 $d_\parallel$=6.272×10^{-10} θ=1.486 ϕ=-1.594 R=1.966×10^{-6} $d\perp_1$=5.987×10^{-15}	S_0=0.997 f_1=0.283 f_2=1×10^{-8} f_3=0.716 $d_\parallel$=8.55×10^{-10} θ=1.592 ϕ=1.592 R=1.95×10^{-6} $d\perp_1$=8.55×10^{-10}	S_0=0.997 f_1=0.352 f_2=3.415×10^{-5} f_3=0.648 $d_\parallel$=6.285×10^{-10} θ=1.654 ϕ=-1.547 R=1.696×10^{-6} $d\perp_1$=1.155×10^{-12}	0.5693	0.492
TensorCylinderAstrocylinders	S_0=1 f_1=0.269 f_2=0.083 f_3=0.646 $d_\parallel$=7.834×10^{-10} θ=1.570 ϕ=1.562 R=1.849×10^{-6} $d\perp_1$=7.831×10^{-10} $d\perp_2$=2.177×10^{-11} α=18.492	S_0=1 f_1=0.331 f_2=0.093 f_3=0.575 $d_\parallel$=5.668×10^{-10} θ=1.64 ϕ=-1.574 R=1.557×10^{-6} $d\perp_1$=5.601×10^{-10} $d\perp_2$=1.436×10^{-15} α=3.726	S_0=0.995 f_1=0.272 f_2=0.092 f_3=0.635 $d_\parallel$=7.66×10^{-10} θ=1.574 ϕ=1.577 R=1.852×10^{-6} $d\perp_1$=7.66×10^{-10} $d\perp_2$=2.9×10^{-11} α=16.497	S_0=0.995 f_1=0.330 f_2=0.096 f_3=0.573 $d_\parallel$=5.610×10^{-10} θ=1.498 ϕ=-1.566 R=1.576×10^{-6} $d\perp_1$=5.61×10^{-10} $d\perp_2$=9×10^{-15} α=47.7	0.479	0.424
BallGDRCylindersAstrocylinders	S_0=1 f_1=0.408 f_2=1.4×10^{-11} f_3=0.591 k= 2.522 ϑ= 6.630×10^{-7} $d_\parallel$=9.323×10^{-10} θ=1.542 ϕ=1.539 R=1.672×10^{-6}	S_0=1 f_1=0.451 f_2=1.873×10^{-11} f_3=0.548 k= 0.662 ϑ= 2.399×10^{-6} $d_\parallel$=6.291×10^{-10} θ=1.49 ϕ=-1.593 R=1.589×10^{-6}	S_0=1.21 f_1=0.411 f_2=8.47×10^{-10} f_3=0.588 k= 2.476 ϑ= 7.883×10^{-7} $d_\parallel$=8.468×10^{-10} θ=1.593 ϕ=1.593 R=1.952×10^{-6}	S_0=1.89 f_1=0.399 f_2=1.922×10^{-10} f_3=0.601 k= 0.89 ϑ= 2.074×10^{-6} $d_\parallel$=6.148×10^{-10} θ=1.444 ϕ=-1.592 R=1.846×10^{-6}	0.562	0.485
ZeppelinGDRCylindersAstrocylinders	S_0=1 f_1=0.397 f_2=0.050 f_3=0.615 k= 2.395 ϑ= 7.830×10^{-7} $d_\parallel$=8.641×10^{-10} θ=1.606 ϕ=1.599 $d\perp_1$=1.210×10^{-13} R=1.875×10^{-6}	S_0=1 f_1=0.397 f_2=0.023 f_3=0.578 k= 1.442 ϑ= 1.174×10^{-6} $d_\parallel$=6.332×10^{-10} θ=1.487 ϕ=-1.593 $d\perp_1$=1.005×10^{-13} R=1.687×10^{-6}	S_0=1.72 f_1=0.323 f_2=0.005 f_3=0.670 k= 1.934 ϑ= 9×10^{-7} $d_\parallel$=8.599×10^{-10} θ=1.504 ϕ=1.577 $d\perp_1$=9.27×10^{-13} R=1.722×10^{-6}	S_0=1.101 f_1=0.366 f_2=0.05 f_3=0.583 k= 1.996 ϑ= 8.676×10^{-7} $d_\parallel$=6.295×10^{-10} θ=1.484 ϕ=-1.594 $d\perp_1$=8×10^{-14} R=1.732×10^{-6}	0.564	0.489
TensorGDRCylindersAstrocylinders	S_0=1 f_1=0.313 f_2=0.002 f_3=0.664 k = 1.885 ϑ = 8.731×10^{-7} $d_\parallel$=8.488×10^{-10} θ=1.559 ϕ=1.553 $d\perp_1$=6.444×10^{-10} $d\perp_2$=1.031×10^{-10} α=22.411 R=1.646×10^{-6}	S_0=1 f_1=0.312 f_2=0.09 f_3=0.594 k = 1.960 ϑ = 8.780×10^{-7} $d_\parallel$=6.296×10^{-10} θ=1.721 ϕ=-1.477 $d\perp_1$=3.120×10^{-10} $d\perp_2$=1.542×10^{-12} α=3.568 R=1.707×10^{-6}	S_0=1.073 f_1=0.318 f_2=0.055 f_3=0.625 k = 1.864 ϑ = 1.005×10^{-6} $d_\parallel$=8.17×10^{-10} θ=1.559 ϕ=1.552 $d\perp_1$=8.1×10^{-10} $d\perp_2$=5.76×10^{-11} α=21.337 R=1.874×10^{-6}	S_0=1.073 f_1=0.38 f_2=0.012 f_3=0.606 k = 0.935 ϑ = 1.842×10^{-6} $d_\parallel$=6.301×10^{-10} θ=1.652 ϕ=-1.544 $d\perp_1$=1.120×10^{-11} $d\perp_2$=1.673×10^{-13} α=46.212 R=1.702×10^{-6}	0.476	0.422

Table B.4: *Fitted parameters for the three-compartment astrocylinders models.*

Models	Startpoint		Best Estimates		FOBJ	
	dataset A	dataset B	dataset A	dataset B	dataset A	dataset B
BallStickSphere	S_0=1 f_1=0.269 f_2=1.636×10^{-8} f_3=0.730 $d_\parallel$=8.621×10^{-10} θ=1.536 ϕ=1.552 R=2.316×10^{-6}	S_0=1 f_1=0.334 f_2=1.245×10^{-9} f_3=0.665 $d_\parallel$=6.364×10^{-10} θ=1.663 ϕ=-1.545 R=1.977×10^{-6}	S_0=0.987 f_1=0.281 f_2=2.1×10^{-8} f_3=0.718 $d_\parallel$=8.662×10^{-10} θ=1.558 ϕ=1.603 R=2.211×10^{-6}	S_0=0.994 f_1=0.322 f_2=1.3×10^{-9} f_3=0.678 $d_\parallel$=6.415×10^{-10} θ=1.622 ϕ=-1.512 R=1.833×10^{-6}	0.528	0.506
ZeppelinStickSphere	S_0=1 f_1=0.262 f_2=0.007 f_3=0.729 $d_\parallel$=8.582×10^{-10} θ=1.607 ϕ=1.598 R=2.33×10^{-6} $d\perp_1$=2.722×10^{-12}	S_0=1 f_1=0.134 f_2=0.205 f_3=0.659 $d_\parallel$=6.378×10^{-10} θ=1.615 ϕ=-1.533 R=1.91×10^{-6} $d\perp_1$=1.21×10^{-12}	S_0=0.997 f_1=0.27 f_2=0.01 f_3=0.72 $d_\parallel$=8.611×10^{-10} θ=1.633 ϕ=1.601 R=2.213×10^{-6} $d\perp_1$=2.66×10^{-12}	S_0=0.995 f_1=0.136 f_2=0.205 f_3=0.659 $d_\parallel$=6.38×10^{-10} θ=1.652 ϕ=-1.521 R=1.94×10^{-6} $d\perp_1$=1.111×10^{-12}	0.581	0.504
TensorStickSphere	S_0=1 f_1=0.258 f_2=0.059 f_3=0.682 $d_\parallel$=8.26×10^{-10} θ=1.597 ϕ=1.545 R=2.04×10^{-6} $d\perp_1$=8.205×10^{-10} $d\perp_2$=2.112×10^{-11} α=22.734	S_0=1 f_1=0.321 f_2=0.09 f_3=0.589 $d_\parallel$=5.633×10^{-10} θ=1.597 ϕ=-1.576 R=1.763×10^{-6} $d\perp_1$=5.433×10^{-10} $d\perp_2$=4.12×10^{-13} α=0.511	S_0=1.112 f_1=0.322 f_2=0.094 f_3=0.584 $d_\parallel$=8.323×10^{-10} θ=1.589 ϕ=1.545 R=2.174×10^{-6} $d\perp_1$=7.919×10^{-10} $d\perp_2$=2.242×10^{-11} α=22.766	S_0=0.993 f_1=0.318 f_2=0.099 f_3=0.583 $d_\parallel$=5.585×10^{-10} θ=1.601 ϕ=-1.576 R=1.799×10^{-6} $d\perp_1$=5.502×10^{-10} $d\perp_2$=1.162×10^{-13} α=0.586	0.503	0.437
BallCylinderSphere	S_0=1 f_1=0.279 f_2=1.1×10^{-11} f_3=0.721 $d_\parallel$=8.623×10^{-10} θ=1.543 ϕ=1.601 R=1.928×10^{-6}	S_0=1 f_1=0.356 f_2=7.167×10^{-10} f_3=0.643 $d_\parallel$=6.241×10^{-10} θ=1.489 ϕ=-1.593 R=1.814×10^{-6}	S_0=1.011 f_1=0.293 f_2=1.6×10^{-10} f_3=0.707 $d_\parallel$=8.734×10^{-10} θ=1.558 ϕ=1.599 R=2.077×10^{-6}	S_0=1.004 f_1=0.348 f_2=9×10^{-10} f_3=0.652 $d_\parallel$=6.329×10^{-10} θ=1.477 ϕ=-1.621 R=1.953×10^{-6}	0.569	0.492
ZeppelinCylinderSphere	S_0=1 f_1=0.287 f_2=7×10^{-10} f_3=0.712 $d_\parallel$=8.646×10^{-10} θ=1.536 ϕ=1.598 R=2.064×10^{-6} $d\perp_1$=1.608×10^{-10}	S_0=1 f_1=0.354 f_2=0.0015 f_3=0.643 $d_\parallel$=6.266×10^{-10} θ=1.489 ϕ=-1.593 R=1.796×10^{-6} $d\perp_1$=3.712×10^{-14}	S_0=0.998 f_1=0.285 f_2=1.2×10^{-9} f_3=0.715 $d_\parallel$=8.655×10^{-10} θ=1.535 ϕ=1.612 R=2.103×10^{-6} $d\perp_1$=1.525×10^{-10}	S_0=1.022 f_1=0.355 f_2=6.122×10^{-5} f_3=0.644 $d_\parallel$=6.342×10^{-10} θ=1.454 ϕ=-1.597 R=1.786×10^{-6} $d\perp_1$=2.165×10^{-13}	0.570	0.493
TensorCylinderSphere	S_0=1 f_1=0.275 f_2=0.0676 f_3=0.657 $d_\parallel$=8.144×10^{-10} θ=1.581 ϕ=1.584 R=1.943×10^{-6} $d\perp_1$=8.131×10^{-10} $d\perp_2$=1.382×10^{-11} α=-14.927	S_0=1 f_1=0.334 f_2=0.095 f_3=0.570 $d_\parallel$=5.625×10^{-10} θ=1.505 ϕ=-1.567 R=1.737×10^{-6} $d\perp_1$=5.623×10^{-10} $d\perp_2$=2.110×10^{-15} α=3.721	S_0=1.328 f_1=0.294 f_2=0.007 f_3=0.699 $d_\parallel$=8.166×10^{-10} θ=1.584 ϕ=1.587 R=1.955×10^{-6} $d\perp_1$=7.886×10^{-10} $d\perp_2$=1.655×10^{-11} α=14.696	S_0=1.001 f_1=0.401 f_2=0.085 f_3=0.514 $d_\parallel$=5.877×10^{-10} θ=1.523 ϕ=-1.584 R=1.747×10^{-6} $d\perp_1$=5.786×10^{-10} $d\perp_2$=6.231×10^{-14} α=46.667	0.487	0.423
BallGDRCylindersSphere	S_0=1 f_1=0.358 f_2=2.828×10^{-10} f_3=0.641 k= 1.415 ϑ= 1.476×10^{-6} $d_\parallel$=8.513×10^{-10} θ=1.553 ϕ=1.533 R=2.088×10^{-6}	S_0=1 f_1=0.447 f_2=2.664×10^{-11} f_3=0.552 k=0.688 ϑ= 2.541×10^{-6} $d_\parallel$=6.331×10^{-10} θ=1.490 ϕ=-1.595 R=1.750×10^{-6}	S_0=1.111 f_1=0.360 f_2=5.222×10^{-8} f_3=0.639 k= 2.113 ϑ= 9.85×10^{-7} $d_\parallel$=8.713×10^{-10} θ=1.552 ϕ=1.552 R=2.081×10^{-6}	S_0=1.19 f_1=0.463 f_2=9.533×10^{-10} f_3=0.536 k=0.675 ϑ= 2.818×10^{-6} $d_\parallel$=6.252×10^{-10} θ=1.488 ϕ=-1.590 R=1.904×10^{-6}	0.571	0.497
ZeppelinGDRCylindersSphere	S_0=1 f_1=0.369 f_2= 8.9×10^{-10} f_3=0.63 k= 2.092 ϑ= 1.042×10^{-6} $d_\parallel$=8.544×10^{-10} θ=1.595 ϕ=1.595 $d\perp_1$=4.663×10^{-10} R=2.181×10^{-6}	S_0=1 f_1=0.364 f_2=0.07 f_3=0.565 k= 2.34 ϑ= 7.812×10^{-7} $d_\parallel$=6.302×10^{-10} θ=1.487 ϕ=-1.594 $d\perp_1$=1.32×10^{-14} R=1.827×10^{-6}	S_0=1.119 f_1=0.371 f_2= 8.823×10^{-10} f_3=0.628 k= 2.126 ϑ= 1.139×10^{-6} $d_\parallel$=8.624×10^{-10} θ=1.587 ϕ=1.592 $d\perp_1$=5.433×10^{-10} R=2.097×10^{-6}	S_0=1.231 f_1=0.435 f_2=0.042 f_3=0.521 k= 2.495 ϑ= 7.368×10^{-7} $d_\parallel$=6.300×10^{-10} θ=1.485 ϕ=-1.593 $d\perp_1$=4.104×10^{-14} R=1.838×10^{-6}	0.570	0.494
TensorGDRCylindersSphere	S_0=1 f_1=0.313 f_2=0.008 f_3=0.607 k = 1.011 ϑ = 8.731×10^{-7} $d_\parallel$=7.613×10^{-10} θ=1.569 ϕ=1.586 $d\perp_1$=7.601×10^{-10} $d\perp_2$=1.595×10^{-11} α=16.4 R=2.079×10^{-6}	S_0=1 f_1=0.316 f_2=0.010 f_3=0.673 k = 1.578 ϑ = 1.316×10^{-6} $d_\parallel$=8.611×10^{-10} θ=1.5 ϕ=-1.523 $d\perp_1$=8.502×10^{-10} $d\perp_2$=3.852×10^{-11} α=10.512 R=2.072×10^{-6}	S_0=1.08 f_1=0.333 f_2=0.001 f_3=0.667 k = 1.777 ϑ = 1.161×10^{-6} $d_\parallel$=8.943×10^{-10} θ=1.583 ϕ=1.591 $d\perp_1$=3.071×10^{-10} $d\perp_2$=3.831×10^{-11} α=17.1 R=2.079×10^{-6}	S_0=1.07 f_1=0.383 f_2=0.046 f_3=0.57 k = 1.974 ϑ = 8.961×10^{-7} $d_\parallel$=6.113×10^{-10} θ=1.508 ϕ=-1.572 $d\perp_1$=7.813×10^{-10} $d\perp_2$=6.332×10^{-12} α=10.631 R=2.106×10^{-6}	0.566	0.484

Table B.5: *Fitted parameters for the three-compartment Sphere models.*

Models	Startpoint		Best Estimates		FOBJ	
	dataset A	dataset B	dataset A	dataset B	dataset A	dataset B
BallStickSphere	S_0=1 f_1=0.269 f_2=2.7×10^{-8} f_3=0.730 $d_\parallel$=8.62×10^{-10} θ=1.55 ϕ=1.553 R=2.225×10^{-6}	S_0=1 f_1=0.344 f_2=2.1×10^{-10} f_3=0.655 $d_\parallel$=6.37×10^{-10} θ=1.655 ϕ=-1.544 R=1.92×10^{-6}	S_0=0.996 f_1=0.268 f_2=2.5×10^{-9} f_3=0.731 $d_\parallel$=8.63×10^{-10} θ=1.6 ϕ=1.533 R=2.26×10^{-6}	S_0=0.995 f_1=0.335 f_2=4.2×10^{-11} f_3=0.666 $d_\parallel$=6.39×10^{-10} θ=1.665 ϕ=-1.544 R=1.91×10^{-6}	0.58	0.506
ZeppelinStickSphere	S_0=1 f_1=0.260 f_2=0.0009 f_3=0.739 $d_\parallel$=8.466×10^{-10} θ=1.597 ϕ=1.577 R=2.22×10^{-6} $d\perp_1$=2.112×10^{-12}	S_0=1 f_1=0.136 f_2=0.204 f_3=0.658 $d_\parallel$=6.37×10^{-10} θ=1.63 ϕ=-1.55 R=1.987×10^{-6} $d\perp_1$=1.45×10^{-12}	S_0=0.996 f_1=0.271 f_2=3.5×10^{-7} f_3=0.728 $d_\parallel$=8.63×10^{-10} θ=1.6 ϕ=1.5581 R=2.28×10^{-6} $d\perp_1$=8.2×10^{-10}	S_0=0.995 f_1=0.135 f_2=0.205 f_3=0.659 $d_\parallel$=6.38×10^{-10} θ=1.65 ϕ=-1.56 R=1.94×10^{-6} $d\perp_1$=1.11×10^{-12}	0.576	0.504
TensorStickSphere	S_0=1 f_1=0.253 f_2=0.061 f_3=0.685 $d_\parallel$=7.45×10^{-10} θ=1.544 ϕ=1.545 R=2.1×10^{-6} $d\perp_1$=7.01×10^{-10} $d\perp_2$=2.112×10^{-11} α=22.22	S_0=1 f_1=0.315 f_2=0.094 f_3=0.589 $d_\parallel$=5.744×10^{-10} θ=1.485 ϕ=-1.563 R=1.749×10^{-6} $d\perp_1$=5.740×10^{-10} $d\perp_2$=5.1×10^{-14} α=3.724	S_0=0.995 f_1=0.244 f_2=0.11 f_3=0.645 $d_\parallel$=7.56×10^{-10} θ=1.545 ϕ=1.545 R=2.13×10^{-6} $d\perp_1$=6.76×10^{-10} $d\perp_2$=2.89×10^{-11} α=22.4	S_0=0.989 f_1=0.321 f_2=0.011 f_3=0.668 $d_\parallel$=6.125×10^{-10} θ=1.502 ϕ=-1.594 R=1.822×10^{-6} $d\perp_1$=5.632×10^{-10} $d\perp_2$=8.124×10^{-14} α=3.722	0.492	0.437
BallCylinderSphere	S_0=1 f_1=0.285 f_2=1.6×10^{-10} f_3=0.714 $d_\parallel$=8.529×10^{-10} θ=1.57 ϕ=1.578 R=2.09×10^{-6} R_s=2.03×10^{-6}	S_0=1 f_1=0.358 f_2=4×10^{-11} f_3=0.640 $d_\parallel$=6.263×10^{-10} θ=1.499 ϕ=-1.593 R=1.923×10^{-6} R_s=1.7×10^{-6}	S_0=0.996 f_1=0.288 f_2=1.7×10^{-10} f_3=0.712 $d_\parallel$=8.54×10^{-10} θ=1.558 ϕ=1.574 R=2.09×10^{-6} R_s=2.02×10^{-6}	S_0=0.995 f_1=0.361 f_2=3.7×10^{-12} f_3=0.639 $d_\parallel$=6.27×10^{-10} θ=1.499 ϕ=-1.592 R=1.92×10^{-6} R_s=1.7×10^{-6}	0.568	0.491
ZeppelinCylinderSphere	S_0=1 f_1=0.286 f_2=0.0035 f_3=0.709 $d_\parallel$=8.672×10^{-10} θ=1.555 ϕ=1.548 R=2.04×10^{-6} R_s=2×10^{-6} $d\perp_1$=1.5×10^{-11}	S_0=1 f_1=0.354 f_2=0.0016 f_3=0.644 $d_\parallel$=6.372×10^{-10} θ=1.532 ϕ=-1.599 R=1.878×10^{-6} R=1.57×10^{-6} $d\perp_1$=2.135×10^{-14}	S_0=0.998 f_1=0.287 f_2=0.0035 f_3=0.710 $d_\parallel$=8.678×10^{-10} θ=1.553 ϕ=1.55 R=2.05×10^{-6} R_s=2×10^{-6} $d\perp_1$=1.5×10^{-10}	S_0=0.996 f_1=0.356 f_2=0.00165 f_3=0.641 $d_\parallel$=6.375×10^{-10} θ=1.545 ϕ=-1.596 R=1.89×10^{-6} R_s=1.53×10^{-6} $d\perp_1$=2.02×10^{-14}	0.55	0.490
TensorCylinderSphere	S_0=1 f_1=0.28 f_2=0.06 f_3=0.66 $d_\parallel$=8.077×10^{-10} θ=1.593 ϕ=1.582 R=1.998×10^{-6} R_s=1.88×10^{-6} $d\perp_1$=8.044×10^{-10} $d\perp_2$=2.15×10^{-11} α=-14.65	S_0=1 f_1=0.345 f_2=0.092 f_3=0.563 $d_\parallel$=5.61×10^{-10} θ=1.493 ϕ=-1.565 R=1.85×10^{-6} R_s=1.38×10^{-6} $d\perp_1$=5.6×10^{-10} $d\perp_2$=2.02×10^{-12} α=22.5	S_0=0.994 f_1=0.282 f_2=0.053 f_3=0.665 $d_\parallel$=8.06×10^{-10} θ=1.61 ϕ=1.578 R=2.04×10^{-6} R_s=1.87×10^{-6} $d\perp_1$=7.955×10^{-10} $d\perp_2$=2.15×10^{-11} α=14.74	S_0=0.994 f_1=0.346 f_2=0.091 f_3=0.562 $d_\parallel$=5.61×10^{-10} θ=1.499 ϕ=-1.567 R=1.85×10^{-6} R_s=1.37×10^{-6} $d\perp_1$=5.455×10^{-10} $d\perp_2$=2.012×10^{-12} α=22.5	0.499	0.424
BallGDRCylindersSphere	S_0=1 f_1=0.352 f_2=2.122×10^{-10} f_3=0.647 k= 1.445 ϑ= 1.433×10^{-6} $d_\parallel$=8.622×10^{-10} θ=1.550 ϕ=1.545 R=1.999×10^{-6}	S_0=1 f_1=0.421 f_2=5.12×10^{-10} f_3=0.578 k=0.744 ϑ= 2.011×10^{-6} $d_\parallel$=6.334×10^{-10} θ=1.533 ϕ=-1.575 R=1.751×10^{-6}	S_0=1.122 f_1=0.365 f_2=5.277×10^{-9} f_3=0.634 k= 1.458 ϑ= 1.457×10^{-6} $d_\parallel$=8.679×10^{-10} θ=1.550 ϕ=1.550 R=1.998×10^{-6}	S_0=1.109 f_1=0.412 f_2=5.127×10^{-10} f_3=0.587 k=0.822 ϑ= 2.09×10^{-6} $d_\parallel$=6.379×10^{-10} θ=1.491 ϕ=-1.587 R=1.725×10^{-6}	0.565	0.489
ZeppelinGDRCylindersSphere	S_0=1 f_1=0.399 f_2= 9×10^{-11} f_3=0.6 k= 0.622 ϑ= 4.12×10^{-6} $d_\parallel$=8.977×10^{-10} θ=1.587 ϕ=1.579 $d\perp_1$=2.001×10^{-10} R=1.62×10^{-6}	S_0=1 f_1=0.450 f_2=0.009 f_3=0.541 k= 0.7 ϑ= 2.63×10^{-6} $d_\parallel$=6.711×10^{-10} θ=1.491 ϕ=-1.586 $d\perp_1$=3.02×10^{-11} R=1.522×10^{-6}	S_0=1.12 f_1=0.414 f_2= 5.12×10^{-11} f_3=0.585 k= 0.63 ϑ= 4.33×10^{-6} $d_\parallel$=9.02×10^{-10} θ=1.582 ϕ=1.581 $d\perp_1$=1.977×10^{-10} R=1.702×10^{-6}	S_0=1.2 f_1=0.452 f_2=0.008 f_3=0.54 k= 0.666 ϑ= 2.45×10^{-6} $d_\parallel$=6.677×10^{-10} θ=1.482 ϕ=-1.573 $d\perp_1$=3.053×10^{-11} R=1.55×10^{-6}	0.530	0.487
TensorGDRCylindersSphere	S_0=1 f_1=0.346 f_2=0.07 f_3=0.584 k = 1.501 ϑ = 1.376×10^{-6} $d_\parallel$=7.502×10^{-10} θ=1.526 ϕ=1.589 $d\perp_1$=7.476×10^{-10} $d\perp_2$=3.34×10^{-12} α=16.532 R=2.01×10^{-6}	S_0=1 f_1=0.354 f_2=0.045 f_3=0.601 k = 1.8 ϑ = 1.02×10^{-6} $d_\parallel$=6.33×10^{-10} θ=1.59 ϕ=-1.57 $d\perp_1$=2.7×10^{-11} $d\perp_2$=9.013×10^{-13} α=10.233 R=1.45×10^{-6}	S_0=1.1 f_1=0.349 f_2=0.071 f_3=0.58 k = 1.491 ϑ = 1.391×10^{-6} $d_\parallel$=7.492×10^{-10} θ=1.525 ϕ=1.590 $d\perp_1$=7.001×10^{-10} $d\perp_2$=3.331×10^{-12} α=14.92 R=2.07×10^{-6}	S_0=1.079 f_1=0.355 f_2=0.046 f_3=0.599 k = 1.803 ϑ = 1.02×10^{-6} $d_\parallel$=6.33×10^{-10} θ=1.599 ϕ=-1.571 $d\perp_1$=2.73×10^{-11} $d\perp_2$=9.04×10^{-13} α=10.25 R=1.44×10^{-6}	0.494	0.419

Table B.6: *Fitted parameters for the three-compartment Sphere models with unconstrained radius.*

Appendix C

Tables with in vivo microstructural estimates

Models	Startpoint		Best Estimates		FOBJ	
	dataset A	dataset B	dataset A	dataset B	dataset A	dataset B
DT	-	-	$d_{\parallel}$=2.565×10^{-10} $d\perp_1$= 2.285×10^{-10} $d\perp_2$=-1.381×10^{-8} θ=1.573 ϕ=-0.783	$d_{\parallel}$=4.536×10^{-10} $d\perp_1$= 4.421×10^{-10} $d\perp_2$=-1.161×10^{-8} θ=1.571 ϕ=-3.923	50.2	41.37
Bitensor	S_0=1 f_1=0.297 f_2=0.702 $d_{\parallel}$=1.404×10^{-9} θ=1.686 ϕ=3.141 $d\perp_{1a}$=1.244×10^{-9} $d\perp_{1b}$=5.718×10^{-11}	S_0=1 f_1=0.170 f_2=0.829 $d_{\parallel}$=1.313×10^{-9} θ=1.546 ϕ=-3.141 $d\perp_{1a}$=5.096×10^{-10} $d\perp_{1b}$=8.612×10^{-10}	S_0=1.011 f_1=0.709 f_2=0.290 $d_{\parallel}$=1.414×10^{-9} θ=1.439 ϕ=18.849 $d\perp_{1a}$=1.238×10^{-9} $d\perp_{1b}$=4.289×10^{-11}	S_0=1.018 f_1=0.383 f_2=0.616 $d_{\parallel}$=1.396×10^{-9} θ=1.656 ϕ=-3.141 $d\perp_{1a}$=2.996×10^{-10} $d\perp_{1b}$=1.351×10^{-9}	1.261	0.791
BallStick	S_0=1 f_1=0.311 f_2=0.689 $d_{\parallel}$=1.412×10^{-9} θ=1.331 ϕ=0.189	S_0=1 f_1=0.259 f_2=0.741 $d_{\parallel}$=1.267×10^{-9} θ=1.186 ϕ=-2.734	S_0=1.101 f_1=0.321 f_2=0.678 $d_{\parallel}$=1.443×10^{-9} θ=1.349 ϕ=0.19	S_0=1.024 f_1=0.260 f_2=0.740 $d_{\parallel}$=1.319×10^{-9} θ=1.199 ϕ=-2.741	1.293	0.9074
ZeppelinStick	S_0=1 f_1=0.302 f_2=0.698 $d_{\parallel}$=1.401×10^{-9} θ=1.411 ϕ=-0.072 $d\perp_1$=1.022×10^{-9}	S_0=1 f_1=0.080 f_2=0.920 $d_{\parallel}$=1.322×10^{-9} θ=1.528 ϕ=-3.141 $d\perp_1$=9.101×10^{-10}	S_0=1.009 f_1=0.240 f_2=0.759 $d_{\parallel}$=1.426×10^{-9} θ=1.427 ϕ=-0.068 $d\perp_1$=1.133×10^{-9}	S_0=1.012 f_1=0.073 f_2=0.927 $d_{\parallel}$=1.351×10^{-9} θ=1.552 ϕ=-3.141 $d\perp_1$=9.135×10^{-10}	1.267	0.817
TensorStick	S_0=1 f_1=0.296 f_2=0.704 $d_{\parallel}$=1.436×10^{-9} θ=1.453 ϕ=-3.164 $d\perp_1$=1.398×10^{-9} $d\perp_2$=9.677×10^{-10} α=0.644	S_0=1 f_1=0.140 f_2=0.860 $d_{\parallel}$=1.410×10^{-9} θ=1.766 ϕ=-3.325 $d\perp_1$=1.387×10^{-9} $d\perp_2$=6.036×10^{-10} α=0.754	S_0=1.012 f_1=0.280 f_2=0.720 $d_{\parallel}$=1.445×10^{-9} θ=1.373 ϕ=-3.154 $d\perp_1$=1.405×10^{-9} $d\perp_2$=9.847×10^{-10} α=0.629	S_0=1.017 f_1=0.135 f_2=0.865 $d_{\parallel}$=1.412×10^{-9} θ=1.818 ϕ=-3.283 $d\perp_1$=1.402×10^{-9} $d\perp_2$=6.288×10^{-10} α=0.781	1.236	0.781
BallCylinder	S_0=1 f_1=0.313 f_2=0.686 $d_{\parallel}$=1.443×10^{-9} θ=1.347 ϕ=-0.19 R=9.245×10^{-7}	S_0=1 f_1=0.323 f_2=0.677 $d_{\parallel}$=1.318×10^{-9} θ=1.195 ϕ=-2.788 R=1.008×10^{-7}	S_0=1.019 f_1=0.327 f_2=0.672 $d_{\parallel}$=1.461×10^{-9} θ=1.345 ϕ=-0.20 R=1×10^{-7}	S_0=1.023 f_1=0.268 f_2=0.731 $d_{\parallel}$=1.318×10^{-9} θ=1.195 ϕ=-2.788 R=1.008×10^{-7}	1.293	0.9076
ZeppelinCylinder	S_0=1 f_1=0.32 f_2=0.68 $d_{\parallel}$=1.627×10^{-9} θ=1.422 ϕ=0.085 R=1.411×10^{-7} $d\perp_1$=1.034×10^{-9}	S_0=1 f_1=0.125 f_2=0.875 $d_{\parallel}$=1.401×10^{-9} θ=1.587 ϕ=-3.15 R=4.122×10^{-6} $d\perp_1$=9.766×10^{-10}	S_0=1.01 f_1=0.24 f_2=0.76 $d_{\parallel}$=1.427×10^{-9} θ=1.426 ϕ=0.07 R=1.370×10^{-7} $d\perp_1$=1.134×10^{-9}	S_0=1.014 f_1=0.112 f_2=0.888 $d_{\parallel}$=1.382×10^{-9} θ=1.681 ϕ=-3.141 R=4.075×10^{-6} $d\perp_1$=9.644×10^{-10}	1.267	0.8141
TensorCylinder	S_0=1 f_1=0.280 f_2=0.720 $d_{\parallel}$=1.447×10^{-9} θ=1.365 ϕ=-3.154 R=1.466×10^{-6} $d\perp_1$=1.4×10^{-9} $d\perp_2$=9.744×10^{-10} α=5.661	S_0=1 f_1=0.142 f_2=0.858 $d_{\parallel}$=1.432×10^{-9} θ=1.897 ϕ=-3.176 R=3.044×10^{-7} $d\perp_1$=1.398×10^{-9} $d\perp_2$=6.033×10^{-10} α=-2.503	S_0=1.012 f_1=0.280 f_2=0.720 $d_{\parallel}$=1.445×10^{-9} θ=1.371 ϕ=-3.164 R=1.360×10^{-6} $d\perp_1$=1.402×10^{-9} $d\perp_2$=9.692×10^{-10} α=5.661	S_0=1.016 f_1=0.133 f_2=0.867 $d_{\parallel}$=1.412×10^{-9} θ=1.821 ϕ=-3.153 R=3.423×10^{-7} $d\perp_1$=1.402×10^{-9} $d\perp_2$=6.122×10^{-10} α=-2.405	1.235	0.780
BallGDRCylinders	S_0=1 f_1=0.433 f_2=0.566 k = 0.653 ϑ = 1×10^{-7} $d_{\parallel}$=1.444×10^{-9} θ=1.343 ϕ=-0.199	S_0=1 f_1=0.512 f_2=0.488 k = 1.073 ϑ = 1.747×10^{-5} $d_{\parallel}$=1.328×10^{-9} θ=1.408 ϕ=-0.211	S_0=1.311 f_1=0.470 f_2=0.529 k = 0.548 ϑ = 1.076×10^{-7} $d_{\parallel}$=1.442×10^{-9} θ=1.346 ϕ=1.193	S_0=1.160 f_1=0.530 f_2=0.469 k = 1.073 ϑ = 1.747×10^{-5} $d_{\parallel}$=1.328×10^{-9} θ=1.408 ϕ=-0.211	1.294	0.9031
ZeppelinGDRCylinders	S_0=1 f_1=0.244 f_2=0.756 k = 0.946 ϑ = 1.759×10^{-7} $d_{\parallel}$=1.399×10^{-9} θ=1.546 ϕ=-0.293 $d\perp_1$=1.102×10^{-9}	S_0=1 f_1=0.114 f_2=0.886 k = 1.152 ϑ = 3.544×10^{-6} $d_{\parallel}$=1.366×10^{-9} θ=1.623 ϕ=3.142 $d\perp_1$=1.103×10^{-9}	S_0=1.1 f_1=0.310 f_2=0.690 k = 0.804 ϑ = 1.003×10^{-7} $d_{\parallel}$=1.439×10^{-9} θ=1.407 ϕ=-0.102 $d\perp_1$=1.162×10^{-9}	S_0=1.044 f_1=0.125 f_2=0.875 k = 1.115 ϑ = 3.725×10^{-6} $d_{\parallel}$=1.347×10^{-9} θ=1.643 ϕ=3.141 $d\perp_1$=1.001×10^{-9}	1.267	0.814
TensorGDRCylinders	S_0=1 f_1=0.420 f_2=0.580 k = 2.103 ϑ = 1.321×10^{-7} $d_{\parallel}$=1.468×10^{-9} θ=1.427 ϕ=-3.142 $d\perp_1$=1.463×10^{-9} $d\perp_2$=9.122×10^{-10} α=5.622	S_0=1 f_1=0.160 f_2=0.840 k = 1.143 ϑ = 1.036×10^{-7} $d_{\parallel}$=1.376×10^{-9} θ=1.756 ϕ=-3.147 $d\perp_1$=1.354×10^{-9} $d\perp_2$=5.877×10^{-10} α=-18.076	S_0=1.181 f_1=0.406 f_2=0.594 k = 2.444 ϑ = 1×10^{-7} $d_{\parallel}$=1.447×10^{-9} θ=1.366 ϕ=-3.142 $d\perp_1$=1.444×10^{-9} $d\perp_2$=9.472×10^{-10} α=5.658	S_0=1.049 f_1=0.153 f_2=0.847 k = 1.029 ϑ = 1.217×10^{-7} $d_{\parallel}$=1.398×10^{-9} θ=1.807 ϕ=-3.142 $d\perp_1$=1.388×10^{-9} $d\perp_2$=6.036×10^{-10} α=-18.116	1.235	0.780

Table C.1: *Fitted parameters for the two-compartment models.*

Models	Startpoint		Best Estimates		FOBJ	
	dataset A	dataset B	dataset A	dataset B	dataset A	dataset B
BallStickDot	S_0=1 f_1=0.303 f_2=0.583 f_3=0.113 $d_\parallel$=1.738×10^{-9} θ=1.915 ϕ=-0.336	S_0=1 f_1=0.264 f_2=0.661 f_3=0.075 $d_\parallel$=1.401×10^{-9} θ=1.175 ϕ=-3.166	S_0=1.032 f_1=0.303 f_2=0.583 f_3=0.113 $d_\parallel$=1.738×10^{-9} θ=1.915 ϕ=-0.33	S_0=1.026 f_1=0.270 f_2=0.715 f_3=0.015 $d_\parallel$=1.367×10^{-9} θ=1.180 ϕ=-3.51	1.045	0.9021
ZeppelinStickDot	S_0=1 f_1=0.065 f_2=0.720 f_3=0.215 $d_\parallel$=2.011×10^{-9} θ=1.542 ϕ=0.223 $d\perp_1$=1.203×10^{-9}	S_0=1 f_1=0.050 f_2=0.908 f_3=0.044 $d_\parallel$=1.520×10^{-9} θ=1.611 ϕ=-3.141 $d\perp_1$=9.603×10^{-10}	S_0=1.01 f_1=0.077 f_2=0.790 f_3=0.132 $d_\parallel$=1.896×10^{-9} θ=1.581 ϕ=0.199 $d\perp_1$=1.074×10^{-9}	S_0=1.015 f_1=0.049 f_2=0.907 f_3=0.044 $d_\parallel$=1.516×10^{-9} θ=1.623 ϕ=-3.141 $d\perp_1$=9.595×10^{-10}	0.895	0.779
TensorStickDot	S_0=1 f_1=0.177 f_2=0.711 f_3=0.112 $d_\parallel$=1.365×10^{-9} θ=1.526 ϕ=-3.142 $d\perp_1$=1.263×10^{-9} $d\perp_2$=9.631×10^{-10} α=5.266	S_0=1.024 f_1=0.210 f_2=0.765 f_3=0.025 $d_\parallel$=1.466×10^{-9} θ=1.897 ϕ=-3.143 $d\perp_1$=1.460×10^{-9} $d\perp_2$=1.004×10^{-9} α=-1.205	S_0=1.036 f_1=0.3 f_2=0.557 f_3=0.143 $d_\parallel$=1.752×10^{-9} θ=1.543 ϕ=-3.163 $d\perp_1$=1.654×10^{-9} $d\perp_2$=1.485×10^{-9} α=4.711	S_0=1.024 f_1=0.219 f_2=0.780 f_3=0.001 $d_\parallel$=1.433×10^{-9} θ=1.820 ϕ=-3.143 $d\perp_1$=1.421×10^{-9} $d\perp_2$=1.089×10^{-9} α=-1.205	0.894	0.774
BallCylinderDot	S_0=1 f_1=0.510 f_2=0.177 f_3=0.311 $d_\parallel$=3.375×10^{-10} θ=1.477 ϕ=1.478 R=2.060×10^{-6}	S_0=1 f_1=0.250 f_2=0.720 f_3=0.030 $d_\parallel$=1.362×10^{-9} θ=1.154 ϕ=-3.433 R=1.003×10^{-7}	S_0=1.031 f_1=0.323 f_2=0.562 f_3=0.114 $d_\parallel$=1.768×10^{-9} θ=1.208 ϕ=-3.141 R=1.002×10^{-7}	S_0=1.027 f_1=0.263 f_2=0.719 f_3=0.017 $d_\parallel$=1.367×10^{-9} θ=1.18 ϕ=-3.50 R=1.044×10^{-7}	1.0483	0.902
ZeppelinCylinderDot	S_0=1 f_1=0.065 f_2=0.654 f_3=0.281 $d_\parallel$=2.021×10^{-9} θ=1.622 ϕ=0.187 R=2.001×10^{-6} $d\perp_1$=1.455×10^{-9}	S_0=1 f_1=0.070 f_2=0.867 f_3=0.063 $d_\parallel$=1.489×10^{-9} θ=1.526 ϕ=-3.174 R=2.995×10^{-6} $d\perp_1$=1.003×10^{-9}	S_0=1.020 f_1=0.079 f_2=0.787 f_3=0.132 $d_\parallel$=1.865×10^{-9} θ=1.632 ϕ=0.195 R=2.609×10^{-6} $d\perp_1$=1.082×10^{-9}	S_0=1.018 f_1=0.050 f_2=0.906 f_3=0.044 $d_\parallel$=1.465×10^{-9} θ=1.599 ϕ=-3.14 R=4.286×10^{-6} $d\perp_1$=9.680×10^{-10}	0.896	0.7833
TensorCylinderDot	S_0=1 f_1=0.090 f_2=0.775 f_3=0.135 $d_\parallel$=1.933×10^{-9} θ=1.464 ϕ=-3.148 R=1×10^{-7} $d\perp_1$=1.9×10^{-9} $d\perp_2$=3.506×10^{-10} α= 5.521	S_0=1 f_1=0.137 f_2=0.766 f_3=0.097 $d_\parallel$=1.698×10^{-9} θ=1.433 ϕ=-3.146 R=1.021×10^{-5} $d\perp_1$=1.621×10^{-9} $d\perp_2$=8.004×10^{-12} α= -11.112	S_0=1.022 f_1=0.094 f_2=0.774 f_3=0.132 $d_\parallel$=1.936×10^{-9} θ=1.424 ϕ=-3.146 R=1.006×10^{-7} $d\perp_1$=1.904×10^{-9} $d\perp_2$=3.323×10^{-10} α= 5.521	S_0=1.017 f_1=0.140 f_2=0.806 f_3=0.054 $d_\parallel$=1.695×10^{-9} θ=1.453 ϕ=-3.153 R=1.116×10^{-5} $d\perp_1$=1.622×10^{-9} $d\perp_2$=7.542×10^{-12} α= -11.38	0.886	0.748
BallGDRCylindersDot	S_0=1 f_1=0.320 f_2=0.577 f_3=0.101 k=0.999 ϑ=6.840×10^{-7} $d_\parallel$=1.687×10^{-9} θ=1.905 ϕ=0.321	S_0=1 f_1=0.427 f_2=0.603 f_3=0.03 k=1.022 ϑ=1.053×10^{-5} $d_\parallel$=1.310×10^{-9} θ=1.635 ϕ=-0.264	S_0=1.099 f_1=0.437 f_2=0.474 f_3=0.088 k=0.99 ϑ=1.394×10^{-5} $d_\parallel$=1.655×10^{-9} θ=1.441 ϕ=-3.141	S_0=1.097 f_1=0.416 f_2=0.568 f_3=0.015 k=0.951 ϑ=1.263×10^{-5} $d_\parallel$=1.332×10^{-9} θ=1.894 ϕ=-0.26	1.047	0.898
ZeppelinGDRCylindersDot	S_0=1 f_1=0.232 f_2=0.587 f_3=0.181 k=0.464 ϑ=2.153×10^{-6} $d_\parallel$=1.766×10^{-9} θ=1.634 ϕ=-3.233 $d\perp_1$=1.112×10^{-9}	S_0=1 f_1=0.103 f_2=0.789 f_3=0.108 k=0.766 ϑ=3.435×10^{-7} $d_\parallel$=1.477×10^{-9} θ=1.601 ϕ=-3.186 $d\perp_1$=9.732×10^{-10}	S_0=1.283 f_1=0.256 f_2=0.638 f_3=0.106 k=0.218 ϑ=2.825×10^{-6} $d_\parallel$=1.826×10^{-9} θ=1.608 ϕ=-3.188 $d\perp_1$=1.062×10^{-9}	S_0=1.055 f_1=0.069 f_2=0.893 f_3=0.038 k=0.536 ϑ=4.071×10^{-7} $d_\parallel$=1.421×10^{-9} θ=1.553 ϕ=-3.215 $d\perp_1$=9.523×10^{-10}	0.895	0.782
TensorGDRCylindersDot	S_0=1 f_1=0.101 f_2=0.764 f_3=0.153 k=1.246 ϑ=1.726×10^{-5} $d_\parallel$=1.945×10^{-9} θ=1.457 ϕ=-3.142 $d\perp_1$=1.877×10^{-9} $d\perp_2$=2.399×10^{-10} α=5.518	S_0=1 f_1=0.083 f_2=0.865 f_3=0.052 k=1.465 ϑ=2.477×10^{-6} $d_\parallel$=1.524×10^{-9} θ=1.688 ϕ=-3.143 $d\perp_1$=1.377×10^{-9} $d\perp_2$=5.677×10^{-10} α=-18.222	S_0=1.043 f_1=0.099 f_2=0.767 f_3=0.134 k=1.505 ϑ=1.771×10^{-5} $d_\parallel$=1.949×10^{-9} θ=1.456 ϕ=-3.143 $d\perp_1$=1.893×10^{-9} $d\perp_2$=2.392×10^{-10} α=5.518	S_0=1.044 f_1=0.086 f_2=0.872 f_3=0.042 k=1.396 ϑ=3.08×10^{-6} $d_\parallel$=1.525×10^{-9} θ=1.708 ϕ=-3.143 $d\perp_1$=1.232×10^{-9} $d\perp_2$=6.995×10^{-10} α=-18.12	0.885	0.747

Table C.2: *Fitted parameters for the three-compartment dot models.*

Models	Startpoint		Best Estimates		FOBJ	
	dataset A	dataset B	dataset A	dataset B	dataset A	dataset B
BallStickAstrosticks	S_0=1 f_1=0.250 f_2=0.397 f_3=0.352 $d_\parallel$=2.111×10^{-9} θ=1.850 ϕ=-0.251	S_0=1 f_1=0.253 f_2=0.632 f_3=0.115 $d_\parallel$=1.422×10^{-9} θ=1.197 ϕ=-2.582	S_0=1.037 f_1=0.250 f_2=0.397 f_3=0.352 $d_\parallel$=2.111×10^{-9} θ=1.842 ϕ=-0.251	S_0=1.029 f_1=0.262 f_2=0.660 f_3=0.077 $d_\parallel$=1.458×10^{-9} θ=1.178 ϕ=-2.772	1.046	0.8927
ZeppelinStickAstrosticks	S_0=1 f_1=0.111 f_2=0.494 f_3=0.395 $d_\parallel$=2.466×10^{-9} θ=1.623 ϕ=-3.141 $d\perp_1$=1.177×10^{-9}	S_0=1 f_1=0.064 f_2=0.785 f_3=0.151 $d_\parallel$=2.655×10^{-9} θ=1.573 ϕ=-3.143 $d\perp_1$=1.006×10^{-9}	S_0=1.029 f_1=0.109 f_2=0.471 f_3=0.420 $d_\parallel$=2.521×10^{-9} θ=1.642 ϕ=-3.141 $d\perp_1$=1.237×10^{-9}	S_0=1.020 f_1=0.039 f_2=0.800 f_3=0.161 $d_\parallel$=2.671×10^{-9} θ=1.520 ϕ=-3.144 $d\perp_1$=9.947×10^{-10}	0.914	0.764
TensorStickAstrosticks	S_0=1 f_1=0.110 f_2=0.477 f_3=0.413 $d_\parallel$=2.494×10^{-9} θ=1.486 ϕ=-3.143 $d\perp_1$=2.440×10^{-9} $d\perp_2$=5.734×10^{-12} α=5.522	S_0=1 f_1=0.057 f_2=0.788 f_3=0.155 $d_\parallel$=1.677×10^{-9} θ=1.795 ϕ=-3.148 $d\perp_1$=1.605×10^{-9} $d\perp_2$=4.075×10^{-10} α=-2.483	S_0=1.029 f_1=0.109 f_2=0.478 f_3=0.413 $d_\parallel$=2.495×10^{-9} θ=1.488 ϕ=-3.145 $d\perp_1$=2.439×10^{-9} $d\perp_2$=5.399×10^{-12} α=5.527	S_0=1.022 f_1=0.061 f_2=0.790 f_3=0.149 $d_\parallel$=1.681×10^{-9} θ=1.787 ϕ=-3.146 $d\perp_1$=1.611×10^{-9} $d\perp_2$=3.832×10^{-10} α=-2.387	0.905	0.741
BallCylinderAstrosticks	S_0=1 f_1=0.241 f_2=0.435 f_3=0.322 $d_\parallel$=2.215×10^{-9} θ=1.354 ϕ=-0.197 R=1.031×10^{-7}	S_0=1 f_1=0.188 f_2=0.646 f_3=0.166 $d_\parallel$=1.327×10^{-9} θ=1.357 ϕ=-3.122 R=2.634×10^{-7}	S_0=1.038 f_1=0.232 f_2=0.431 f_3=0.335 $d_\parallel$=2.038×10^{-9} θ=1.826 ϕ=-0.218 R=1.031×10^{-7}	S_0=1.028 f_1=0.251 f_2=0.674 f_3=0.073 $d_\parallel$=1.443×10^{-9} θ=1.183 ϕ=-3.502 R=5.751×10^{-7}	1.0506	0.8941
ZeppelinCylinderAstrosticks	S_0=1 f_1=0.101 f_2=0.433 f_3=0.466 $d_\parallel$=2.532×10^{-9} θ=1.546 ϕ=-0.334 R=1.866×10^{-7} $d\perp_1$=1.011×10^{-9}	S_0=1 f_1=0.102 f_2=0.703 f_3=0.195 $d_\parallel$=1.743×10^{-9} θ=1.512 ϕ=0.019 R=2.844×10^{-6} $d\perp_1$=1.037×10^{-9}	S_0=1.027 f_1=0.090 f_2=0.460 f_3=0.448 $d_\parallel$=2.607×10^{-9} θ=1.518 ϕ=0.022 R=1.954×10^{-7} $d\perp_1$=1.119×10^{-9}	S_0=1.022 f_1=0.066 f_2=0.767 f_3=0.167 $d_\parallel$=1.674×10^{-9} θ=1.543 ϕ=0.022 R=5.355×10^{-6} $d\perp_1$=1.037×10^{-9}	0.920	0.7677
TensorCylinderAstrosticks	S_0=1.028 f_1=0.102 f_2=0.476 f_3=0.422 $d_\parallel$=2.477×10^{-9} θ=1.496 ϕ=-3.142 R=3.177×10^{-6} $d\perp_1$=1.812×10^{-9} $d\perp_2$=5.566×10^{-10} α= 5.552	S_0=1 f_1=0.060 f_2=0.786 f_3=0.154 $d_\parallel$=1.687×10^{-9} θ=1.698 ϕ=-3.142 R=1.016×10^{-7} $d\perp_1$=1.599×10^{-9} $d\perp_2$=3.448×10^{-10} α= -18	S_0=1.028 f_1=0.098 f_2=0.488 f_3=0.414 $d_\parallel$=2.507×10^{-9} θ=1.493 ϕ=-3.145 R=3.283×10^{-6} $d\perp_1$=1.822×10^{-9} $d\perp_2$=5.387×10^{-10} α= 5.55	S_0=1.022 f_1=0.055 f_2=0.792 f_3=0.152 $d_\parallel$=1.697×10^{-9} θ=1.793 ϕ=-3.142 R=1.007×10^{-7} $d\perp_1$=1.6×10^{-9} $d\perp_2$=3.458×10^{-10} α= -18.08	0.910	0.741
BallGDRCylindersAstrosticks	S_0=1 f_1=0.342 f_2=0.362 f_3=0.295 k = 2.407 ϑ = 1×10^{-7} $d_\parallel$=2.056×10^{-9} θ=1.852 ϕ=-0.254	S_0=1 f_1=0.215 f_2=0.668 f_3=0.117 k = 1.033 ϑ = 1.568×10^{-7} $d_\parallel$=1.368×10^{-9} θ=1.634 ϕ=-3.545	S_0=1.185 f_1=0.343 f_2=0.362 f_3=0.295 k = 2.407 ϑ = 1.001×10^{-7} $d_\parallel$=2.056×10^{-9} θ=1.853 ϕ=-3.142	S_0=1.068 f_1=0.270 f_2=0.684 f_3=0.046 k = 0.945 ϑ = 2.258×10^{-7} $d_\parallel$=1.371×10^{-9} θ=1.948 ϕ=-3.213	1.047	0.890
ZeppelinGDRCylindersAstrosticks	S_0=1 f_1=0.141 f_2=0.555 f_3=0.304 k = 0.902 ϑ = 1.952×10^{-7} $d_\parallel$=1.952×10^{-9} θ=1.504 ϕ=-3.026 $d\perp_1$=1.185×10^{-9}	S_0=1 f_1=0.101 f_2=0.532 f_3=0.306 k = 1.002 ϑ = 1.897×10^{-7} $d_\parallel$=1.989×10^{-9} θ=1.634 ϕ=-3.236 $d\perp_1$=8.885×10^{-10}	S_0=1.035 f_1=0.080 f_2=0.655 f_3=0.265 k = 1.061 ϑ = 2.248×10^{-7} $d_\parallel$=1.744×10^{-9} θ=1.475 ϕ=-3.145 $d\perp_1$=1.024×10^{-9}	S_0=1.042 f_1=0.063 f_2=0.523 f_3=0.414 k = 0.966 ϑ = 2.011×10^{-7} $d_\parallel$=1.712×10^{-9} θ=1.675 ϕ=-3.201 $d\perp_1$=1.688×10^{-10}	0.962	0.786
TensorGDRCylindersAstrosticks	S_0=1 f_1=0.050 f_2=0.410 f_3=0.540 k = 0.944 ϑ = 8.223×10^{-7} $d_\parallel$=3.125×10^{-9} θ=1.457 ϕ=-3.167 $d\perp_1$=9.663×10^{-10} $d\perp_2$=5.432×10^{-10} α=6.234	S_0=1 f_1=0.070 f_2=0.784 f_3=0.146 k = 0.865 ϑ = 2.214×10^{-7} $d_\parallel$=1.674×10^{-9} θ=1.765 ϕ=-3.267 $d\perp_1$=1.536×10^{-10} $d\perp_2$=5.965×10^{-10} α=-13.135	S_0=1.035 f_1=0.048 f_2=0.412 f_3=0.540 k = 0.921 ϑ = 8.283×10^{-7} $d_\parallel$=3.192×10^{-9} θ=1.494 ϕ=-3.192 $d\perp_1$=8.435×10^{-10} $d\perp_2$=5.566×10^{-10} α=6.141	S_0=1.040 f_1=0.072 f_2=0.783 f_3=0.145 k = 0.813 ϑ = 2.476×10^{-7} $d_\parallel$=1.680×10^{-9} θ=1.744 ϕ=-3.288 $d\perp_1$=1.443×10^{-10} $d\perp_2$=5.854×10^{-10} α=-13.291	0.907	0.740

Table C.3: *Fitted parameters for the three-compartment astrosticks models.*

Models	Startpoint		Best Estimates		FOBJ	
	dataset A	dataset B	dataset A	dataset B	dataset A	dataset B
BallStickAstrocylinders	S_0=1 f_1=0.249 f_2=0.387 f_3=0.362 $d_{\|\|}$=2.116×10^{-9} θ=1.848 ϕ=-0.25 R=2.531×10^{-6}	S_0=1.025 f_1=0.245 f_2=0.076 f_3=0.677 $d_{\|\|}$=1.551×10^{-9} θ=1.228 ϕ=-2.827 R=1.885×10^{-5}	S_0=1 f_1=0.265 f_2=0.103 f_3=0.632 $d_{\|\|}$=1.477×10^{-9} θ=1.438 ϕ=-2.246 R=2.002×10^{-5}	S_0=1.025 f_1=0.245 f_2=0.076 f_3=0.677 $d_{\|\|}$=1.551×10^{-9} θ=1.228 ϕ=-2.827 R=1.885×10^{-5}	1.044	0.869
ZeppelinStickAstrocylinders	S_0=1 f_1=0.122 f_2=0.742 f_3=0.136 $d_{\|\|}$=2.621×10^{-9} θ=1.544 ϕ=-3.121 R=4.633×10^{-6} $d\perp_1$=1.156×10^{-9}	S_0=1 f_1=0.047 f_2=0.730 f_3=0.223 $d_{\|\|}$=1.622×10^{-9} θ=1.547 ϕ=-3.124 R=4.788×10^{-6} $d\perp_1$=9.566×10^{-10}	S_0=1.030 f_1=0.107 f_2=0.448 f_3=0.445 $d_{\|\|}$=2.598×10^{-9} θ=1.485 ϕ=-3.142 R=2.855×10^{-6} $d\perp_1$=1.209×10^{-9}	S_0=1.020 f_1=0.043 f_2=0.763 f_3=0.194 $d_{\|\|}$=1.655×10^{-9} θ=1.606 ϕ=-3.118 R=5.087×10^{-6} $d\perp_1$=9.960×10^{-10}	0.911	0.753
TensorStickAstrocylinders	S_0=1 f_1=0.115 f_2=0.465 f_3=0.420 $d_{\|\|}$=2.634×10^{-10} θ=1.533 ϕ=-3.327 R=2.766×10^{-6} $d\perp_1$=2.433×10^{-9} $d\perp_2$=3.877×10^{-11} α=3.887	S_0=1.023 f_1=0.057 f_2=0.723 f_3=0.220 $d_{\|\|}$=1.727×10^{-9} θ=1.633 ϕ=-3.321 R=5.322×10^{-6} $d\perp_1$=1.710×10^{-9} $d\perp_2$=3.247×10^{-10} α=-2.42	S_0=1.029 f_1=0.109 f_2=0.463 f_3=0.428 $d_{\|\|}$=2.509×10^{-10} θ=1.492 ϕ=-3.276 R=2.808×10^{-6} $d\perp_1$=2.308×10^{-9} $d\perp_2$=4.021×10^{-11} α=3.892	S_0=1.023 f_1=0.061 f_2=0.724 f_3=0.214 $d_{\|\|}$=1.724×10^{-9} θ=1.654 ϕ=-3.234 R=5.447×10^{-6} $d\perp_1$=1.705×10^{-9} $d\perp_2$=3.200×10^{-10} α=-2.388	0.902	0.729
BallCylinderAstrocylinders	S_0=1 f_1=0.253 f_2=0.424 f_3=0.322 $d_{\|\|}$=2.246×10^{-9} θ=1.35 ϕ=-0.209 R=1.243×10^{-6}	S_0=1 f_1=0.240 f_2=0.653 f_3=0.107 $d_{\|\|}$=1.397×10^{-9} θ=1.175 ϕ=-3.455 R=1.755×10^{-7}	S_0=1.038 f_1=0.232 f_2=0.431 f_3=0.335 $d_{\|\|}$=2.038×10^{-9} θ=1.826 ϕ=-0.218 R=1.031×10^{-7}	S_0=1.028 f_1=0.252 f_2=0.679 f_3=0.067 $d_{\|\|}$=1.428×10^{-9} θ=1.187 ϕ=-3.495 R=1.925×10^{-7}	1.050	0.893
ZeppelinCylinderAstrocylinders	S_0=1 f_1=0.201 f_2=0.427 f_3=0.372 $d_{\|\|}$=2.165×10^{-9} θ=1.544 ϕ=-0.267 R=2.074×10^{-6} $d\perp_1$=2.003×10^{-9}	S_0=1 f_1=0.105 f_2=0.678 f_3=0.217 $d_{\|\|}$=1.533×10^{-9} θ=1.478 ϕ=-3.176 R=4.102×10^{-6} $d\perp_1$=1.121×10^{-9}	S_0=1.03 f_1=0.106 f_2=0.478 f_3=0.414 $d_{\|\|}$=2.462×10^{-9} θ=1.518 ϕ=-0.221 R=2.182×10^{-6} $d\perp_1$=1.211×10^{-9}	S_0=1.020 f_1=0.05 f_2=0.760 f_3=0.190 $d_{\|\|}$=1.659×10^{-9} θ=1.613 ϕ=-3.141 R=4.416×10^{-6} $d\perp_1$=1×10^{-9}	0.912	0.7600
TensorCylinderAstrocylinders	S_0=1 f_1=0.110 f_2=0.470 f_3=0.420 $d_{\|\|}$=2.466×10^{-9} θ=1.489 ϕ=-3.141 R=2.064×10^{-6} $d\perp_1$=2.286×10^{-9} $d\perp_2$=1.193×10^{-10} α=5.530	S_0=1 f_1=0.054 f_2=0.760 f_3=0.186 $d_{\|\|}$=1.724×10^{-9} θ=1.764 ϕ=-3.164 R=3.933×10^{-6} $d\perp_1$=1.700×10^{-9} $d\perp_2$=3.101×10^{-10} α=-22.7	S_0=1.029 f_1=0.110 f_2=0.473 f_3=0.416 $d_{\|\|}$=2.493×10^{-9} θ=1.491 ϕ=-3.141 R=2.059×10^{-6} $d\perp_1$=2.301×10^{-9} $d\perp_2$=1.199×10^{-10} α=5.535	S_0=1.022 f_1=0.056 f_2=0.758 f_3=0.186 $d_{\|\|}$=1.713×10^{-9} θ=1.728 ϕ=-3.221 R=3.956×10^{-6} $d\perp_1$=1.700×10^{-9} $d\perp_2$=3.16×10^{-10} α=-22.7	0.905	0.736
BallGDRCylindersAstrocylinders	S_0=1 f_1=0.361 f_2=0.356 f_3=0.282 k= 0.607 ϑ= 1.006×10^{-7} $d_{\|\|}$=2.266×10^{-9} θ=1.352 ϕ=-0.199 R=6.115×10^{-8}	S_0=1 f_1=0.417 f_2=0.358 f_3=0.225 k= 1.004 ϑ= 1.603×10^{-5} $d_{\|\|}$=1.417×10^{-9} θ=1.498 ϕ=-3.141 R=1.42×10^{-5}	S_0=1.157 f_1=0.319 f_2=0.376 f_3=0.303 k= 0.746 ϑ= 1.051×10^{-7} $d_{\|\|}$=2.282×10^{-9} θ=1.351 ϕ=-0.2 R=8×10^{-8}	S_0=1.103 f_1=0.421 f_2=0.382 f_3=0.197 k= 0.955 ϑ= 1.489×10^{-5} $d_{\|\|}$=1.476×10^{-9} θ=1.553 ϕ=-3.141 R=1.42×10^{-5}	1.0768	0.898
ZeppelinGDRCylindersAstrocylinders	S_0=1 f_1=0.076 f_2=0.487 f_3=0.437 k= 1.472 ϑ= 1.633×10^{-6} $d_{\|\|}$=2.483×10^{-9} θ=1.538 ϕ=-3.472 $d\perp_1$=1.167×10^{-9} R=2.377×10^{-6}	S_0=1 f_1=0.074 f_2=0.733 f_3=0.193 k= 0.634 ϑ= 6.738×10^{-6} $d_{\|\|}$=1.642×10^{-9} θ=1.536 ϕ=-3.142 $d\perp_1$=1.102×10^{-9} R=4.694×10^{-6}	S_0=1.044 f_1=0.111 f_2=0.479 f_3=0.409 k= 1.660 ϑ= 1.31×10^{-6} $d_{\|\|}$=2.433×10^{-9} θ=1.608 ϕ=-3.242 $d\perp_1$=1.116×10^{-9} R=2.182×10^{-6}	S_0=1.047 f_1=0.080 f_2=0.730 f_3=0.190 k= 0.673 ϑ= 7.319×10^{-6} $d_{\|\|}$=1.641×10^{-9} θ=1.538 ϕ=-3.142 $d\perp_1$=1.064×10^{-9} R=4.931×10^{-6}	0.915	0.762
TensorGDRCylindersAstrocylinders	S_0=1 f_1=0.048 f_2=0.322 f_3=0.628 k = 1.467 ϑ = 1.981×10^{-6} $d_{\|\|}$=3.922×10^{-9} θ=7.759 ϕ=-6.613 $d\perp_1$=2.852×10^{-9} $d\perp_2$=1.581×10^{-9} α=3.573 R=2.911×10^{-6}	S_0=1 f_1=0.068 f_2=0.741 f_3=0.191 k = 1.035 ϑ = 4.466×10^{-6} $d_{\|\|}$=1.695×10^{-9} θ=1.654 ϕ=-3.126 $d\perp_1$=1.143×10^{-9} $d\perp_2$=8.566×10^{-10} α= -15.161 R=4.705×10^{-6}	S_0=1.048 f_1=0.060 f_2=0.276 f_3=0.663 k = 1.039 ϑ = 3.532×10^{-6} $d_{\|\|}$=3.921×10^{-9} θ=1.563 ϕ=-2.841 $d\perp_1$=3.901×10^{-9} $d\perp_2$=3.30×10^{-9} α= 0.476 R=3.662×10^{-6}	S_0=1.036 f_1=0.066 f_2=0.742 f_3=0.192 k = 1.024 ϑ = 4.594×10^{-6} $d_{\|\|}$=1.695×10^{-9} θ=1.655 ϕ=-3.124 $d\perp_1$=1.133×10^{-9} $d\perp_2$=8.630×10^{-10} α= -15.159 R=4.703×10^{-6}	0.904	0.734

Table C.4: *Fitted parameters for the three-compartment astrocylinders models.*

Models	Startpoint		Best Estimates		FOBJ	
	dataset A	dataset B	dataset A	dataset B	dataset A	dataset B
BallStickSphere	S_0=1 f_1=0.249 f_2=0.387 f_3=0.363 $d_{\|\|}$=2.116×10^{-9} θ=1.848 ϕ=-0.246 R=2.852×10^{-6}	S_0=1 f_1=0.311 f_2=0.132 f_3=0.557 $d_{\|\|}$=1.470×10^{-9} θ=1.187 ϕ=-2.533 R=1.744×10^{-5}	S_0=1.037 f_1=0.249 f_2=0.387 f_3=0.363 $d_{\|\|}$=2.116×10^{-9} θ=1.842 ϕ=-0.247 R=2.852×10^{-6}	S_0=1.025 f_1=0.246 f_2=0.122 f_3=0.631 $d_{\|\|}$=1.540×10^{-9} θ=1.218 ϕ=-2.825 R=2.001×10^{-5}	1.044	0.870
ZeppelinStickSphere	S_0=1 f_1=0.105 f_2=0.478 f_3=0.422 $d_{\|\|}$=2.473×10^{-9} θ=1.636 ϕ=-3.142 R=3.0183×10^{-6} $d\perp_1$=1.748×10^{-9}	S_0=1 f_1=0.055 f_2=0.743 f_3=0.202 $d_{\|\|}$=1.701×10^{-9} θ=1.511 ϕ=-3.141 R=6.055×10^{-6} $d\perp_1$=9.987×10^{-10}	S_0=1.026 f_1=0.102 f_2=0.477 f_3=0.421 $d_{\|\|}$=2.476×10^{-9} θ=1.639 ϕ=-3.142 R=3.0186×10^{-6} $d\perp_1$=1.753×10^{-9}	S_0=1.023 f_1=0.052 f_2=0.745 f_3=0.203 $d_{\|\|}$=1.702×10^{-9} θ=1.494 ϕ=-3.141 R=6.052×10^{-6} $d\perp_1$=9.984×10^{-10}	0.9125	0.749
TensorStickSphere	S_0=1 f_1=0.110 f_2=0.464 f_3=0.426 $d_{\|\|}$=2.501×10^{-9} θ=1.492 ϕ=-3.145 R=3.156×10^{-6} $d\perp_1$=2.339×10^{-9} $d\perp_2$=3.165×10^{-11} α=7.035	S_0=1 f_1=0.060 f_2=0.726 f_3=0.214 $d_{\|\|}$=1.717×10^{-9} θ=1.523 ϕ=-3.215 R=6.076×10^{-6} $d\perp_1$=1.710×10^{-9} $d\perp_2$=3.493×10^{-10} α=-2.382	S_0=1.029 f_1=0.110 f_2=0.463 f_3=0.427 $d_{\|\|}$=2.502×10^{-9} θ=1.492 ϕ=-3.145 R=3.156×10^{-6} $d\perp_1$=2.338×10^{-9} $d\perp_2$=3.174×10^{-11} α=7.036	S_0=1.023 f_1=0.062 f_2=0.725 f_3=0.213 $d_{\|\|}$=1.721×10^{-9} θ=1.464 ϕ=-3.146 R=6.124×10^{-6} $d\perp_1$=1.733×10^{-9} $d\perp_2$=3.226×10^{-10} α=-2.388	0.902	0.729
BallCylinderSphere	S_0=1 f_1=0.239 f_2=0.460 f_3=0.300 $d_{\|\|}$=2.117×10^{-9} θ=1.359 ϕ=-0.19 R=6.673×10^{-7}	S_0=1 f_1=0.227 f_2=0.638 f_3=0.135 $d_{\|\|}$=1.438×10^{-9} θ=1.357 ϕ=-3.432 R=2.003×10^{-7}	S_0=1.037 f_1=0.245 f_2=0.409 f_3=0.345 $d_{\|\|}$=2.088×10^{-9} θ=4.436 ϕ=2.895 R=1.144×10^{-7}	S_0=1.030 f_1=0.259 f_2=0.662 f_3=0.078 $d_{\|\|}$=1.460×10^{-9} θ=1.177 ϕ=-3.512 R=1×10^{-7}	1.0472	0.8930
ZeppelinCylinderSphere	S_0=1 f_1=0.167 f_2=0.428 f_3=0.405 $d_{\|\|}$=2.133×10^{-9} θ=1.576 ϕ=-6.446 R=1.177×10^{-6} $d\perp_1$=1.368×10^{-9}	S_0=1 f_1=0.053 f_2=0.716 f_3=0.231 $d_{\|\|}$=1.660×10^{-9} θ=1.576 ϕ=-3.147 R=3.733×10^{-6} $d\perp_1$=9.997×10^{-10}	S_0=1.028 f_1=0.108 f_2=0.484 f_3=0.407 $d_{\|\|}$=2.429×10^{-9} θ=1.516 ϕ=-6.283 R=1.093×10^{-6} $d\perp_1$=1.234×10^{-9}	S_0=1.021 f_1=0.041 f_2=0.799 f_3=0.160 $d_{\|\|}$=1.656×10^{-9} θ=1.633 ϕ=-3.141 R=3.663×10^{-6} $d\perp_1$=9.831×10^{-10}	0.915	0.7612
TensorCylinderSphere	S_0=1 f_1=0.115 f_2=0.466 f_3=0.419 $d_{\|\|}$=2.346×10^{-9} θ=1.453 ϕ=-3.175 R=1.877×10^{-6} $d\perp_1$=2.032×10^{-9} $d\perp_2$=3.457×10^{-10} α=5.536	S_0=1 f_1=0.065 f_2=0.754 f_3=0.181 $d_{\|\|}$=1.743×10^{-9} θ=1.765 ϕ=-3.263 R=4.281×10^{-6} $d\perp_1$=1.589×10^{-9} $d\perp_2$=3.766×10^{-10} α=-19.573	S_0=1.029 f_1=0.110 f_2=0.475 f_3=0.415 $d_{\|\|}$=2.492×10^{-9} θ=1.492 ϕ=-3.211 R=1.921×10^{-6} $d\perp_1$=2.109×10^{-9} $d\perp_2$=2.424×10^{-10} α=5.532	S_0=1.022 f_1=0.057 f_2=0.763 f_3=0.180 $d_{\|\|}$=1.709×10^{-9} θ=1.741 ϕ=-3.244 R=4.075×10^{-6} $d\perp_1$=1.694×10^{-9} $d\perp_2$=3.125×10^{-10} α=-19.604	0.903	0.728
BallGDRCylindersSphere	S_0=1 f_1=0.346 f_2=0.409 f_3=0.244 k= 0.623 ϑ= 6.408×10^{-7} $d_{\|\|}$=2.019×10^{-9} θ=1.368 ϕ=-0.175 R=3.998×10^{-7}	S_0=1 f_1=0.510 f_2=0.390 f_3=0.100 k= 0.467 ϑ= 1.876×10^{-5} $d_{\|\|}$=1.473×10^{-9} θ=1.752 ϕ=-3.142 R=8.004×10^{-6}	S_0=1.211 f_1=0.346 f_2=0.409 f_3=0.244 k= 0.623 ϑ= 6.408×10^{-7} $d_{\|\|}$=2.019×10^{-9} θ=1.369 ϕ=-0.175 R=3.998×10^{-7}	S_0=1.507 f_1=0.510 f_2=0.383 f_3=0.106 k= 0.399 ϑ= 2×10^{-5} $d_{\|\|}$=1.472×10^{-9} θ=1.922 ϕ=-3.143 R=8.04×10^{-6}	1.044	0.884
ZeppelinGDRCylindersSphere	S_0=1 f_1=0.110 f_2= 0.478 f_3=0.412 k= 1.466 ϑ= 1.683×10^{-6} $d_{\|\|}$=2.466×10^{-9} θ=1.587 ϕ=-3.141 $d\perp_1$=1.078×10^{-9} R=2.644×10^{-6}	S_0=1 f_1=0.015 f_2= 0.323 f_3=0.662 k= 2.166 ϑ= 1.213×10^{-5} $d_{\|\|}$=1.532×10^{-9} θ=1.466 ϕ=-3.141 $d\perp_1$=2.413×10^{-10} R=2.544×10^{-5}	S_0=1.047 f_1=0.113 f_2= 0.475 f_3=0.410 k= 1.566 ϑ= 1.711×10^{-6} $d_{\|\|}$=2.448×10^{-9} θ=1.606 ϕ=-3.141 $d\perp_1$=1.156×10^{-9} R=2.684×10^{-6}	S_0=1.023 f_1=0.001 f_2= 0.304 f_3=0.695 k= 2.285 ϑ= 1.181×10^{-5} $d_{\|\|}$=1.527×10^{-9} θ=1.445 ϕ=-3.142 $d\perp_1$=2.474×10^{-10} R=2.657×10^{-5}	0.917	0.776
TensorGDRCylindersSphere	S_0=1 f_1=0.139 f_2=0.458 f_3=0.403 k = 1.047 ϑ = 2.228×10^{-6} $d_{\|\|}$=2.486×10^{-9} θ=1.492 ϕ=-3.153 $d\perp_1$=2.292×10^{-9} $d\perp_2$=1.301×10^{-10} α=5.531 R=2.393×10^{-6}	S_0=1 f_1=0.127 f_2=0.674 f_3=0.199 k = 0.520 ϑ = 1.112×10^{-5} $d_{\|\|}$=1.725×10^{-9} θ=1.645 ϕ=-3.127 $d\perp_1$=1.128×10^{-9} $d\perp_2$=8.233×10^{-10} α=-15.115 R=5.463×10^{-6}	S_0=1.060 f_1=0.138 f_2=0.459 f_3=0.403 k = 1.047 ϑ = 2.228×10^{-6} $d_{\|\|}$=2.487×10^{-9} θ=1.492 ϕ=-3.154 $d\perp_1$=2.292×10^{-9} $d\perp_2$=1.286×10^{-10} α=5.532 R=2.393×10^{-6}	S_0=1.079 f_1=0.103 f_2=0.701 f_3=0.196 k = 0.514 ϑ = 1.059×10^{-5} $d_{\|\|}$=1.725×10^{-9} θ=1.662 ϕ=-3.132 $d\perp_1$=1.154×10^{-9} $d\perp_2$=8.471×10^{-10} α=-15.132 R=5.452×10^{-6}	0.902	0.733

Table C.5: *Fitted parameters for the three-compartment Sphere models.*

Appendix D

Imaging Protocols

Delta (s)	**delta (s)**	$\|G\|$**(T/m)**	**TE (s)**	**TR (s)**
0.01000	0.00300	0.04000	0.02092	3.00000
0.01000	0.00300	0.08000	0.02093	3.00000
0.03000	0.00300	0.04000	0.02095	3.00000
0.05000	0.00300	0.04000	0.02096	3.00000
0.01000	0.00300	0.12000	0.02098	3.00000
0.07000	0.00300	0.04000	0.02092	3.00000
0.08000	0.00300	0.04000	0.02092	3.00000
0.01000	0.00300	0.16000	0.02092	3.00000
0.03000	0.00300	0.08000	0.02092	3.00000
0.10000	0.00300	0.04000	0.02092	3.00000
0.01000	0.00300	0.20000	0.02092	3.00000
0.05000	0.00300	0.08000	0.02092	3.00000
0.01000	0.00300	0.24000	0.02092	3.00000
0.03000	0.00300	0.12000	0.02092	3.00000
0.07000	0.00300	0.08000	0.02092	3.00000
0.03000	0.01000	0.04000	0.04045	3.00000
0.01000	0.00300	0.28000	0.02092	3.00000
0.08000	0.00300	0.08000	0.02092	3.00000
0.01000	0.00300	0.32000	0.02092	3.00000
0.05000	0.00300	0.12000	0.02092	3.00000
0.03000	0.00300	0.16000	0.02092	3.00000
0.10000	0.00300	0.08000	0.02092	3.00000
0.01000	0.00300	0.36000	0.02092	3.00000
0.05000	0.01000	0.04000	0.04045	3.00000
0.07000	0.00300	0.12000	0.02092	3.00000
0.01000	0.00300	0.40000	0.02092	3.00000
0.03000	0.00300	0.20000	0.02092	3.00000
0.07000	0.01000	0.04000	0.04045	3.00000
0.05000	0.00300	0.16000	0.02092	3.00000
0.08000	0.00300	0.12000	0.02092	3.00000
0.03000	0.00300	0.24000	0.02092	3.00000
0.08000	0.01000	0.04000	0.04045	3.00000
0.10000	0.00300	0.12000	0.02092	3.00000
0.03000	0.02000	0.04000	0.06042	3.00000
0.07000	0.00300	0.16000	0.02092	3.00000

Table D.1: *Imaging protocol for biological phantom DW-MRI experiment Part A.*

Delta (s)	**delta (s)**	$\|G\|$**(T/m)**	**TE (s)**	**TR (s)**
0.03000	0.01000	0.08000	0.04045	3.00000
0.05000	0.00300	0.20000	0.02092	3.00000
0.10000	0.01000	0.04000	0.04045	3.00000
0.03000	0.00300	0.28000	0.02092	3.00000
0.08000	0.00300	0.16000	0.02092	3.00000
0.07000	0.00300	0.20000	0.02092	3.00000
0.05000	0.00300	0.24000	0.02092	3.00000
0.03000	0.00300	0.32000	0.02092	3.00000
0.10000	0.00300	0.16000	0.02092	3.00000
0.05000	0.02000	0.04000	0.06042	3.00000
0.05000	0.01000	0.08000	0.04045	3.00000
0.03000	0.00300	0.36000	0.02092	3.00000
0.08000	0.00300	0.20000	0.02092	3.00000
0.10000	0.00300	0.28000	0.02092	3.00000
0.07000	0.02000	0.24000	0.06042	3.00000
0.03000	0.01000	0.12000	0.04045	3.00000
0.03000	0.00300	0.40000	0.02092	3.00000
0.10000	0.00300	0.20000	0.02092	3.00000
0.07000	0.02000	0.04000	0.06042	3.00000
0.07000	0.01000	0.08000	0.04045	3.00000
0.05000	0.00300	0.32000	0.02092	3.00000
0.08000	0.00300	0.24000	0.02092	3.00000
0.07000	0.00300	0.28000	0.02092	3.00000
0.08000	0.02000	0.04000	0.06042	3.00000
0.05000	0.00300	0.36000	0.02092	3.00000
0.08000	0.01000	0.08000	0.04045	3.00000
0.10000	0.00300	0.24000	0.02092	3.00000
0.03000	0.02000	0.08000	0.06042	3.00000
0.08000	0.00300	0.28000	0.02092	3.00000

Table D.2: *Imaging protocol for biological phantom DW-MRI experiment Part B.*

x	y	z
1	0	0
0	0	1

Table D.3: *Gradient directions for the biological phantom DW-MRI experiment.*

Delta (s)	**delta (s)**	$\|G\|$**(T/m)**	**TE (s)**	**TR (s)**
0.01000	0.00300	0.04000	0.02020	2.00000
0.01000	0.00300	0.08000	0.02022	2.00000
0.01000	0.00300	0.12000	0.02023	2.00000
0.01000	0.00300	0.16000	0.02025	3.00000
0.01000	0.00300	0.20000	0.02026	3.00000
0.01000	0.00300	0.24000	0.02028	3.00000
0.01000	0.00300	0.28000	0.02030	3.00000
0.01000	0.00300	0.32000	0.02031	3.00000
0.01000	0.00300	0.36000	0.02033	3.00000
0.01000	0.00300	0.40000	0.02034	3.00000
0.02000	0.00300	0.04000	0.02985	2.00000
0.02000	0.00300	0.08000	0.02986	2.00000
0.02000	0.00300	0.12000	0.02987	2.00000
0.02000	0.00300	0.16000	0.02988	3.00000
0.02000	0.00300	0.20000	0.02989	3.00000
0.02000	0.00300	0.24000	0.02990	3.00000
0.02000	0.00300	0.28000	0.02991	3.00000
0.02000	0.00300	0.32000	0.02992	3.00000
0.02000	0.00300	0.36000	0.03985	3.00000
0.02000	0.00300	0.40000	0.03986	3.00000
0.03000	0.00300	0.04000	0.03987	2.00000
0.03000	0.00300	0.08000	0.03988	2.00000
0.03000	0.00300	0.12000	0.03989	2.00000
0.03000	0.00300	0.16000	0.03990	3.00000
0.03000	0.00300	0.20000	0.03991	3.00000
0.03000	0.00300	0.24000	0.03992	3.00000
0.03000	0.00300	0.28000	0.04985	3.00000
0.03000	0.00300	0.32000	0.04986	3.00000
0.03000	0.00300	0.36000	0.04987	3.00000
0.03000	0.00300	0.40000	0.04988	3.00000
0.04000	0.00300	0.04000	0.04989	3.00000
0.04000	0.00300	0.08000	0.04990	3.00000
0.04000	0.00300	0.12000	0.04991	3.00000
0.04000	0.00300	0.16000	0.04992	3.00000

Table D.4: *Imaging protocol for fixed brain DW-MRI experiment Part A.*

Delta (s)	**delta (s)**	$\|G\|$**(T/m)**	**TE (s)**	**TR (s)**
0.04000	0.00300	0.20000	0.05985	3.00000
0.04000	0.00300	0.24000	0.05986	3.00000
0.04000	0.00300	0.28000	0.05987	3.00000
0.04000	0.00300	0.32000	0.05988	3.00000
0.04000	0.00300	0.36000	0.05989	3.00000
0.04000	0.00300	0.40000	0.05990	3.00000
0.04000	0.03000	0.04000	0.05991	3.00000
0.04000	0.03000	0.08000	0.05992	3.00000
0.04000	0.03000	0.12000	0.07685	3.00000
0.04000	0.03000	0.16000	0.07686	3.00000
0.04000	0.03000	0.20000	0.07687	3.00000
0.05000	0.00300	0.04000	0.07688	3.00000
0.05000	0.00300	0.08000	0.08685	3.00000
0.05000	0.00300	0.12000	0.08686	3.00000
0.05000	0.00300	0.16000	0.08687	3.00000
0.05000	0.00300	0.20000	0.08688	3.00000
0.05000	0.00300	0.24000	0.08685	3.00000
0.05000	0.00300	0.28000	0.08686	3.00000
0.05000	0.00300	0.32000	0.08687	3.00000
0.05000	0.00300	0.36000	0.08688	3.00000
0.05000	0.00300	0.40000	0.08685	3.00000
0.05000	0.03000	0.04000	0.08686	3.00000
0.05000	0.03000	0.08000	0.08687	3.00000
0.05000	0.03000	0.12000	0.08688	3.00000
0.05000	0.03000	0.16000	0.08688	3.00000

Table D.5: *Imaging protocol for fixed brain DW-MRI experiment Part B.*

x	y	z
0	1	0
1	0	0
-0.7071	0	0.7071
0	0	1
0.7071	0	0.7071

Table D.6: *Gradient directions for the fixed brain DW-MRI experiment.*

Delta (s)	delta (s)	$\|G\|$(T/m)	TE (s)	TR (s)
0.01000	0.00300	0.03000	0.01976	3.00000
0.01000	0.00300	0.06000	0.01976	3.00000
0.01000	0.00300	0.09000	0.01976	3.00000
0.01000	0.00300	0.12000	0.01976	3.00000
0.01000	0.00300	0.15000	0.01976	3.00000
0.01000	0.00300	0.18000	0.01976	3.00000
0.01000	0.00300	0.21000	0.01976	3.00000
0.01000	0.00300	0.24000	0.01976	3.00000
0.01000	0.00300	0.27000	0.01976	3.00000
0.01000	0.00300	0.30000	0.01976	3.00000
0.02000	0.00300	0.03000	0.01976	3.00000
0.02000	0.00300	0.06000	0.01976	3.00000
0.02000	0.00300	0.09000	0.01976	3.00000
0.02000	0.00300	0.12000	0.01976	3.00000
0.02000	0.00300	0.15000	0.01976	3.00000
0.02000	0.00300	0.18000	0.01976	3.00000
0.02000	0.00300	0.21000	0.01976	3.00000
0.02000	0.00300	0.24000	0.01976	3.00000
0.02000	0.00300	0.27000	0.01976	3.00000
0.02000	0.00300	0.30000	0.01976	3.00000
0.03000	0.00300	0.03000	0.01976	3.00000
0.03000	0.00300	0.06000	0.01976	3.00000
0.03000	0.00300	0.09000	0.01976	3.00000
0.03000	0.00300	0.12000	0.01976	3.00000
0.03000	0.00300	0.15000	0.01976	3.00000
0.03000	0.00300	0.18000	0.01976	3.00000
0.03000	0.00300	0.21000	0.01976	3.00000
0.03000	0.00300	0.24000	0.01976	3.00000
0.03000	0.00300	0.27000	0.01976	3.00000
0.03000	0.00300	0.30000	0.01976	3.00000
0.03000	0.01200	0.03000	0.03776	3.00000
0.03000	0.01200	0.06000	0.03776	3.00000
0.03000	0.01200	0.09000	0.03776	3.00000
0.03000	0.01200	0.12000	0.03776	3.00000
0.03000	0.01200	0.15000	0.03776	3.00000
0.03000	0.01200	0.18000	0.03776	3.00000
0.04000	0.00300	0.03000	0.01976	3.00000

Table D.7: *Imaging protocol for in vivo rat DW-MRI experiment Part A.*

Delta (s)	**delta (s)**	$\|G\|$**(T/m)**	**TE (s)**	**TR (s)**
0.04000	0.00300	0.06000	0.01976	3.00000
0.04000	0.00300	0.09000	0.01976	3.00000
0.04000	0.00300	0.12000	0.01976	3.00000
0.04000	0.00300	0.15000	0.01976	3.00000
0.04000	0.00300	0.18000	0.01976	3.00000
0.04000	0.00300	0.21000	0.01976	3.00000
0.04000	0.00300	0.24000	0.01976	3.00000
0.04000	0.00300	0.27000	0.01976	3.00000
0.04000	0.00300	0.30000	0.01976	3.00000
0.04000	0.01200	0.03000	0.03776	3.00000
0.04000	0.01200	0.06000	0.03776	3.00000
0.04000	0.01200	0.09000	0.03776	3.00000
0.04000	0.01200	0.12000	0.03776	3.00000
0.04000	0.01200	0.15000	0.03776	3.00000
0.05000	0.00300	0.03000	0.01976	3.00000
0.05000	0.00300	0.06000	0.01976	3.00000
0.05000	0.00300	0.09000	0.01976	3.00000
0.05000	0.00300	0.12000	0.01976	3.00000
0.05000	0.00300	0.15000	0.01976	3.00000
0.05000	0.00300	0.18000	0.01976	3.00000
0.05000	0.00300	0.21000	0.01976	3.00000
0.05000	0.00300	0.24000	0.01976	3.00000
0.05000	0.00300	0.27000	0.01976	3.00000
0.05000	0.00300	0.30000	0.01976	3.00000
0.05000	0.01200	0.03000	0.03776	3.00000
0.05000	0.01200	0.06000	0.03776	3.00000
0.05000	0.01200	0.09000	0.03776	3.00000
0.05000	0.01200	0.12000	0.03776	3.00000

Table D.8: *Imaging protocol for in vivo rat DW-MRI experiment Part B.*

x	y	z
0	-1	0
1	0	0
0	0	1
0.7071	0	-0.7071

Table D.9: *Gradient directions for the in vivo rat DW-MRI experiment.*

Delta (s)	delta (s)	$\|G\|$(T/m)	TE (s)	TR (s)
0.01000	0.00300	0.04000	0.043	6.00000
0.01000	0.00300	0.08000	0.043	6.00000
0.01000	0.00300	0.12000	0.043	6.00000
0.01000	0.00300	0.16000	0.043	6.00000
0.01000	0.00300	0.20000	0.043	6.00000
0.01000	0.00300	0.24000	0.043	6.00000
0.01000	0.00300	0.28000	0.043	6.00000
0.01000	0.00300	0.32000	0.043	6.00000
0.01000	0.00300	0.36000	0.043	6.00000
0.01500	0.00300	0.04000	0.043	6.00000
0.01500	0.00300	0.08000	0.043	6.00000
0.01500	0.00300	0.12000	0.04226	6.00000
0.01500	0.00300	0.16000	0.043	6.00000
0.01500	0.00300	0.20000	0.043	6.00000
0.01500	0.00300	0.24000	0.043	6.00000
0.01500	0.00300	0.28000	0.043	6.00000
0.01500	0.00300	0.32000	0.043	6.00000
0.01500	0.00300	0.36000	0.043	6.00000
0.02000	0.00300	0.04000	0.050	6.00000
0.02000	0.00300	0.08000	0.050	6.00000
0.02000	0.00300	0.12000	0.050	6.00000
0.02000	0.00300	0.16000	0.050	6.00000
0.02000	0.00300	0.20000	0.050	6.00000
0.02000	0.00300	0.24000	0.050	6.00000
0.02000	0.00300	0.28000	0.050	6.00000
0.02000	0.00300	0.32000	0.050	6.00000
0.02000	0.00300	0.36000	0.050	6.00000
0.02000	0.01500	0.04000	0.074	6.00000
0.02000	0.01500	0.08000	0.050	6.00000
0.02000	0.01500	0.12000	0.050	6.00000
0.02000	0.01500	0.16000	0.050	6.00000
0.02000	0.01500	0.20000	0.050	6.00000
0.02000	0.01500	0.24000	0.050	6.00000
0.02000	0.01500	0.28000	0.050	6.00000
0.02000	0.01500	0.32000	0.050	6.00000

Table D.10: *Imaging protocol for in vivo rat DW-MRI experiment in Copenhagen Part A.*

Delta (s)	**delta (s)**	$\|G\|$**(T/m)**	**TE (s)**	**TR (s)**
0.02500	0.00300	0.04000	0.050	6.00000
0.02500	0.00300	0.08000	0.050	6.00000
0.02500	0.00300	0.12000	0.050	6.00000
0.02500	0.00300	0.16000	0.050	6.00000
0.02500	0.00300	0.20000	0.050	6.00000
0.02500	0.00300	0.24000	0.050	6.00000
0.02500	0.00300	0.28000	0.050	6.00000
0.02500	0.00300	0.32000	0.050	6.00000
0.02500	0.00300	0.36000	0.050	6.00000
0.02500	0.01500	0.04000	0.074	6.00000
0.02500	0.01500	0.08000	0.074	6.00000
0.02500	0.01500	0.12000	0.074	6.00000
0.03500	0.00300	0.04000	0.060	6.00000
0.03500	0.00300	0.08000	0.060	6.00000
0.03500	0.00300	0.12000	0.060	6.00000
0.03500	0.00300	0.16000	0.060	6.00000
0.03500	0.00300	0.20000	0.060	6.00000
0.03500	0.00300	0.24000	0.060	6.00000
0.03500	0.00300	0.28000	0.060	6.00000
0.03500	0.00300	0.32000	0.060	6.00000
0.03500	0.01500	0.04000	0.074	6.00000
0.03500	0.01500	0.08000	0.074	6.00000

Table D.11: *Imaging protocol for in vivo rat DW-MRI experiment in Copenhagen Part B.*

Bibliography

[AAS01] I. Agartz, J.L.R. Andersson, and S. Skare. Abnormal brain white matter in schizophrenia: a diffusion tensor imaging study. *Neuroreport*, 12(10):2251, 2001.

[AB05] Y. Assaf and P.J. Basser. Composite hindered and restricted model of diffusion (CHARMED) MR imaging of the human brain. *Neuroimage*, 27(1):48–58, 2005.

[AB09] N.J. Allen and B.A. Barres. Neuroscience: gliamore than just brain glue. *Nature*, 457(7230):675–677, 2009.

[ABA01] D.C. Alexander, G.J. Barker, and S.R. Arridge. Detection and Modelling of non-Gaussianity in MR Diffusion Imaging. *Relation*, 10(1.127):1025, 2001.

[ABKYB08] Y. Assaf, T. Blumenfeld-Katzir, Y. Yovel, and P. J. Basser. Axcaliber: A method for measuring axon diameter distribution from diffusion MRI. *Magnetic Resonance in Medicine*, 59:1347–1354, 2008.

[AC98] Y. Assaf and Y. Cohen. Non-Mono-Exponential Attenuation of Water andN-Acetyl Aspartate Signals Due to Diffusion in Brain Tissue* 1. *Journal of Magnetic Resonance*, 131(1):69–85, 1998.

[AFNK+08] S. Aja-Fernandez, M. Niethammer, M. Kubicki, M.E. Shenton, and C.F. Westin. Restoration of DWI data using a rician LMMSE estimator. *Medical Imaging, IEEE Transactions on*, 27(10):1389–1403, 2008.

[AFRB04] Y. Assaf, R.Z. Freidlin, G.K. Rohde, and P.J. Basser. New modeling and experimental framework to characterize hindered and restricted water diffusion in brain white matter. *Magnetic Resonance in Medicine*, 52(5):965–978, 2004.

[AHH+10] D.C. Alexander, P.L. Hubbard, M.G. Hall, E.A. Moore, M. Ptito, G.J.M. Parker, and T.B. Dyrby. Orientationally invariant indices of axon diameter and density from diffusion MRI. *NeuroImage*, 2010.

[AHL+01] A.L. Alexander, K.M. Hasan, M. Lazar, J.S. Tsuruda, and D.L. Parker. Analysis of partial volume effects in diffusion-tensor MRI. *Magnetic Resonance in Medicine*, 45(5):770–780, 2001.

[AK00] H. Axer and D.G.v. Keyserlingk. Mapping of fiber orientation in human internal capsule by means of polarized light and confocal scanning laser microscopy. *Journal of Neuroscience Methods*, 94:165–175, 2000.

[Ale07] D. C. Alexander. Axon radius measurements in vivo from diffusion MRI: a feasibility study. *Proc ICCV, MMBIA - workshop*, 2007.

[Ale08] D. C. Alexander. A general framework for experiment design in diffusion MRI and its application in measuring direct tissue-microstructure features. *Magnetic Resonance in Medicine*, 60:439–448, 2008.

[Ale09] D.C. Alexander. Modelling, fitting and sampling in diffusion MRI. *Visualization and Processing of Tensor Fields*, pages 3–20, 2009.

[ALS09] F.A Azevedo, Carvalho L.R, and Grinberg L.T.and Farfel J.M.and Ferretti R.E.and Leite R.E.and Jacob Filho W.and Lent R.and Herculano-Houzel S. Equal numbers of neuronal and nonneuronal cells make the human brain an isometrically scaled-up primate brain. *The Journal of comparative neurology*, 513:532–41, 2009.

[Ana] URL: http://serversbonnett.hostddl.tk.

[ANH+03] B.A. Ardekani, J. Nierenberg, M.J. Hoptman, D.C. Javitt, and K.O. Lim. MRI study of white matter diffusion anisotropy in schizophrenia. *Neuroreport*, 14(16):2025, 2003.

[Arn] http://phym.unige.ch/cmi/docs/arnaudeau-confocal.pdf.

[ASFZ92a] F. Aboitiz, A. B. Scheibel, R. S. Fisher, and E. Zaidel. Fiber composition of the human corpus callosum. *Brain Research*, 598:143–153, 1992.

[ASFZ92b] F. Aboitiz, A. B. Scheibel, R. S. Fisher, and E. Zaidel. Individual differences in brain asymmetries and fiber composition in the human corpus callosum. *Brain Research*, 598:154–161, 1992.

[ASvK99] H. Axer, J. Stegelmeyer, and D. Graf von Keyserlingk. Comparison of tissue impedance measurements with nerve fiber architecture in human telencephalon: value in identification of intact subcortical structures. *J Neurosurg*, 90:902–909, 1999.

[Bam03] R. Bammer. Basic principles of diffusion-weighted imaging. *European Journal of Radiology*, 45(3):169–184, 2003.

[BBA09] D. Barazany, P.J. Basser, and Y. Assaf. In-vivo measurement of the axon diameter distribution in the corpus callosum of a rat brain. *Brain*, 132:1210–1220, 2009.

[Bea02] C. Beaulieu. The basis of anisotropic water diffusion in the nervous system–a technical review. *NMR in Biomedicine*, 15(7-8):435–455, 2002.

[BF09] G.T. Balls and L.R. Frank. A simulation environment for diffusion weighted MR experiments in complex media. *Magnetic Resonance in Medicine*, 62(3), 2009.

[BFF+02] M. Bozzali, A. Falini, M. Franceschi, M. Cercignani, M. Zuffi, G. Scotti, G. Comi, and M. Filippi. White matter damage in Alzheimer's disease assessed in vivo using diffusion tensor magnetic resonance imaging. *Journal of Neurology, Neurosurgery & Psychiatry*, 72(6):742, 2002.

[BJ02] P. J. Basser and D. K. Jones. Diffusion-tensor MRI: theory, experimental design and data analysis - a technical review. *NMR in Biomedicine*, 15:456–467, 2002.

[BKZF05] M.A. Bernstein, K.E. King, X.J. Zhou, and W. Fong. Handbook of MRI pulse sequences. *Medical Physics*, 32:1452, 2005.

[Bla32] C.H. Blasberg. Phases of the anatomy of asparagus officinalis. *Botanical Gazette*, 94(1):206–214, 1932.

[BLEO01] S. Boujraf, R. Luypaert, H. Eisendrath, and M. Osteaux. Echo planar magnetic resonance imaging of anisotropic diffusion in asparagus stems. *Magnetic Resonance Materials in Physics, Biology and Medicine*, 13(2):82–90, 2001.

[BML94] P. J. Basser, J. Mattiello, and D. LeBihan. MR diffusion tensor spectroscopy and imaging. *Biophysical Journal*, 66:259–267, 1994.

[BMP+01] D. L. Bihan, J. Mangin, C. Poupon, C. A. Clark, S. Pappata, N. Molko, and H. Chabriat. Diffusion tensor imaging: Concepts and applications. *Journal of Magnetic Resonance in Medicine*, 13:534–546, 2001.

[BP96a] P. J. Basser and C. Pierpaoli. Microstructural and physiological features of tissues elucidated by quantitative-diffusion-tensor MRI. *Journal of Magnetic Resonance*, 111:209–219, 1996.

[BP96b] P.J. Basser and C. Pierpaoli. Microstructural and physiological features of tissues elucidated by quantitative-diffusion-tensor MRI. *Journal of Magnetic Resonance-Series B*, 111(3):209–219, 1996.

[BS10] M.A. Brown and R.C. Semelka. *MRI: basic principles and applications*. Wiley-Blackwell, 2010.

[BTP+98] M.S. Buchsbaum, C.Y. Tang, S. Peled, H. Gudbjartsson, D. Lu, E.A. Hazlett, J. Downhill, M. Haznedar, J.H. Fallon, and S.W. Atlas. MRI white matter diffusion anisotropy and PET metabolic rate in schizophrenia. *Neuroreport*, 9(3):425, 1998.

[BWJJ03] T. E. J. Behrens, M. W. Woolrich, M. Jenkinson, and H. Johansen. Characterization and propagation of uncertainty in diffusion-weighted MR imaging. *Magnetic Resonance in Medicine*, 50:1077–1088, 2003.

[Cal95] P. T. Callaghan. Pulse-Gradient Spin Echo NMR for planar, cylindrical and spherical pores under conditions of wall relaxation. *Journal of Magnetic Resonance*, Series A 113:53–59, 1995.

[CBNG+06] P. A. Cook, Y. Bai, S. Nedjati-Gilani, K. K. Seunarine, M. G. Hall, G. J. Parker, and D. C. Alexander. Camino: Open source diffusion-MRI reconstruction and processing. *Proc 14th Scientific Meeting of ISMRM, Seatle, WA, USA*, page 2759, 2006.

[CFD06] N.S. Claxton, T.J. Fellers, and M.W. Davidson. Laser scanning confocal microscopy. *Olympus. Available online at http://www. olympusconfocal. com/theory/LSCMIntro. pdf*, 2006.

[CHSM89] R.M. Cotts, M.J.R. Hoch, T. Sun, and J.T. Markert. Pulsed field gradient stimulated echo methods for improved NMR diffusion measurements in heterogeneous systems. *Journal of Magnetic Resonance (1969)*, 83(2):252–266, 1989.

[CL05] J.A. Conchello and J.W. Lichtman. Optical sectioning microscopy. *Nature Methods*, 2(12):920–931, 2005.

[CLB00] C.A. Clark and D. Le Bihan. Water diffusion compartmentation and anisotropy at high b values in the human brain. *Magnetic Resonance in Medicine*, 44(6):852–859, 2000.

[CNH+09] J. Clayden, Z. Nagy, M. Hall, C. Clark, and D. Alexander. Active Imaging with Dual Spin-Echo Diffusion MRI. pages 264–275, 2009.

[CPL00] B. Couteau, Y. Payan, and S. Lavallee. The mesh-matching algorithm: an automatic 3D mesh generator for finite element structures. *Journal of biomechanics*, 33(8):1005–1009, 2000.

[CRSS07] H. Cho, X.H. Ren, E.E. Sigmund, and Y.Q. Song. Rapid measurement of three-dimensional diffusion tensor. *The Journal of chemical physics*, 126:154501, 2007.

[CS95] P.T. Callaghan and J. Stepisnik. Frequency-domain analysis of spin motion using modulated-gradient NMR. *Journal of Magnetic Resonance Series A*, 117:118–122, 1995.

[CWH+02] C.L. Chin, F.W. Wehrli, S.N. Hwang, M. Takahashi, and D.B. Hackney. Biexponential diffusion attenuation in the rat spinal cord: computer simulations based on anatomic images of axonal architecture. *Magnetic Resonance in Medicine*, 47(3):455–460, 2002.

[CWM00] C.A. Clark, D.J. Werring, and D.H. Miller. Diffusion imaging of the spinal cord in vivo: estimation of the principal diffusivities and application to multiple sclerosis. *Magnetic Resonance in Medicine*, 43(1):133–138, 2000.

[DBA+] T.B. Dyrby, W.F.C. Baaré, D.C. Alexander, J. Jelsing, E. Garde, and L.V. Søgaard. An ex vivo imaging pipeline for producing high-quality and high-resolution diffusion-weighted imaging datasets. *Human Brain Mapping*.

[DM58] D. C. Douglass and D. W. McCall. Diffusion in paraffin hydrocarbons. *The Journal of Physical Chemistry*, 62:1102, 1958.

[DMS01] A. Duh, A. Mohoric, and J. Stepisnik. Computer simulation of the spin-echo spatial distribution in the case of restricted self-diffusion. *Journal of Magnetic Resonance*, 148:257–266, 2001.

[DPG03] M.D. Does, E.C. Parsons, and J.C. Gore. Oscillating gradient measurements of water diffusion in normal and globally ischemic rat brain. *Magnetic Resonance in Medicine*, 49(2):206–215, 2003.

[DSA10] I. Drobnjak, B. Siow, and D.C. Alexander. Optimizing gradient waveforms for microstructure sensitivity in diffusion-weighted MR. *Journal of Magnetic Resonance*, 2010.

[DWC+04] Q. Dong, R.C. Welsh, T.L. Chenevert, R.C. Carlos, P. Maly-Sundgren, D.M. Gomez-Hassan, and S.K. Mukherji. Clinical applications of diffusion tensor imaging. *Journal of Magnetic Resonance Imaging*, 19(1):6–18, 2004.

[Ede01] H. Edelsbrunner. *Geometry and topology for mesh generation*. Cambridge Univ Pr, 2001.

[EmsamvI09] J. M. Edgar and I.R. Griffiths. White matter structure: a microscopist's view. In. *In Diffusion MRI: from quantitative measrement to in vivo neuroanatomy.* Academic Press, 2009.

[FH97] J.C. Ford and D.B. Hackney. Numerical model for calculation of apparent diffusion coefficients (ADC) in permeable cylinders-comparison with measured ADC in spinal cord white matter. *Magnetic Resonance in Medicine*, 37(3):387–394, 1997.

[FHA+94] J.C. Ford, D.B. Hackney, D.C. Alsop, H. Jara, P.M. Joseph, C.M. Hand, and P. Black. MRI characterization of diffusion coefficients in a rat spinal cord injury model. *Magnetic Resonance in Medicine*, 31(5):488–494, 1994.

[Fle91] C.A.J. Fletcher. *Computational techniques for fluid dynamics: Fundamental and general techniques*. Springer, 1991.

[Fou22] J.B.J. Fourier. Théorie analytique de la chaleur. *Academie des Sciences*, 1822.

[Fre05] Scott Freeman. *Biological Science and CW+ Grade Tracker Access Card, 2/E*. Benjamin Cummings, 2005.

[GCP+95] F.H. Gage, P.W. Coates, T.D. Palmer, H.G. Kuhn, L.J. Fisher, J.O. Suhonen, D.A. Peterson, S.T. Suhr, and J. Ray. Survival and differentiation of adult neuronal progenitor cells transplanted to the adult brain. *Proceedings of the National Academy of Sciences of the United States of America*, 92(25):11879, 1995.

[GDZM94] P. Van Gelderen, D. Despres, P. C. M. Van Zijl, and C. T. W. Moonen. Evaluation of restricted diffusion in cylinders phosphocreatine in rabbit leg muscle. *Journal of Magnetic Resonance*, Series B 103:255–260, 1994.

[GP95] H. Gudbjartsson and S. Patz. The Rician distribution of noisy MRI data. *Magnetic Resonance in Medicine*, 34(6):910–914, 1995.

[GWDL01] V. Gulani, A.G. Webb, I.D. Duncan, and P.C. Lauterbur. Apparent diffusion tensor measurements in myelin-deficient rat spinal cords. *Magnetic Resonance in Medicine*, 45(2):191–195, 2001.

[HA09] M. G. Hall and D. C. Alexander. Convergence and Parameter Choice for Monte-Carlo Simulations for Diffusion MRI. *IEEE transactions on medical imaging*, 28:1354–1364, 2009.

[HAS+99] H. Hanyu, T. Asano, H. Sakurai, Y. Imon, T. Iwamoto, M. Takasaki, H. Shindo, and K. Abe. Diffusion-weighted and magnetization transfer imaging of the corpus callosum in Alzheimer's disease. *Journal of the neurological sciences*, 167(1):37–44, 1999.

[HCWH03] S.N. Hwang, C.L. Chin, F.W. Wehrli, and D.B. Hackney. An image-based finite difference model for simulating restricted diffusion. *Magnetic Resonance in Medicine*, 50(2):373–382, 2003.

[Hen85] R.M. Henkelman. Measurement of signal intensities in the presence of noise in MR images. *Medical Physics*, 12:232, 1985.

[HHS00] M. Holz, S.R. Heil, and A. Sacco. Temperature-dependent self-diffusion coefficients of water and six selected molecular liquids for calibration in accurate 1 H NMR PFG measurements. *Physical Chemistry Chemical Physics*, 2(20):4740–4742, 2000.

[Hog54] J. Hogg. *The microscope: its history, construction, and applications...* Illustrated London Libr., 1854.

[Hor95] P.J. Hore. Nuclear Magnetic Resonance. *Oxford Chemistry Primers, Oxford Science Publications, Oxford*, 1995.

[HSI+98] H. Hanyu, H. Sakurai, T. Iwamoto, M. Takasaki, H. Shindo, and K. Abe. Diffusion-weighted MR imaging of the hippocampus and temporal white matter in Alzheimer's disease. *Journal of the neurological sciences*, 156(2):195–200, 1998.

[HSK+97] H. Hanyu, H. Shindo, D. Kakizaki, K. Abe, T. Iwamoto, and M. Takasaki. Increased water diffusion in cerebral white matter in Alzheimers disease. *Gerontology*, 43(6):343–351, 1997.

[Hur39] J. B. Hursh. Conduction velocity and diameter of nerve fibers. *American journal of physiology*, 127:131139, 1939.

[JAFK98] S. Jinno, Y. Aika, T. Fukuda, and T. Kosaka. Quantitative analysis of GABAergic neurons in the mouse hippocampus, with optical disector using confocal laser scanning microscope. *Brain research*, 814(1-2):55–70, 1998.

[JB04] D.K. Jones and P.J. Basser. Squashing peanuts and smashing pumpkins: How noise distorts diffusion-weighted MR data. *Magnetic Resonance in Medicine*, 52(5):979–993, 2004.

[JBN+10] S.N. Jespersen, C.R. Bjarkam, J.R. Nyengaard, M.M. Chakravarty, B. Hansen, T. Vosegaard, L. Østergaard, D. Yablonskiy, N.C. Nielsen, and P. Vestergaard-Poulsen. Neurite density from magnetic resonance diffusion measurements at ultrahigh field: comparison with light microscopy and electron microscopy. *Neuroimage*, 49(1):205–216, 2010.

[JHS99] D.K. Jones, M.A. Horsfield, and A. Simmons. Optimal strategies for measuring diffusion in anisotropic systems by magnetic resonance imaging. *Magnetic Resonance in Medicine*, 42(3):515–525, 1999.

[JKØ+07] S.N. Jespersen, C.D. Kroenke, L. Østergaard, J.J.H. Ackerman, and D.A. Yablonskiy. Modeling dendrite density from magnetic resonance diffusion measurements. *NeuroImage*, 34(4):1473–1486, 2007.

[Kay93] S.M. Kay. *Fundamentals of statistical signal processing: estimation theory*. 1993.

[KFCO06] B.M. Klingner, B.E. Feldman, N. Chentanez, and J.F. O'Brien. Fluid animation with dynamic meshes. *ACM Transactions on Graphics (TOG)*, 25(3):825, 2006.

[KPH88] J. Kärger, H. Pfeifer, and W. Heinik. Principles and application of self-diffusion measurements by nuclear magnetic resonance. *Advances in magnetic resonance*, 12:1–89, 1988.

[LB06] D. Le Bihan. Looking into the functional architecture of the brain with diffusion MRI. 1290:1–24, 2006.

[LBAM04] C. Liu, R. Bammer, B. Acar, and M.E. Moseley. Characterizing non-gaussian diffusion by using generalized diffusion tensors. *Magnetic Resonance in Medicine*, 51(5):924–937, 2004.

[LBBL+86] D. Le Bihan, E. Breton, D. Lallemand, P. Grenier, E. Cabanis, and M. Laval-Jeantet. MR imaging of intravoxel incoherent motions: application to diffusion and perfusion in neurologic disorders. *Radiology*, 161(2):401, 1986.

[LBPH08] C. Lobos, M. Bucki, Y. Payan, and N. Hitschfeld. Techniques on mesh generation for the brain shift simulation. In *IFMBE PROCEEDINGS*, volume 18, page 642. Springer, 2008.

[LC87] W. E. Lorensen and H. E. Cline. Marching cubes: A high resolution 3D surface construction algorithm. *Computer Graphics*, 21:Number 4, 1987.

[LFH+08] B.A. Landman, J.A.D. Farrell, H. Huang, J.L. Prince, and S. Mori. Diffusion tensor imaging at low SNR: Nonmonotonic behaviors of tensor contrasts. *Magnetic resonance imaging*, 26(6):790–800, 2008.

[LFS+09] B.A. Landman, J.A.D. Farrell, S.A. Smith, D.S. Reich, P.A. Calabresi, and P.C.M. van Zijl. Complex geometric models of diffusion and relaxation in healthy and damaged white matter. *NMR in biomedicine*, 2009.

[LGG+07] Luiza Larsen, Lewis D. Griffin, David GRel, Otto W. Witte, and Hubertus Axer. Polarized light imaging of white matter architecture. *Microscopy Research and Technique*, 70:851–863, 2007.

[Lip90] H.G. Lipinski. Monte Carlo simulation of extracellular diffusion in brain tissues. *Physics in Medicine and Biology*, 35:441, 1990.

[LLiMS00] Z.P. Liang, P.C. Lauterbur, IEEE Engineering in Medicine, and Biology Society. *Principles of magnetic resonance imaging: a signal processing perspective*. SPIE Optical Engineering Press, 2000.

[LNR+07] J. Lätt, M. Nilsson, A. Rydhög, R. Wirestam, F. Ståhlberg, and S. Brockstedt. Effects of restricted diffusion in a biological phantom: a q-space diffusion MRI study of asparagus stems at a 3T clinical scanner. *Magnetic Resonance Materials in Physics, Biology and Medicine*, 20(4):213–222, 2007.

[LP88] R. Lohner and P. Parikh. Generation of three-dimensional unstructured grids by the advancing-front method. *International Journal for Numerical Methods in Fluids*, 8(10):1135–1149, 1988.

[LR90] A. S. Lamantia and P. Rakic. Cytological and quantitative characteristics of four cerebral commissures in the rhesus monkey. *Journal of comparative neurology*, 291:520–537, 1990.

[LS98] PR Laming and E. Syková. *Glial cells: their role in behaviour*. Cambridge Univ Pr, 1998.

[Mac03] DJC MacKay. *Information theory, inference, and learning algorithms*. Cambridge University Press, 2003.

[MB49] A.A. Maximow and W. Bloo. A textbook of histology. *The American Journal of the Medical Sciences*, 218, Issue 5:598, 1949.

[MC84] J. S. Murday and R. M. Cotts. Self-diffusion coefficient of liquid lithium. *Journal of Chemical Physics*, 48:4938–4945, 1984.

[MHF91] K.D. Merboldt, W. Hänicke, and J. Frahm. Diffusion imaging using stimulated echoes. *Magnetic Resonance in Medicine*, 19(2):233–239, 1991.

[MSD+72] T. Miyakawa, S. Sumiyoshi, M. Deshimaru, T. Suzuki, H. Tomonari, F. Yasuoka, and S. Tatetsu. Electron microscopic study on schizophrenia. *Acta Neuropathologica*, 20(1):67–77, 1972.

[NDN+96] T. Niendorf, R.M. Dijkhuizen, D.G. Norris, M. van Lookeren Campagne, and K. Nicolay. Biexponential diffusion attenuation in various states of brain tissue: implications for diffusion-weighted imaging. *Magnetic Resonance in Medicine*, 36(6):847–857, 1996.

[Neu74] C. H. Neuman. Spin echo of spins diffusing in a bounded medium. *Journal of Chemical Physics*, 60:4508–4511, 1974.

[NY06] T.S. Newman and H. Yi. A survey of the marching cubes algorithm. *Computers & Graphics*, 30(5):854–879, 2006.

[Ots75] N. Otsu. A threshold selection method from gray-level histograms. *Automatica*, 11:285–296, 1975.

[PA03] G. Parker and D. Alexander. Probabilistic Monte Carlo based mapping of cerebral connections utilising whole-brain crossing fibre information. pages 684–695, 2003.

[PCR+99] S. Peled, D.G. Cory, S.A. Raymond, D.A. Kirschner, and F.A. Jolesz. Water diffusion, T2, and compartmentation in frog sciatic nerve. *Magnetic Resonance in Medicine*, 42(5):911–918, 1999.

[PFS+09] E. Panagiotaki, H. Fonteijn, B. Siow, M. Hall, A. Price, M. Lythgoe, and D. Alexander. *Two-Compartment Models of the Diffusion MR Signal in Brain White Matter*. Springer, 2009.

[PFT88] W.H. Press, BP Flannery, and SA Teukolsky. WT Vetterling WT Numerical Recipes in C. 1988.

[PHZ+10] E. Panagiotaki, M. G. Hall, H. Zhang, B. Siow, M. F. Lythgoe, and D. C. Alexander. *High-fidelity meshes from tissue samples for diffusion MRI simulations*. Lecture Notes in Computer Science. Springer. MICCAI 2010, 2010.

[PLSK06] S. Pieper, B. Lorensen, W. Schroeder, and R. Kikinis. The na-mic kit: Itk, vtk, pipelines, grids and 3d slicer as an open platform for the medical image computing community. pages 698–701, 2006.

[PM08] J.B. Pawley and B.R. Masters. Handbook of biological confocal microscopy. *Journal of Biomedical Optics*, 13:029902, 2008.

[PMO03] G. Partadiredja, R. Miller, and D. E. Oorschot. The number, size, and type of axons in rat subcortical white matter on left and right sides: A stereological, ultrastructural study. *Journal of Neurocytology*, 32:1165–1179, 2003.

[Pri97] W. S Price. Pulse-Field Gradient Nuclear Magnetic Resonace as a tool for studying translational diffusion: Part 1. Basic theory. *Magnetic Resonance: an Educational Journal*, 9:299–336, 1997.

[RCC+00] S.E. Rose, F. Chen, J.B. Chalk, F.O. Zelaya, W.E. Strugnell, M. Benson, J. Semple, and D.M. Doddrell. Loss of connectivity in Alzheimer's disease: an evaluation of white matter tract integrity with colour coded MR diffusion tensor imaging. *British Medical Journal*, 69(4):528, 2000.

[RHM87] M. Roberts, J. Hanaway, and D.K. Morest. *Atlas of the human brain in section*. Lea & Febiger Philadelphia, 1987.

[RHWW03] T.G. Reese, O. Heid, R.M. Weisskoff, and V.J. Wedeen. Reduction of eddy-current-induced distortion in diffusion MRI using a twice-refocused spin echo. *Magnetic Resonance in Medicine*, 49(1):177–182, 2003.

[RK03] D. G. Regan and P. W. Kuchel. Simulations of NMR-detected diffusion in suspensions of red cells: the "signatures" in q-space plots of various lattice arrangements. *European Biophysics Journal*, 31:563–574, 2003.

[RSGR98] G. Rajkowska, L.D. Selemon, and P.S. Goldman-Rakic. Neuronal and glial somal size in the prefrontal cortex: a postmortem morphometric study of schizophrenia and Huntington disease. *Archives of General Psychiatry*, 55(3):215, 1998.

[SB05a] P. N. Sen and P. J. Basser. A model for diffusion in white matter in the brain. *Biophysical*, 89:2927–2938, 2005.

[SB05b] D.L. Sherman and P.J. Brophy. Mechanisms of axon ensheathment and myelin growth. *Nature Reviews Neuroscience*, 6(9):683–690, 2005.

[SBL+95] P. Scheltens, F. Barkhof, D. Leys, E.C. Wolters, R. Ravid, and W. Kamphorst. Histopathologic correlates of white matter changes on MRI in Alzheimer's disease and normal aging. *Neurology*, 45(5):883, 1995.

[Sch78] G. Schwarz. Estimating the dimension of a model. *The Annals of Statistics*, 6:461–464, 1978.

[Sfbtdt09] K. K. Seunarine and D. C. Alexander. Multiple fibres: beyond the diffusion tensor. *In Diffusion MRI: from quantitative measrement to in vivo neuroanatomy.* Academic Press, 2009.

[SG91] M. Shephard and M. Georges. Automatic three-dimensional mesh generation by the finite octree technique. *International Journal for Numerical Methods in Engineering*, 32(4):709–749, 1991.

[SH03] E.D. Schwartz and D.B. Hackney. Diffusion-weighted MRI and the evaluation of spinal cord axonal integrity following injury and treatment. *Experimental Neurology*, 184(2):570–589, 2003.

[SJ95] O. Söderman and B. Jönsson. Restricted diffusion in cylindrical geometry. *Journal of magnetic resonance. Series A*, 117(1):94–97, 1995.

[Som06] P. Somasundaran. *Encyclopedia of surface and colloid science*. CRC Press, 2006.

[SRA10] A. Sherbondy, M. Rowe, and D. Alexander. MicroTrack: An Algorithm for Concurrent Projectome and Microstructure Estimation. *Medical Image Computing and Computer-Assisted Intervention–MICCAI 2010*, pages 183–190, 2010.

[SS06] E.E. Sigmund and Y.Q. Song. Multiple echo diffusion tensor acquisition technique. *Magnetic resonance imaging*, 24(1):7, 2006.

[SSWH97] G. J. Stanisz, A. Szafer, G. A. Wright, and R. M. Henkelman. An analytical model of restricted diffusion in bovine optic nerve. *Magnetic Resonance in Medicine*, 37:103–111, 1997.

[Sta03] G. J. Stanisz. Diffusion MR in biological systems: tissue compartments and exchange. *Israel Journal of Chemistry*, 43:33–44, 2003.

[Ste93] J. Stepisnik. Time-dependent self-diffusion by NMR spin-echo. *Physica B: Condensed Matter*, 183(4):343–350, 1993.

[Ste04] J. Stepisnik. Averaged propagator of restricted motion from the Gaussian approximation of spin echo. *Physica B: Condensed Matter*, 344(1-4):214–223, 2004.

[STSB09] T.M. Shepherd, P.E. Thelwall, G.J. Stanisz, and S.J. Blackband. Aldehyde fixative solutions alter the water relaxation and diffusion properties of nervous tissue. *Magnetic Resonance in Medicine*, 62(1):26–34, 2009.

[Sue02] P. Suetens. *Fundamentals of medical imaging*. Cambridge Univ Pr, 2002.

[SW05] D. Semwogerere and E.R. Weeks. Confocal microscopy. *Encyclopedia of Biomaterials and Biomedical Engineering. G. Wnek, and G. Bowlin, editors. Taylor and Francis, New York*, 2005.

[SWKB+07] K. Schmierer, C.A.M. Wheeler-Kingshott, P.A. Boulby, F. Scaravilli, D.R. Altmann, G.J. Barker, P.S. Tofts, and D.H. Miller. Diffusion tensor imaging of post mortem multiple sclerosis brain. *Neuroimage*, 35(2):467–477, 2007.

[SZG95] A. Szafer, J. Zhong, and J. C. Gore. Theoretical model for water diffusion in tissues. *Magnetic Resonance in Medicine*, 33:697–712, 1995.

[SZL+92] W.J. Schroeder, J.A. Zarge, W.E. Lorensen, et al. Decimation of triangle meshes. *CG NY ACM*, 26:65–65, 1992.

[THMG05] M. Teschner, B. Heidelberger, M. Muller, and M. Gross. A versatile and robust model for geometrically complex deformable solids. pages 312–319, 2005.

[Tof03] P. Tofts. *Quantitative MRI of the brain: measuring changes caused by disease*. John Wiley & Sons Inc, 2003.

[TRW+02] D. S. Tuch, T. G. Reese, M. R. Wiegell, N. Makrisand J. W. Belliveau, and V. J. Wedeen. High angular resolution diffusion imaging reveals intravoxel white matter fibre heterogeneity. *Magnetic Resonance in Medicine*, 48:577–582, 2002.

[TS68] J. E. Tanner and E. O. Stejskal. Restricted self-diffusion of protons in colloidal systems by the Pulsed-Gradient Spin-Echo method. *Journal of Chemical Physics*, 49:1768–1777, 1968.

[TYT+02] S. Takahashi, H. Yonezawa, J. Takahashi, M. Kudo, T. Inoue, and H. Tohgi. Selective reduction of diffusion anisotropy in white matter of Alzheimer disease brains measured by 3.0 Tesla magnetic resonance imaging. *Neuroscience letters*, 332(1):45–48, 2002.

[UOV+01] N. Uranova, D. Orlovskaya, O. Vikhreva, I. Zimina, N. Kolomeets, V. Vostrikov, and V. Rachmanova. Electron microscopy of oligodendroglia in severe mental illness. *Brain research bulletin*, 55(5):597–610, 2001.

[VdKVB05] M.S. Van der Knaap, J. Valk, and F. Barkhof. *Magnetic resonance of myelination and myelin disorders*. Springer Verlag, 2005.

[W+89] P.L. Williams et al. *Gray's anatomy*. Churchill livingstone Edinburgh, 1989.

[Wax95] S. G. Waxman. *The axon: structure, function and pathophysiology*. Oxford University Press, 1995.

[WKS95] S.G. Waxman, J.D. Kocsis, and P.K. Stys. *The axon: structure, function, and pathophysiology*. Oxford University Press, USA, 1995.

[WNJ00] T. Wilson, M.A.A. Neil, and R. Juskaitis. *Confocal microscope*. November 7 2000. US Patent 6,144,489.

[WSHH02] G.H. Weber, G. Scheuermann, H. Hagen, and B. Hamann. Exploring scalar fields using critical isovalues. In *Proceedings of the conference on Visualization'02*, pages 171–178. IEEE Computer Society Washington, DC, USA, 2002.

[WW92] A. Watt and M. Watt. *Advanced animation and rendering techniques*. Citeseer, 1992.

[WWV+09] E. Widjaja, X. Wei, L. Vidarsson, R. Moineddin, C. Macgowan, and D. Nilsson. Alteration of diffusion tensor parameters in postmortem brain. *Magnetic Resonance Imaging*, 27:865–870, 2009.

[ZA10] H. Zhang and D.C. Alexander. Axon Diameter Mapping in the Presence of Orientation Dispersion with Diffusion MRI. *Medical Image Computing and Computer-Assisted Intervention–MICCAI 2010*, pages 640–647, 2010.